

Physics and Control of Transonic Buffet

D'Aguanno, A.

DOI

[10.4233/uuid:7e4f868b-7716-4c36-8fa0-b55572d1572b](https://doi.org/10.4233/uuid:7e4f868b-7716-4c36-8fa0-b55572d1572b)

Publication date

2023

Document Version

Final published version

Citation (APA)

D'Aguanno, A. (2023). *Physics and Control of Transonic Buffet*. [Dissertation (TU Delft), Delft University of Technology]. <https://doi.org/10.4233/uuid:7e4f868b-7716-4c36-8fa0-b55572d1572b>

Important note

To cite this publication, please use the final published version (if applicable).
Please check the document version above.

Copyright

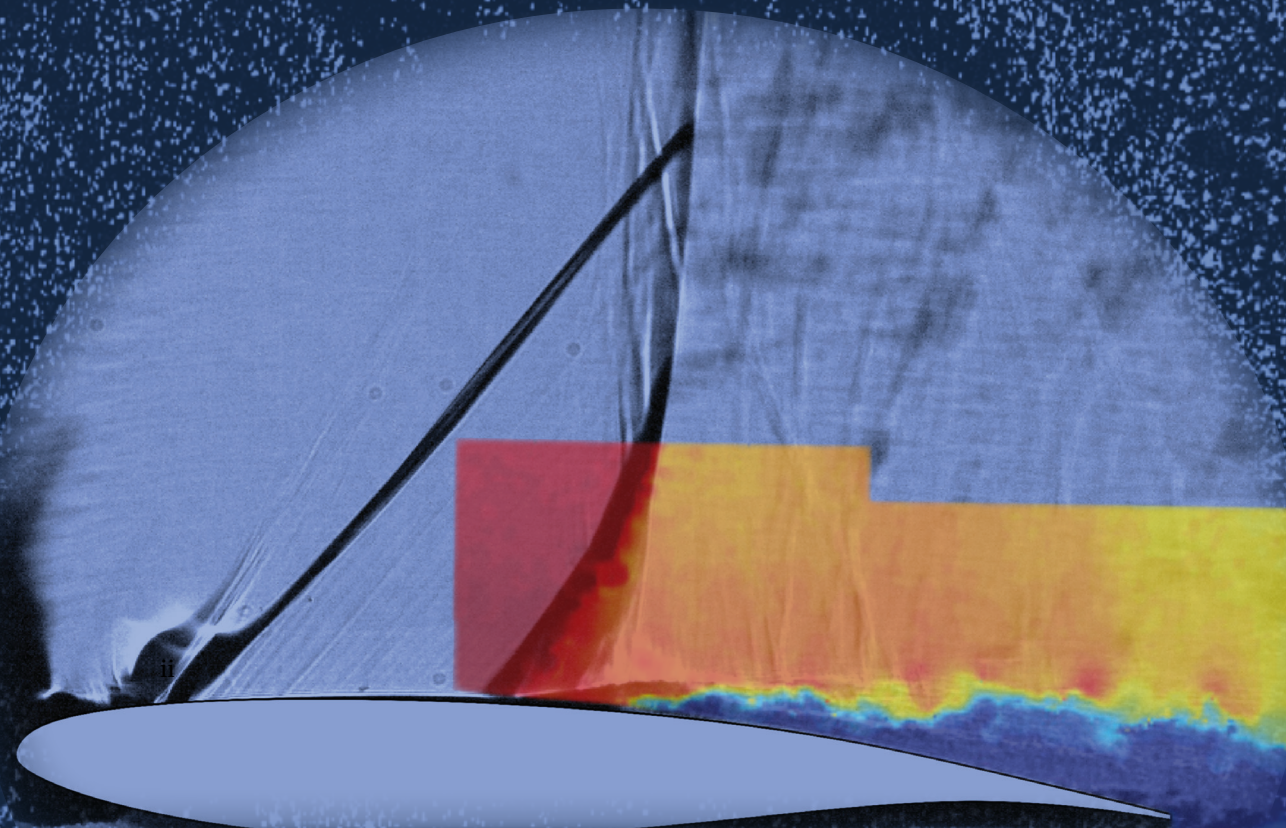
Other than for strictly personal use, it is not permitted to download, forward or distribute the text or part of it, without the consent of the author(s) and/or copyright holder(s), unless the work is under an open content license such as Creative Commons.

Takedown policy

Please contact us and provide details if you believe this document breaches copyrights.
We will remove access to the work immediately and investigate your claim.

Alessandro D'Aguanno

Physics and Control of Transonic Buffet



PHYSICS AND CONTROL OF TRANSONIC BUFFET

Dissertation

for the purpose of obtaining the degree of doctor
at Delft University of Technology,
by the authority of the Rector Magnificus, Prof.dr.ir. T.H.J.J. van der Hagen,
chair of the Board of Doctorates,
to be defended publicly on
Friday 20 January 2023 at 12:30 o'clock

by

Alessandro D'AGUANNO

Master of Science in Aeronautical Engineering,
Sapienza University of Rome, Italy,
born in Cassino, Italy.

This dissertation has been approved by the *promotor* and *copromotor*.

Composition of the doctoral committee:

Rector Magnificus	chairperson
Dr. ir. B.W. van Oudheusden	Delft University of Technology, <i>promotor</i>
Dr. ir. EEJ. Schrijer	Delft University of Technology, <i>copromotor</i>

Independent members:

Prof. dr. A. Gangoli Rao	Delft University of Technology
Prof. dr. rer. nat. habil. C.J. Kähler	Univ. der Bundeswehr München, Germany
Dr. P. Bruce	Imperial College London, United Kindom
Dr. -Ing. M. Klaas	RWTH-Aachen, Germany
Dr. V. Brion	ONERA, France
Prof. dr. F. Scarano	Delft University of Technology, <i>reserve member</i>



This work has been carried out as part of the project HOMER (Holistic Optical Metrology for Aero-Elastic Research), funded by the European Commission, program H2020 under Grant No. 769237.

Keywords: Transonic buffet, Shockwave, Control systems, Supercritical airfoil, Swept wings, PIV, Schlieren, BOS.

Printed by: Uitgeverij U2pi- Den Haag, Nederland.

Front & Back: Design by Alessandro D'Aguanno.

Copyright © 2023 by A. D'Aguanno

ISBN 978-94-6366-652-7

An electronic version of this dissertation will be available at
<http://repository.tudelft.nl/>.

Contents

Summary	ix
Prologue	1
1 Introduction	3
1.1 Motivation	3
1.2 Historical Background	4
1.3 Objective and structure of this thesis	7
2 Fundamental concepts in transonic flow	9
2.1 Transonic flow	9
2.1.1 Airfoil	9
2.1.2 Swept wing	15
2.2 Shockwave boundary layer interaction	16
2.3 State of the art on transonic buffet	19
2.4 Control of transonic buffet	28
2.5 Research questions	31
3 Experimental arrangement	33
3.1 Wind tunnel facility	33
3.2 Blockage	35
3.3 OAT15A airfoil	37
3.4 Wind tunnel configurations and models	37
3.5 Oil flow visualization	39
3.6 Schlieren	41
3.6.1 Working principle	41
3.6.2 Schlieren set-up	44
3.7 Background Oriented Schlieren (BOS)	44
3.8 Particle Image Velocimetry (PIV)	46
3.8.1 Working principle of planar PIV	47
3.8.2 Stereo PIV	48
3.8.3 PIV set-up	50
3.9 Uncertainty analysis	53

4	Data Analysis methods	57
4.1	PIV data processing	57
4.2	Phase averaging	58
4.3	POD analysis	58
4.4	Spectral Analysis	59
4.5	Aerodynamic loads determination	61
Part I	Investigation of the physical mechanism of transonic buffet	65
5	Characterization of the transonic buffet cycle	67
5.1	Introduction	68
5.2	Experimental procedures	69
5.2.1	Model and flow conditions	69
5.2.2	Experimental measurements techniques	69
5.2.3	Data processing	69
5.2.4	Uncertainty analysis	70
5.3	Flow dynamics	70
5.3.1	Spectral analysis	72
5.4	Phase-averaged flow description	73
5.4.1	Time-average velocity field	73
5.4.2	Phase definition	73
5.4.3	Phase average velocity fields	74
5.5	Modal description of flow features	76
5.5.1	POD energy spectrum	77
5.5.2	Spatial modes	77
5.5.3	Time coefficients	81
5.6	UTWs and vortex dynamics	87
5.6.1	UTW	88
5.6.2	Shear layer vortices	89
5.7	Discussion and conclusions	90
6	Spanwise Organization of Upstream Traveling Waves	93
6.1	Introduction	93
6.2	Experimental procedures	96
6.2.1	Model	96
6.2.2	Measurement techniques	96
6.2.3	Data Processing	97
6.2.4	Uncertainty analysis	98
6.3	Shockwave dynamics	99
6.3.1	Shock Position	99
6.3.2	Spectral analysis	101
6.3.3	Phase average description	102
6.4	UTWs analysis	103
6.4.1	Detection of UTWs	103
6.4.2	Propagation properties of UTWs	105

6.4.3	Frequency of UTWs	108
6.4.4	UTW strength	109
6.5	Conclusions	109
7	Finite wing and sweep effects	113
7.1	Introduction	113
7.2	Experimental investigation	115
7.2.1	Wing models	115
7.2.2	Experimental set-up	116
7.2.3	Data processing and uncertainty	118
7.3	Comparison of airfoil and unswept wing behavior	118
7.3.1	Flow features analysis by means of oil flow visualizations	118
7.3.2	Shock dynamics comparison by means of BOS	120
7.3.3	Flow field analysis for the unswept wing	121
7.4	Effect of sweep angle	123
7.4.1	Instantaneous flow field	123
7.4.2	Averaged velocity fields	124
7.4.3	Shock dynamics	126
7.4.4	Spanwise velocity component	127
7.5	Conclusion	128
	Part II Control of transonic buffet	131
8	Upper trailing edge flap flow control	133
8.1	Introduction	133
8.2	Experimental procedures	135
8.2.1	Model	135
8.2.2	Upper trailing edge flaps	135
8.2.3	Experimental techniques	135
8.2.4	Data processing	136
8.2.5	Uncertainty analysis	136
8.3	Shock dynamics	136
8.3.1	Shock position	138
8.3.2	Spectral analysis	140
8.4	Velocity field comparison	141
8.4.1	Flow field statistics	141
8.4.2	Separated area extent	143
8.4.3	Effect of serrated UTEF	145
8.4.4	Circulation evaluation	147
8.5	Sensitivity of UTEF operation to the flow condition	149
8.6	Conclusion	150
9	Shock control bumps	153
9.1	Introduction	153
9.2	Experimental investigation	154

9.2.1	Models	154
9.2.2	Shock control bump geometry	154
9.2.3	Experimental set-up	155
9.2.4	Processing parameters	158
9.2.5	Uncertainty analysis	159
9.3	Shock dynamics	160
9.4	Flow field analysis	162
9.4.1	Buffet cycle dynamics	162
9.4.2	Main statistics of the velocity field	164
9.4.3	Separated area behavior	165
9.4.4	Effect of SCB spacing on the average flow field	168
9.5	Loads determination	171
9.6	Conclusion	174
Epilogue		177
10 Conclusion and perspectives		179
10.1	Conclusion	179
10.2	Perspectives and recommendations	184
Bibliography		187
Acknowledgements		199
Biographical Note		201
List of Publications		203

SUMMARY

The flight envelope of an aircraft operating at high subsonic velocities is bounded by several limitations, one of these consists in the wing experiencing oscillations of a shockwave on its suction side for a certain range of Mach number (Ma), angle of attack (α) and Reynolds number (Re). This phenomenon is referred to as transonic buffet and it may ultimately result in violent structural oscillations of the wing (the so-called buffeting), in addition to the oscillations of the aerodynamics loads. Notwithstanding the relevance of this topic, there is not yet an only explanation regarding its mechanism, therefore, the first aim of this experimental project is to obtain further insight on the physics of transonic buffet (Part I). As a second objective, in Part II different strategies for the control of buffet have been investigated.

The experiments of this study have been carried out in the transonic-supersonic wind tunnel of TU Delft on supercritical airfoil and wings based on the OAT15A airfoil. The behavior of this phenomenon has been scrutinized using optical experimental techniques, such as particle image velocimetry (PIV), schlieren, and, background oriented schlieren (BOS).

At first, the transonic buffet cycle is characterized for fully developed buffet condition ($Ma = 0.7$, $\alpha = 3.5^\circ$, $Re = 2 \cdot 10^6$). By means of schlieren visualizations, high amplitude shockwave oscillations ($\Delta X_{SW} \approx 25\%$ of the chord, c) are observed, with a characteristic frequency contribution of 160 Hz ($St = 0.07$), in good agreement with existing literature. High speed PIV has allowed the description of the time behavior of both the shockwave and the separated area dynamics, which has been further investigated with a POD analysis. In detail, the first and the third POD modes well represent the shock oscillation and the pulsation of the separated area. Instead, the second mode is associated with an asymmetrical behavior of the separated area and of the shear layer. This asymmetry reflects the distinct behavior during the upstream and the downstream travel of the shock motion, both in terms of shock velocity and extent of the separated area. An analysis of the vortex convection velocity in the trailing edge area has indicated that the vortices created at the shock foot, which then convect into the separated region in an area detached from the airfoil, cannot be responsible for the creation of the UTWs (upstream traveling waves), which are pressure waves supposed to sustain the shockwave oscillation.

To better understand the production, organization and propagation of UTWs, a further study has been carried out on a spanwise-chordwise oriented field of view. The experimental set-up used has confirmed the two-dimensionality of the velocity field and of the shockwave, whilst revealing that the UTWs propagate at a non-zero orientation at the speed of sound relative to the flow. BOS measurements have also suggested that the UTWs are produced during the complete buffet cycle but with a modulated strength. Their intensity is observed to be higher just before the shockwave reaches its most downstream position, while it is decreasing during the upstream travel of the shockwave.

The comparison of the behavior of the airfoil model (clamped to both the side windows of the wind tunnel) and of swept and unswept wings (clamped to the wind tunnel only at their root) has revealed that the buffet oscillations are much stronger for the airfoil. This difference is particularly meaningful for the unswept wing in correspondence of the more outboard spanwise locations, suggesting that, for the unswept wing, an important role could be played by finite-wing effects, notably the tip vortex. A spectral analysis has shown that for the swept wings ($\Lambda = 15^\circ, 30^\circ$) the classical "two-dimensional" buffet peak (occurring at $f=160$ Hz) is substantially attenuated, while additional contributions in the range of 450-850 Hz appear.

Together with the study of the physics of transonic buffet, its control was also attempted by using two types of passive control systems: upper trailing edge flaps (UTEFs) placed at the trailing edge of the airfoil and shock control bumps (SCBs) positioned near the average shockwave position. The UTEFs demonstrated to be effective in reducing the relevance of transonic buffet when their height was of about 1.5-2% c , suggesting that the vortices responsible for the production of UTWs are traveling very close to the surface of the airfoil. The use of UTEFs allowed a reduction of both the shockwave oscillation range and of the pulsation of the separated area, resulting in an increase of circulation and a reduction of its variation during the different buffet phases.

Regarding the use of SCBs, an array of three-dimensional SCBs has been adopted. This control system demonstrated to be effective in reducing the oscillation range of the shockwave, thanks to the formation of a less dissipative lambda structure, with a steady oblique shockwave in correspondence of the leading edge of the bump and a quasi-normal shockwave oscillating in proximity of its crest. The SCB effectiveness proved to be highly dependent on the spanwise spacing of the bumps, with the best performance obtained when a spacing of 25% of the chord was selected. PIV analysis revealed that the SCB spacing affects the interaction between shockwave structures and the production of vortices from the tail of the bumps. A loads determination algorithm based on PIV data, has shown a reduction of drag and an increase of lift in presence of SCBs compared to the clean configuration.

PROLOGUE

1

INTRODUCTION

1.1. MOTIVATION

Flow phenomena that may result in unsteadiness of the aerodynamic loads on an aircraft have utmost relevance for the safe and reliable flight operation in both civil and military aircraft. In some applications this instability can be caused by an interaction between aerodynamic, inertial, and elastic forces, such as in the case of aerodynamic flutter. Particular to the transonic regime is the mechanism of buffet, where the oscillation of the aerodynamic loads is induced by a self-sustained oscillation of a shockwave (SW) which occurs in the transonic regime (see Fig.1.1) for a certain range of Ma , α , and Re values. This specific phenomenon will be the study object of this thesis. The interaction with the structure could result in oscillation of the wing structure itself (in which case it is referred to as buffeting), eventually bringing it to its failure due to fatigue. It is therefore not surprising that transonic buffet was found to strongly limit the performance of the first aircraft experiencing (near-)sonic conditions in the 1940s and 1950s, and led to some fatal accidents. Although today this problem is recognized especially as a factor that limits the performance of civil aircraft, in the past the occurrence of transonic buffet was originally encountered in relation to limiting defense aircraft, as discussed in the following historical background.

Nowadays the regulation work of flight authorities has ensured that catastrophic consequences as a result of transonic buffet are avoided, but of course this has come with some compromises. In fact, in order to ensure safe operation, the aircraft regulation authorities impose conservative margins on the flight envelope. As described by the Federal Aviation Administration (FAA), for transport aircraft with operative Mach number higher than 0.6 or with an operative altitude greater than 25000 ft, the buffet onset should always be evaluated. An example of the buffet boundaries in terms of load factor and equivalent air speed is given in Fig.1.2, which shows that this phenomenon bounds the flight envelope before reaching the dive speed (V_D). On real aircraft the buffet onset is often defined by a qualitative evaluation of the pilot or when a vertical acceleration of $\pm 0.05g$ takes place. With respect to this buffet onset, aircraft regulations impose a

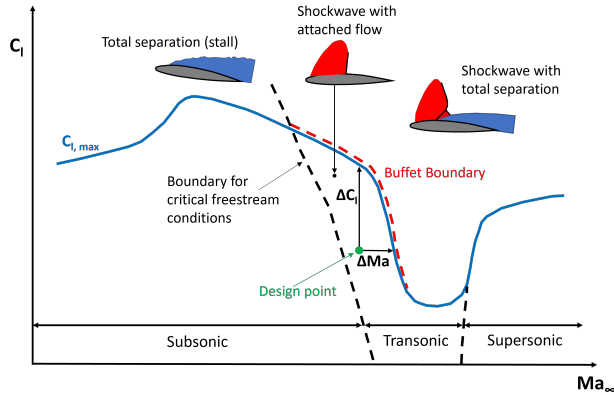


Figure 1.1: Effect of transonic buffet on the flight envelope in terms of maximum lift coefficient ($C_{l,max}$) and freestream Mach number (Ma_{∞}), adapted from Stanewsky and Basler (1990)

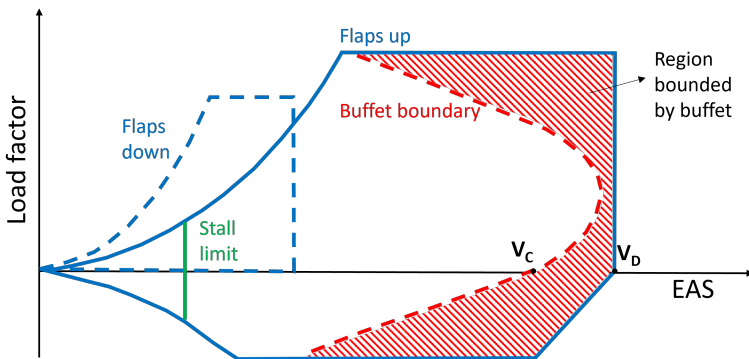


Figure 1.2: Typical flight envelope of a civil aircraft in terms of load factor and EAS.

0.3 g margin (Piccola (2012)). This is summarized by Fig.1.1, which clearly shows the requirement of a safety margin for both lift and Mach number at the design condition. Transonic buffet can be expected to become even more limiting for future generation aircraft, as they are increasingly characterized by light and flexible wings and therefore more sensitive to buffeting loads.

In this context, understanding and consequently controlling (i.e., suppressing or mitigating) transonic buffet could ultimately contribute to an increase of the available flight envelope of a civil aircraft. Potentially then, this could allow the aircraft to fly in a more efficient region of the flight envelope where its performance, from both an aerodynamic and an energetic point of view, could be optimized.

1.2. HISTORICAL BACKGROUND

The study of compressible flows has for many years interested researchers around the world. First experimental studies on this phenomenon were carried out by Ernst Mach in



Figure 1.3: Macchi M.C.72 seaplane.

1887, who was able to visualize shockwaves developing around a bullet moving at supersonic velocities using the novel shadowgraph technique (see [Mach and Salcher \(1887\)](#)). Around the same years the Swedish scientist Gustaf de Laval developed a nozzle to increase the stream jet to supersonic speeds ([de Laval \(1894\)](#)). This nozzle (nowadays referred to as a 'de Laval nozzle') had an important impact on the aeronautic world and was used for the first time in the liquid-propellant rocket engine nozzle designed by Robert Goddard in 1926 ([Goddard \(1970\)](#)).

At the beginning of 20th century a large amount of theoretical research was carried out on compressible flows by, among the others, Ludwig Prandtl, Theodore von Karman, Theodor Meyer, and Ascher Shapiro. Nevertheless, it took until the 1930s before that compressible flows became relevant for actual aeronautical applications.

First local compressible phenomena started to be of interest for the tip of propellers following the increase in power of aeronautical engines. Because of this growing interest, Lynam tested a propeller model at tip speeds up to 360 m/s, revealing a loss of thrust and an increase in blade drag ([Lynam \(1919\)](#)). To better substantiate this phenomenon, in the United States Caldwell and Fales built the first wind tunnel with the main goal of understanding the occurrence of these high speed losses ([Caldwell and Fales \(1920\)](#)). In these tests a maximum speed of "only" 205 m/s was reached at the propeller tip, which was nevertheless sufficient to observe compressibility effects in terms of both decrease of lift and increase of drag. Additional tests undertaken by Reed on metal propellers revealed that, by using thin sections, the detrimental compressibility effects were avoided. The velocity at which these compressibility effects were taking place was defined as the critical speed, however, the relation between the occurrence of the critical velocity and the speed of sound was given only later by [Briggs and Dryden \(1927\)](#).

First compressible effects on airplane wings took place in the late 1930s, it is the case of seaplanes which were constructed to participate in the prestigious Schneider Trophy. One of these seaplanes, the Macchi M.C.72 (see [Fig.1.3](#)), was able to reach the record velocity of 709 km/h which is still the record for a seaplane today. The pilots of the Macchi M.C.72 complained about the occurrence of strong buffeting which was thought to be



Figure 1.4: Bell X-1 aircraft

caused by flow separation induced by compressibility effects. The appearance of these problems in aviation motivated Italy (and in particular General G. Arturo Crocco) to organize in 1935 one of the most influential fluid dynamic congresses of all times: the Fifth Volta Congress on the topic of "High Velocities in Aviation" (see Ferrari (1996)). The importance of this conference may be illustrated by considering that some of the participants' names were Prandtl, Taylor, von Karman, Pistolesi, Busemann, Douglas, Ackeret, Jacobs. Despite the most influential and relevant aerodynamicist of the time being Ludwig Prandtl, the researcher that had the most important impact on this congress was the 34-year-old Adolf Busemann. During his lecture, for the first time Busemann proposed the concept that the compressibility effects felt by a wing are only dependent on the component of the Mach number normal to the leading edge (Busemann (1935)). Therefore, by rotating a wing to a certain sweep angle, it is possible to reduce, or better delay, the occurrence of compressibility effects. This idea was so innovative that it was not understood by many of the other researchers of the time. Von Karman, for example, many years later confirmed that Busemann's innovation was crucial for the design of modern jet aircraft but he also admitted that at the time of the Volta conference he "did not pay much attention to this suggestion".

Notwithstanding the remarkable work of Busemann and the limited case of the Macchi M.C.72, at the time of the Volta conference, most of the researchers were aware that in order to reach high flight Mach numbers and high altitudes on operational aircraft, also a new form of propulsion system was required, therefore, they considered the manifestation of similar problems still distant in time. However, compressibility problems became more and more important for strategic reasons during World War II. Apart from the propeller tip, these problems started to be observed in particular flight maneuvers such as in shallow dives bringing to compressible effects on wings/stabilizers. This was the case for the Messerschmitt Me 109, whose pilots experienced control forces which were not tolerable and eventually also brought to a fatal accident in 1937. In the US, compressibility effects were both considered responsible for the crash of the Lockheed

P-38 aircraft and for buffeting and problem of controllability of the Republic P-47 aircraft. Similarly in the UK, compressibility effects were considered responsible for the drag rise of the Supermarine Spitfire.

Recurrent problems consisted of: low controllability of the aircraft and the requirement for relevant control forces for the control of the elevator. A series of reactions of the aircraft phrased as: wing drop, nose slice, snaking, pitch up, pitch down, and buffet were all encountered. A great development of the airplanes of this period was achieved with the introduction of jet-turbine engines. The first test on a turbojet was done in 1939 in Germany on the Heinkel He178, although at a velocity which was too low for compressibility effects ($Ma = 0.5$) to manifest. With the Arado Ar234A compressibility effects started to be relevant, with elevator buffeting and problems in the controllability happening for $V = 850\text{ km/h}$. Similar problems were also encountered by the Messerschmitt Me262.

A solution for these issues was urgently required, so, it is not surprising that by the end of the war many countries had adopted swept wing aircraft configurations, the first one being the Messerschmitt Me 262. This aircraft had a clear technical advantage compared to the unswept wing aircraft used by the British and the United State armies, who started to use them in 1950s (such as the North American F-86 Sabre and the Boeing B-47 Stratojet). The limiting factors of the different airplanes of this period have been summarized by Hans-Ulrich Meier in his book (Meier (2010)) and some of these findings are reported in Table 1.1.

Together with the problem of controllability, it is clear that most of the aircraft of that time were limited by buffeting phenomena which explains the global interest in the understanding of transonic buffet in the following years.

Some years later, initial research in wind tunnels will allow NACA to widen the knowledge on existing airfoils up to $Ma = 1$, providing first measurement data at sonic conditions. This knowledge will also eventually allow the operation of aircraft at fully supersonic conditions, with the first flight with $Ma_\infty > 1$ taking place on 14 October 1947 with the rocket propelled Bell X-1 (see Fig.1.4).

1.3. OBJECTIVE AND STRUCTURE OF THIS THESIS

Notwithstanding the important achievements by many researchers in understanding transonic buffet, this phenomenon has not been completely understood yet. Because of this, the flight envelope of contemporary aircraft is still bounded by the limitations associated to the occurrence of this phenomenon. Therefore, to further optimize the performance of an aircraft (both in civil and in military applications) with respect to this phenomenon, two main goals should be achieved first:

1. Obtaining a deeper understanding of the transonic buffet mechanism;
2. Controlling transonic buffet.

This thesis will first give a more detailed discussion of transonic flows in general and more specifically of transonic buffet in Chapter 2. Drawing on this assessment of the literature, the state-of-the-art knowledge and corresponding research gaps are identified. From this, the research questions are accordingly formulated in more detail. Sub-

Table 1.1: Limiting factors of several aircraft in 1940s-50s

Aircraft	Propulsion system	Max Ma_∞	Limiting factors
Mustang I	Propeller	0.80	Pitch oscillations
Mustang III	Propeller	0.82	Nose-heaviness, porpoising
Spitfire IX	Propeller	0.85	Drag rise
Spitfire XXI	Propeller	0.85	Drag rise, buffeting, propeller effic.
Me 109	Propeller	0.80	Nose-heaviness, elevator ineffective
Do 335	Propeller	0.76	Yawing, porpoising
FW 190	Propeller	0.82	Trimming, drag rise, buffeting
Ta 152	Propeller	0.80	Buffeting
Tempest V	Propeller	0.85	Nose-heaviness
E28/39	Jet	0.82	Buffeting
Vampire I	Jet	0.80	Pitch oscillations, tail-heavy
Meteor I	Jet	0.8	Buffeting, tail-heavy
Are 234	Jet	0.80	Buffeting, drag rise
Me 262	Jet	0.86	Buffeting, nose-heaviness, yaw, roll
He 162	Jet	0.80	Buffeting
He 280 V7	Jet	0.75	Buffeting
Me 163	Rocket	0.80	Buffeting, nose-heaviness, roll

sequently, the methodology used in this thesis is described in Chapter 3 (Experimental arrangement) and Chapter 4 (Data analysis methods). The discussion of the results is organized into two Parts, each of them addressing one of the previously listed main goals. The specific content of each Part will be further clarified in Section 2.5. Finally, conclusions are drawn in Chapter 10.

2

FUNDAMENTAL CONCEPTS IN TRANSONIC FLOW

2.1. TRANSONIC FLOW

Transonic flow is defined as the flow regime where there is a simultaneous presence of regions with a local velocity lower and higher than the speed of sound. This is the typical flow regime experienced by most modern civil aircraft on their wings.

2.1.1. AIRFOIL

When the freestream velocity upstream of an airfoil is gradually increased (see Fig.2.1), at first the entire surrounding flow field will be subsonic, with the stagnation point located in proximity of the leading edge. At a specific location of the suction side, depending on the geometry of the airfoil and the angle of attack, the lowest value of C_p will be reached and correspondingly the highest flow velocity. An increase of the Mach number will lead to a further decrease of the pressure on the suction side of the airfoil. For a specific value of the Mach number, the pressure distribution on the suction side will be such that in a single point sonic conditions are first achieved. The freestream Mach number for which this condition is met is defined as the critical Mach number (Ma_{cr}).

When Ma_∞ is increased above Ma_{cr} , a local supersonic area is formed on the airfoil, which causes that on the convex surface of the suction side, expansion waves are generated. These waves reflect on the sonic line as compression waves with the same slope. The reflected waves, after impinging on the surface of the airfoil are reflected once again with the topology of the reflected wave being dependent on the local shape of the airfoil. For a flat panel surface (or close to flat), as is the case of many supercritical airfoils (in the supersonic bubble), the wave is reflected again as a pressure wave of the same family (see Fig.2.2, left). In contrast, if the surface is sufficiently convex the wave is reflected as a pressure wave of the opposite family. Nevertheless, if the airfoil is properly designed a situation without secondary reflections can be achieved. In practice, however, this type of airfoil geometry is not used in view of its sensitivity to the specific flow condition. For

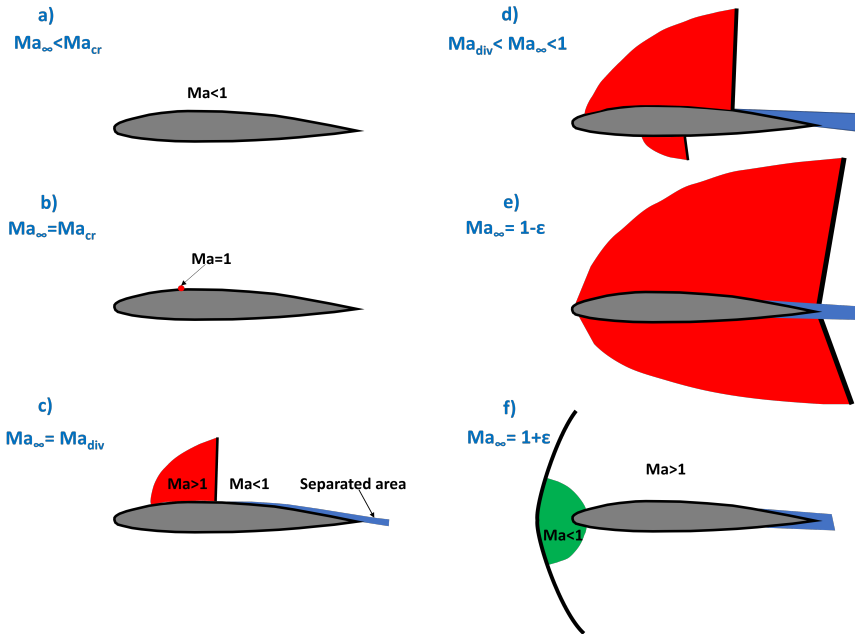


Figure 2.1: Effect of an increasing Mach number on the flow features developing on an airfoil.

geometric reasons the compression waves are convergent and tend to coalesce forming a near-normal shockwave as sketched on the right of Fig.2.2.

With a further increase of the freestream Mach number, the supersonic region expands, with shockwave becoming stronger and located more downstream. Depending on the angle of attack and the shape of the airfoil, a shockwave will also eventually appear on its pressure side. Since the airfoil is relatively flat on the pressure side, the shockwave could reach the trailing edge earlier on this side compared to the suction side. For a certain value of the Mach number, both shockwaves are located at the trailing edge and connected by a curved shockwave. For a Mach number slightly higher than one, corresponding to a supersonic inflow, a detached shockwave appears upstream of the leading edge of the airfoil. Upstream of this shockwave the flow is supersonic and a region of subsonic flow is formed in the vicinity of the leading edge. By further increasing the freestream Mach number, the distance between the detached shockwave and the leading edge of the airfoil is reduced. Although a small subsonic region will always persist, flows with a freestream Mach number higher than 1 are considered to be fully supersonic.

After increasing Ma above Ma_{cr} , the near-normal shockwave on the airfoil moves downstream and increases in strength, and as a consequence a separation of the boundary layer may occur. The boundary layer separation and in particular the "losses" connected to the formation of the normal shock (wave drag) dramatically increase the drag of the airfoil. The Mach number at which the increase in drag become significant is defined as the drag-divergence Mach number (Ma_{div}), and further increases of Ma could

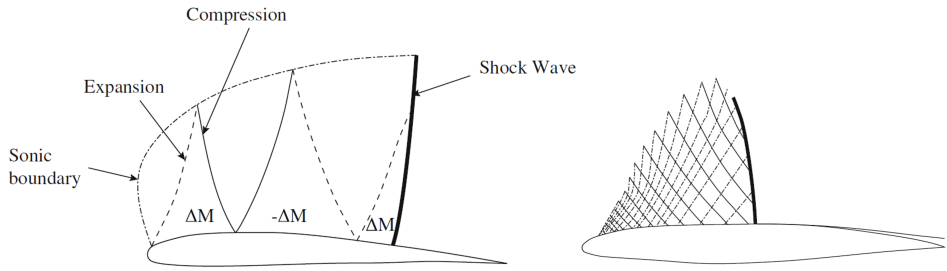


Figure 2.2: Formation of a shockwave on an airfoil experiencing transonic conditions (Vos and Farokhi (2015)).

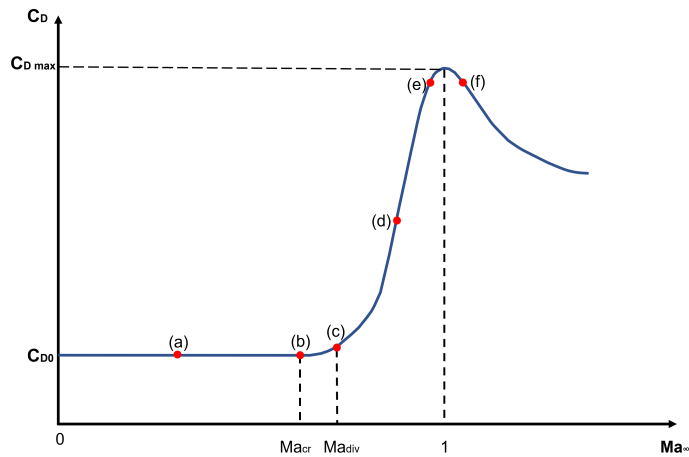


Figure 2.3: Effect of Mach number on drag coefficient. Figure adapted from Anderson (2011).

bring to values up to 10 times higher than the incompressible drag coefficient value. This increase in drag coefficient is indicated in Fig. 2.3, which clearly shows an abrupt increase in drag for $Ma > Ma_{div}$ and a reduction for $Ma > 1$.

In contrast, the lift coefficient at first increases with the Mach number, while with the occurrence of flow separation increasing values of Ma cause a relevant reduction. In view of the aerodynamic coefficients behavior, it may be evident that for the operation of a civil aircraft in the transonic regime, it is beneficial to postpone the formation of sonic areas on the suction side of a wing (increasing critical Mach number). In addition, the presence of shock/separated area (see Section 2.3 for more details), for particular values of α and Ma could result in unsteady effects which consist in an oscillation of the shockwave and a pulsation of the separated area (transonic buffet).

For the Volta conference Jacobs, in addition to a visualization of the burble phenomenon, derived the first relation between the low speed suction pressure peak and the Mach number at which the speed of sound would be reached locally. For the first time it was understood that a change of the critical Mach number could be achieved by a modification of the shape of the airfoil.

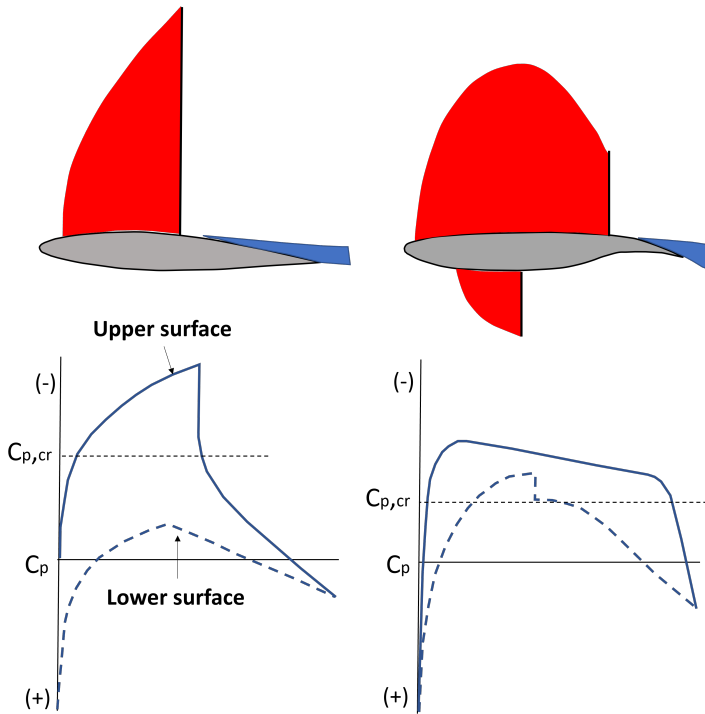


Figure 2.4: Comparison of pressure distribution for a 6-digit (left) and a supercritical airfoil (right). Figure adapted from [Whitcomb and Clark \(1965\)](#).

Initially, it was believed that the only strategy for limiting compressibility effects on an airfoil was that of using an as thin as possible airfoil (like the NACA 64 airfoil series), as this result in an increase of the critical Mach number. In view of this it is understandable that the first airplane that reached supersonic velocities (the Bell X-1) made use of a very thin airfoil (10 percent of the chord). Unfortunately, for a general aircraft the thickness parameter could not be decreased beyond a certain level in view of structural and fuel capacity reasons.

To solve this problem a new typology of airfoil, referred to as supercritical airfoils, was designed with the goal of postponing the occurrence of the divergence Mach number. A typical supercritical airfoil is characterized by a large leading edge radius (when compared to a NACA 6 digits airfoil), a flattened upper surface and a highly cambered aft section. In Fig.2.4 a supercritical and a 6-digit NACA airfoil are compared. In view of the flattened upper surface, for the supercritical airfoil the front part contributes less to the total lift when compared to the classical airfoil. However, for a supercritical airfoil additional lift is created by its aft part, thanks to its additional camber (aft loading).

The first supercritical airfoils were designed by the German aerodynamicist Kawalki during World War II and similar airfoils were introduced in the USA in 1964 by Richard T. Whitcomb at the Langley Research Center ([Whitcomb and Clark \(1965\)](#)). As a result of the specific geometry of the supercritical airfoils the local supersonic area on the suction

side is followed by a weaker shockwave (when compared to the case of a conventional airfoil), which reduces the strength of the shockwave-boundary layer interaction occurring on the suction side of an airfoil.

To appreciate the difference in C_p distribution along a supercritical and a NACA 6-digit airfoil, both distributions are shown in Fig. 2.4 for $Ma = 0.75$ (figure adapted from Whitcomb and Clark (1965)).

Also for supercritical airfoils, the occurrence of compressible phenomena depends on the relative thickness, as described by the following empirical relation derived in Torenbeek (2013) (and based on the experimental data of Harris (1990)) between Ma_{div} , the thickness ratio of the airfoil (t/c) and the value of the lift coefficient (C_l):

$$Ma_{div} = 0.935 - \frac{t}{c} - 0.1C_l^{1.5} \quad (2.1)$$

Thus, supercritical airfoils with the same chord length but with larger thickness will result in a higher perturbation (increase) of the freestream velocity when compared to a thinner airfoil, yielding lower values of the divergence (and critical) Mach number. As for the thickness parameter, an increase in lift is generally associated with a higher perturbation of velocity and therefore, to a lower value of the critical/divergence Mach number.

In addition to these two-dimensional considerations, further effects preventing aircraft from reaching supersonic velocities were associated with the drag caused by three-dimensional shape and the presence of the fuselage and other non-lifting surfaces. To address this issue, the American scientist Whitcomb took into account the pre-existing knowledge on bullets which were known to be able to reach supersonic speed, thanks to their particular shape. Previous studies had shown that bullets with a smooth variation of the cross-sectional area outperform bullets with an abrupt variation in shape, therefore, the same variation of the cross sectional area was proposed for aircraft. To reduce or eliminate the discontinuous variation in cross-sectional area, which generally occurs at the leading and trailing edge of the wing, the cross-sectional area of the fuselage was reduced in correspondence to that of the wing. Experimental tests in transonic wind tunnels confirmed Whitcomb's intuition, referred to as "area rule concept", allowing to clearly reduce the drag peak close to $Ma = 1$.

Linearized description of transonic flows

For the compressible, inviscid flow around thin airfoils, a simplified small-perturbation potential equation can be derived. Defining Ma_∞ as the freestream Mach number, ϕ as the perturbation velocity potential, γ as the ratio between specific heat at constant pressure and volume, and as δ the ratio between $(\gamma - 1)/2$, the following equation is obtained:

$$\begin{aligned} (1 - M_\infty^2)\phi_{xx} + \phi_{yy} &= M_\infty^2 [2(1 + \delta)\phi_x + (1 + \delta)\phi_x^2 + \delta\phi_y^2]\phi_{xx} \\ &+ M_\infty^2 [2\delta\phi_x + \delta\phi_x^2 + (1 + \delta)\phi_y^2]\phi_{yy} + M_\infty^2 \phi_y 2(1 + \phi_x)\phi_{xy} \end{aligned} \quad (2.2)$$

In the case of a subsonic or a supersonic flow, the terms on the right side of the equation are of higher order and therefore negligible, bringing to:

$$(1 - M_\infty^2)\phi_{xx} + \phi_{yy} = 0 \quad (2.3)$$

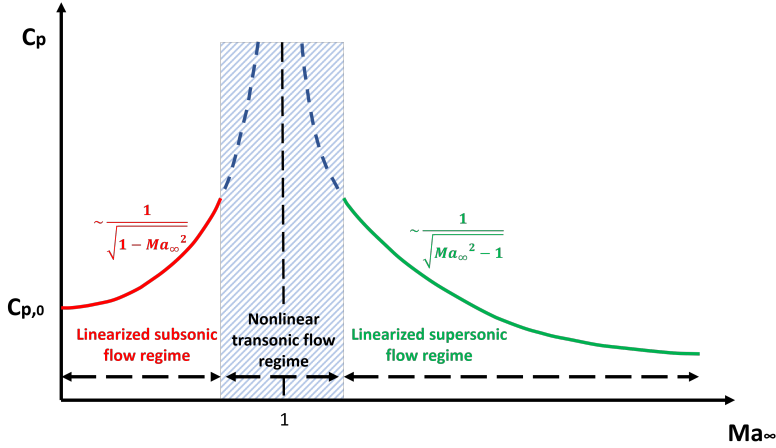


Figure 2.5: Behavior of pressure coefficients predicted from linearized subsonic and supersonic theories.

These simplified models allow for these two regimes the evaluation of the compressibility effect on pressure, drag and lift coefficients (C_x) for an airfoil operating at a certain Mach number from its respective incompressible value. In the subsonic regime defining $\beta = \sqrt{1 - M_\infty^2}$, it holds that:

$$C_x = \frac{C_{xinc}}{\beta} \quad (2.4)$$

while for supersonic conditions ($\lambda = \sqrt{M_\infty^2 - 1}$):

$$C_x = \frac{C_{xinc}}{\lambda} \quad (2.5)$$

This behavior is indicated in Fig.2.5 with both the linearized flow regimes estimating asymptotically infinite values of the load coefficients for $Ma \rightarrow 1$. Therefore, the previous model is evidently inappropriate for transonic flows in view of the approximations previously taken into consideration. In particular, for transonic flows the term $(1 - M_\infty^2)$ becomes of the same order of magnitude of other terms which have been previously neglected. Taking into account these additional terms, the transonic small disturbances equation is derived:

$$\left[(1 - M_\infty^2) - M_\infty^2 (\gamma + 1) \frac{\phi_x}{V_\infty} \right] \phi_{xx} + \phi_{yy} = 0 \quad (2.6)$$

Unfortunately, there is no analytical solution for this equation, although some similarity solutions are possible for affinely-related bodies (Shapiro (1955), Vos and Farokhi (2015)). The lack of analytical solutions even for simple geometries justifies the great demand for experiments on transonic flows in the last 70 years. At the infancy of the transonic wind tunnel testing, these experiments produced a series of empirical rules for

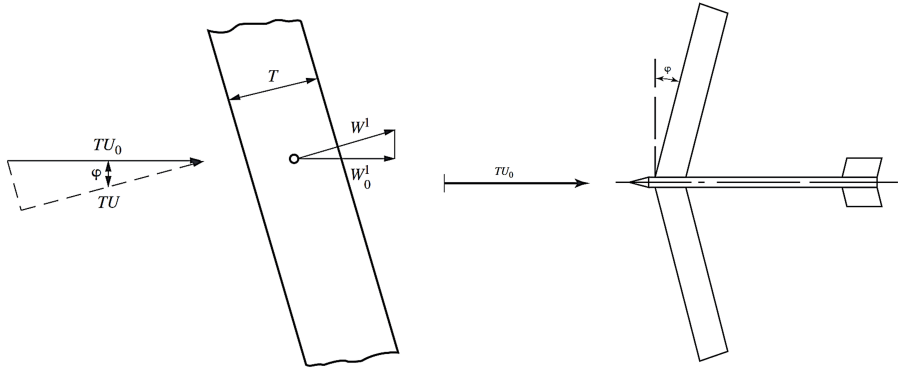


Figure 2.6: Swept wing: on the left, decomposition of normal and parallel to the leading edge velocity components. On the right, original sketch from Busemann of a swept wing aircraft (Busemann (1935)).

the study of transonic flows. Nowadays, the development of computational power offers the possibility of studying transonic flows from a numerical point of view. However, the necessity of experimental data to properly validate new simulations is still required.

2.1.2. SWEEP WING

As previously anticipated in the historical background, another revolutionary innovation to postpone the occurrence of detrimental compressible phenomena was the employment of swept wings (Busemann (1935)).

The use of a swept wing is based on the concept that the formation of supersonic areas (and consequently of shockwaves) on the suction side of a wing depends only on the velocity component normal to the leading edge of the wing. For a flow approaching a swept wing with a sweep angle Λ (see Fig.2.6) the freestream velocity component can be described as the combination of a tangential component $V_{\infty t}$ parallel to the leading edge of the wing and a normal component $V_{\infty n}$ orthogonal to it.

$$V_{\infty t} = V_{\infty} \cos(\Lambda) \quad (2.7)$$

$$V_{\infty n} = V_{\infty} \sin(\Lambda) \quad (2.8)$$

The velocity component parallel to the leading edge does not induce any variation in pressure and therefore the aerodynamic problem is analogous to that of a freestream flow with velocity $V_{\infty n}$ on an unswept wing. Therefore, for a supersonic freestream (depending on the specific value of sweep angle), the normal velocity component can still be subsonic, such that the flow field around the wing behaves as if the inflow would still be subsonic.

Swept wings are therefore associated to relatively high critical and drag divergence Mach numbers, allowing flight operations at higher Mach numbers compared to unswept wings. It is worth mentioning that, since the velocity component parallel to the leading edge is not contributing to a variation in pressure, also the production of lift is only associated with the velocity component normal to the leading edge of the airfoil. This could

result in insufficient lift in stages such as take off and landing and, thus, requires the use of runways with appropriate lengths.

A different perspective of the beneficial effect of a swept wing is given by [Anderson \(2011\)](#), who states that a straight wing with sweep angle Λ has an effective chord which is larger by a factor $1/\cos(\Lambda)$. Since there is no variation in the effective thickness of the airfoil, the ratio t/c is clearly reduced in presence of sweep angle. Therefore, the airfoil can be considered "thinner" with respect to the airfoil of an unswept wing, and thus, with a higher associated critical Mach number.

2

2.2. SHOCKWAVE BOUNDARY LAYER INTERACTION

In transonic buffet a shockwave interacts with the boundary layer, and for these flow conditions the shockwave oscillates with a clearly periodic fashion. This interaction between the shockwave and the boundary layer can be considered as a particular case of the so called shockwave-boundary layer interaction (SWBLI). Different forms of SWBLIs have been defined in literature, based on the interaction geometry, such as the case of a compression ramp ([Beresh et al. \(1998\)](#), [Ganapathisubramani et al. \(2009\)](#)), an oblique impinging shockwave ([Piponnier et al. \(2009\)](#), [van Oudheusden et al. \(2011\)](#)), and the case of a normal shockwave ([Bruce and Babinsky \(2008\)](#), [Pirozzoli et al. \(2010\)](#)).

For the transonic study of an airfoil, the case of the normal shockwave interaction is the most relevant. The interaction may exhibit changes in character according to the state of the boundary layer and allow to distinguish between either a laminar or a turbulent SWBLI. However, for the very high Reynolds number values typical for the operation of a wing at transonic conditions, the flow can always be considered turbulent. Therefore, this specific interaction will be discussed in more detail.

Transonic SWBLI may be encountered in a variety of applications such as on aircrafts, helicopters or launch vehicles and, thus, both in internal and external flows. As discussed by [Babinsky and Harvey \(2011\)](#), two typologies of SWBLI can be distinguished according to the shockwave strength: a weak and a strong interaction. For transonic buffet both interactions may occur at different phases of the buffet cycle. This is illustrated in [Fig.2.7](#) with two instantaneous schlieren images. The image on the left shows a situation in which the shockwave is quasi-normal and no flow separation is induced at the shock foot (weak interaction), and the image on the right illustrates the case where the shockwave has adopted a λ -shape and is strong enough to trigger separation (strong interaction).

In the case of a weak interaction ([Moulden \(1984\)](#)), the strength of the shockwave is such that no flow separation occurs, although an increase in the boundary layer thickness is observed, as sketched in [Fig.2.8](#). In view of this increase in thickness, the streamlines are diverted, causing the formation of compression waves (in correspondence of the sonic line), which will eventually merge in a shockwave outside of the boundary layer. Although the pressure gradient is very high across the shockwave (in view of the sudden jump in pressure), within the boundary layer the situation is different, since the pressure increase is spread on a wider region. This gradual increase in pressure is the main reason that no separation occurs immediately downstream of the shockwave in a weak interaction. However, in view of the increased adverse pressure gradient, separa-

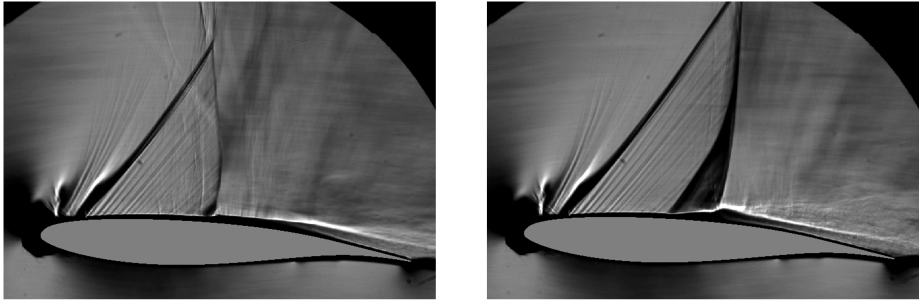


Figure 2.7: Two different typologies of transonic-SWBLI developing on an airfoil for $\alpha = 3.5^\circ$, $Ma = 0.7$: on the left weak and on the right strong interaction.

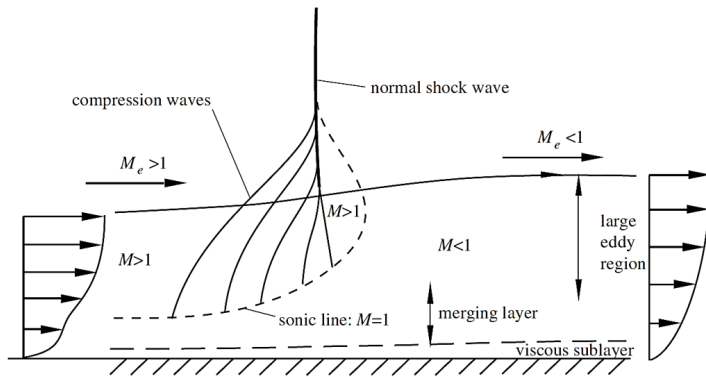


Figure 2.8: Sketch of a weak SWBLI on a flat plate (Moulden (1984)).

tion could still take place further downstream.

In the case of a strong interaction (Babinsky and Delery (2011)), as sketched in Fig.2.9, the shock strength triggers boundary layer separation (at the point marked with the letter S), so that within the boundary layer a region of reversed flow occurs, which is terminated by the reattachment point, indicated by R. The separation causes an upward bending of the streamlines (and of the sonic line), causing the formation of compression waves from the sonic line which will merge into an oblique shockwave. To realign the streamlines with the surface of the wall, a second oblique shockwave has to occur. The two oblique shockwaves meet in the triple point where they connect to the normal shockwave above them. In view of this particular configuration, this shockwave structure is referred to as a lambda (λ) shockwave. Because the decrease in total pressure across the normal shockwave is larger than for the two oblique shockwaves, while the static pressure behind them is the same, a slip line emanates from the triple point.

Since the drop in total pressure is larger in the case of a normal shockwave, it is convenient to increase the distance between the two legs of the shockwave as much as possible. A similar application will be treated in Chapter 9 with the use of shock control bumps.

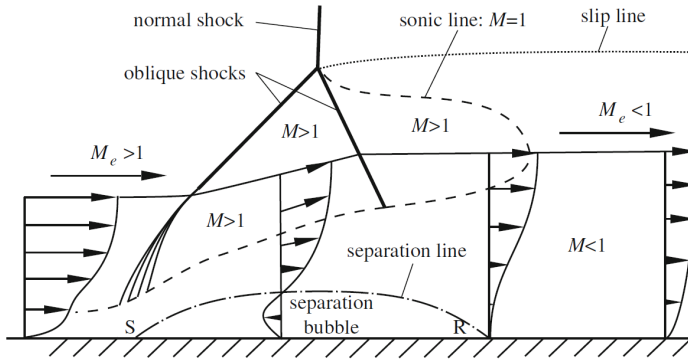


Figure 2.9: Schematic of a strong SWBLI on a flat plate (Vos and Farokhi (2015)).

From literature (Babinsky and Harvey (2011)) it is known that on a flat plate, shock induced separation starts for normal Mach numbers of 1.3-1.35. This information is also applicable to a supercritical airfoil, with the shockwave being typically located (on the suction side) in the neighborhood of its almost-flat region. In many cases the flow is further decelerated downstream of the shockwave in view of the geometry of the airfoil. This additional adverse pressure gradient may result in the formation of a separated area at the trailing edge. With a further increase of the Mach number the location at which the trailing edge separated area is triggered moves upstream. For particular cases, the reattachment behind the λ -shockwave does not take place, and the separated area extends from the front leg shock foot to the trailing edge of the airfoil (as in the schlieren image in Fig.2.7, right). A similar situation could also lead to transonic buffet (see Fig.1.1, left).

In some applications the shockwave could impinge in a location where the curvature of the airfoil has to be taken into account. As demonstrated by (Pearcey (1955), Inger (1983), Inger and Sobieczky (1978)), the shock strength required for separation is larger for an airfoil than for a surface, in view of the streamwise decrease in pressure due to the curvature of the airfoil. Additionally, Bohning and Zierep (1981) commented that, on an airfoil, disturbances associated with post shock expansion travel upstream by means of the subsonic region of the boundary layer and reduce the shock-induced pressure rise. A stronger surface curvature can also lead to a more detrimental shock interaction behavior, such as the formation of secondary shockwave structures which cause additional total pressure losses.

The numerical investigation of transonic SWBLI has received a significant amount of attention in previous years. An example is the study of Sandham et al. (2003), who performed LES on a circular-arc bump at $Ma_\infty=1.16$. Pirozzoli et al. (2010) have applied DNS to the study of SWBLI induced by a normal shockwave on a turbulent boundary layer developing on a flat plate for $Ma_\infty=1.3$ and $Re_\theta = 1200$ (with θ defined as the momentum thickness). For these conditions the flow did not show any mean flow separation, although the flow was characterized by intermittent separation.

Relevant research on transonic-SWBLI was also carried out experimentally by Bruce and

Babinsky (2008) both with and without passive flow-control devices. In their study a shockwave oscillation in a parallel walled duct is induced by a periodic forcing. The study, using schlieren and LDA measurements, shows a typical weak interaction with attached flow and a compression fan ahead of the main shockwave. However, some differences are distinguished between the upstream and the downstream shockwave movement, with the leading leg of the lambda-shockwave structure becoming stronger during the upstream movement as a result of the variation of the extent of the shockfoot separation.

For both the transonic and the supersonic regimes, SWBLI is characterized by both low and medium frequency unsteadiness, where the low-frequency is associated to the shockwave movement and the medium frequency to the mixing layer (typically related to Kelvin Helmholtz instabilities). These unsteadiness have been studied in detail for oblique shockwave interactions (Babinsky and Harvey (2011)). For example, Ganapathisubramani et al. (2009) investigated the nature of the low frequency unsteadiness of the separated area for the case of an oblique shockwave induced by a compression ramp. Using high-speed PIV (6kHz), it was concluded that the low frequency unsteadiness is associated to both "global" and "local" influences of the incoming boundary layer. Using tomographic PIV, Humble et al. (2009) analyzed the instantaneous 3D flow structure of a SWBLI induced by an impinging oblique shockwave, confirming the presence of long coherent structures (hairpin-type vortical structures associated with low-momentum regions) which affect the shockwave dynamics. Differently, according to Dupont et al. (2006), the low frequency unsteadiness depends on a coupling between the separated area pulsation and the reflected shockwave motion. Additionally, Piponniau et al. (2009) has noticed that the low-frequency unsteadiness is also present in absence of separated flow. Therefore, the origin of this unsteadiness remains an issue of discussion and of great interest (Dolling (2001), Shinde et al. (2019)).

Regardless of the origin of this unsteadiness and of the flow condition, both the low and medium frequency contributions have a broadband spectrum and are associated to low amplitude shockwave oscillations (as also documented by Sartor (2014)). However, this behavior is not observed for the transonic buffet behavior of an airfoil. In this case, high amplitude shockwave oscillations with a narrowband low frequency contribution are observed.

2.3. STATE OF THE ART ON TRANSONIC BUFFET

As already described in the introduction, buffet is a phenomenon that appears in the transonic regime and is characterized by a large-range low frequency oscillation of a shockwave over the suction side of the airfoil. It results in an unstable flow over the airfoil and is highly influenced by Mach number, Reynolds number, and angle of attack.

The first authors to study buffet were Hilton and Fowler (1952) who distinguished between two typologies of transonic buffet:

- Type I, which occurs at zero angle of attack on both pressure and suction side, typical on biconvex sections;
- Type II, which occurs on supercritical airfoils with oscillation on the upper surface at non-zero angle of attack.

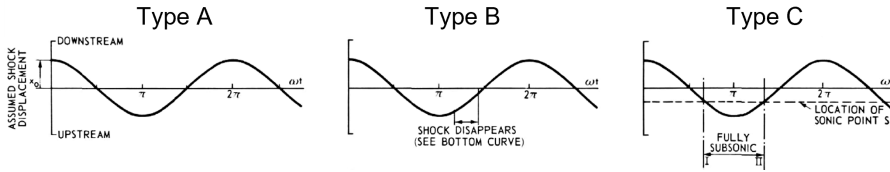


Figure 2.10: Sketch of typical shock position behaviors for Type A, B, C (Tijdeman (1977)).

A description of the physical mechanism of Type I buffet was given in Mabey (1981) and Gibb (1988) who noticed a 180° phase shift between the shockwave oscillation on the suction and the pressure side. When the shockwave moves upstream, it weakens and as a consequence also the flow reattaches causing the starting of its downstream travel. Thus, this kind of behavior is critically dependent on the strength of the shockwave, which has to have sufficient strength to produce separation. Type II buffet is characteristic of operative conditions of modern aircraft and because of that, it will be investigated in detail in this thesis.

A first explanation of this type of shockwave movement was given by Pearcey (1955), who described bubble bursting as responsible for transonic buffet onset, although this description was later disproved. A detailed description of Type II buffet is given by Tijdeman (1977) who performed measurements on an airfoil oscillating sinusoidally and recognized the presence of three different types of instability denoted as Types A, B, and C, respectively. A sketch of the the shock position behavior for the three types of instability is given in Fig.2.10. In Type A the shockwave oscillation is almost sinusoidal and is present during the entire buffet cycle, although with a variation in strength. Differently, in Type B a relevant variation in strength of the shockwave along the cycle is observed, with the shockwave disappearing in a part of the buffet cycle.

In Type C, while moving upstream, the shockwave at first increases and then decreases in strength propagating in the incoming flow as a free shockwave.

Effect of Mach number and angle of attack

The occurrence of transonic buffet is highly affected by the values of Ma , α , and Re , as summarized in the review paper of Giannelis et al. (2017).

A first analysis of this kind was given by McDevitt and Okuno (1985), who performed different experiments on a NACA 0012 airfoil. The results showed that the buffet onset is clearly dependent on the Mach number and angle of attack, with the minimum angle for which buffet occurs decreasing for an increasing freestream Mach number. In the same paper it is also mentioned that variations in the Reynolds number (in the turbulent regime) have an almost negligible influence on the buffet onset. A similar study was also carried out by Giannelis et al. (2018) who performed URANS simulations on the OAT15A airfoil, using the Mach number and the angle of attack as parameters. The results confirmed the experiments of McDevitt and Okuno (1985) in terms of buffet onset, as summarized in Fig.2.11 (left). It was also mentioned that at the buffet onset, the shockwave oscillations are similar to Type A, while at higher angles of attack a combination of Type A and C oscillations appears, with a non-linear response of the aerodynamic

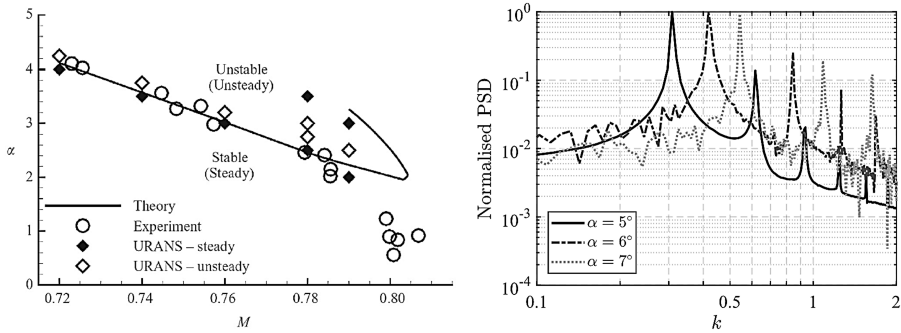


Figure 2.11: Effect of angle of attack and Mach number on transonic buffet (Giannelis et al. (2018)).

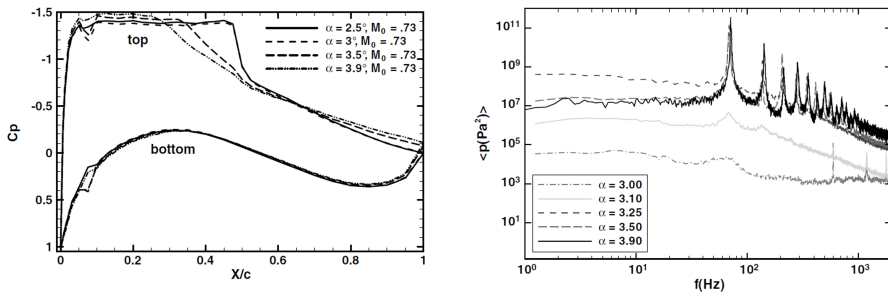


Figure 2.12: Effect of angle attack on the buffet onset. On the left the effect is visualized on the pressure distribution. On the right the spectral content of the pressure fluctuations in the shockwave oscillation range is shown (Jacquin et al. (2009)).

coefficients.

In Jacquin et al. (2009) the effects of the angle of attack and of the Mach number were investigated experimentally for the OAT15A airfoil, obtaining that fully developed buffet oscillations are reached for $Ma = 0.73$ and $\alpha = 3.5^\circ$. Some of the results of this study are reported in Fig.2.12, in particular on the left the average pressure distribution around the airfoil is shown for different angles of attack. The plot clarifies that for $\alpha < 3^\circ$ a sharp jump in pressure is observed around $x/c = 0.45$, indicating that the shockwave is steady and that no shock oscillation is expected for these angles. Differently for higher angles of attack, the jump in pressure is spread over a large portion of the chord of the airfoil, suggesting the occurrence of shockwave oscillations.

Spectral content of 2D transonic buffet

As it was anticipated in Section 2.2, transonic buffet is characterized by a narrow band frequency contribution. Independently from the specific airfoil, this peak usually takes place at Strouhal numbers (based on the chord and the freestream velocity, $St = f \cdot c / U_\infty$) in the range of $St = 0.05 - 0.08$ with good agreement between experimental (McDevitt and Okuno (1985), Jacquin et al. (2009), Hartmann et al. (2013)) and numerical studies (Deck (2005), Giannelis et al. (2018), Thiery and Coustols (2006), Iovnovich and Raveh

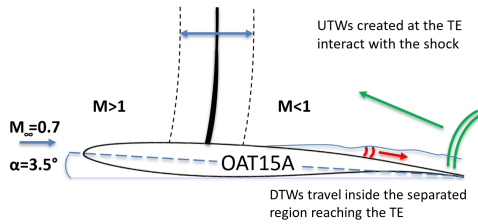


Figure 2.13: Sketch of transonic buffet feedback mechanism.

(2012)). Differently, for laminar flow conditions (where transition takes place at the shock foot) the physics of the phenomenon changes appreciably and the buffet frequency corresponds to $St \approx 1$ instead (see [Brion et al. \(2019\)](#) and [Dandois et al. \(2018\)](#)).

In [Jacquin et al. \(2009\)](#) the spectral content of pressure fluctuations in the shock-wave oscillation range (Fig.2.12, right) confirms the presence of a relevant frequency peak (buffet main contribution), only for $\alpha > 3.1^\circ$. Furthermore, with an increase of the angle of attack a slight increase in the buffet frequency is observed. Similar results were obtained by [Giannelis et al. \(2018\)](#), who highlighted that an increase in both the Mach number and the angle of attack leads to an increase in the buffet frequency (see Fig.2.11, right).

Physical mechanism of 2D transonic buffet

A first attempt to explain the transonic buffet mechanism was made by [Lee \(1990\)](#), who described the shock buffet oscillation as being sustained by a feedback mechanism. In this model, disturbances created at the shock foot travel downstream towards the trailing edge inside the separated area (indicated in red in the schematic representation in Fig.2.13). Once these downstream traveling waves (DTWs) reach the trailing edge, upstream traveling waves (UTWs) are created in order to satisfy the Kutta condition. These UTWs (indicated in green) travel upstream towards the shockwave thereby sustaining the shock oscillation. According to this model the period of a transonic buffet oscillation cycle T is described as the sum of the time required by DTWs to reach the trailing edge plus the time that UTWs take to reach the shockwave itself. Although this model gave results that are reasonably close to the ones reported in literature, it was found not accurate enough to compute the buffet frequency, as reported by [Deck \(2005\)](#) and [Jacquin et al. \(2009\)](#).

The model introduced by Lee was updated by [Deck \(2005\)](#), who considered the UTWs to be able to travel not only along the suction side, but along the pressure side as well, which resulted in a better prediction of the buffet frequency. This model confirms the previous experimental results of [Finke \(1975\)](#). This description is also substantiated by the correlation analysis of [Jacquin et al. \(2009\)](#) who took into account the data of unsteady pressure taps on the surface of the airfoil. The results of this correlation analysis are represented in Fig.2.14, showing the presence of pressure structures moving downstream on the suction side with a velocity of $(0.07 \cdot U_\infty)$ 17 m/s (DTWs), while on the pressure side the pressure waves are moving upstream with a velocity of nearly $(0.27 \cdot U_\infty)$ 80 m/s (UTWs), which is close to the average velocity of the speed of sound with respect

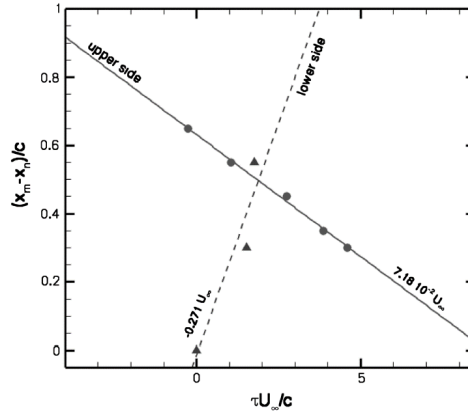


Figure 2.14: Correlation analysis of pressure fluctuations on both the suction and the pressure side of the airfoil (Jacquin et al. (2009)).

to the flow. Similar propagation velocities have also been computed by Hartmann et al. (2013) using both pressure and velocity data.

Despite buffet being widely studied in the past 30 years, its mechanism has not been completely understood yet, in particular regarding the precise nature and behavior of these upstream and downstream traveling waves. The mechanism by which the DTWs are generated and consequently where they originate in the flow (e.g., in the separated trailing edge area or in the shear layer) remain unclear, although Lee (1990) (in whose study the flow at the shock foot does not reattach during the whole buffet cycle) and Jacquin et al. (2009) described that the DTWs are created at the shock foot.

A detailed experimental study on the characterization of UTWs on an airfoil was carried out by Hartmann et al. (2013), where high speed stereo-PIV was used in order to corroborate the findings of Lee (1990). The results confirmed the presence of a feedback loop between the shockwave and the disturbances produced at the trailing edge (where the UTWs are generated).

The dynamics of the main flow structures of the buffet cycle, as proposed by Hartmann et al. (2013), is sketched in Fig.2.15. According to this description, the strength of the downstream propagating vortices (ω) is supposed to be associated with the strength of the shockwave and, therefore, with its velocity with respect to the flow, which is maximal in stage II (b). The sound pressure level (SPL) of the upstream propagating pressure waves originated at the trailing edge is instead dependent on both the strength of the vortices (ω) and the extent of the shear layer, with the SPL being higher for a thinner shear layer. Thus, the stronger UTWs are supposed to be originated in stage I (a), where at the trailing edge both the strongest vortices and the smaller shear layer thickness are present. These pressure waves will reach the shockwave at stage II (b), sustaining its upstream movement. In following phases the reduction of the SPL of the UTWs will be such that the shockwave will stop its upstream travel (c), and start its downstream travel (d). According to this description the model predicts that the UTWs are produced during the entire buffet cycle but with a strength which is modulated during the different stages of

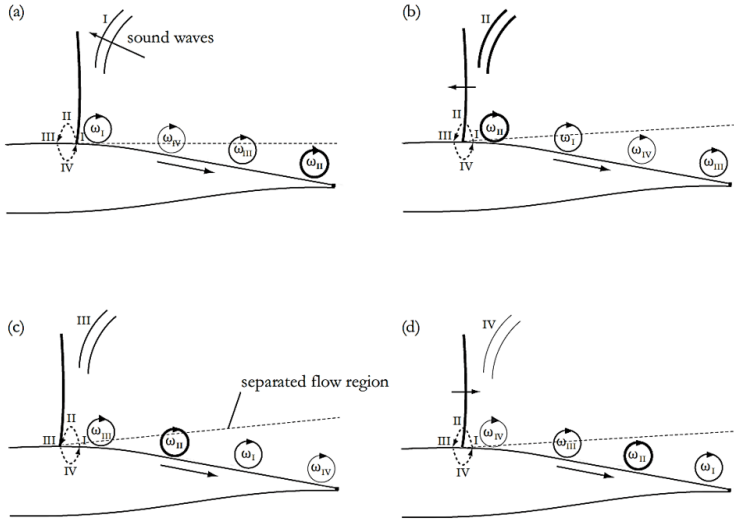


Figure 2.15: Schematic of DTWs and UTWs dynamics as theorized by [Hartmann et al. \(2013\)](#).

the cycle.

A visualization of the upstream propagating pressure waves is also given in the combined numerical and experimental study of [Gageik et al. \(2018\)](#) for similar flow conditions on a BAC 3-11 airfoil. In this study, a good agreement of the pressure wave distribution between numerical and experimental schlieren images is also reported, with a propagation frequency of the pressure waves in the range of 1-2 kHz, which is similar to the value obtained by [Hartmann et al. \(2013\)](#). Notwithstanding these observations, there is still no clear consensus in literature whether the UTWs are created only during a part of the cycle, or during the whole buffet cycle but with a modulated strength.

An alternative view of buffet was given by Crouch, who described it as a consequence of a global flow instability (see [Crouch et al. \(2007\)](#), [Crouch et al. \(2019\)](#) and [Crouch et al. \(2009\)](#)). The results of this model are based on a stability analysis which is characterized by a perturbation formulation and is solved as an eigenvalue problem. Therefore, the buffet onset can be derived by searching for the least stable eigenvalue. This global stability approach was applied for the first time in [Crouch et al. \(2007\)](#). In [Fig. 2.16](#) the stability of the different eigenvalues is described for $Ma = 0.76$ and for different angles of attack, showing that for the least stable eigenvalue (associated with buffet) there is the occurrence of an instability induced by the increase of the angle of attack. The results of this analysis accurately predict the buffet onset as a function of Ma and α , and are in good agreement with experimental data.

Although usually the feedback mechanism and the global stability analysis are considered to be competing theories, in many aspects the feedback description can be seen as the physical mechanism by which the global instability manifests itself. However, this description differs from the feedback loop theory in some aspects, since in the for-

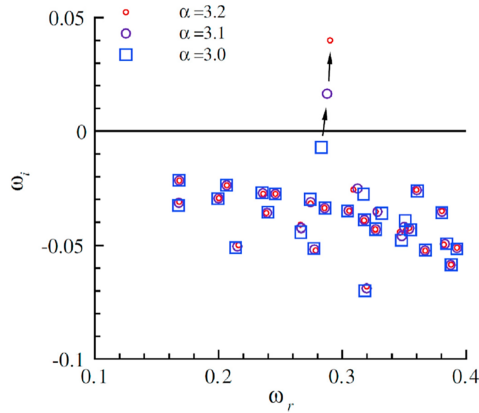


Figure 2.16: Stability of eigenvalues with $Ma = 0.76$ and angle of attack as parameter (Crouch et al. (2007)).

mer the shockwave oscillation is considered self-sustained by disturbances created at the shock-foot, which travel in the wall-normal direction and with less intensity in the boundary layer. Thus, this analysis does not include any acoustic feedback from the trailing edge. Similar results were also obtained by the stability analysis of Sartor et al. (2015). This study also showed that URANS simulations are capable of describing the main buffet flow features with results in fair agreement with the DES simulations discussed by Deck (2005).

Confinement effects on transonic buffet

Confinement effects in connection to airfoils (therefore in absence of free wing-tip) under transonic buffet conditions have been investigated in the last two decades, such as in the numerical study of Thiery and Coustols (2006), where differences in the airfoil performance are noted when modeling top, bottom and side walls of the wind tunnel. Jacquin et al. (2009) by analyzing oil flow visualizations, commented that possible 3D side wall effects are contained in proximity of the two extremities of the airfoil model. In the recent study of Sugioka et al. (2022), confinement effects are studied for a fully clamped airfoil and a 10° swept model, highlighting the relevance of corner separation for the shockwave oscillation in proximity of the side walls. Similarly, Sansica et al. (2022) have investigated the effect of side walls on transonic buffet for both an airfoil and a swept wing (with the models clamped at both side walls) using experiments and RANS simulations. The results from the two approaches are in good agreement, with the effect of corner separation being negligible at a distance of around $c/2$ from the walls for $\alpha = 4^\circ$. A global stability analysis on the fully clamped airfoil model reveals the presence of two unstable modes (see Fig.2.17). The first mode is at $St = 0.056$ and is associated with 2D buffet, and a second at $St = 0.112$, which is an instability originating in correspondence of the walls and propagating downstream along the shear layer.

Notwithstanding these studies on airfoils, finite-wing effects on transonic buffet in connection to unswept wings (with a free wing-tip) have not yet received attention in literature.

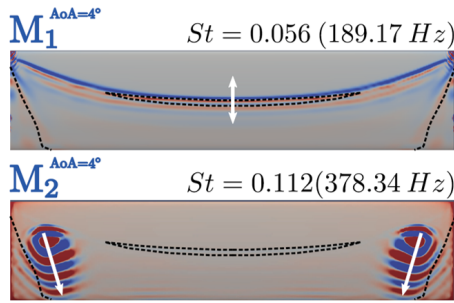


Figure 2.17: First (top) and second (bottom) unstable modes for a fully clamped unswept wing (Sansica et al. (2022)).

Transonic buffet on swept wings

Although the study of buffet on swept wings is very relevant because of its possible occurrence in real flight conditions and actual wing configurations, a complete comprehension of the phenomenon is still far from being achieved and only in the last 10 years extensive research on this topic has been conducted. In presence of wing sweep, the buffet mechanism appears to be much more complicated, with oscillations of the shock-wave in the chordwise direction being of lower amplitude (see Paladini et al. (2019) and Poplinger and Raveh (2022)) compared to the airfoil case and occurring at much higher frequencies. For swept wings the typical 2D isolated peak at $St = 0.07$ is substituted by a broadband peak in the range of $0.2 < St < 0.6$. From recent experiments by Dandois (2016) on a 30° swept wing based on the OAT15A airfoil, a buffet onset of $Ma = 0.82$ at $\alpha = 3^\circ$ is obtained. It should be noticed that the angle of attack has an important influence as well, inducing either simultaneous 2D and three-dimensional (3D) shock-buffet behaviors, or only 3D behavior, depending on the trailing edge separation characteristics (Sugioka et al. (2015)). The simultaneous presence of these two types of behavior is also confirmed by a modal decomposition (of a zonal detached eddy-simulation) on a wing-body configuration (Ohmichi et al. (2018)).

Mayer et al. (2019) described the flow pattern of a 30° swept wing based on the OAT15A airfoil section, resulting in a normal shockwave and a quasi-2D flow for outboard locations, and a λ shock and highly 3D flow for inboard locations.

Iovnovich and Raveh (2015) studied the effect of the sweep angle, obtaining that for infinite wings with sweep angles Λ larger than 20° the difference in behavior with respect to 2D models is very relevant. In contrast, for sweep angles $\Lambda < 20^\circ$ no substantial difference is observed. The main cause for this difference is associated with the span-wise convection of particular flow structures that occurs at high sweep angles, which is referred to in Iovnovich and Raveh (2015) as buffet cells. The buffet cells consist in pressure disturbances of alternating sign, which are periodically convected from the wing root (aft of the λ shock) towards the wing tip.

The presence of buffet cells is also confirmed by different experimental studies such as Paladini et al. (2019), Dandois (2016) and Sugioka et al. (2015). In Paladini et al. (2019), different experimental databases, belonging to four projects (BUFFET'N Co, AVERT, DTP and FLIRET) are compared for the different wing-body models shown in Fig.2.18. The

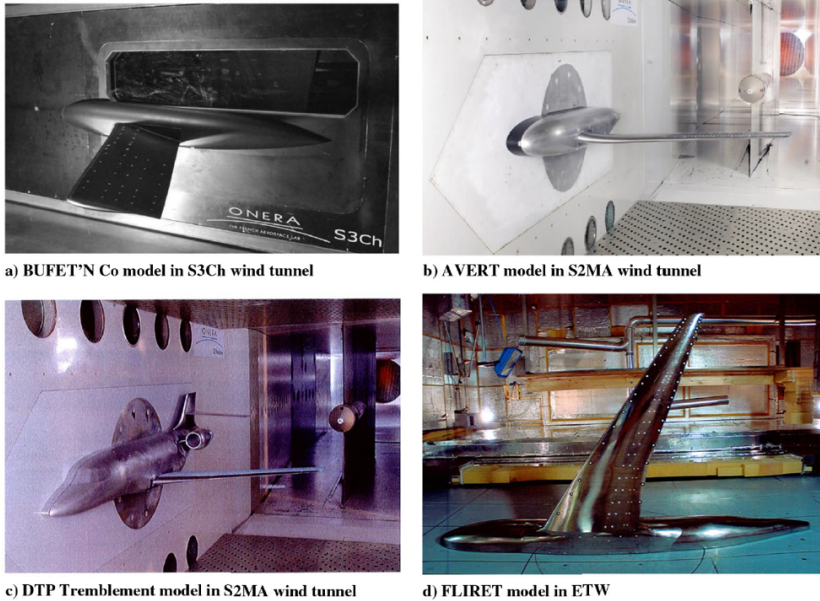


Figure 2.18: Different experimental models of swept wings summarized in [Paladini et al. \(2019\)](#).

different datasets are all based on wings with a sweep angle of 30° and they all show the presence of a spanwise convection velocity equal to $0.25 \cdot U_\infty$ proceeding outboard in the shockwave oscillation range. In addition to the previously mentioned convection phenomenon, another spanwise convection velocity of 100 m/s ($0.36 \cdot U_\infty$) was observed in the separated area, with similar results also obtained by [Roos \(1985\)](#). Convection phenomena are also detected in the chordwise plane and attributed to Kelvin-Helmholtz instability (with typical propagation velocity of $0.65 \cdot U_\infty$). A sketch of the convection phenomena developing on the four models studied is reported in [Fig.2.19](#). A discussion of the origin of the buffet cells is also given in [Plante et al. \(2019\)](#), where they are described as reminiscent of the stall cells observed in low speed conditions.

[Iovnovich and Raveh \(2015\)](#) have also addressed numerically the finite wing effect, showing that for a finite swept wing, end-effects and wall interference are present. These effects cause the formation of tip vortices, which influence the transonic buffet behavior in the more outboard sections ([Iovnovich and Raveh \(2015\)](#)), while recovering the infinite swept wing behavior in the more inboard sections. These results are also confirmed by the numerical study of [Plante et al. \(2017\)](#). Besides the physical description given by [Iovnovich and Raveh \(2015\)](#), [Crouch et al. \(2019\)](#) has also addressed three-dimensional buffet by applying a stability analysis to both swept and unswept infinite wings. In presence of wing sweep, spatial modes were found to become unsteady, propagating periodic flow structures towards the wing-tip, which is in good agreement with existing literature. For an unswept wing, these spatial modes are still present although steady, in addition to the classical 2D buffet mode. This analysis has also been extended by [Timme \(2020\)](#) to finite wings. In their study, [Sansica et al. \(2022\)](#) have given hints that corner

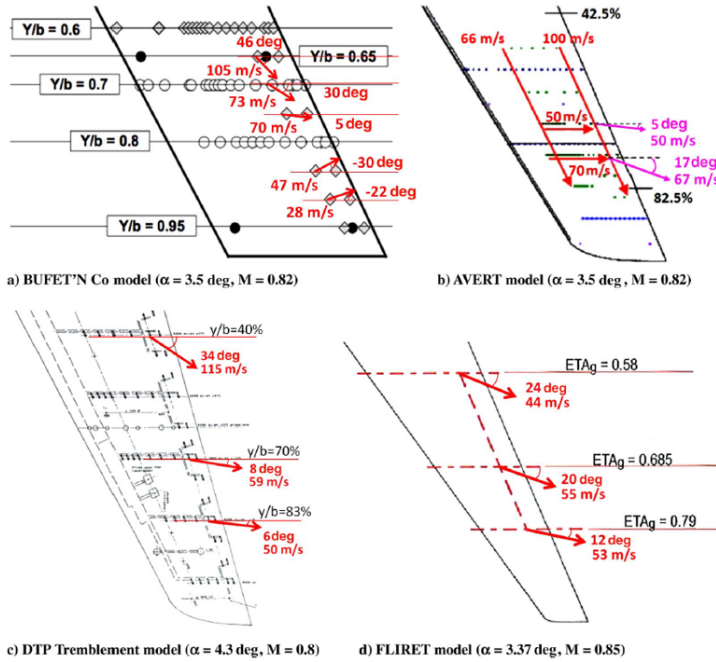


Figure 2.19: Schematic visualization of convection phenomena for different swept wings (Paladini et al. (2019)).

separation on the side walls causes the spanwise convection of cellular structures, even for the case of an unswept wing.

2.4. CONTROL OF TRANSONIC BUFFET

It is clear that to reduce the impact of transonic buffet, and, thus, increase the flight envelope, the use of a control system that would mitigate this effect is beneficial. In the last two decades both active and passive control systems have been investigated as described in the review paper of Giannelis et al. (2017). As discussed in the following outline, buffet control systems are generally located either near the shockwave oscillation range or in the separated area or in the trailing edge area, with the goal of directly stabilizing the shock position or the extent of the separated area.

An example of an active control system for limiting transonic buffet is the use of a trailing edge deflector (TED), whose deflection is controlled in closed loop in response to the instantaneous position of the shock wave. This approach was taken in the study by Caruana et al. (2005), where the instantaneous value of the shock position is inferred from unsteady pressure measurements on the surface of the airfoil. The TED which has been used is sketched in Fig.2.20 (left) and it is attached to the pressure side of the airfoil. The results (Fig.2.20, right) showed the possibility of controlling transonic buffet by virtually eliminating the shock oscillations. Similar TEDs have also been studied numerically.

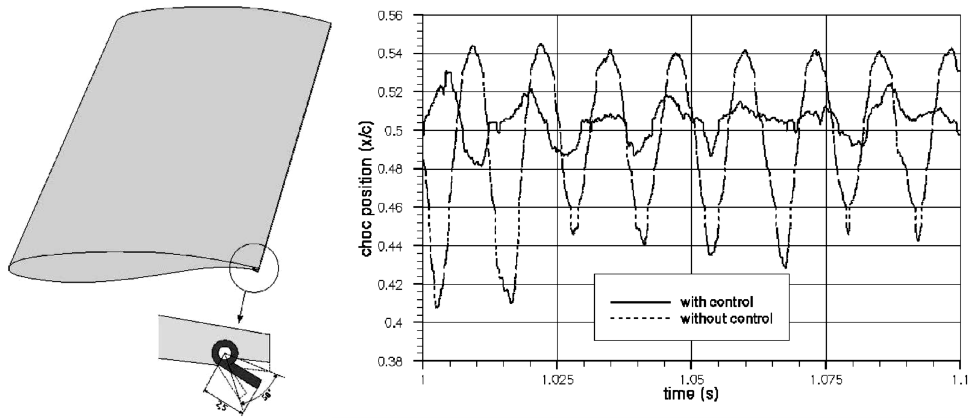


Figure 2.20: Active control of transonic buffet by means of a TED (Caruana et al. (2003a)). On the left a sketch of a TED is shown, while on the right its effect on the shockwave position is plotted.

ically by Gao et al. (2016) and Ren et al. (2020), where respectively a linear delayed control law and an adaptive control strategy based on a neural network (both with a feedback signal on the lift) have been employed, managing in both cases to stabilize the shock movement. The current development in machine learning and artificial intelligence has also allowed the improvement of other closed-loop control strategies as for example the use of smart skin in Ren et al. (2022). It is clear that the use of a closed loop control system is very efficient in controlling transonic buffet, but requires a sophisticated actuation system, which could affect the reliability of the whole system. Thus, when simplicity and robustness is preferred, a passive control system may be more preferable.

Trailing edge modifications can also be used as a passive control system, in the form of a flap with a fixed deflection. This typology of control system has been investigated by Despre et al. (2001), where a delay of the buffet onset was obtained in terms of the lift coefficient, for different values of flap deflections. In particular, for the clean airfoil the buffet onset is obtained at $C_L = 0.97$, while with a deflection of the TED of $\delta = 15^\circ$ at $C_L = 1.04$. A similar application is also reported in Lee (1992) where a flap with a chord of $c_{flap} = 13\%c_{airfoil}$ was tested for a range of low values of deflection. A further example of a trailing edge modification is the use of a serrated trailing edge, which effectiveness in reducing the emission of pressure waves having been confirmed for the low compressible flow regime, making these devices very useful for noise reduction. Notwithstanding these applications, there is as yet no proof of the efficacy of a serrated trailing edge at transonic conditions Nies and Olivier (2013).

Another example of a simple passive control system is a vortex generator, which is a device that energizes the boundary layer helping the flow to remain attached longer and therefore to delay the oscillation of the separation area extent, which is a key element of transonic buffet. This kind of control system as used by Caruana et al. (2003b), demonstrated to be effective in reducing the amplitude of the buffet oscillation and in moving the buffet onset to higher values of the angle of attack. However, it decreases the lift/drag ratio when there is no separated flow. Vortex generators were already used

to avoid buffeting on vertical tails of the Panavia "Tornado" or on the Fiat G-91 with the idea of energizing the flow and avoid a separated area with large velocity fluctuations.

In recent years also fluidic vortex generators in the form of air jets located upstream of the shock location have been investigated [Brion et al. \(2019\)](#). These devices can effectively reduce the extent of the separated area and postpone the buffet onset without increasing drag in cruise conditions [Molton et al. \(2013\)](#). To avoid energy costs in the generation of the air jets, [Brutyan et al. \(2019\)](#) proposed to actuate the jet (located in the supersonic area upstream of the shock) with a passive air by-pass from the high pressure area downstream of the shockwave.

A further system used for the control of transonic and supersonic shock interaction, is achieved by the use of the so-called shock control bump (SCB), a type of device that has been extensively described in the review of [Bruce and Colliss \(2015\)](#). SCBs have been used for different applications, such as the control of transonic flows on wings and airfoils [Ogawa et al. \(2008\)](#), for the control of shockwave/boundary layer interaction as in the study of [Holden and Babinsky \(2003\)](#) and [Bruce and Babinsky \(2012\)](#), and as a flow control device in supersonic engine intakes [Babinsky and Ogawa \(2008\)](#). On transonic airfoils, a SCB is generally placed on the suction side in the approximate location where the normal shock is expected to form.

The SCB geometry consists of a forward facing ramp and a tail oriented in the downstream flow direction. As sketched in [Fig.2.21](#) in correspondence of the leading edge of the SCB an oblique shockwave is formed, with the second leg being located in design conditions in correspondence of the crest of the bump. [Colliss et al. \(2016\)](#) and [Ogawa et al. \(2008\)](#) have shown that three-dimensional shock control bumps are more efficient than two-dimensional SCBs (which have been extensively described by [Zhang et al. \(2021\)](#)), particularly in off-design conditions thanks to the streamwise vortices developing from the tail of a bump. The interaction between the shockwave structures developing around neighboring bumps is also of great interest and has been investigated by [Ogawa et al. \(2008\)](#) (see [Fig.2.21](#), right).

The two possible working principles of three-dimensional SCBs are associated with the formation of a λ -shock structure which replaces the traditional quasi-normal shockwave and the formation of a localized region of attached flow downstream of the shockwave location thanks to the streamwise vortex development.

Regarding the design of SCBs, the study of [Colliss et al. \(2014\)](#) also proved that a combined experimental and numerical approach can be used to achieve a relatively inexpensive parametric study of the effects of the geometry of 3D SCBs on the flow physics. Among the different shapes of SCBs one of the most common is the narrow wedge SCB, (as described in [Colliss et al. \(2016\)](#) and in [Mayer et al. \(2018\)](#)), which is characterized by a flat ramp, crest and tail and by angular side flanks. Three-dimensional SCBs on airfoils have been also employed for drag reduction applications, as in [Deng and Qin \(2021\)](#), where 3D SCBs were integrated with vane-type vortex generators to suppress flow separation. A similar application is also presented in the study of [Jones et al. \(2017\)](#) on swept wings.

Because of its properties, a SCB can also be used as a "smart" vortex generator and applied to transonic buffet control as shown by [Eastwood and Jarrett \(2012\)](#) or in [Tian et al. \(2017\)](#), where two different types of SCBs were proved to be effective in controlling

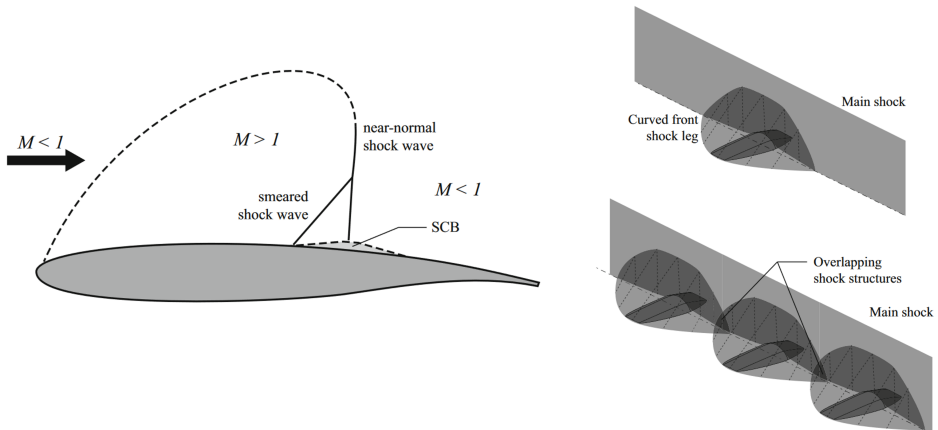


Figure 2.21: Schematic visualization of flow features induced by a shock control bump along the chord (left, Bruce and Babinsky (2012)) and along the span (right, Ogawa et al. (2008)) of an airfoil.

transonic buffet. The study of Mayer et al. (2019), also demonstrated the effectiveness of SCBs for controlling transonic buffet on swept wings. For two-dimensional SCBs, Birke-meyer et al. (2000) proposed that these devices be used to postpone the transonic buffet onset on wings when placed in between the shockwave location and the trailing edge as not to have a negative impact on drag.

2.5. RESEARCH QUESTIONS

As anticipated in Section 1.3, this thesis is divided into two parts, which respectively deal with the understanding of the physics of the buffet phenomenon (Part I) and then with approaches to control it (Part II). Now that some basics concepts as well as the most relevant literature on the topic have been reviewed in the previous sections of this Chapter, it is possible to define the specific research gaps which will lead the investigations in this thesis.

Part I

As described in the previous literature survey, in Type 2A transonic buffet shockwave oscillations are generally taking place in presence of a separated area, however, the variation in extent of the separated area during a buffet cycle is an aspect which is often overlooked and requires further investigation.

Regarding the feedback mechanism which sustains transonic buffet, various aspects are still not clear. One of these aspects is the mechanism by which upstream propagating waves (UTWs) sustain the shockwave movement. In particular, it is not known whether these structures are produced during the entire buffet cycle and if so, whether their strength is modulated in time. Although it is assumed that UTWs generation is dependent on the arrival of downstream propagating waves (DTWs) at the trailing edge, the nature of the DTWs and thus where they originate is still open to investigation. Specific

attention will be given to the characterization of the dynamics of the buffet cycle, as well as its spanwise organization.

For experimental studies, finite wing effects and the coherence of buffet along the span of an airfoil should also be further investigated, analyzing possible wing-tip vortex contributions. Additionally, although in the last decade a lot of effort has been directed to the study of transonic buffet on swept wing, the reason for such a different behavior (especially regarding the convection of buffet cells) has not been fully resolved, yet.

2

Part 2

Although the literature survey has shown that active control systems are efficient in controlling transonic buffet, in this thesis the control of transonic buffet is attempted with passive systems in view of their robustness and simplicity. In literature most of control systems are used with the intention of directly controlling either the shock position or reducing the separated area size, whilst no control system is specifically designed to damage the entire buffet cycle. With this goal, in this thesis, upper trailing edge flaps will be used and compared to another typology of control devices, such as shock control bumps (SCBs).

Section 2.4 has shown the dependence of the control system (in particular SCBs) on the specific flow condition, thus, a proper design of these devices is required. However, literature often lacks guidelines for the design of effective control devices. Some of these aspects, such as the spanwise spacing of 3D SCBs will be therefore studied in more detail in this thesis.

The use of passive control systems is often associated with a variation in circulation of the model, therefore, variation in the aerodynamic loads should and will be evaluated to assess whether the suppression of buffet is accompanied by a reduction in lift or an increase in drag.

3

EXPERIMENTAL ARRANGEMENT

3.1. WIND TUNNEL FACILITY

ALL the experiments of this thesis were carried out in the TST-27 wind tunnel of TU Delft (see Fig.3.1) which is a transonic-supersonic blowdown windtunnel. As clear



Figure 3.1: TST-27 Wind Tunnel (airflow from right to left).

from the name, the wind tunnel can be operated in both transonic and supersonic conditions.

Supersonic conditions ($Ma = 1.15 - 4.2$) are achieved by means of a continuously variable throat A_{t1} and by flexible upper and lower walls (see Fig.3.2). The transonic conditions ($Ma = 0.5 - 0.85$) are instead obtained using a variable choke mechanism (A_{t2})

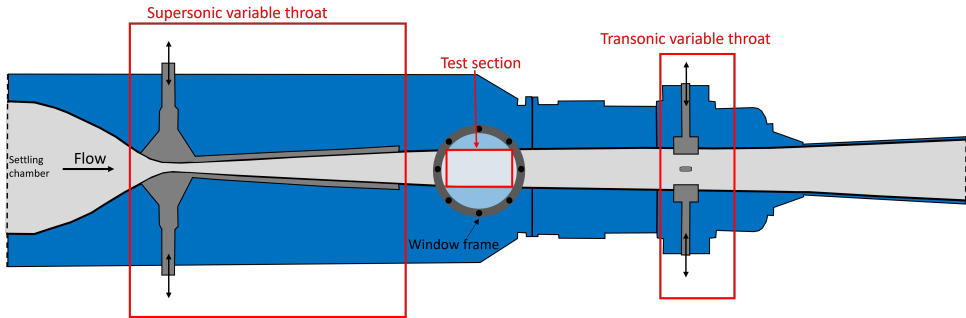


Figure 3.2: Technical drawing of TST-27 with indication of supersonic throat (A_{t1}), test section (A_{test}) and transonic throat (A_{t2}).

downstream of the test section (A_{test}) and which is controlled by a Labview program (described in detail by [van Rijswijk \(2012\)](#)). When the tunnel is operated in transonic conditions, the cross sectional area of the upstream throat A_{t1} is such that no supersonic condition is achieved in correspondence of it. The transonic choke consists of eight biconvex rods (four biconvex rods are connected at the bottom wall of the tunnel and four at the top) and a wing as sketched in [Fig.3.3](#). By means of the excursion of the rods (H) the blockage of the flow, and hence the effective area of the downstream throat A_{t2} , is varied and as a consequence also the Mach number in the test section, while the further rotation of the wing allows a fine adjustment of the Mach number. This wing has a thickness of 6 mm and can rotate between 0 and 60 degrees. In practice, the rods are set before the beginning of the run according to the target freestream Mach number. Minor adjustments of the Mach during the run are obtained by rotating the central wing, allowing to achieve an accuracy of the Mach number to the third decimal digit.

Since the transonic throat is located downstream of the test section, the effective cross sectional choke area is highly affected by the model wake. To account for this effect, a solid blockage parameter is taken into account and estimated as the approximated height of the wake. This parameter is inserted in the Labview program to speed up the control of the Mach number.

The wind tunnel is made up of four main parts (see [Bannink \(1987\)](#)):

1. the settling chamber;
2. the adjustable convergent-divergent nozzle directly connected to the settling chamber;
3. the test section module;
4. a module downstream of the test section that contains the transonic choke and is connected with the exhaust.

The settling chamber is supplied by air from a separate storage reservoir at a pressure ranging between 20 and 40 bars, which allows a continuous running time of 300 s. Relatively independent of the pressure in the storage vessel, the pressure in the settling

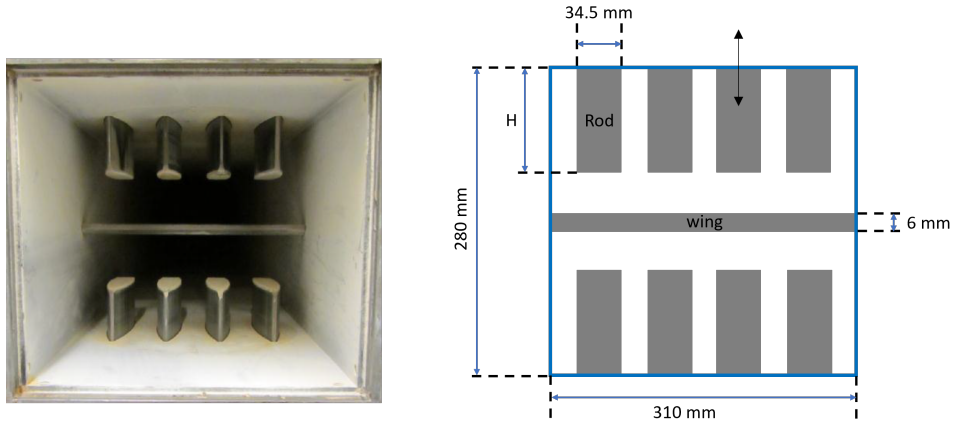


Figure 3.3: Transonic throat visualization (left) and schematic (right).

chamber can be set between 1.5 and 4 bars according to the desired Reynolds number in the test section.

The modularity of the wind tunnel allows the use of three different test sections, with either closed wall, slotted walls or perforated walls. Each module is supported on wheels and connected with the rest of the wind tunnel by quick-lock couplings. In this thesis, all the experiments have been carried out in the solid walls test section, which optimizes the quality of the PIV raw images (in view of the specific windows used). This test-section is rectangular with a height of 0.255 m and a width of 0.280 m.

The experiments have been conducted with a total pressure $p_0 = 2$ bar and a total temperature $T_0 = 288$ K. Regarding the freestream Mach number, the wind tunnel has been operated in the Mach range 0.7-0.81, which corresponds to a freestream velocity range of 225-260 m/s; all the conditions are summarized in Tab. 3.1.

Table 3.1: Flow conditions

Parameter	Symbol	Value	Unit
Freestream Mach number	Ma_∞	0.7-0.81	
Corrected freestream Mach number	Ma	0.73-0.85	
Freestream velocity	U_∞	225-260	m/s
Total pressure	p_0	2	bar
Total temperature	T_0	288	K
Reynolds number per unit length	Re/l	$26 \cdot 10^6$	

3.2. BLOCKAGE

Due to the presence of the model and its wake, the effective freestream Mach number in the test section is different from the nominal one. To calculate the corrected Mach number, a blockage correction coefficient needs to be evaluated. In this thesis, only an

estimate of the blockage effect due to the direct presence of the model will be given, while the contribution due to the wake of the model is neglected.

The blockage correction factor is computed using an empirical model derived by [Bannink and Bakker \(1983\)](#) based on experiments on a NACA0012 airfoil model (with a chord of 10 cm) carried out in the TST-27 of TU Delft. Following [Bannink and Bakker \(1983\)](#), the corrected values of Mach number and freestream velocity can be computed in relation to the blockage parameter k as:

$$Ma_{corr} = Ma_{\infty} + Ma_{\infty} k \left(1 + \frac{\gamma - 1}{2} Ma_{\infty}^2 \right) \quad (3.1)$$

$$U_{corr} = U_{\infty} (1 + k) \quad (3.2)$$

Following a simple first order procedure and considering an adiabatic flow in the wind tunnel, the empirical value obtained for the blockage effect related to the presence of the model is:

$$k_i = \frac{\pi^2}{12} \left(\frac{d}{r} \right)^2 \lambda \cdot b \quad (3.3)$$

where $d = 0.0123m$ is the maximum thickness of the OAT15A, $r = 0.255m$ is the height of the test section, $\lambda = 3.8$ is a particular shape factor valid for the NACA 0012 and b is a term that takes into account the angle of attack of the airfoil (α):

$$b = \left(1 + 1.2 \cdot (1 - Ma_{\infty}^2)^{1/2} \cdot \frac{d}{c} \right) \cdot \left(1 + 1.1 \alpha^2 \frac{c}{d} \right) \quad (3.4)$$

The value of k_i is only valid for incompressible flow, while compressible effects are included using the Prandtl-Glauert correction (even though as described in Section 2.1.1 this correction becomes less and less precise as the value of the Mach number approaches 1):

$$k = \frac{k_i}{(1 - Ma_{\infty}^2)^{3/2}} \quad (3.5)$$

This blockage correction is certainly not 100 % exact, however, it offers a good approximation. The main errors are committed when the blockage of the wake is neglected and when the shape factor of an NACA 0012 instead of an OAT15A (model tested in this thesis, see the following section) is used. Following this procedure, for a freestream velocity $U_{\infty} = 225m/s$, freestream Mach number $Ma_{\infty} = 0.7$, and an angle of attack of $\alpha = 3.5^\circ$, the following values are obtained:

- $Ma_{corr} = 0.72$
- $U_{corr} = 230.4 m/s$.

Notwithstanding this correction, except if expressly specified, all the values reported in the thesis are uncorrected for the blockage.

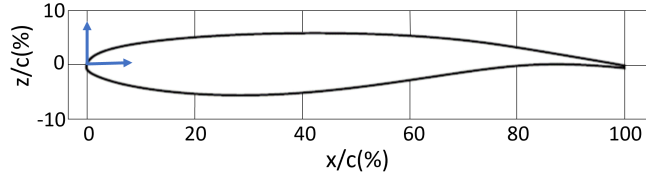


Figure 3.4: Profile of the OAT15A airfoil.

3.3. OAT15A AIRFOIL

All the models used in this dissertation are based on the OAT15A airfoil, which is a supercritical airfoil designed by ONERA. The airfoil (Fig.3.4) has a 12.3 % thickness-to-chord ratio and a trailing edge thickness of 0.75%c. This airfoil was selected because of its relevance in literature for transonic buffet studies, being used in both numerical and experimental studies, such as: [Jacquin et al. \(2009\)](#), [Thiery and Coustols \(2006\)](#), [Deck \(2005\)](#), [Grossi et al. \(2014\)](#), [Szubert et al. \(2015\)](#), [Giannelis et al. \(2018\)](#), [Huang et al. \(2012\)](#), [Giannelis et al. \(2018\)](#), [Accorinti et al. \(2022\)](#) and [Kokmanian et al. \(2022\)](#). In all these studies a very good agreement between the numerical and the experimental results is present, with the shockwave position having similar amplitude of oscillation and frequency contributions (in terms of Strouhal number). To ensure a fully turbulent boundary layer, a transition trip (2 mm wide) at 7% of the chord is introduced. In this thesis, the transition trip is realized by using Carborundum particles. This specific transition trip was chosen by comparing oil flow visualizations on various transition trip configurations with different Carborundum particle sizes. Since transition to turbulence occurred for all the particle size tested, the smallest Carborundum particles have been selected (particle size of 0.0139 mm). More details are given in Section 3.5.

3.4. WIND TUNNEL CONFIGURATIONS AND MODELS

The test section of the wind tunnel could be fitted with different side windows, allowing for different configurations for testing the airfoil/wings, in detail:

- airfoil clamped horizontally on both sides of the tunnel ("horizontal airfoil");
- airfoils mounted vertically in the test section ("vertical airfoil");
- finite (swept and unswept) wings clamped at their root and free at the tip.

According to the specific configuration tested, some dedicated connecting pieces are required. In detail, the test section is accessible by means of two circular slots of the diameter of 440 mm. According to the specific wind tunnel test, these slots are fitted with a particular window frame.

For the first configuration, the window frame consists of two solid blocks with small circular glass windows of 160 mm of diameter which allows the testing of the "horizontal model". The airfoil is clamped at each of the two circular windows by means of two screws, as clear from Fig.3.5 (left). This configuration allows optical access from both

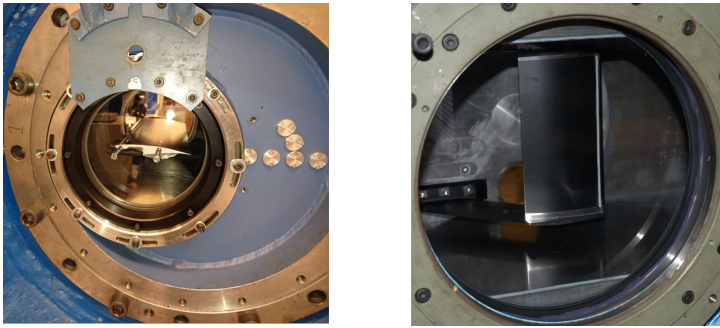


Figure 3.5: Wind tunnel windows/clamping piece for first (left) and second (right) testing configurations.

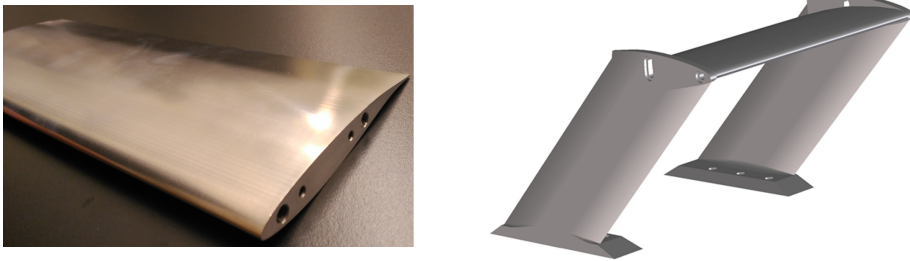


Figure 3.6: Horizontal (left) and vertical model (right) of the OAT15A.

sides of the tunnel, enabling the possibility of performing both schlieren and PIV measurements on a model of 28 cm of span. Both windows are connected to a system to change the angle of incidence, which allows for the investigation of a wide range of angles of attack.

The second configuration allows the testing of models oriented vertically inside the wind tunnel ("vertical airfoil"), by providing a direct optical access to the suction side of the airfoil (see Fig.3.5, right). In this configuration, the model is clamped on a full metal block by means of two pylons, as shown in Fig.3.6 (right), enabling the testing of models of 200 mm of span. The other side slot of the tunnel is instead fitted with a glass window of 300 mm in diameter.

To avoid the occurrence of wing tip effects, additional wing fences (side plates) were mounted at the two extremities of the span of the model. The fences were designed with a NACA 0012 shaped leading edge (see Fig.3.7), to avoid strong pressure gradients in the regions just ahead of the fence itself. The fences were realized in two separate halves and clamped to each other onto the model by means of M2 screws. The length of the fences is 140 mm, extending 20 mm upstream and 20 mm downstream with respect to the airfoil model used in this thesis ($c=100$ mm). The maximum height of the fence is 32 mm, extending up to 8 mm above the surface of the airfoil in its thickest point. The maximum width of the fence was dictated by the presence of the M2 skew and is equal to 4 mm, which is reduced up to 0.5 mm at the trailing edge. In this thesis, the side plates



Figure 3.7: CAD design of a wing fence, with top half in grey and bottom in red.

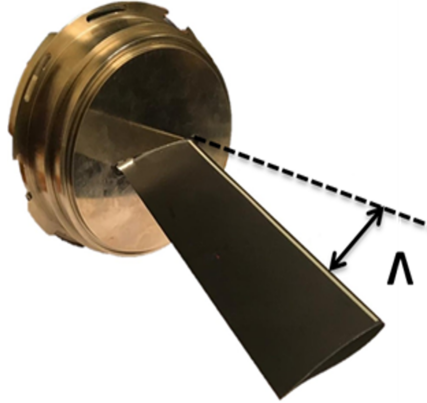


Figure 3.8: 15° swept wing attached to its clamping piece (third configuration).

have been placed at the two wing-tips (with a resulting wingspan of 20 cm), but thanks to their design, the fences can be shifted along the span of the model to investigate the effect of the aspect ratio on transonic buffet.

The third wind tunnel configuration was used for the configurations where the wing was connected only to one side of the tunnel. This assembly uses the same window frame as in the first configuration, although in this case instead of the small circular glass window, an additional metal clamping piece is used, as sketched in Fig.3.8. This additional piece is used to connect finite wing models with a free tip with different sweep angles and angles of attack. On the opposite side, the full glass window frame, used for the second configuration, is adopted. This configuration allows for the investigation of finite wing with different sweep angles and angles of attack. As for the second configuration, in view of the lack of optical access from both sides of the tunnel, schlieren visualizations in presence of finite wings are not feasible.

3.5. OIL FLOW VISUALIZATION

In this thesis, oil flow visualizations have been used with the goal of having a preliminary qualitative understanding of the different flow features developing on the model. In order to perform the oil flow measurements, the airfoil is covered with a thin layer of a particular oil (see sketch in Fig.3.9). In correspondence of the interface between the oil and the air, for the non-slip condition, the oil moves at the same velocity of the air and thus, the visualized streamlines are indicative of the direction of the flow in correspon-

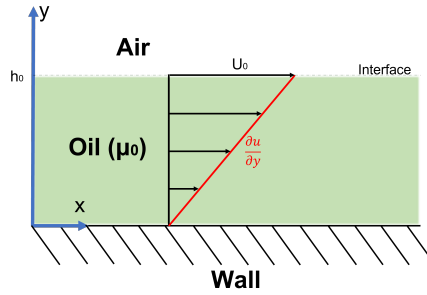


Figure 3.9: Schematic representation of oil layer and velocity.

dence of the surface of the airfoil. As described by [Brown and Naughton \(1999\)](#), the oil moves at a speed $U = \tau_x h / \mu_0$, where τ_x is the wall shear stress, h the height of the oil layer, and μ_0 its dynamic viscosity. Thus, the velocity of the oil is proportional to the wall shear stress and inversely to the viscosity of the oil.

At the oil-air interface ($h = h_0$) the shear stress is continuous, therefore, in view of the higher dynamic viscosity of the oil, the gradients of velocity are much smaller for the oil than for the air. For these reasons, the inertial forces are generally negligible and the momentum equation describing the oil dynamics is given from a balance of viscous (applied by the air on the surface of the airfoil) and pressure forces.

In absence of flow separation the pressure gradients are negligible in comparison to the wall shear stresses, and the motion of the oil can be used to indicate the direction of the flow. Differently, in presence of separated flow, the oil motion is locally governed by pressure forces, thus surface skin-friction lines are not correctly visualized. In an oil flow visualization, the separated area is generally visualized as an area where the oil accumulates, while regions in which the flow reattaches are characterized by a depletion of oil in view of the surface shear stress. Depending on the flow condition, the friction forces might be capable of completely removing the oil on the surface of the airfoil, as for supersonic conditions.

In this thesis, the oil was produced using the Shell oil Tellus 29 (viscosity of $3.0 \cdot 10^{-5} m^2/s$ at $50^\circ C$), mixed with some TiO_2 and oleic acid. The amount of oil and oleic acid is adjusted to achieve the desired settling time. For the applications in this thesis, the oil is characterized by a high value of dynamic viscosity and therefore moves at a relatively low velocity, with the advantage of being less influenced by transient effect during start up and shut down of the wind tunnel.

As an example of surface oil flow visualizations, [Fig.3.10](#) illustrates the effect of the transition trip. In the case of free transition (a), initial laminar flow, separated area, and wall effects are visualized. In sub-figure (e) the simultaneous presence of tripped (right) and non tripped flow (left) is reported, highlighting that for the non-tripped flow, small defects on the airfoil surface can trigger sudden transition to turbulent boundary layer. This observation confirms that the laminar boundary layer is very unstable and highly affected by such defects. Thus, to ensure that the flow over the airfoil is as homogeneous as possible, the application of a transition trip is highly advisable, and is indeed

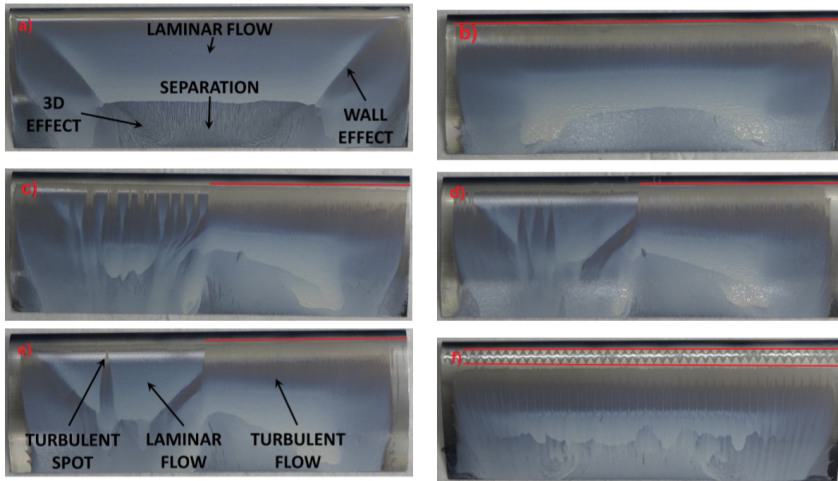


Figure 3.10: Oil flow visualization for different trip conditions (the trip presence and location is indicated in red) on the OAT15A for $Ma = 0.71$ and $\alpha = 3.5^\circ$: a) Free transition; b) Carborundum 150; c) Carborundum 320; d) Carborundum 400; e) Carborundum 500; f) zig zag.

common practice in literature. A similar triggering procedure was used in other experimental studies, with the location of the trip also placed in proximity of the leading edge of the airfoil, as for [Jacquin et al. \(2009\)](#), [Feldhusen-Hoffmann et al. \(2021\)](#), and [Accorinti et al. \(2022\)](#).

3.6. SCHLIEREN

3.6.1. WORKING PRINCIPLE

Schlieren is an optical flow diagnostic technique which allows for the visualization of density variations in the flow field and, therefore, of several flow structures, such as shockwaves, pressure waves, and regions of separated flow. The working principle of this technique was first described by Toepler (see [Settles \(2001\)](#)) and since then a large variety of modifications have been produced.

The Toepler schlieren is a system working with parallel light and is composed of a light source, lenses, mirrors, a knife edge, and a recording plane as sketched in [Fig. 3.11](#). The light beam of a light source is condensed in a point by means of a lens. To fix the dimension of the light beam to a circle of radius a , at its convergent point, a pinhole (slit) is used. The light rays are then made parallel by the use of a second lens and afterwards the rays will traverse the test section of the wind tunnel. Subsequently, by means of a further lens, the light rays are made convergent again. In correspondence of this converging point a knife edge (perpendicular to the light rays) allows only a portion of the beam to pass through ($\bar{a} < a$), cutting off the remaining portion. This portion is expanded again and reaches the recording plane of the camera. To increase the sensitivity of the system and the contrast in the schlieren image, the light beam that arrives in correspondence of

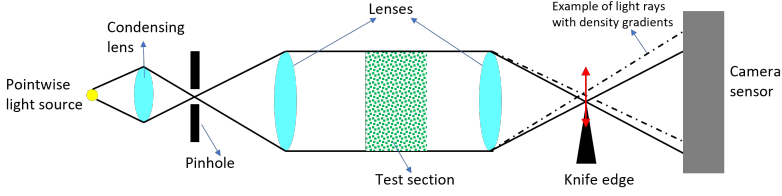


Figure 3.11: Sketch of Toepler schlieren configuration.

3

the knife edge should be as small as possible circle. The dimension of this circle in a well aligned system is equal to the size of the light beam set by the pinhole.

With a small modification of the schlieren set-up (removing the knife edge), the shadowgraph technique is obtained, which was the technique used by Ernst Mach to visualize the pressure waves developing around a bullet, already in 1887. Both these systems are able to detect differences in the density field but, while the shadowgraph detects second order derivatives of the density fields, schlieren evaluates first order derivatives. For a homogeneous test section (no density variations), the recording plane is illuminated with a uniform intensity that diminishes as \bar{a} becomes smaller. Differently, in presence of density gradients in the test section, the light rays will be refracted by certain angle ϵ , and therefore shifted (with respect to their undisturbed location) in correspondence of the knife edge, introducing a change in the transmitted beam area, Δa , according to:

$$\Delta a = f \tan(\epsilon_y) \quad (3.6)$$

Here, it has been assumed that the knife edge is parallel to the x-direction ("horizontal knife edge"), making the schlieren system responsive to light ray deflections in the y-direction. This shift Δa of the light beam can be related to the change of intensity in the recording plane:

$$\frac{\Delta I}{I} = \frac{\Delta a}{\bar{a}} = \frac{f}{\bar{a}} \tan(\epsilon_y) \quad (3.7)$$

where f is the focal length of the schlieren head. It is possible to further relate the deflection angle to the refractive index variation in the test section, obtaining:

$$\frac{\Delta I(x, y)}{I} = \frac{f}{\bar{a}} \int_{z_1}^{z_2} \frac{1}{n} \frac{\partial n}{\partial y} dz \quad (3.8)$$

n is the refractive index, defined as the ratio between the velocity of light in vacuum, c , and the velocity of light in the medium, c_v :

$$n = \frac{c_v}{c} \quad (3.9)$$

The refractive index for a gas is related to the density of the medium through the Gladstone-Dale equation:

$$n = 1 + k\rho \quad (3.10)$$

Where k is the Gladstone-Dale constant (typical value is $k_{air} = 0.23 \text{ cm}^3/\text{g}$) and is a function of air temperature and the wave length of the light. This last relation states that a

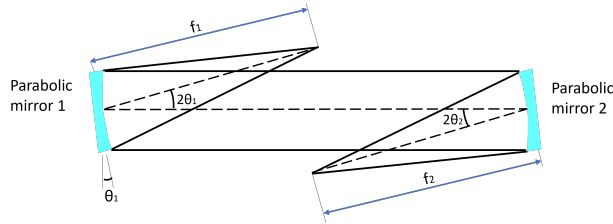


Figure 3.12: Schematic overview of schlieren z-configuration (adapted from Settles (2001)).

variation in density can be seen as a variation in the refractive index. Considering the value of $n \approx 1$ it is obtained that:

$$\frac{\Delta I(x, y)}{I} = \frac{fk}{\bar{a}} \int_{z_1}^{z_2} \frac{\partial \rho}{\partial y} dz \quad (3.11)$$

Alternatively, with the knife edge rotated by 90° ("vertical knife edge"), density gradients in the x-direction are imaged and the following relation is obtained:

$$\frac{\Delta I(x, y)}{I} = \frac{fk}{\bar{a}} \int_{z_1}^{z_2} \frac{\partial \rho}{\partial x} dz \quad (3.12)$$

Thus, the ratio $\frac{\Delta I(x, y)}{I}$ that can be detected depends on the ratio $\frac{f}{\bar{a}}$. The value of f is generally a given quantity for a specific wind tunnel, while it is possible to increase the sensibility of the system by decreasing \bar{a} . However, it is important that the value of \bar{a} is not leading to either an increase of diffraction or to a decrease of the mean signal amplitude.

The use of the Toepler schlieren configuration could introduce errors induced by, among others, astigmatism and coma. An off-axis configuration using spherical (or parabolic) mirrors is sufficient to eliminate coma. This configuration is also called a z-configuration, in view of the characteristic shape that derives from this set-up as clear from Fig.3.12. With respect to the Toepler configuration, two parabolic mirrors are used instead of the two lenses upstream and downstream of the test section. For optical reasons, when the pinhole is in the focal point of the first parabolic mirror, the light rays are collimated after the latter.

The quality of the schlieren images apart from the specific set-up and pinhole depends on the acquisition camera properties. Together with the pixel size of the camera (which determines the resolution of the measurement) another key parameter is the exposure time (τ_{exp}). The exposure time has to be chosen in such a way that the displacement of the flow structures (within this time) is not too large (limiting the exposure time to avoid blurring) while at the same time having enough average light intensity (not too short exposure time).

Another important parameter needs to be properly set is the orientation and depth of the knife edge. For the airfoil case, a vertical orientation of the knife edge favors the visualization of pressure waves moving along the chordwise direction, while with a horizontal orientation the visualization of the separated area is optimized. The depth of the

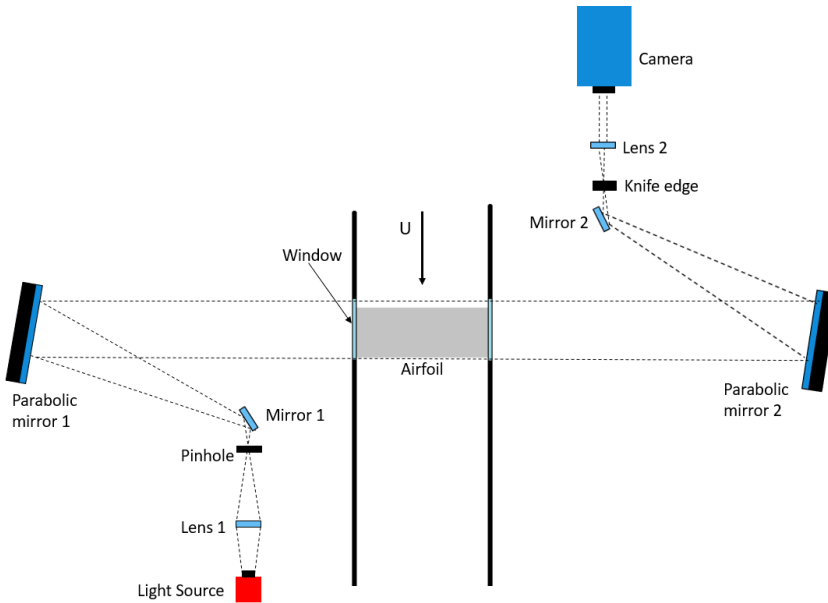


Figure 3.13: Sketch of schlieren set-up

knife edge determines the luminosity intensity in the final image and the contrast with which the compressibility effects are visualized.

3.6.2. SCHLIEREN SET-UP

In this thesis, a z-configuration schlieren set-up was used with the same settings for all the experiments, as illustrated in Fig.3.13. As sketched in the figure, the set-up includes a light source, lenses, mirrors, a recording camera, a pinhole, and a knife edge. A LED based continuous illumination system was adopted together with the Imager Pro high speed camera with an acquisition frequency of 5 kHz (allowing to resolve the shockwave position in time) with the sensor cropped to 912×816 pixels (at 7.6 pix/mm). The exposure time of the camera was set to $15 \mu\text{s}$ to sufficiently freeze the shockwave position. A pinhole diameter of 2 mm was selected, while the knife edge has been placed with a horizontal orientation to simultaneously visualize pressure waves and the separated area. An overview of the schlieren parameters is reported in Table 3.2.

3.7. BACKGROUND ORIENTED SCHLIEREN (BOS)

In applications where there is no optical access from both sides of the wind tunnel possible, traditional schlieren cannot be applied. In these applications, a similar technique, background oriented schlieren (BOS) is used, since it requires optical access from just one side of the wind tunnel (Raffel (2015)).

This techniques employs a speckle pattern, which can be directly attached to the

Table 3.2: Schlieren parameters

Parameter	Value	Unit
Resolution camera	912×816	pixels
Acquisition frequency	5	kHz
Exposure time	15	μs
Pinhole	2	mm
Knife position	Horizontal	-

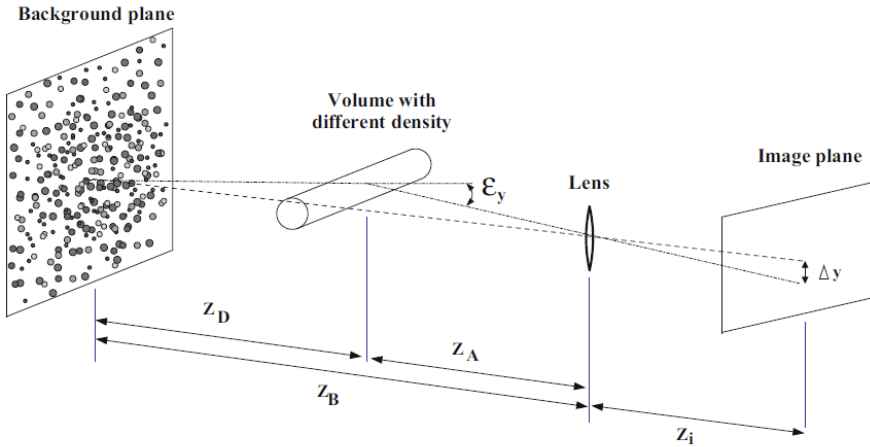


Figure 3.14: BOS working principle (Raffel et al. (2018)).

model under investigation or used as a background on the opposite wall of the wind tunnel. BOS has been applied in a variety of compressible flow studies, including transonic conditions, like in the work of Klinge et al. (2003) where BOS was used together with PIV to investigate the wing tip vortex.

A typical BOS set-up (see Fig.3.14) consists of a camera, a lens and a light source. In normal operation mode, the image of the speckle pattern acquired in presence of density gradients is compared with the undisturbed image of the speckle pattern. By means of a cross-correlation procedure between these images, the regions in which the speckle pattern is deformed allows density gradients to be extracted.

The advantages of this technique with respect to schlieren are associated with the use of a simpler optical arrangement (no need for expensive mirrors or lenses). Moreover, from the cross-correlation procedure both deflections in x and y are obtained, so there is no need for specific settings like in schlieren to distinguish between these components in the density gradient field. On the other hand, since the raw images should always be processed and thus, are not directly usable for a qualitative investigation of the flow field, e.g. for an on-line visual representation. In addition, the spatial resolution is no longer the dimension of a pixel, but dependent on the dimension of the specific window size used for the cross correlation procedure (see for more details Section 3.8).

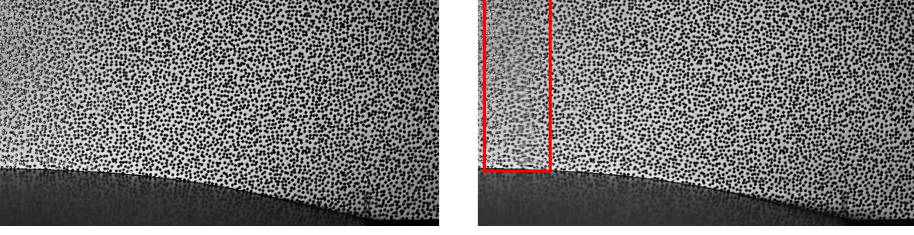


Figure 3.15: BOS raw images with (right) and without (left) flow in the wind tunnel. The rectangle indicates the area where the strongest density gradients are present.

3

For small deflections angles of the light rays within the measurement volume, the displacement in the sensor of the camera (image plane) can be written as:

$$\Delta y = Z_D \cdot M \cdot \tan \epsilon_y \approx Z_D \cdot M \cdot \epsilon_y \quad (3.13)$$

with M being the magnification of the background $M = z_i / Z_B$, Z_D the distance between the background plane and the volume with different density, Z_B the distance between the background plane and the camera lens, and z_i the distance between the camera lens and the image plane/camera sensor (see Fig.3.14). ϵ_y is instead expressed as:

$$\epsilon_y = \frac{1}{n_0} \int \frac{\partial n}{\partial y} dz \quad (3.14)$$

so the image displacement can be rewritten as:

$$\Delta y = f \left(\frac{Z_D}{Z_D + Z_A - f} \right) \cdot \epsilon_y \quad (3.15)$$

where f is, considering the background in focus, $\frac{1}{f} = \frac{1}{z_i} + \frac{1}{Z_B}$.

An example of a raw BOS image is shown for an experiment on the OAT15A ($Ma = 0.7$, $\alpha = 3.5^\circ$) on the right of Fig.3.15 and is compared with the corresponding reference image acquired with the wind tunnel off (left). Density effects are evident in correspondence of the rectangle, which is located in the shockwave oscillation region, while no other relevant difference is distinguishable with the naked eye.

Since different BOS set-ups have been used for the different investigations, these experiments and the relative set-ups will be discussed in more detail in the appropriate chapters.

3.8. PARTICLE IMAGE VELOCIMETRY (PIV)

Particle image velocimetry (PIV) is a flow measurement optical technique that has seen wide application in the last decades (Raffel et al. (2018)). Different from many other techniques it is not pointwise, but instead allows the evaluation of the velocity field on a plane (with Planar or Stereo PIV) or in a volume (Tomo PIV).

PIV is a non intrusive technique, since differently than other techniques such as pressure probes or hot wire anemometry (HWA) no probe is inserted the flow. This feature is

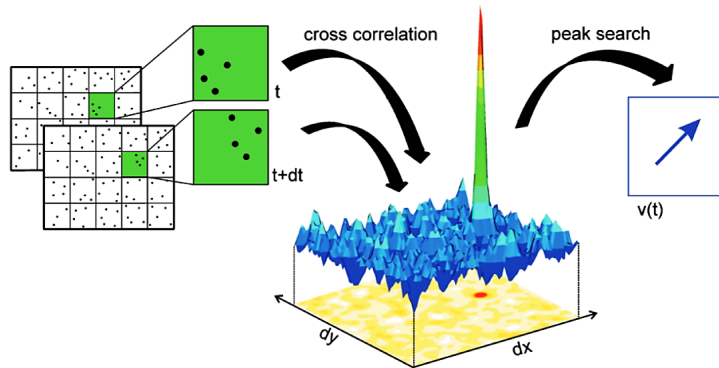


Figure 3.16: PIV working principle (Wieneke (2017)).

very useful in high speed conditions, where closed wind tunnel with limited accessibility are generally employed. The spatial resolution (SR) of PIV is relatively high and is limited by the resolution of the camera. For technological reasons a higher spatial resolution can be achieved when a low speed acquisition (low temporal resolution) PIV system is operated. With a low speed PIV system frequency of acquisition in the order of the 10-50 Hz ($SR \approx 10$ Mega pix) are obtained, while with a high speed-PIV system frequencies up to 10 kHz ($SR \approx 1$ Mega pix) can be easily achieved. The temporal resolution of the PIV system is constrained by technological limitations of both the light source and the acquisition camera (e.g. pulse separation time) and is general lower than the temporal resolution which can be achieved with a HWA system. In consideration with the specific flow structures which are investigated in this thesis both low speed and high speed systems have been separately used.

3.8.1. WORKING PRINCIPLE OF PLANAR PIV

In particle image velocimetry the velocity field is computed by evaluating the displacement of seeding particles between two consecutive images. To have particles in the field of view, a seeding system has to be adopted together with an illumination system.

The image acquired by the camera is discretized in pixels, and to each of them a level of luminosity is assigned. To compute the velocity vectors, the images are first divided in smaller regions that are referred to as interrogation windows. At this stage a cross-correlation between the same interrogation window in the same images obtained at time step t_0 and $t = t_0 + \Delta t$ is carried out. As drawn in Fig.3.16, the result of this correlation are evaluated in a correlation map. The distance between the peak of the correlation map and the origin represents the most probable displacement within that specific interrogation window. Knowing the Δt between consecutive images, it is possible to obtain the projection of the velocity vector in the plane of measurement. To avoid outliers in the determination of velocity vectors, the ratio between the magnitude of the largest and the

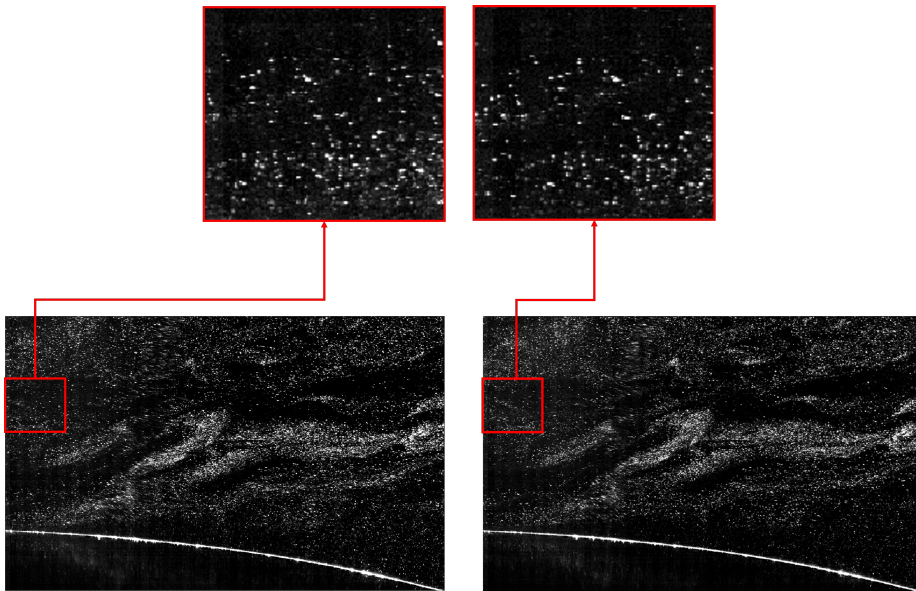


Figure 3.17: Consecutive PIV raw images with details on a window of interrogation of 64×64 pixels.

second largest peaks in the correlation map should be as high as possible. An example of two PIV raw images is shown in Fig.3.17, which also highlight in a selected area (see inserts) the downstream movement of the seeding particles.

Among the different operating modes of PIV, two of the most relevant are double-frame PIV and multi-frame PIV (Fig.3.18). In double-frame, a pair of snapshots is acquired within a very short time interval (Δt). This procedure requires appropriate cameras and a dual cavity laser to accommodate this short time interval. Once one pair of images is acquired, it takes a relatively long time (ΔT) interval to recharge the light source in order to capture an additional pair of images, thus the distribution of seeding particles in consecutive pairs of images is generally uncorrelated. Note, with reference to Fig.3.18, that pulse separation Δt and the acquisition interval ΔT , can be selected independently, within the constraints set by the system hardware. In multi-frame PIV (also referred to as time resolved PIV) images are taken continuously with a constant time interval. This interval should be small enough such that a correlation between consecutive images is possible, which is also dependent on the flow time scale. In practice, in multi-frame the Δt is too large for transonic and supersonic applications in view of the high velocity of the flow therefore, a double-frame strategy is generally adopted.

3.8.2. STEREO PIV

When a two-dimensional description is not sufficient to characterize the flow field, a Stereo PIV system can be used to also recover the out-of-plane velocity component in the measurement plane.

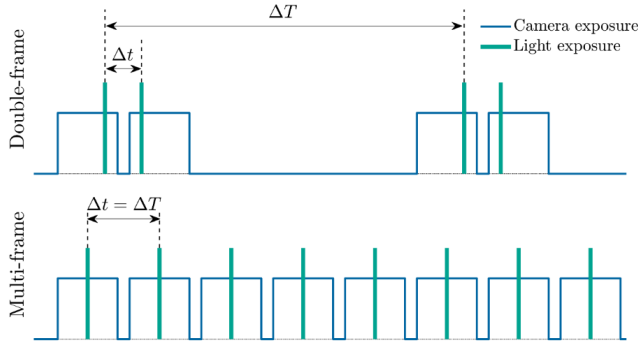


Figure 3.18: Sketch of camera and light exposure in double-frame (top) and multi-frame (bottom) PIV (Jux (2022)).

Stereo PIV is based on the same principle that allows human vision to have a 3D reconstruction of objects. The human brain, by comparing the different images from our two eyes, is able to recognize movement towards and away from the body. In the same way, by comparing the slightly different images obtained from the two cameras in stereo-configuration, it is possible to reconstruct the out-of-plane velocity component. The most accurate evaluation of the out-of-plane velocity is obtained when an angle of 90° is applied between the two cameras (Raffel et al. (2018)). However, in case of actual motion only in the out-of-plane direction, there is a perspective error that is minimized by reducing the angle in between the two cameras.

According to the Scheimpflug condition, to have the object plane correctly in focus notwithstanding the skewed viewing angle, the image, the lens and the object planes should intersect each other on a common straight line, as sketched in Fig.3.19. To achieve this condition an adapter (Scheimpflug adapter) is mounted between the camera sensor and the lens to shift the image plane with respect to the lens plane.

Through a calibration process, the viewing angles (α_1, α_2 in the XZ-plane and β_1, β_2 in the YZ-plane) of the cameras are computed. Calibration provides for correcting perspective errors and the distortions caused by the lenses. In this way a mapping function, which transforms the object coordinates in the image coordinates, is generated. Residual misalignments between calibration and measurement planes are evaluated and corrected using PIV raw images (self-calibration).

Once the self-calibration is completed, the velocity components are computed. First of all the two in plane velocity components (U_1, V_1 for camera 1 and U_2, V_2 for camera 2, see Fig.3.19) are evaluated separately in each image plane and from them the U and V velocity components are derived:

$$U = \frac{U_1 \tan \alpha_2 + U_2 \tan \alpha_1}{\tan \alpha_1 + \tan \alpha_2} \quad (3.16)$$

$$V = \frac{V_1 \tan \beta_2 + V_2 \tan \beta_1}{\tan \beta_1 + \tan \beta_2} \quad (3.17)$$

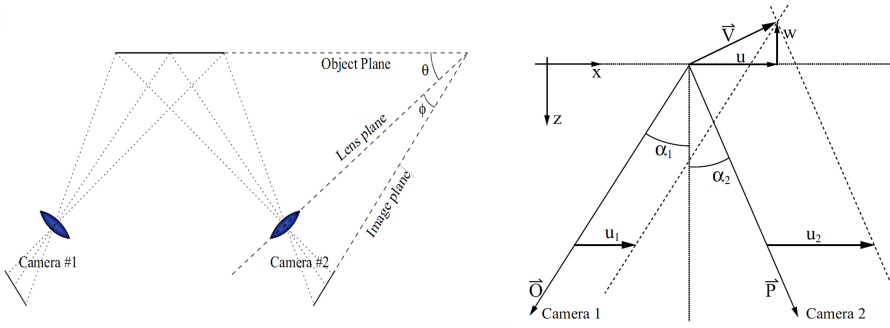


Figure 3.19: Scheimpflug condition for object, lens and image plane (left). On the right there is a sketch for the reconstruction of the out-of-plane velocity component (adapted from Raffel et al. (2018)).

While the out-of-plane component is obtained as:

$$W = \frac{U_1 - U_2}{\tan \alpha_1 + \tan \alpha_2} \quad (3.18)$$

A more detailed description of the Stereo PIV technique can be found in literature Raffel et al. (2018) .

3.8.3. PIV SET-UP

Some aspects of the PIV experiments which have been carried out in this thesis are specific to the different experiments and will be treated in detail at the appropriate place in the following chapters. Differently, aspects which are common to the different experiments are discussed in this section.

Laser system

As it was anticipated in the previous section, in this thesis two different types of laser systems have been used, namely a high speed and a low speed system. Both lasers are Nd:YAG dual-cavity lasers, operated in double pulse mode with a pulse duration of 150 ns and a wavelength of 532 nm with the pulse energy ranging from 10 mJ to 1 J. An Nd:YAG is the most common laser system used in PIV and is also referred to more explicitly as a solid state frequency-doubled neodymium-doped yttrium aluminium garnet laser. The pulse duration between 5 ns and 10 ns justifies its use for high speed flow applications. The standard architecture of this PIV laser consists of two separate laser cavities which can fire independently (dual cavity) at the required pulse separation. More specific information on the laser operation settings are given in connection to the particular experiments.

In the current thesis, the measurement plane is always oriented in a streamwise-vertical plane, thus to introduce the laser sheet inside the wind tunnel a laser probe is required. The probe can be inserted in the wind tunnel downstream of the test section from either the upper or the side wall. In this thesis, the side wall access point has been chosen, location which allows to slide the probe along the width of the tunnel. The probe

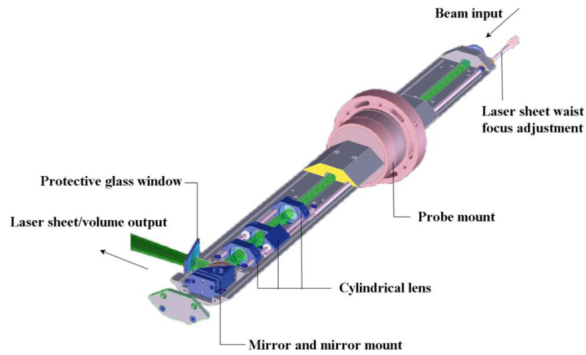


Figure 3.20: 3D CAD of laser probe with cut-outs. (Donker Duyvis (2005)).

was designed by F. J. Donker Duyvis (Donker Duyvis (2005)) and is shown in Fig.3.20, where the various constitutive elements are highlighted. The laser probe consists of a system of lenses and mirrors to create and orient the laser sheet in the test section. According to the orientation of the different elements the laser sheet can be oriented either in the streamwise-vertical plane or in a streamwise-width plane.

Seeding system

The laser is used to illuminate seeding particles, which are part of the seeding system, that consists of:

1. the seeding generator;
2. the seeding rake (distributor);
3. the seeding particles

The seeding generator used for the experiments of this thesis is the PIVTEC GMBH PIV-part45 seeder and it is directly connected to the seeding rake. The latter is placed in the settling chamber of the wind tunnel and consists of several nozzles which eject the particles in the stream tube. The density of the seeding stream can be varied remotely from the control room by selecting the number of active nozzles. In this study, all the 45 Laskin nozzles available have been used to achieve a sufficient seeding density during the measurements.

A good property of light scattering and homogeneous distribution of flow tracers in the flow field requires appropriate seeding particles to be used. The seeding particles should guarantee a good flow-tracing fidelity, which behavior is characterized by the Stokes number value (defined as the ratio between the particle response time and the flow characteristic time). Samimy and Lele (1991) showed that an acceptable flow tracing condition is achieved when $S_k < 0.1$. Unfortunately, this target condition cannot be reached in presence of a shock wave in view of the sudden jump in velocity across it, such that in its neighborhood there will always be a region with $S_k \gg 1$. To minimize this issue for the remainder of the flow fields, however, the seeding particles should be care-

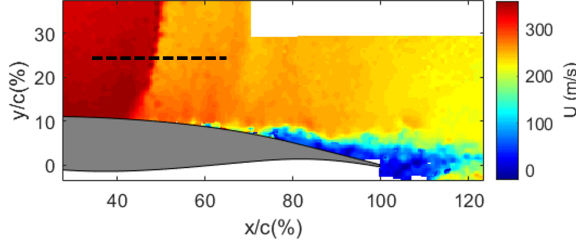


Figure 3.21: Horizontal instantaneous velocity field on the OAT15A for $\alpha = 3.5^\circ$, $Ma = 0.7$.

3

fully selected, such to achieve the smallest response time possible, yet with the particles sufficiently large (bright) that they can be detected in the PIV images.

In the experiments of this thesis, DEHS seeding particles (Di-Ethyl-Hexyl-Sebacat) with a median particle size of $1 \mu m$ (see Kähler et al. (2002)) have been adopted. The flow-tracing performance of these particles were investigated in Ragni et al. (2011) in previous experiments conducted in the TST-27, computing a relaxation time of the order of $\tau = 2 \mu s$. To compare findings from literature, an experimental estimate of the relaxation time was made for the seeding and flow conditions of the experiments described in this thesis.

Starting from the theoretical model provided in the study of Melling (1997), the motion of a spherical particle of diameter d_p and velocity V_p moving in a fluid of velocity U , can be described as:

$$\frac{dV_p}{dt} = -\frac{3}{4} C_D Re_p \frac{\mu}{\rho_p d_p^2} (V_p - U) = -K(V_p - U) \quad (3.19)$$

where ρ_p is the density of the particle, C_D its drag coefficient, Re_p its Reynolds number, μ the viscosity of the flow, and K can be considered constant in the Stokes regime ($Re_p \ll 1$). When subject to a jump in flow velocity, as in the case of when the particle crosses a shock wave, the relaxation of the particle velocity component normal to the shock can be described by a negative exponential behavior from the initial velocity value u_{n1} to the final value u_{n2} , as:

$$\ln(u_n^*) = -\ln\left(\frac{u_n - u_{n2}}{u_{n1} - u_{n2}}\right) = -Kt = -\frac{t}{\tau_p} \quad (3.20)$$

where τ_p is the relaxation time of the particles, which is the time required to the particle for reaching the velocity $u_n = u_{n2} + (u_{n1} - u_{n2})e^{-1}$.

However, from experimental data (PIV), instead of the temporal behavior of the particle velocity across the shock, its position (x_n) is generally retrieved. The particle position can be obtain by a further integration and yields to:

$$x_n = u_{n2} \tau_p \ln(u_n^*) + \tau_p (u_{n1} - u_n) \quad (3.21)$$

which can also be written in terms of the relaxation length ($\zeta_p = \tau_p [u_{n1} - (u_{n1} - u_{n2})e^{-1}]$). For supersonic conditions and for small deflection angles, an approximately linear rela-

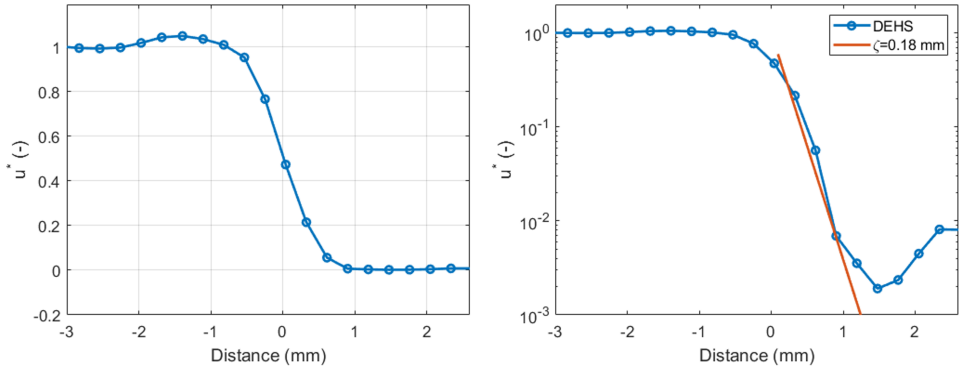


Figure 3.22: Relaxation time of DEHS particles: the behavior of the u^* component is indicated in both linear (left) and semi-logarithmic (right) scale.

tion can be established between x_n/ζ_p and t/τ_p :

$$\ln(u_n^*) = -\frac{t}{\tau_p} \approx -\frac{x_n}{\zeta_p} \quad (3.22)$$

Because the flow field in proximity of the shock is highly unsteady, as in the applications of this thesis, it is in general not possible to extract the relaxation time of the particles using average flow field data as done in [Ragni et al. \(2011\)](#) using the particle velocity relaxation across a steady oblique shock. Therefore, to make an estimation of the relaxation time of the DEHS particles under the current conditions a typical instantaneous PIV image has been used (see [Fig.3.21](#)). The value of u^* in the direction orthogonal to the shockwave (see dashed line in [Fig.3.21](#)) is reported in [Fig.3.22](#) (left). Together with the expected gradual decrease in velocity across the shockwave, upstream of the shockwave a slight increase in velocity is observable. This effect is associated with optical aberration and is minimized when the viewing direction intersects the shockwave from a small angle upstream (typically $2 - 5^\circ$, for more details see [Elsinga et al. \(2005\)](#)). The behavior of u^* is also shown in semi-logarithmic scale and with a linear line fit, an estimate of the relaxation length is obtained, which is $\zeta_p = 0.18 \text{ mm}$, that in terms of τ_p corresponds to $2.1 \mu\text{s}$.

3.9. UNCERTAINTY ANALYSIS

All the experimental data are affected by uncertainties and their quantification is of utmost importance, especially when assessing flow property fluctuations. In this section, the general background and nature of different sources of error and uncertainty that affect the measurement are reviewed, while the values for the specific experiments are provided in the corresponding chapters.

A first source of uncertainty on the mean value is the statistical convergence uncertainty due to the finite ensemble size, that for the two components of velocity can be

obtained as (Benedict and Gould (1996)):

$$\epsilon_{\bar{u}} = \frac{\sqrt{u'^2}}{\sqrt{N}}; \epsilon_{\bar{v}} = \frac{\sqrt{v'^2}}{\sqrt{N}} \quad (3.23)$$

where the numerator contains the corresponding standard deviation, whereas N is the number of uncorrelated images taken to compute the average (ensemble size). A similar uncertainty can also be computed on the standard deviation:

$$\epsilon_{u'} = \frac{\sqrt{u'^2}}{\sqrt{2N}}; \epsilon_{v'} = \frac{\sqrt{v'^2}}{\sqrt{2N}} \quad (3.24)$$

However, in some applications of this thesis the velocity vectors cannot be considered uncorrelated because of the use of a high sampling frequency ($f \approx 5 \text{ kHz}$) with respect to the characteristic frequency that governs the fluid dynamics (160 Hz). A first conservative estimation of the uncertainty could be obtained substituting instead for N the number of buffet cycles. In order to obtain a more accurate estimate, an effective number of uncorrelated images should be considered by using a correction factor. Starting from the uncertainty definition of a variable (here u is taken as example), it is possible to obtain that (Coleman and Steele (2009), Sciacchitano and Wieneke (2016)):

$$\epsilon_{\bar{u}}^2 = \sum_{i=1}^N \sum_{j=1}^N \frac{1}{N^2} \rho(u_i, u_j) \sigma_x^2 \quad (3.25)$$

where ρ is computed as the autocorrelation in time of each velocity component, and which is evaluated in each spatial point. Rearranging, ρ can be expressed as a function of the time separation between samples, $n\Delta t$, (where n indicates the different time steps and $\Delta t = (1/f)$ the time separation between consecutive snapshots):

$$\epsilon_{\bar{u}}^2 = \frac{\sum_{n=-\infty}^{\infty} \rho(n\Delta t)}{N} \sigma_u^2 = \frac{\sigma_u^2}{N_{eff}} \quad (3.26)$$

As suggested in Sciacchitano and Wieneke (2016) the summation $\sum_{n=-\infty}^{\infty} \rho(n\Delta t)$ is truncated when $\rho(n\Delta t)$ reaches zero for the first time. The resulting value of N_{eff} depends on the location in the FOV, having higher values in the shock location and in the oscillating separated area. It is worthwhile to mention that for $f \approx 5 \text{ kHz}$ (which is the typical acquisition frequency used in several experiments discussed in this thesis) the values of $\frac{N}{N_{eff}}$ are in the order of seven images. With the typical buffet frequency being around 160 Hz (see above), a full cycle is covered by approximately 30 images, so that this indicates that subsequent snapshots remain correlated for about 1/4 of the buffet cycle.

Apart from the statistical uncertainties that affect the mean and standard deviation, there are additional sources of uncertainty on the individual velocity values. An important effect particular to PIV measurements in high-speed flows is the finite time response of the seeding particles, which is most notable in particular in correspondence of

a shockwave. This results in a particle slip velocity, which is defined as the difference between the particle velocity and the actual flow velocity, and which is described by [Melling \(1997\)](#) as:

$$\epsilon_{slip} = \vec{U}_{slip} \approx \tau_p \cdot \vec{a}_p \quad (3.27)$$

The corresponding uncertainty value is evaluated by approximating the acceleration term from the measured flow field and considering that the DEHS particles which have been used, have a response time of approximately $\tau_p = 2\mu\text{s}$ (see Section 3.8.3 and [Ragni et al. \(2011\)](#)).

Also, the cross correlation procedure used in PIV, introduces an uncertainty on the individual velocity vectors, which is estimated as ([Humble \(2009\)](#)):

$$\epsilon_{cc} = \frac{\epsilon_{corr}}{M\delta t} \quad (3.28)$$

where M is the magnification factor and δt the laser pulse separation. For planar PIV it is assumed that the correlation uncertainty itself is $\epsilon_{corr} = 0.1$ pixel.

Finally, there is an uncertainty due to the fact that the use of a specific window size (WS) allows the resolution of the flow only up to a certain scale (with corresponding wavelength λ). For a single step interrogation the ratio between measured and real velocity (u/u_0) has been modelled by [Schrijer and Scarano \(2008\)](#) as:

$$\frac{u}{u_0} = \text{sinc}\left(\frac{WS}{\lambda}\right) \quad (3.29)$$

This effect is reduced in the case of a multi-step correlation, in particular for $WS/\lambda < 0.5$ (see [Sun \(2014\)](#)) and considering that typically the smallest resolvable scale in the flow has twice the size of the WS ([de Kat and van Oudheusden \(2012\)](#)), a value of $\epsilon_{sr} = \frac{|u-u_0|}{u_0} < 1\%$ is in general estimated.

Furthermore, also the schlieren data are affected by uncertainty. In this thesis, these images are analyzed mainly to obtain the instantaneous shock position, in order to evaluate the shock dynamics. Therefore, it must be taken into account that the density gradients visualized in a schlieren image do not provide a cross-sectional view, but are integrated along the entire span of the airfoil. For this reason, when a shock is not perpendicular to the light propagation vector, the shock is displayed in the schlieren image from its projected area, and therefore, it occurs thicker than it really is. The error can be evaluated as half of the thickness of the projected shock image (t_{SW}), considering the real local thickness of the shockwave to be negligible.

$$\epsilon_{schlieren} = \frac{t_{SW}}{2} \approx 3\text{mm} \quad (3.30)$$

In the following sections the different sources of uncertainty will be quantified. Generally the highest value is associated with the particle slip in the shock region, although it is completely negligible in the remaining FOV.

4

DATA ANALYSIS METHODS

4.1. PIV DATA PROCESSING

The computation of the velocity vectors from the raw PIV data (images) requires some pre-processing, processing and post-processing steps. Pre-processing is carried out to improve the quality of the particle images mainly by reducing the effect of laser light reflections, which in the current experiments occur in particular on the surface of the airfoil and at the trailing edge. This operation is carried out with either time-minimum subtraction or using a Butterworth filter, both with specific filter lengths.

Subsequently a cross correlation procedure of pair of images provides the velocity field. To avoid the loss of information of particles that move from an interrogation window to a contiguous one within dt , a partial overlap (typically 75%) of the interrogation windows is used. Additionally, the cross-correlation is performed with a multi-pass approach, using two initial passes with a larger window size, followed by two passes with a final smaller "circular" interrogation window. The "circular" interrogation window is obtained by applying a weighting function to the square interrogation window, and is described in more detail in [Nogueira et al. \(1999\)](#) and [Astarita \(2007\)](#). In this way the final solution in the small interrogation window is obtained through an iterative process that starts from a coarse grid and with successive passes arrives at the solution on the final grid.

Post-processing has the objective of correcting or eliminating possible outliers and a first step is achieved by applying the universal outlier detection ([Sciacchitano and Scarano \(2014\)](#)). An additional validation of the velocity vectors was performed in *Matlab*. A first detection of outliers was based on discarding vectors when their values was not included in ± 3 standard deviations with respect to the average value for both the velocity components. Those outliers were substituted with an interpolation of the neighboring vectors. It should be noted that this operation is not effective for large patches of outliers, which may occur in situation of intermittent particle seeding. To resolve this problem an interpolation in time instead of in space has been applied as well. For both schlieren and PIV, the additional processing has been carried out mostly in *MATLAB*.

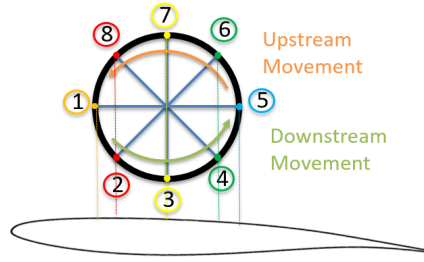


Figure 4.1: Definition of buffet cycle phases, in accordance to shock position and movement

4

4.2. PHASE AVERAGING

A time-average representation of the flow does not allow the visualization of the various elements of the dynamics of shock buffet, in the way they vary during the buffet cycle. However, for a quasi-periodic phenomenon like transonic buffet these elements can be conveniently retrieved by means of a phase average visualization approach. For the phase averaging procedure, the velocity field is represented by means of a triple decomposition, as:

$$\vec{u} = \vec{u}_{avg} + \vec{u}_{per} + \vec{u}_{turb} \quad (4.1)$$

where \vec{u}_{avg} is the average contribution, \vec{u}_{per} represents the periodic component and \vec{u}_{turb} is the quasi-random fluctuating contribution.

In the phase average analysis, the corresponding phase averaged velocity field is considered, which is obtained as the sum of the mean and the periodic contributions ($\vec{u}_{per} + \vec{u}_{avg} = \vec{u}_{phs}$). For high speed acquisitions (for which the shock position is time resolved), the buffet cycle is divided into eight phases according to the position and direction of movement of the shock, such that the first phase corresponds to the most upstream position and the fifth to the most downstream shock location (as shown by the sketch in Fig.4.1).

4.3. POD ANALYSIS

The phase averaging procedure can be considered as a form of reduced order modeling, based on shock position and motion. For a more rigorous approach, a representation of the time-varying flow dynamics associated with buffet is made based on Proper Orthogonal Decomposition (POD), by which the most energetic modes are extracted from a signal with particular spatial and temporal dynamics.

Considering $u(\vec{x}, t)$ as a function of both time (t) and spatial coordinates ($\vec{x}(x, y, z)$), the fluctuation component u' can be described with a spatio-temporal decomposition

$$u(\vec{x}, t) = u_{avg}(\vec{x}) + u'(\vec{x}, t) = u_{avg}(\vec{x}) + \sum_{j=1}^M a_j(t) \cdot \phi_j(\vec{x}) \quad (4.2)$$

where $a_j(t)$ and $\phi_j(\vec{x})$ are respectively the temporal and spatial POD modes, while M is the total number of modes.

In this thesis, the so-called Snapshot-POD method (Sirovich (1987)) is used. In this method the data are collected in a matrix U of dimensions $P \times N_t$ where P is the number of points in the space domain while N_t the number of time instances ("snapshots"). The i -th row of the matrix U is represented by the spatial components of the fluctuations of the i -th snapshot for both the velocity components (u and v), the matrix U is therefore called snapshots matrix. From the snapshots matrix it is possible to build the time coefficient matrix C as:

$$C_{POD} = \frac{1}{N_t} U U^T \quad (4.3)$$

Aranyi et al. (2013) explains that solving the eigenvalue problem associated with this $[N_t \times N_t]$ matrix C is equivalent to obtaining the decomposition which maximizes the energy related to the snapshots matrix U in an orthogonal way. From this eigenvalue problem the time coefficient matrix A_{POD} and the eigenvalues λ_j (whose square root gives the energy associated with each mode) are computed, and from the projection of the snapshots on the time coefficients the spatial functions Φ_{POD} are obtained:

$$\Phi_{POD} = U^T A_{POD} \quad (4.4)$$

providing orthonormal time coefficients and orthogonal spatial functions. Once the eigenvalues and the eigenvectors are obtained, the spatial modes are computed as:

$$U_{mode}(j) = \sqrt{\lambda(j)} \cdot \phi_j(\vec{x}) \quad (4.5)$$

The Snapshot method is particularly efficient in reducing the size of the eigenvalue problem with respect to the direct method, where $C = \frac{1}{N_t} U^T U$ has dimensions $P \times P$ and so dependent on the number of the spatial coordinates $P = P_x \cdot P_y \cdot 2$ (the factor 2 takes into account the presence of two velocity components). It is evident that snapshot-POD is more efficient than direct-POD when the number of spatial coordinates is (much) larger than the number of snapshots (P is much larger than N_t), which is always the case of this thesis. A similar problem is encountered when a singular value decomposition (SVD) would be applied. However, apart from scaling factors the same results of the snapshot-POD method are achieved. Note that the number of non-zero modes is equal to $M = \min(N_t, P)$. More details about POD, SVD and snapshot-POD can be found in Weiss (2019) and Aranyi et al. (2013).

As anticipated, POD may be used to reconstruct the velocity field using a subset of the (most dominant) modes, therefore realizing a reduced order reconstruction. For the snapshot at time step i the reconstruction then is obtained as follows, where M is the number of modes included in the reconstruction:

$$u(\vec{x}, t_i) = u_{avg}(\vec{x}) + u'(\vec{x}, t_i) = u_{avg}(\vec{x}) + \sqrt{N_t} \cdot \sum_{j=1}^M \sqrt{\lambda_j} \cdot c_j(t_i) \cdot \phi_j(\vec{x}) \quad (4.6)$$

4.4. SPECTRAL ANALYSIS

Spectral analysis will be used to characterize the physics of the phenomenon as well as to highlight quantitative differences in behavior among various configurations to assess,

for example, the impact of a control system. Starting from a signal in the time domain $x(t)$, its Fourier transform $X(f)$ is defined as:

$$X(f) = \int_{-\infty}^{\infty} x_n \cdot e^{-i2\pi f t} dt \quad (4.7)$$

From this exact definition, it is possible to derive the Discrete Fourier Transform (DTF), considering that the signal is represented by a finite number of samples equal to N :

$$X_k = \sum_{n=0}^{N-1} x_n \cdot e^{-\frac{i2\pi kn}{N}} \quad (4.8)$$

The Fourier Transform is sufficient for a spectral analysis if there is no noise or random effect, which is generally not the case for experimental data. In this situation the computation of the power spectral density (PSD) is preferred. The PSD is obtained using the square of the amplitude instead of the amplitude itself. This value indicates how the power of a signal is distributed in the frequency domain. From a mathematical point of view the PSD is obtained as the Fourier transform of the autocorrelation function:

$$P(f) = \sum_{n=-\infty}^{\infty} r(k) \cdot e^{-i2\pi kn} \quad (4.9)$$

Where $r(k)$ is defined as:

$$r(k) = E \{y(t)y^*(t-k)\} = |Y(k)|^2 \quad (4.10)$$

In this thesis, the power spectral density is computed using Welch's method (Welch (1967)) to further reduce the effect of noise which affects the experimental data, although also reducing the frequency resolution. With this method, the initial signal is divided into overlapping segments (with a overlapping percentage which goes from 0 to 50 %). The separate segments are windowed in the time domain and in each of them a Fast Fourier Transform is computed. This operation is concluded by evaluating the squared amplitude of the result, obtaining the periodogram $P_j(f)$ for each segment. By averaging each periodogram (Welch's method) it is possible to sensibly reduce the variance of the individual power measurements. Indicating with L the number of periodograms, the power spectral density according to the Welch's method is then obtained as:

$$P(f) = \frac{1}{L} \sum_{j=1}^L P_j(f) \quad (4.11)$$

For computing the PSD, the *MATLAB* *pwelch* function has been used, with its default parameters, which are:

- Using 8 segments of equal length;
- Choosing an overlap between the segments of 50%.

In this thesis, the PSD is often pre-multiplied for the frequency, which provides a quantity which is proportional to the energy of the signal at every frequency value.

4.5. AERODYNAMIC LOADS DETERMINATION

The airfoil/wing models used in this thesis are not equipped with pressure sensors. However, an estimation of the pressure field around the airfoil can be made using the PIV velocity data. The advantages of this velocity-based pressure-estimation are associated with the simplicity of the experimental models, the non-intrusivity of the technique and the high spatial resolution of the extracted pressure data. However, this determination is associated with higher uncertainties when compared to more classical pressure determination methods that rely on wall-mounted sensors in view of the hypothesis drawn and the propagation of the uncertainty on the velocity measurements (Ragni et al. (2009)).

Using the velocity and the pressure data derived from it, integral loads (lift and drag) can be obtained by a control-volume approach (van Oudheusden et al. (2007)). This requires as a first step the estimation of the pressure field. Sufficiently far away from the airfoil the flow can be considered inviscid and adiabatic, thus the isentropic relations (in combination with the ideal gas law) can be used to obtain the temperature and the pressure field:

$$\frac{T}{T_\infty} = 1 + \frac{\gamma-1}{2} M_\infty^2 \left(1 - \frac{V^2}{V_\infty^2}\right) \quad (4.12)$$

$$\frac{p}{p_\infty} = \left(1 + \frac{\gamma-1}{2} M_\infty^2 \left(1 - \frac{V^2}{V_\infty^2}\right)\right)^{\frac{\gamma-1}{\gamma}} \quad (4.13)$$

These considerations are not valid in the wake, where the flow is rotational. However, using the assumption (as a first approximation) that viscous effects are only relevant in the region in close proximity to the airfoil surface and that the flow is steady, the differential form of the momentum equation allows to obtain the local pressure gradient, as:

$$-\frac{\nabla p}{p} = \frac{\rho}{p} (V \cdot \nabla) V \quad (4.14)$$

The term ρ/p can be derived from the steady, adiabatic energy equation (equivalent to constant total temperature) and from the ideal gas equation (van Oudheusden et al. (2007)), yielding to:

$$\frac{\rho}{p} = \frac{\gamma M_\infty^2}{V_\infty^2 + \frac{\gamma-1}{2} M_\infty^2 (V_\infty^2 - V^2)} \quad (4.15)$$

From which an equation that relates the pressure field to the velocity field is obtained:

$$-\frac{\nabla p}{p} = -\nabla \ln(p) = \frac{\gamma M_\infty^2}{V_\infty^2 + \frac{\gamma-1}{2} M_\infty^2 (V_\infty^2 - V^2)} (V \cdot \nabla) V \quad (4.16)$$

A space marching algorithm is subsequently used to extract the pressure from Eq.4.16, imposing isentropic pressure as initial conditions in the freestream, similarly to van Oudheusden (2008). The pressure field is thus obtained by a spatial integration, using at each step all the immediate neighbors in which the pressure was previously known or computed as in Baur and Kongeter (1999). This procedure is illustrated in Fig.4.2.

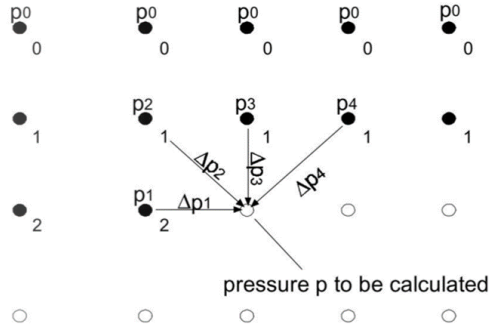


Figure 4.2: Sketch of pressure marching algorithm, from [Baur and Kongeter \(1999\)](#).

Assuming a two-dimensional and statistically steady flow the resultant aerodynamic force (R) on the airfoil can be evaluated, by using Reynolds averaging momentum equation in its integral form on a contour integral around the airfoil (see [Anderson \(2011\)](#)). Following the same procedure as in [Ragni et al. \(2009\)](#), the freestream momentum is subtracted to reduce uncertainties.

$$R = - \iint \rho (V \cdot n)(V - V_\infty) dS + \iint (-pn + \bar{\tau} \cdot n) dS \quad (4.17)$$

From R , both lift and drag components can be derived using a Cartesian frame of reference.

Evaluating the flow quantities around the entire contour can result in accumulation of uncertainty, which could lead to inaccurate estimation of the loads, in particular for the drag ([van Oudheusden et al. \(2006\)](#)). For this reason, in this thesis the drag is evaluated from the momentum deficit in the wake, based on the same approach proposed by [Jones \(1936\)](#). Following the sketch in Fig.4.3 from [Ragni et al. \(2009\)](#), it is assumed that at a certain location (1) sufficiently downstream of the airfoil, the pressure has recovered the freestream (∞) value $p_1 = p_\infty$. However, in view of the limited optical access in the wind tunnel, this location is not available and, instead, the pressure is reconstructed up to a location (2) where the pressure has not reached the freestream value yet. By using momentum balance between locations ∞ and 1, in combination with conservation of mass between station 1 and 2, the drag (D) is computed as:

$$D = \int \rho_1 u_1 (U_\infty - u_1) dy_1 = \int \rho_2 u_2 (U_\infty - u_1) dy_2 \quad (4.18)$$

Here, u_1 is derived assuming that the total pressure does not change along streamlines between locations 1 and 2. Including also compressibility effects, the following expres-

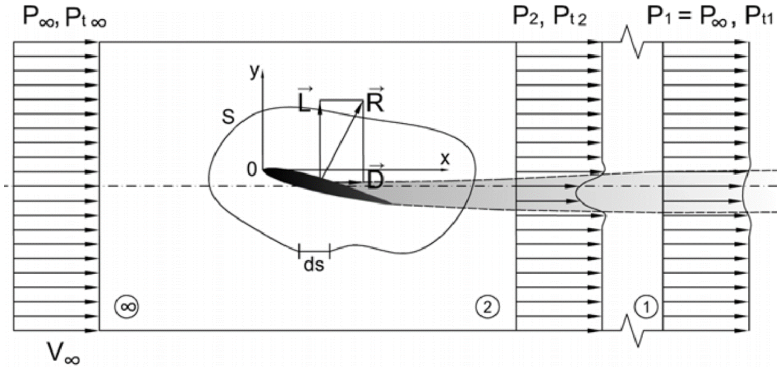


Figure 4.3: Sketch for loads determination procedure, illustrating the wake defect approach for the drag (Ragni et al. (2009)).

sion for the drag coefficient (c_d) is derived (Ragni et al. (2009)):

$$c_d = 2 \int_{y_2/c}^{y_1/c} \left(\frac{p_2}{p_\infty} \right)^{\frac{1}{\gamma}} \left(\frac{p_{t2}}{p_{t\infty}} \right)^{\frac{1}{\gamma}} \sqrt{\frac{1 - \left(\frac{p_2}{p_{t2}} \right)^{\frac{\gamma-1}{\gamma}}}{1 - \left(\frac{p_{t2}}{p_{t\infty}} \right)^{\frac{\gamma-1}{\gamma}}}} \left[1 - \sqrt{\frac{1 - \left(\frac{p_\infty}{p_{t2}} \right)^{\frac{\gamma-1}{\gamma}}}{1 - \left(\frac{p_\infty}{p_{t\infty}} \right)^{\frac{\gamma-1}{\gamma}}}} \right] d(y/c) \quad (4.19)$$

PART I
INVESTIGATION OF THE PHYSICAL
MECHANISM OF TRANSONIC BUFFET

5

CHARACTERIZATION OF THE TRANSONIC BUFFET CYCLE

Transonic buffet behavior is here investigated experimentally at flow conditions $Ma = 0.7$ and $\alpha = 3.5^\circ$ using schlieren and particle image velocimetry (PIV).

The general behavior of the buffet cycle was characterized with short-exposure schlieren visualization and phase-averaged PIV measurements. A spectral analysis showed that the shock oscillation occurs with a dominant contribution at 160 Hz ($St=0.07$, in good agreement with literature) and between 25 and 55 % of the chord of the airfoil.

Proper Orthogonal Decomposition (POD) was applied to the PIV data to extract the main modes connected with buffet. It is found that the first three most energetic modes capture around 65 % of the total fluctuating kinetic energy. The first and the third mode have a main frequency peak at 160 Hz and are well representing the separated area and the shock oscillation. The second mode was, instead, associated with an asymmetrical behavior of the separated area and of the shear layer and displays a main peak at 320 Hz, being double the main buffet cycle frequency. Finally it was shown that by using the 11 most energetic POD modes, an accurate reduced order model (ROM) is obtained, which when subtracted from the instantaneous velocity fields allows the visualization of the small-scale structures present in the flow, such as the upstream traveling waves (UTWs) and the vortex shedding in the separated area near the trailing edge. The analysis allowed to estimate the velocity of the UTWs, obtaining values in good agreement with literature. In contrast, the analysis of the vortex dynamics in the trailing edge area revealed that vortices shed at the shock foot, which convect downstream in an area detached from the airfoil surface, cannot be considered responsible for the creation of UTWs in view of the mismatch in frequency of the two phenomena.

5.1. INTRODUCTION

The mechanism by which the DTWs are generated and consequently where they originate in the flow (e.g. in the separated trailing edge area or in the shear layer) remain unclear, although [Lee \(1990\)](#) (in whose study the flow at the shock foot does not reattach during the whole buffet cycle) and [Jacquin et al. \(2009\)](#) described that the DTWs are created at the shock foot.

Since the buffet behavior over a two-dimensional airfoil is quite periodic, a modal decomposition of the data has been attempted by different research groups, in particular on CFD data. Several studies have been reported in recent years that use Proper Orthogonal Decomposition (POD) to investigate transonic buffet. [Szubert et al. \(2015\)](#) applied POD to scrutinize both the Kelvin Helmholtz (KH) and the Von Kármán (VK) instabilities as possible mechanism by which vortical structures are produced and shed downstream. It has also been demonstrated that the energy associated with the buffet mode is of almost two orders of magnitude greater than the modes associated with VK and KH instabilities themselves. In a similar way [Hall et al. \(2000\)](#) proposed a reduced order model (ROM) based on POD for describing transonic flows, showing that by using just a few modes it is possible to obtain a highly accurate reduced order model in a wide frequency range. An experimental application is presented in [Masini et al. \(2019\)](#), where POD is applied to Pressure Sensitive Paint (PSP) measurements. In [Poplingher et al. \(2019\)](#) a combination of POD and DMD (Dynamic Mode decomposition) is used in order to obtain the modes related to buffet on the RA16SC1 airfoil. Good agreement between the POD and DMD modes was obtained, with the first modes representing the shock oscillation and variation of the separated area with main spectral contribution at the buffet frequency. Higher order modes at frequency multiples of the buffet show small coherent structures in the shock oscillation area. [Ohmichi et al. \(2018\)](#) used both DMD and POD to study transonic buffet on a swept wing, giving particular attention to the formation of the buffet cells. [Feldhusen-Hoffmann et al. \(2021\)](#) obtained, by using dynamic mode decomposition (DMD), a vortex shedding mode with the same characteristic frequency of the UTWs, supporting the feedback loop description of buffet. Recently, [Moise et al. \(2022\)](#) have used spectral POD to study the transonic buffet behavior of infinite wings, highlighting the presence of a low frequency mode associated with buffet and high frequency mode associated with vortex shedding. Obtaining similar results with respect to turbulent buffet, it has been concluded that the mechanisms which describe both laminar and turbulent buffet are the same.

It is evident from literature that the full mechanism of transonic buffet has not been completely resolved yet, especially concerning the formation and behavior of the downstream traveling waves, but that the use of modal decomposition is a powerful tool to obtain new insight. In this chapter, POD will also be used to gain further information on the buffet mechanism from the experimental observations. In addition to characterizing the main features of the buffet cycle, POD will be used to further construct an efficient reduced order model (as in [Hall et al. \(2000\)](#)), which allows to extract the small structures in the flow field, like UTWs and vortices being shed in the separated area.

In Section 5.2 a detailed description of the experimental set-up and procedures will be given. This will be followed by a description of the buffet cycle, using schlieren snapshots and PIV phase-averaged velocity fields (Sections 5.3, 5.4). In Section 5.5 the main

fluid-dynamics features are analyzed by means of POD. Next, in Section 5.6 the propagation of UTWs and of downstream propagating vortices is achieved by making use of POD as a reduced order model. The chapter is concluded with a discussion of the buffet mechanism, based on the results obtained (Section 5.7).

5.2. EXPERIMENTAL PROCEDURES

5.2.1. MODEL AND FLOW CONDITIONS

The airfoil model used for this investigation (see "horizontal airfoil" in Section 3.4) spans the full width of the test section and was mounted on the side windows of the wind tunnel which provide optical access from both sides. The experiments have been performed at a freestream $Ma=0.7$, $\alpha = 3.5^\circ$, and $Re_c = 2.6 \cdot 10^6$ (based on the chord of the airfoil). In previous experiments performed in the same wind tunnel on the same airfoil (Schrijer et al. (2018)), buffet has been demonstrated to be fully developed for these conditions.

5.2.2. EXPERIMENTAL MEASUREMENTS TECHNIQUES

High speed schlieren and particle image velocimetry (PIV) have been applied as flow diagnostic techniques to investigate the flow dynamics. In this chapter, schlieren technique has been operated to have a first qualitative overview of the flow field and quantitative estimation of the shockwave oscillation, For a detailed description of the schlieren set-up the reader is referred to Section 3.6.2.

In order to characterize the buffet phenomenon in more detail a planar high-speed PIV investigation was performed using the set-up shown in Fig.5.1 (right), comprising a high-speed laser (Continuum MESA PIV 532-120-M) and two Photron Fastcam SA-1 cameras. The image acquisition frequency was 4650 Hz in double pulse mode ($\delta t=3\mu s$) with a resolution of 1024×640 pixels and an acquisition time of 0.94 s. The two cameras were placed on opposite sides of the wind tunnel in order to have overlapping fields of views (FOVs) as shown in Fig. 5.1 (left). The measurement plane is located in the mid-span of the airfoil and oriented in the streamwise direction, with both FOVs having a size of 50×30 % of the chord (50×30 mm). FOV_1 starts at 26 %c from the leading edge of the airfoil, while FOV_2 stars at 72 %c.

The laser sheet, which had a thickness of approximately 1.5 mm, was generated by the light sheet optics probe described in more detail in Section 3.8.3. The cameras and lasers were synchronized using a LaVision high speed controller (art. 1108075). PIV image acquisition and processing was done using LaVision Davis 8.4.0.

5.2.3. DATA PROCESSING

For this data-set the laser reflections are reduced by means of an 11 image time-minimum subtraction. Thereafter, the cross-correlation procedure is computed with a multi-pass approach: two passes with a window size of 64×64 pixels; and two passes with a final circular window size of 24×24 pixels. In both cases an overlap of 75% has been selected obtaining a final vector spacing of 0.3% of the chord (0.3 mm). For both schlieren and PIV additional processing has been carried out mostly in *MATLAB*.

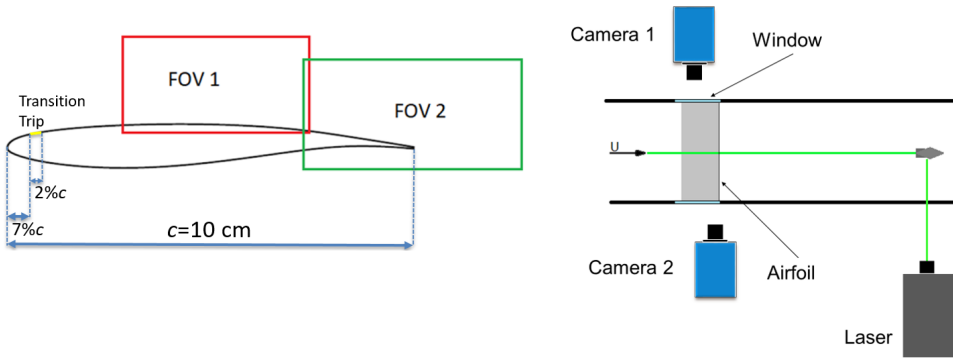


Figure 5.1: FOVs on the OAT15A airfoil (left) and sketch of PIV set-up (right).

5.2.4. UNCERTAINTY ANALYSIS

Based on the equations of Section 3.9, the values of the different sources of uncertainty are reported in the Table 5.1. The highest value is associated with the particle slip and is computed in the shock region which contains the largest velocity gradients. This estimation of the slip velocity in the shock region is highly influenced by the value of τ_p for DEHS particles in combination with the large particle deceleration across a shock.

Table 5.1: Uncertainty values

Uncertainty source	Error	Unit
Statistical (ϵ_u)	≤ 6.7	m/s
Statistical (ϵ_v)	≤ 2.2	m/s
Cross-correlation (ϵ_{cc})	≤ 6.3	m/s
Spatial resolution (ϵ_{sr})	≤ 1	%
Particle slip (ϵ_{slip})	≤ 60	m/s
Line of sight effect ($\epsilon_{schlieren}$)	≤ 3	mm

5.3. FLOW DYNAMICS

In this section, the unsteady behavior of transonic buffet will be studied starting from the instantaneous schlieren images by examining a typical buffet cycle. The cycle is divided into different phases in accordance to the shock position. The most relevant phases are those with the shock in the most upstream and downstream position as well as the two in between, i.e., with the shock in an intermediate position, traveling either upstream or downstream. The schlieren images corresponding to these phases are shown in Fig. 5.2 for the time instants that are indicated in Fig. 5.3 (left) with an '*'. In the images the phases are numbered 1, 3, 5, and 7 respectively in order to correspond to the phases that are defined in Section 5.4.

The supersonic region is clearly visible on the suction side including the terminating shock. Close to the leading edge a prominent stationary wave appears, which is associated with the presence of the transition trip at the 7% of the chord. For reference, in

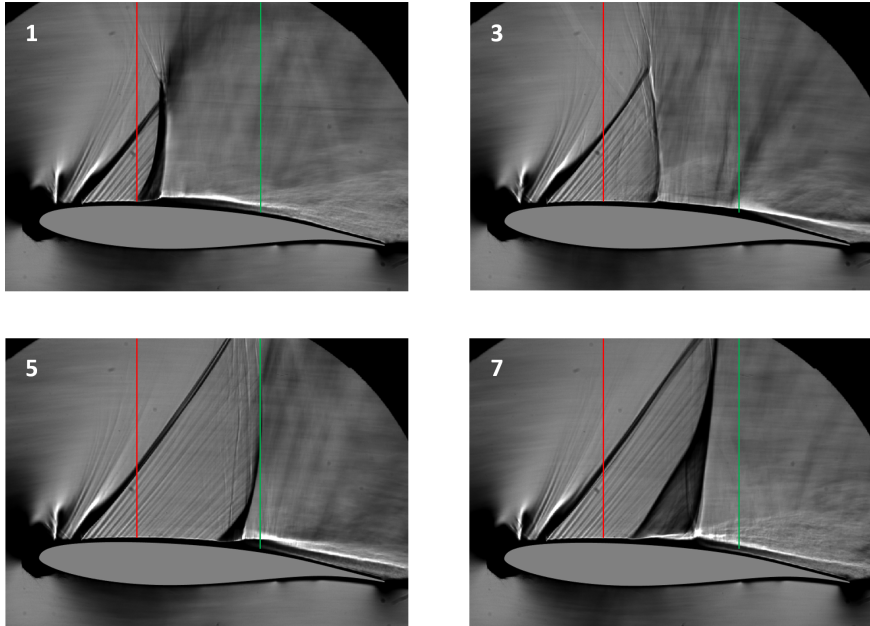


Figure 5.2: Instantaneous schlieren images in four main phases, the red and the green bars indicate, respectively, the most upstream and downstream position of the SW among all the images. *Top left*: SW is in the most upstream position. *Top right*: SW traveling downstream. *Bottom left*: SW in the most downstream position. *Bottom right*: SW traveling upstream.

all the snapshots the absolute most upstream (27% c) and the most downstream (55% c) positions of the SW are indicated, with a red and a green vertical line, respectively. In the image on the *top left*, the shockwave is in the most upstream position, around 27% of the chord. When the shock is at this location there is a large separated region which starts at the shock foot and develops till the trailing edge.

Continuing (figure in the *top right*), the shockwave starts its downstream movement and due to the decreasing relative velocity with respect to the flow it becomes weaker. This is confirmed by the fact that the separated area is smaller and develops only downstream of the SW oscillation range. Both in this and the previous phase, the presence of UTWs are observed, close to the vertical green line, as quasi-normal black lines.

In the following phase (*bottom left*) the shock reaches the most downstream position of this particular buffet cycle, which is at approximately 53% c . Although the separated region is still relatively small in the direction normal to the airfoil upper surface, it is again triggered at the shock foot in this phase.

Next, (*bottom right*) the shockwave moves upstream, becomes stronger and reaches the situation in which the separated area is the largest. The shock appears wider than in the previous schlieren image. This is due to the simultaneous presence of a λ -shock structure (close to the surface of the airfoil) and three-dimensional effects.

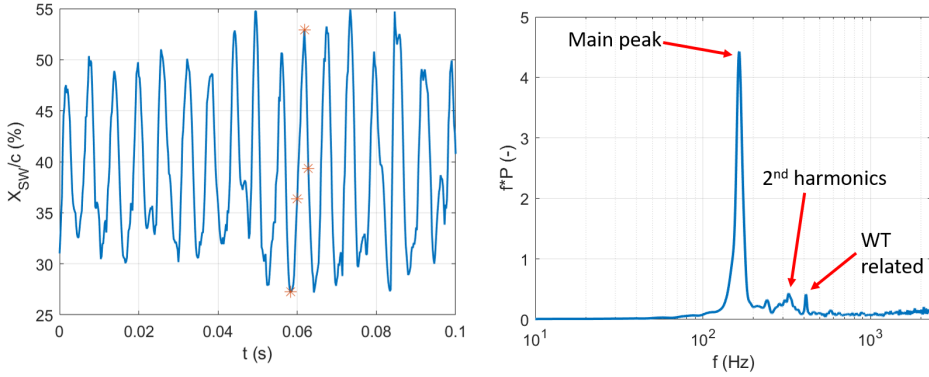


Figure 5.3: Temporal variation of shock position (*left*) (the * corresponds to the snapshots shown in Fig. 5.2). Pre-multiplied PSD related to SW position (*right*).

5

5.3.1. SPECTRAL ANALYSIS

The shock location as a function of time is extracted from the schlieren images by evaluating the maximum horizontal gradient of the image intensity. In order to reduce the random errors related to the shock detection, the shock position obtained along five parallel horizontal lines was averaged. The lines considered have been taken at a distance of 0.1c (1 cm) from the airfoil chord in order to avoid possible double detections close to the surface of the airfoil because of the λ -shock structure. A similar shock detection procedure was applied to the instantaneous PIV images based on the streamwise gradient of the u component of the velocity.

In Fig. 5.3 (*left*) the shock position obtained from the schlieren images is plotted in time showing an oscillation from a most upstream to a most downstream position with nearly constant period, however, the phenomenon cannot be considered perfectly periodic as secondary low frequency phenomena are present as well. When considering all the snapshots, an average shock position $(X_{SW})_{avg} = 37.7\%c$ and a relative standard deviation $(X_{SW})_{std} = 6.7\%c$ is obtained.

To characterize the shock oscillation, a spectral analysis is performed by evaluating the power spectral density (PSD) as commented in Section 4.4 with the Welch method (Welch (1967)). The maximum resolved frequency is 2500 Hz and 2325 Hz for the schlieren and PIV measurements respectively, with a resolution of 1 Hz. In Fig. 5.3 (*right*) the PSD ($P(f)$) is shown, in pre-multiplied form, $f \cdot P(f)$ on a frequency log scale. From the plot the presence of a dominant peak at 160 Hz is evident. This value corresponds to a Strouhal number $St = \frac{f \cdot c}{U_\infty} = 0.07$ which is in perfect agreement with the results obtained by Jacquin et al. (2009) for experiments carried out for similar conditions and airfoil geometry. In addition to a 2nd-harmonics contribution, there is also an additional secondary peak at 410 Hz which is associated with the characteristic noise of the wind tunnel. The apparent increase of $f \cdot P(f)$ for $f > 1\text{kHz}$ is associated with the uncertainty in the shock detection.

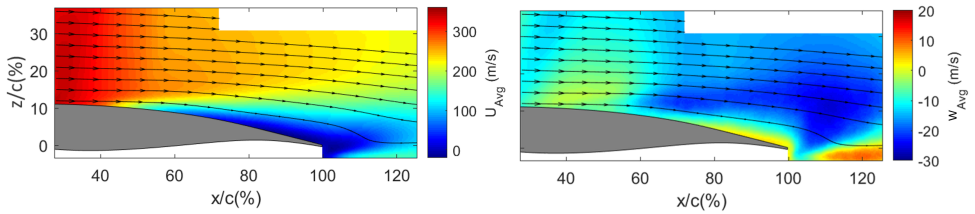


Figure 5.4: Average velocity field for horizontal (*left*) and vertical component (*right*).

5.4. PHASE-AVERAGED FLOW DESCRIPTION

5.4.1. TIME-AVERAGE VELOCITY FIELD

A more quantitative description of the buffet flow field has been obtained from the PIV velocity data, which will be used from this section on. Fig. 5.4 shows the time-average velocity distribution for both the horizontal (u) and the vertical velocity (w) components. For both velocity fields, streamlines are included in order to illustrate the flow topology. The visualization of the horizontal velocity components reveals the supersonic region upstream of the shock, the shear layer and the separated area over the rear part of the airfoil. From the vertical velocity component a region of increased velocity in the shock foot oscillation area (between 30 and 55% c) appears as well as a region of positive velocity (upwash) in the separated trailing edge area.

5.4.2. PHASE DEFINITION

Evidently, the time-average representation of the flow does not allow the visualization of the various elements of the dynamics of shock buffet. Therefore, a phase average visualization approach based on the procedure discussed in Section 4.2 is adopted. In Tab. 5.2 the number of images belonging to each phase is reported together with the corresponding statistical uncertainties, which are here obtained using Eq. 3.23 (it is assumed that the snapshots belonging to each phase are uncorrelated).

Table 5.2: Statistical uncertainty per phase

Statistical errors	Error Vx (m/s)	Error Vz (m/s)	Number of images
1 st Phase (ϵ_{Phs1})	≤ 4.9	≤ 1.6	1110
2 nd Phase (ϵ_{Phs2})	≤ 7.6	≤ 2.5	476
3 rd Phase (ϵ_{Phs3})	≤ 8.4	≤ 2.7	394
4 th Phase (ϵ_{Phs4})	≤ 8.0	≤ 2.6	427
5 th Phase (ϵ_{Phs5})	≤ 5.7	≤ 1.9	839
6 th Phase (ϵ_{Phs6})	≤ 9.7	≤ 3.1	295
7 th Phase (ϵ_{Phs7})	≤ 10.3	≤ 3.3	260
8 th Phase (ϵ_{Phs8})	≤ 8.5	≤ 2.7	387

Once the phases have been defined and the images associated to the corresponding phase bins (group of images belonging to the same phase) have been identified, it is possible to quantitatively characterize the different phases by looking at the probabil-

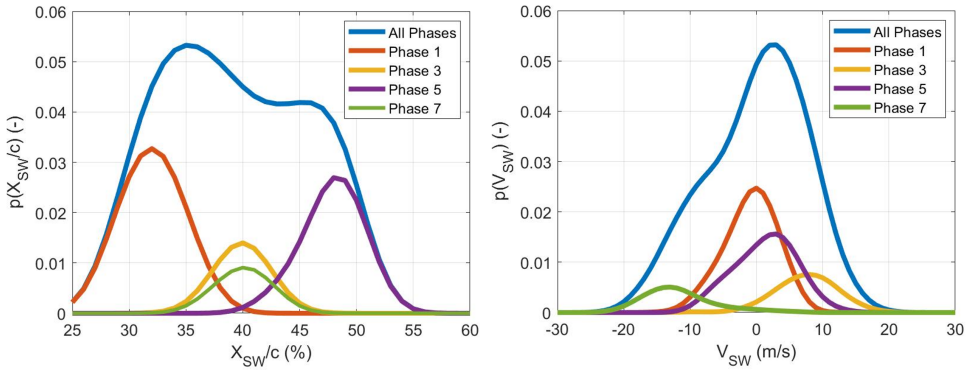


Figure 5.5: Pdf of shock position (*left*) and velocity (*right*).

ity density function (pdf) associated to the shock position $p(X_{SW}/c)$ and shock velocity $p(V_{SW})$ as shown in Fig. 5.5. The pdf has been obtained using bins with a bandwidth of 2% of the chord for the shock position and of 2 m/s for the shock velocity. The values of the pdf for the different phases are normalized by the total number of snapshots.

Starting with the shock position (Fig. 5.5, *left*) it is observed that the pdf associated to all the shock positions (indicated as "all phases") is significant in the region that ranges from 25% to 55% of the chord, having two local maxima upstream and downstream of the average shock position, which is at 40% of the chord. These results were expected since the shock position is oscillatory therefore having a pdf similar to that of a sinusoidal signal. This result is clarified when looking at the pdf of the shock velocity (Fig. 5.5, *right*) for which in phase 1 and 5 (most extreme shock positions) the maximum likelihood is close to zero, while for phases 3 and phase 7 where the maximum likelihood is respectively positive and negative. In particular, in absolute terms the higher velocity is reached during phase 7 with an average velocity of -12 m/s. Going back to the pdf of the shock position, there is quite a symmetrical behavior between the different phases in terms of shock location. In phase 3 and phase 7, as expected from the way they have been defined, the shock is located in exactly the same region, while the region of interest of phase 1 and 5 (most upstream and downstream position) is equally far from the average shock position. It should be noted that the pdf relative to the shock position in phases 3 and 7 differs in magnitude only because of the fewer number of images present in phase 7 (in which the shock moves faster and therefore less images are captured).

The pdf associated to all images ("all phases") has an asymmetrical shape which indicates that the shock tends to dwell a longer time in the forward position. Furthermore, the number of images belonging to the each phase (see Tab. 5.2), suggests that the downstream motion is on average slower than the upstream motion. This is confirmed by $p(V_{SW})$, which is skewed towards positive values.

5.4.3. PHASE AVERAGE VELOCITY FIELDS

Fig. 5.6 shows the phase average of the u (*left*) and of the w (*right*) component of the velocity for the 1st, 3rd, 5th, and 7th phase (i.e., the same phases as shown in Fig. 5.2), with

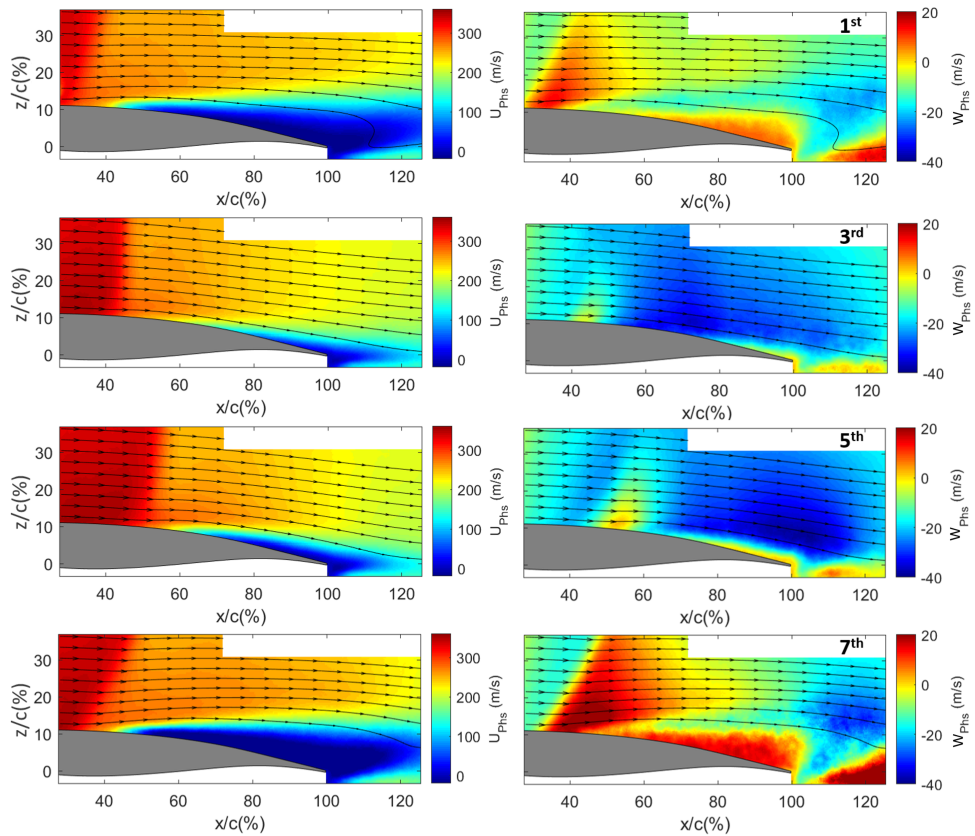


Figure 5.6: PIV phase average for u (left) and w (right) velocity component for the 1st, 3rd, 5th, and 7th phase (going from top to bottom).

the number of snapshots belonging to each phase summarized in Table 5.2. Streamlines are included to show the local flow direction.

In the first phase the shock is in the most upstream position and has a slightly oblique orientation. Correspondingly, an increase of vertical velocity at the shock foot is observed, resulting from the flow deflection associated with the upward displacement of the shear layer, similar to the corresponding schlieren visualization in Fig. 5.2 (Top left). More downstream it is possible to observe the trailing edge separated area, which extends upstream till 60% of the chord. The separation can also be observed in the vertical velocity with an increase of the w -component of the velocity at the trailing edge.

In the third phase (second row in Fig. 5.6) the shock is visualized during its downstream movement and since the velocity of the shockwave relative to the flow is the lowest in this phase, the separated region is smaller compared to the previous case, as it is clear from both the u and the w velocity component. No increase of vertical velocity is observed at the shock foot and thus the shockwave is more normal with respect to the flow than in the previous phase.

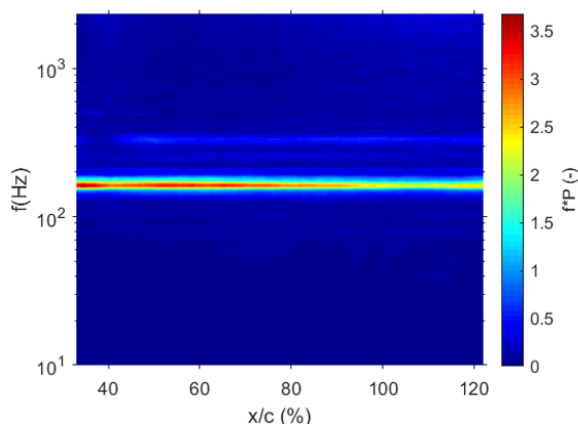


Figure 5.7: Spectrogram of the horizontal component of velocity on a horizontal line at $z/c=12\%$ c.

5

In the fifth phase (third row in Fig. 5.6) the shockwave has reached the most downstream location. Because of this, the supersonic region is larger as the velocity field is accelerated for a longer distance upstream of the shockwave. In this phase the shock starts moving upstream again and therefore increases in strength. This is reflected in the fact that the size of the separated region has increased again.

In the seventh phase (fourth row in Fig. 5.6), as was already mentioned before, the shock has the largest velocity with respect to the flow and therefore it is expected to be the strongest in this stage. The shock appears more oblique and the separated area at the shock-foot is wider, as both the u and the w -component of the velocity indicate. After this phase, the shockwave will complete the buffet cycle reaching again the most upstream position.

5.5. MODAL DESCRIPTION OF FLOW FEATURES

While in Section 5.3.1 a spectral analysis of the shock motion based on the schlieren images was presented, Fig. 5.7 shows a spectrogram of the u -component of the velocity for a horizontal line of the PIV FOV at $z/c=12\%$ (see z -axis' scale in Fig. 5.4), with the spectrogram expressed in terms of the pre-multiplied PSD.

It is evident that there is a strong contribution at 160 Hz in the shock oscillation region and in the separated area, while a contribution at 320 Hz appears mainly downstream of the average shock position (around $45\%c$). Contributions at higher frequencies are not relevant in the whole spectrogram. The dominant frequencies extracted from the spectrogram agree with the ones that were obtained for the shock position from the schlieren snapshots (Fig. 5.3 (right)). However, from this analysis it is not evident which kind of flow structures are associated with the peaks at 160 Hz and 320 Hz. Therefore, a more detailed investigation based on a modal decomposition of the PIV flow field data was performed.

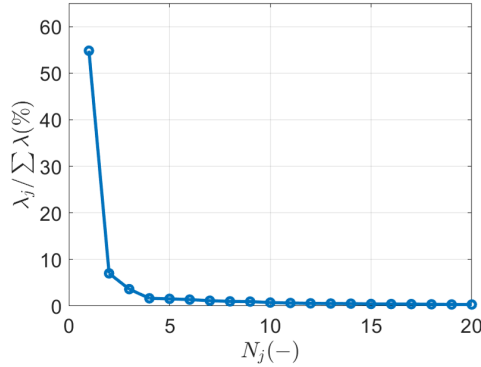


Figure 5.8: Energy fraction associated with the first 20 POD modes.

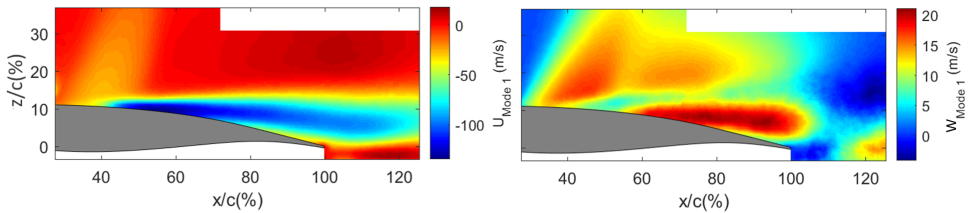


Figure 5.9: First spatial POD mode for horizontal (*left*) and vertical (*right*) velocity component.

5.5.1. POD ENERGY SPECTRUM

The phase averaging procedure that has been discussed in Section 5.4 can be considered as a form of reduced order modelling, based on shock position and motion. For a more rigorous approach, a representation of the time-varying flow dynamics associated with buffet is made based on Proper Orthogonal Decomposition (POD), using the so called snapshot-POD (see Section 4.3 for more information).

By using the POD algorithm the eigenvalues associated with the different modes are obtained and shown in Fig. 5.8 in terms of energy fraction for the first 20 modes. The energy fraction is computed as the ratio of the eigenvalue of each mode λ_j and the cumulative energy of all the modes $\sum_{j=1}^N \lambda_j$.

The first mode contains 55% of the overall energy, with 65% of the energy represented by the first three modes (80% for the first 20 modes). From the fourth mode on, the energy contribution of each mode is always lower than 2% of the total energy, with only 35% of the energy being associated with the remaining 4322 modes. The first three modes will be discussed in more detail in Section 5.5.2 and 5.5.3.

5.5.2. SPATIAL MODES

FIRST POD MODE

The first spatial mode shown in Fig. 5.9 is associated with velocity fluctuations in the separated and in the shock oscillation area. The most important variations are involving both the vertical displacement of the shear layer and the trailing edge separated area.

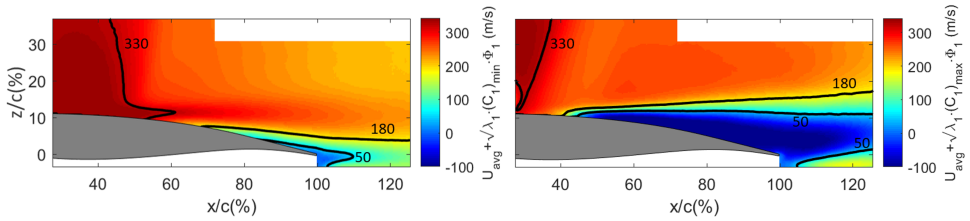


Figure 5.10: First spatial mode subtracted (*left*) and summed (*right*) to the average flow field, with contour lines at 330, 180, 50 m/s

The latter region of oscillation is well described by the w -component and it starts at 55% of the chord towards the trailing edge, whereas the former starts at 40% of the chord (most upstream location at which separation is occurring) and persists until downstream of the trailing edge.

The other aspect which is characterized by the first mode are the fluctuations induced by the shock movement which are observed between 30 and 50% of the chord (Fig. 5.9, *left*), in agreement with the phase average analysis of Section 5.4. In presence of an oblique shockwave (occurring during the upstream movement) an increase of velocity is observed at the shock foot, which is described in Fig. 5.9 (*right*) by the area of positive velocity close to 40% c .

To better assess the contribution of the first mode to the flow dynamics, the spatial mode has been added and subtracted to the average flow field using Eq.4.6. By doing so, the two extreme conditions in which the mode is in the peak (most positive time coefficient) and in the valley (most negative time coefficient) of its temporal variation are visualized. The results are discussed with visualization of only the u -component of the velocity.

The results obtained for the first mode are shown in Fig. 5.10, where on the *left* the mode is subtracted while on the *right* it is added. In order to better appreciate the general flow field, three contour lines have been added, corresponding to 330, 180, and 50 m/s, respectively. This representation distinguishes a situation in which the separated area is wide and the shock wave oblique (*right*) from a situation in which the shock wave is more normal and located downstream with the separated area almost absent (*left*). It is evident that between these two extreme situations no strong variation occurs in the shear layer thickness (which is approximated by the region in between the contour lines belonging to 180 and 50 m/s), but only in its position.

SECOND POD MODE

The second mode can be associated with the temporal asymmetry between the behavior of the shear layer and of the separated area. As evident in Fig. 5.11, the main activity of the second mode occurs in the separated area. As shown for the u -component (Fig. 5.11, *left*), in the region where the flow is separated the mode is divided into two horizontal bands of opposite sign. This describes the behavior of the shear layer and the separated area during the buffet cycle, with the possibility for the shear layer to expand when the separated area is reducing and vice versa. As a consequence, when the shear layer becomes thicker the streamlines are deflected more upwards, while when the shear layer

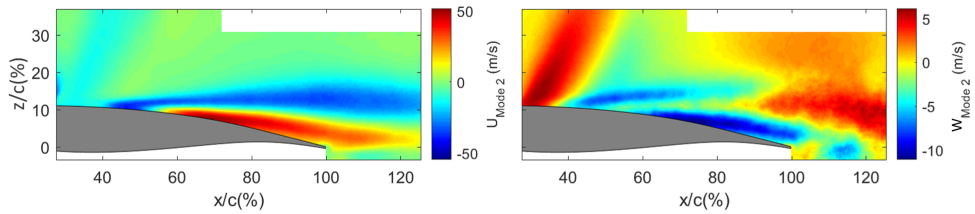


Figure 5.11: Second spatial POD mode for horizontal (*left*) and vertical (*right*) velocity component

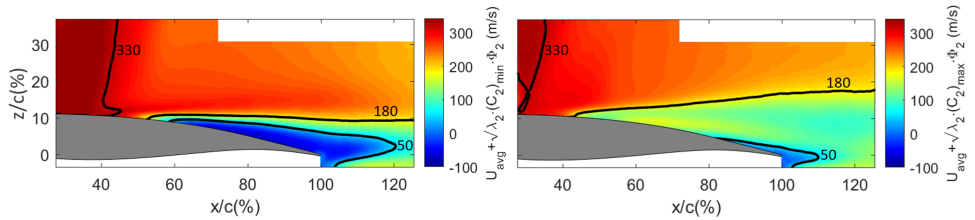


Figure 5.12: Second spatial mode subtracted (*left*) and summed (*right*) to the average flow field.

gets thinner the streamlines are tilted downwards as shown by the vertical component (Fig. 5.11, *right*).

By subtracting and adding the second mode to the average flow field (Fig. 5.12), its contribution to the flow dynamics is visualized. In fact, when adding this mode to the average velocity field a small separated area and a thick shear layer is obtained (*right*), while when the mode is subtracted a contraction of the shear layer and an increase of the separated trailing edge area is observed (*right*). Thus, this mode represents the thinning and thickening of the separated shear layer. The most upstream location of the shear layer region is seen to remain basically the same (between 45 and 50%*c*), therefore this mode is purely representing the variable thickness of the shear layer. In addition a variation in the shock position is present as well, but no variation in the shock shape is observed.

THIRD POD MODE

The third mode (Fig. 5.13) can be mainly associated with shock dynamics. The horizontal velocity component of this mode shows important velocity variations in the region where the shock oscillates (between 30% and 50% of the chord) and smaller fluctuations in the trailing edge area. Because of the shock oscillation, a deflection of the flow in correspondence of the shockwave is observed. In addition, this mode is able to account for flow separation at the shock-foot (between 50 and 65% *c*). Both these aspects are represented by the vertical component of the third mode (Fig. 5.13, *right*).

When subtracting and adding the mode (Fig. 5.14), it is clear that its main contribution is to the shock oscillation area. In addition, when the shock is located more downstream (adding the mode to the average velocity field, *right*), a change in the structure of the shock wave in the region close to the surface is observed, and with it an upstream elongation of the separated trailing edge area, which gets closer to the shock wave posi-

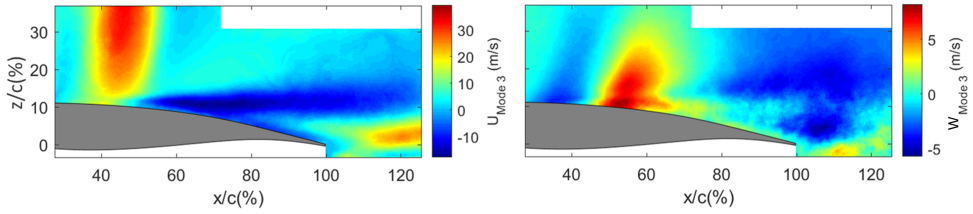


Figure 5.13: Third spatial POD mode for horizontal (*left*) and vertical (*right*) velocity component.

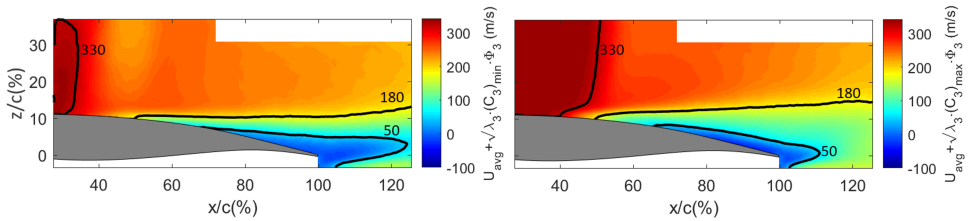


Figure 5.14: Third spatial mode subtracted (*left*) and summed (*right*) to the average flow field.

5

tion. A small increase of the extent of the shear layer is observed as well.

REDUCED-ORDER MODEL BASED ON THE FIRST THREE MODES

As mentioned in Section 5.5.1, higher modes are not further considered here, in view of their low energy contribution, with 65% of the overall energy already being represented by the first three modes. This choice will be further justified in Section 5.5.3.

In the following section the main buffet flow features will be further analyzed using the first three modes only, which according to the previous results capture the essential components of the buffet mechanism:

- Mode 1: Breathing of the separated region in correspondence to the movement of the shock;
- Mode 2: Expansion and contraction of the shear layer;
- Mode 3: Higher order representation of the shock movement and separated region breathing.

When comparing this results with literature, it is worth to stress that the obtained ranking of the modes depends highly on the choice of the FOV and on the physical quantity described (in this study velocity fields).

Poplinger et al. (2019) and Ren et al. (2020) showed leading POD and DMD modes with main activity in the shockwave oscillation range and with limited or no activity in the separated area. Differently in Feldhusen-Hoffmann et al. (2021) and in Szubert et al. (2015) leading spatial modes with variations in both the shockwave oscillation range and the separated area are shown, as in this study. However, it should be noted that in Poplinger et al. (2019) and Ren et al. (2020) the spatial modes are related to the pressure field, while in Feldhusen-Hoffmann et al. (2021) and in Szubert et al. (2015) to the

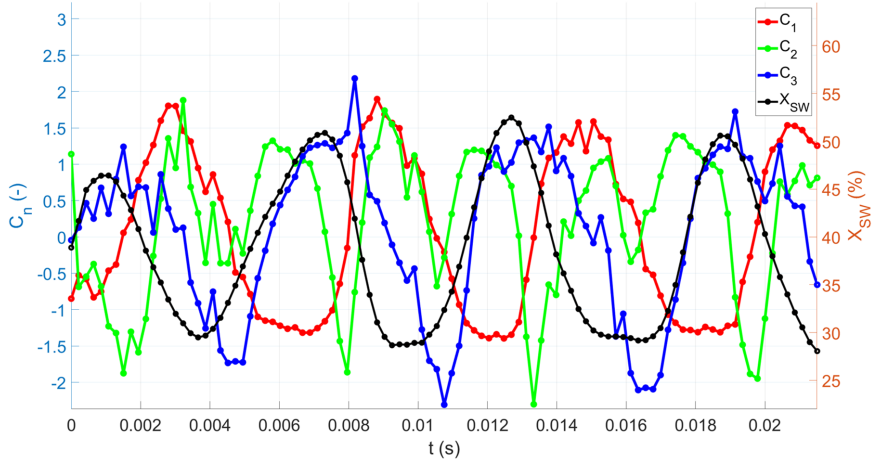


Figure 5.15: Time behavior of C_1 , C_2 , and C_3 and shock position.

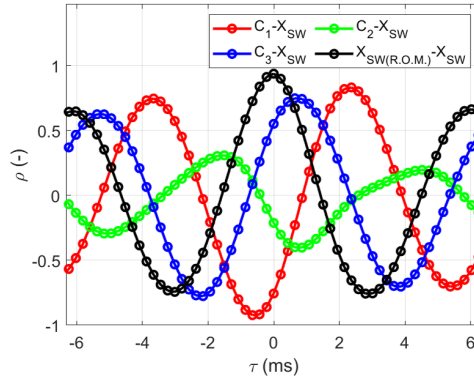


Figure 5.16: Cross-correlation between shock position and first three time coefficients.

streamwise velocity component. This difference in visualization of the spatial mode is confirmed in [Giannelis et al. \(2020\)](#). In this last study simultaneous pressure and streamwise velocity DMD modes are shown, confirming the presence of activity in the separated area for the latter only.

5.5.3. TIME COEFFICIENTS

The temporal contribution of the modes to the flow field is addressed by an analysis of the time coefficients. In Fig. 5.15 the variation of the time-coefficients C_1 , C_2 , and C_3 , connected to the first three modes is shown, together with the shock position (black curve), for a short time interval covering approximately four buffet cycles to illustrate their typical behavior.

Note that with the main buffet frequency being 160 Hz, the cycle period corresponds to 6.25 ms. The temporal coefficients clearly reflect the periodic nature of the flow field.

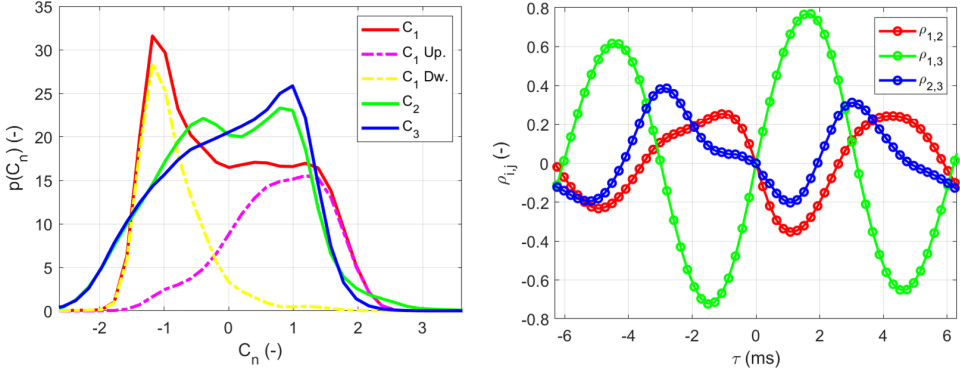


Figure 5.17: Pdf of time coefficients (*left*) and cross-correlation between first three time coefficients (*right*).

5

When comparing their behavior with the shock wave position (black line), a phase shift is observed, with none of the modes being exactly in phase with the shock position. This observation is quantified in Fig. 5.16, where the cross-correlation between the three time-coefficients and the shock position is shown. A high correlation value is present for both the first and the third mode time-coefficient, albeit with a phase delay, with $(\rho_{1,SW})_{\max} = 0.95$ and $(\rho_{3,SW})_{\max} = 0.8$, whereas a much weaker correlation is present for the second mode, where $(\rho_{2,SW})_{\max} = 0.3$. The fourth (black) curve represents the correlation for the shock position that is obtained with the reduced order model based on these first three modes. The high correlation value and zero phase shift confirm that the combination of these three modes indeed provides an accurate and complete reconstruction of the buffet cycle.

To analyze the value of the time coefficients in a more quantitative way, their distribution is shown in Fig. 5.17 (*left*) by means of a pdf ($p(C_n)$). It is highlighted that the C_2 coefficient has an almost symmetrical distribution with respect to zero, while C_3 and in particular C_1 are highly skewed. This aspect will be further discussed in Section 5.5.3. By means of a cross-correlation procedure, the temporal relation between the different modes is described, as shown in Fig. 5.17 (*right*). By virtue of the orthogonality of the POD decomposition, the cross-correlation between different modes is zero for zero lag, while the time delay (τ) for which the maximum of the cross correlation coefficient is reached, represents the phase lag between the modes. From the results it is clear that only the first and third mode are highly correlated, $(\rho_{1,3})_{\max} = 0.75$ with a lag of $\tau = 1.72$ ms (which is approximately a quarter period). Cross-correlation values lower than 0.4 are instead obtained for both $\rho_{1,2}$ and $\rho_{2,3}$, because the dominant frequency of mode 2 lies around twice the buffet frequency (see Fig. 5.15 and the subsequent frequency analysis).

The spectral content of each mode is evaluated by means of the pre-multiplied PSD of the time coefficients, using again Welch's method and the results are presented in Fig. 5.18. The first and third modes show a dominant peak at 160 Hz with negligible contributions at higher frequencies (compare Fig. 5.3, *right*). The second mode, despite having a local maximum at 160 Hz, has the highest peak at 320 Hz. Therefore, all the

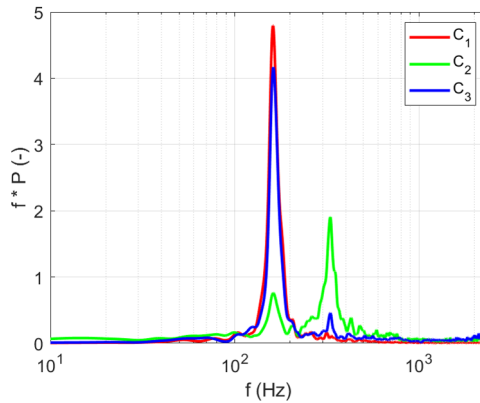


Figure 5.18: PSD associated with the first three modes.

most relevant frequencies shown by the spectrogram in Fig. 5.7 are well represented by the spectral contribution of the first three modes.

From this analysis it is evident that the first three modes are all strongly associated with the buffet phenomenon, albeit with different aspects of the cycle with all having the main peak at the same or at a multiple of the buffet frequency.

In the following sections, each of these first three modes, and in particular their time coefficients, will be scrutinized more in detail to better understand their physical interpretation.

FIRST MODE TIME COEFFICIENT

From Fig. 5.15 the time coefficient C_1 appears to be related to the shock oscillation direction (velocity), being positive when the shock moves upstream and negative during the downstream phase. In particular, the C_1 coefficient reaches its local maximum or minimum in regions where the SW has the highest and lowest relative velocity with respect to the flow. This description is consistent with the behavior of the separated area, which is reducing during the downstream travel and increasing when the shock moves upstream. When looking at one oscillation period, it is observed that the values of C_1 are almost constant during the downstream phase while varying much more during the upstream phase, once again highlighting the asymmetry between these two phases of the cycle.

This observation is confirmed by the probability density functions of the first mode time coefficients shown in Fig. 5.17 (left). A clear peak in the neighborhood of the most negative value ($C_1 = -1.25$) is obtained, confirming that the downstream movement of the shock wave occurs in a more repeatable way; on the other hand a broader distribution of the coefficient occurs for the positive values, which corresponds to the upstream motion of the shock. These conclusions are confirmed by the probability density functions of the C_1 coefficient obtained for only the upstream (C_1 Up.) and only the downstream movement (C_1 Dw.), which are shown in the same plot.

The fact that this mode is mainly connected with the separated area is further shown in Fig. 5.19 which shows the correlation between the C_1 coefficient, the extent of the sep-

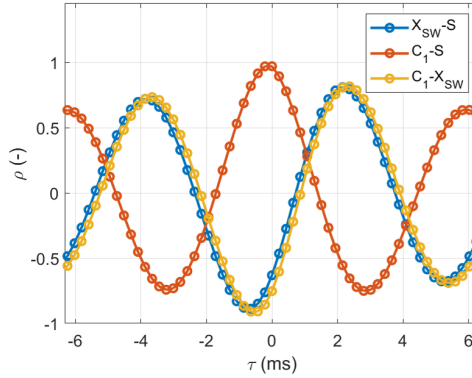


Figure 5.19: Cross-correlation between first mode time coefficient (C_1), separated area (S) and shockwave position (X_{SW}).

5

arated area (S) and the shockwave position. The extent of the separated area is evaluated by computing for each PIV snapshot the percentage of vectors which in the trailing edge area (in a region extending from 60% c to 100% c and with a height of 25% c) have a velocity lower than 50 m/s.

The orange line displays the correlation between the separated area and the C_1 coefficient, showing that the two signals are in phase and highly correlated, with a value of correlation close to unity occurring for $\tau = 0$. Differently, when looking at the correlation between the separated area and the shockwave position, a negative correlation is observed, indicating that increasing values of the SW position (SW located more downstream) are associated with decreasing values of separated area. The delay between the SW signal and the separated area signal is equal to $\tau = 0.645 \text{ ms}$ (three snapshots) indicating that the signals are shifted by one phase of the buffet cycle (as defined in Fig. 4.1). The delay between the two signals is such that the shock after reaching its most downstream position starts its upstream travel. As a consequence the SW increases the relative velocity with respect to the flow and therefore its strength, causing an increase of the extent of the separated area as well. This is consistent with what has been observed for the schlieren snapshots (Fig. 5.2). As expected, a very similar behavior is obtained for the correlation between the C_1 coefficient and the shockwave position.

The pulsating behavior of the separated area is clearly shown in literature, as for example in [Jacquin et al. \(2009\)](#) and [Grossi et al. \(2014\)](#). In the latter, when the shockwave approaches its most downstream position the separated area spans for the first time from the shock foot till the trailing edge. However, a two-dimensional quantitative evaluation of the separated area size and its correlation with the SW position signal was not carried out, differently from the results of this chapter.

SECOND MODE TIME COEFFICIENT

The behavior of the second time coefficient (C_2) is instead more complex. The values of C_2 are mainly positive, with negative peaks appearing shortly after a most upstream or most downstream shock position has been reached, with the most negative value being attained in the neighborhood of the most downstream position of the SW (see Fig. 5.15).

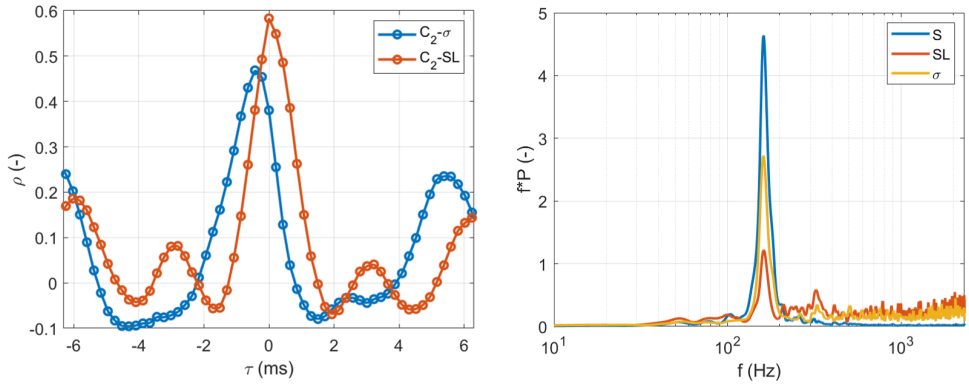


Figure 5.20: On the *left* cross-correlation between C_2 , SW inclination angle (σ) and shear layer extent (SL). On the *right* PSD of the extent of the shear layer, separated area and SW inclination.

Remembering that the second mode was found to be associated with variation in the thickness of the shear layer (see Fig. 5.12), the time behavior of the shear layer extent has been cross-correlated with the C_2 time behavior. The extent of the shear layer (SL) in time has been evaluated from the instantaneous images by determining the percentage of vectors with a horizontal velocity between and 50 and 220 m/s. The results obtained are shown in Fig. 5.20, (*left*) and highlight that the C_2 coefficient and the shear layer extent are perfectly in phase (ρ_{max} for $\tau = 0$) and correlated ($\rho(0) = 0.58$) as expected.

By evaluating the pre-multiplied PSD of the shear layer extent (Fig. 5.20, *right*) two main spectral contributions arise, the primary peak at 160 Hz (and therefore still associated with the basic buffet harmonic frequency) and a second harmonic at 320 Hz, which corresponds to the frequency obtained for the C_2 coefficient in Fig. 5.18 (*right*). The results are compared with the extent of the separated area which displays a single dominant frequency at 160 Hz similarly to what was obtained for C_1 . This result confirms that the shear layer and the separated area region have a different behavior in time. The peak at 320 Hz corresponds to the fact that the shear layer is contracting just after that the SW starts its upstream travel and again after that the SW starts its downstream movement (so twice during the buffet cycle).

At the beginning of the upstream travel the SW experiences a sharp change in inclination, which may be associated to variations in shear layer thickness. In order to investigate such relation, the shock inclination angle (σ) with respect to the freestream direction has been computed for all the snapshots by fitting a straight line to the shock. In Fig. 5.21 the simultaneous value of the shock inclination (a value lower than 90° indicates backward leaning shock) and of the C_2 coefficient are shown for a limited time interval. Despite the two signals not being in perfect agreement, there is a good correlation between the moment where the C_2 coefficient has its local minimum and the moment in which the inclination of the SW changes abruptly. This is represented in a more quantitative way by their correlation, see Fig. 5.20, (*left*) where a maximum value of $\rho = 0.48$ is obtained for $\tau = -0.430$ ms (corresponding to a two snapshots interval), suggesting that the reduction of the extent of the shear layer (and increase of the sep-

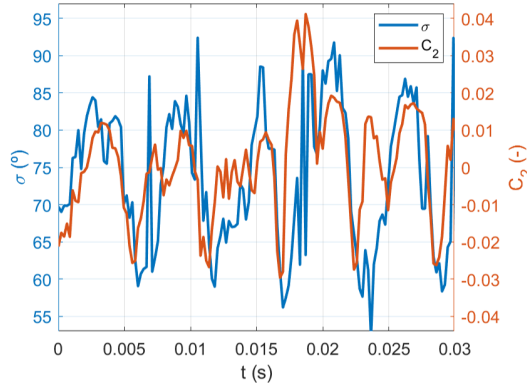


Figure 5.21: Time behavior of C_2 and of SW inclination (σ).

5

arated area) causes the sudden change of the inclination of the SW and not vice-versa. Therefore this mode could account for the rapid change in the extent of the separated area which is present in the first part of the upstream travel. The spectral content of the SW inclination signal is shown in Fig. 5.20 (right). There is a main contribution at 160 Hz but also a secondary one at 320 Hz, confirming once again the link with the flow phenomena captured by the second mode.

THIRD MODE TIME COEFFICIENT

The third mode seems to be the mode which more closely represents the shock behavior, as can be seen in the spatial mode analysis (Fig. 5.14), and with C_3 decreasing from a positive to a negative value during the upstream movement and increasing in the downstream travel (Fig. 5.15), albeit with a small time lag with respect to the SW position (blue line in Fig. 5.16).

As previously discussed, the first mode is perfectly in phase with the extent of the separated area and therefore out of phase with the shock position by 0.65 ms (see Fig. 5.19), thus this mode is not sufficient to correctly reconstruct the SW position and the extent of the separated area. In addition, as discussed in Section 5.5.3, by looking at the correlation between C_3 and the shock position it is clear that they are not in phase as well, with C_3 anticipated of 0.65 ms (about one phase of the buffet cycle) with respect to the shock position. Therefore, by using the first, second and third mode, a reconstructed image, which is perfectly in phase with the instantaneous snapshot in terms of SW position is obtained, as already anticipated in Section 5.5.3. To show this, a reconstruction of the velocity field with the first three modes has been computed using Eq. 4.6. The shock position was subsequently detected for the resulting reconstructed images. A cross-correlation has been performed between this value of the (reconstructed) SW position $X_{SW(R.O.M)}$ and the one obtained from the instantaneous images (real SW position, X_{SW}), with the results plotted in Fig. 5.16. As it is clear (black line) there is no lag between the two signals, confirming the importance of the third mode to properly reconstruct the shock dynamics which, with the first mode only, would not be possible. In

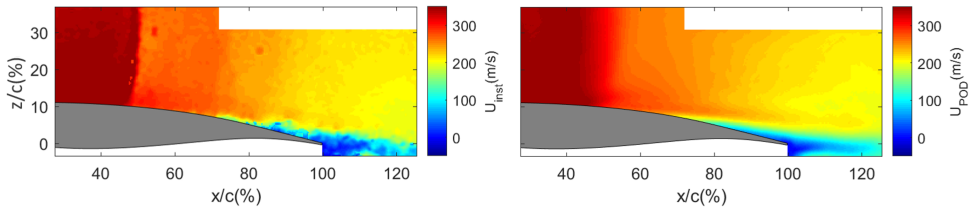


Figure 5.22: Comparison between reconstructed horizontal velocity field (*right*) and corresponding instantaneous image (*left*).

addition (as anticipated previously) a reliable spatial and temporal reconstruction of the shear layer and separated area is achieved by using the first and the second mode. This justifies the use of only the first three modes to reconstruct the dynamics of the shock, shear layer, and separated region.

5.6. UTWS AND VORTEX DYNAMICS

The first three modes accurately describe the large scale structures that characterize the buffet cycle, but they are not able to describe further aspects of the buffet oscillation, notably the propagation of the UTWs and the vortex shedding responsible for the production of the UTWs.

In literature there is no study in which the UTW propagation is directly extracted by modal analysis. This is caused by the relatively low perturbation of velocity induced by the UTWs on the mean flow. On the other hand, the vortex shedding mechanism is successfully described by modal decomposition in many studies, such as Szubert et al. (2015) and Feldhusen-Hoffmann et al. (2021). In the current investigation, the vortex shedding mode shape is only observed from the 12th mode onwards. However, none of these modes present a predominant frequency peak (or spectral bump), as should be expected for the particular phenomenon described. In fact, because of the limited acquisition frequency of the data-set, the unsteadiness associated with the vortex shedding mechanism, and the modulation with the buffet cycle, the relative dynamics is expected to be described by a multitude of modes. Therefore, none of these modes could be singularly associated with the vortex shedding phenomenon, which takes place during the buffet cycle.

Following this discussion, the POD modes are instead employed to analyze the small-scale structures in the velocity field in the form of a high pass filter, rather than by directly analyzing individual modes. To achieve this, the small scale details present in the velocity field are highlighted by subtracting a reduced-order model (ROM) based on a subset of POD modes from the instantaneous velocity field. The ROM corresponds to a low-order reconstruction of the velocity field, according to Eq. 4.6. The ROM is based on the first 11 modes (which captures 75% of the total fluctuating kinetic energy), without including any mode with a vortex shedding shape. The additional modes included in the ROM (modes 4 to 11) are higher order modes refining the SW oscillation area, the separated area and the shear layer.

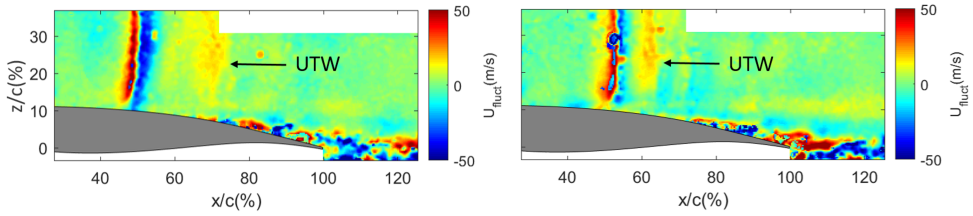


Figure 5.23: Horizontal fluctuation velocity for two consecutive time steps

5.6.1. UTW

In Fig. 5.22 the reconstruction of an instantaneous velocity field (u -component) based on the first 11 modes (*left*) is compared to the corresponding instantaneous PIV snapshot (*right*). A good agreement regarding the overall flow organization is observed, notably in terms of the extent of the separated area and of the supersonic region. As expected, the small structures that are present in the separated area are lost in the reconstruction although the size of the separated area and the shock position is well conserved, while the change in velocity across the shockwave is slightly more gradual than in the real case.

By subtracting the reduced order model reconstruction from the instantaneous velocity field the resulting fluctuating velocity field for the horizontal component is obtained (Fig. 5.23, *left*).

In the shock area two parallel vertical structures can be observed, one red and one blue, which in modal analysis are typically connected with the use of a subrange of the total number of modes (see also the higher order modes in Szubert et al. (2015) and Poplinger et al. (2019)). From this image, vortices produced in the separated trailing edge area as well as the occurrence of UTWs (yellow vertical structures) are identified. The fluctuating velocity field for the consecutive time step is shown in the image on the *right* of Fig. 5.23.

In Fig. 5.23 the UTW is visualized as the marked yellow region that in the first image appears at around 70% of the chord, whereas in the following time step it has been moved forward to a position at around 60% of the chord. From the displacement of the UTW between two consecutive time steps its propagation velocity can be evaluated yielding approximately 46 m/s for the wave shown in (Fig. 5.23). This velocity is in perfect agreement with $U_{loc} - a_{loc} = 45 \text{ m/s}$, which is the speed of sound with respect to the flow at that location. The agreement between this estimation and the actual experimental observation confirms that the observed structure is an upstream propagating pressure wave. However, as the UTWs are relatively weak flow features, for which the associated variation in flow velocity is small, the detection of the UTWs is not possible in every PIV snapshot. As a consequence, an evaluation of the shedding frequency of the UTWs is not possible. In order to have a more quantitative analysis regarding these waves, the reader is referred to the following Chapter (6) in which a clear detection of these waves is achieved by means of the BOS technique. The latter work shows that their velocities range between 40 and 100 m/s, moving always at the speed of sound with respect to the local flow velocity. In Chapter 6 a shedding frequency of the UTWs of ap-

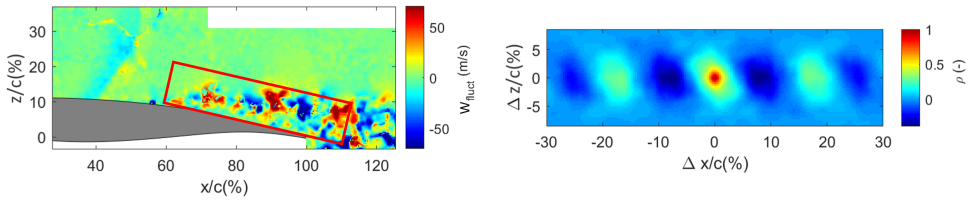


Figure 5.24: Autocorrelation (*right*) of POD subtracted vertical velocity field (*on the left*)

proximately 2000 Hz is obtained, in good agreement with the value of Strouhal number reported by [Hartmann et al. \(2013\)](#) ($St \approx 1$).

5.6.2. SHEAR LAYER VORTICES

When applied to the vertical velocity component, the subtraction of the reconstructed and instantaneous velocity fields allow to detect the presence of vortices in the separated area as shown in Fig. 5.24 (*left*), where the vortices are represented by areas of alternating velocity sign. By computing the autocorrelation in the rectangular region indicated in Fig. 5.24 (*left*) the distance between two consecutive vortices can be determined, therefore obtaining their wavelength.

Fig. 5.24 (*right*) gives the autocorrelation map corresponding to the instantaneous velocity field visualized on the *left*. Relative to the origin, there is a main negative peak at $0.07c$ and a secondary positive peak at approximately double the distance (distance between consecutive vortices). However, because of the variation in time of the extent of the separated area, the autocorrelation images are such that it is not always possible to unambiguously detect a second positive peak because of the lack, for some snapshots, of consecutive vortices.

For this reason, after extending this procedure to all of the instantaneous images, the distance between the central peak and first negative peak has been evaluated as the measure of the mean vortex separation distance. Considering that the generation of the downstream traveling waves (DTWs) is linked with complete vortex-shedding cycles, its wavelength (Δx) has been computed as double the vortex distance identified before. The probability density function of the wavelength $p(\Delta x/c)$ has been evaluated separately for each phase (Fig. 5.25) and is discussed here for the phases 1, 3, 5, and 7. For the different phases the most frequent wavelength is ranging between 15 and 21% c . The distribution is narrower for phase 1 and 5, when the SW is in the most extreme positions of the buffet cycle, while is wider when the SW is moving (higher uncertainty). It is also observed that the wavelength is shorter during the downstream travel.

As a first estimate, the propagation velocity of the vortices is computed as the average of the horizontal velocity in the shear layer region (included in the area where the cross-correlation analysis was carried out, see Fig. 5.24). An average velocity in the range of 100-140 m/s is obtained, which is in good agreement with the approximations of the convection velocity present in literature for similar applications (see [Smits and Dussauge \(2006\)](#) and [Kokmanian et al. \(2022\)](#)). From this data, the shedding frequency of the DTWs

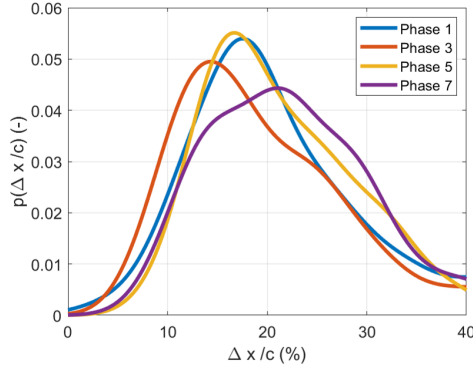


Figure 5.25: Pdf of vortex wavelength per phase, obtained subtracting the first 11 POD modes

is estimated as:

$$f_{DTWs} = \frac{u_{DTWs}}{\Delta x_{DTWs}} \quad (5.1)$$

which yields a shedding frequency between 5000 and 8000 Hz and thus with $St = 2.2 - 3.5$, which is much higher than the Strouhal number obtained for the UTWs by [Hartmann et al. \(2013\)](#) ($St \approx 1$). It should be noted that a more accurate evaluation of the shedding frequency can be obtained from a direct temporal cross-correlation of the fluctuating velocity field, which however requires a much higher acquisition frequency than presently available.

5.7. DISCUSSION AND CONCLUSIONS

The present Chapter has addressed the dynamics of transonic buffet of the OAT15A airfoil (under fully developed conditions, at $Ma = 0.7$ and $\alpha = 3.5^\circ$), using high-speed schlieren and PIV, supported with a phase-averaged description as well as modal analysis by means of snapshot POD.

The POD analysis shows how the buffet cycle displays an asymmetric behavior, with the phase of buffet in which the shock moves downstream being very different from the phase where it moves upstream. In the upstream phase the shock is moving faster with an opposite velocity with respect to the flow which causes an increase in shock strength, in combination with the occurrence of an enlarged separated area. On the other hand, the downstream phase is characterized by a weaker shock strength and smaller separated area. The increase in strength of the SW during the upstream movement is documented also in [Iovnovich and Raveh \(2012\)](#) as a result of the simultaneous change in orientation of the SW and increase of the Mach number ahead of the SW (because of the shock motion velocity).

As revealed by the cross-correlation between the shockwave and the separated area, a phase lead of the shock position with respect to the separated area size is observed (Fig. 5.19). That means that the SW starts its upstream movement before the (relatively sudden) increase of the separated area occurs, suggesting that the increase in the separated area size is a consequence and not a cause of the SW upstream movement. There-

fore, the upstream travel cannot be justified without considering the presence of additional structures, confirming the role played by the UTWs.

The upstream movement of the shock is sustained by the increasing pressure downstream of the shock and by the interaction with the UTWs, while the downstream movement is characterized by a decreasing pressure downstream of the shock position associated with the reduction of the size of the separated area. This results in the shock being faster in the upstream phase (as shown in Fig. 5.5) while moving in a slower and steadier way during the downstream travel (see Fig. 5.17, *left*). The reduction in velocity could be justified by the fact that during the upstream shock movement, the UTWs have the same direction of propagation as the SW (differently from the downstream phase). In fact when the UTWs travel upstream, behind the UTWs the pressure is slightly higher, requiring the SW to become weaker and hence move towards a region with a lower Mach number. The simultaneous growth of the separated area (and the related increase in pressure) could explain the difference in velocity between the two phases.

When analyzing the vortex shedding in the separated area, a frequency in the range of 5000-8000 Hz is obtained in the present investigation. As this value is discordant with the frequency predicted for the UTWs in literature (Hartmann et al. (2013)), it suggests that these features are not correlated. The frequency range of the vortex structures observed is in good agreement in terms of Strouhal number ($St = 2.2 - 3.5$) with the frequency obtained in Szubert et al. (2015) ($St = 2.6$) for the von Kármán shedding.

In this chapter, it has been assumed that the UTWs are produced when vortical structures convecting downstream pass over the trailing edge (i.e., from the wall bounded shear layer to a free shear layer). In view of the observed frequency discrepancy this explanation suggests that the vortices created at the shock foot, which then convect into the separated region in an area detached from the airfoil, cannot be responsible for the creation of the UTWs and a similar hypothesis is also discussed by Kokmanian et al. (2022). Therefore, there must be other structures whose passage over the trailing edge of the airfoil cause the production of pressure waves (UTWs), and so close the buffet feedback mechanism. Even though this could not be proved unambiguously in the present visualization, due to the lack of spatial resolution of the PIV images in the area close to the surface of the airfoil, it is speculated that the structures which are causing the generation of the UTWs are produced in the separated trailing edge area (instead of the shock foot separated area). In particular, a trailing edge separated area can occur even when no separation is triggered at the shock foot. An example of this is shown in Fig. 5.22 (*left*) where an instantaneous PIV image is visualized during the downstream travel of the SW (when there is no shock foot separated area), with separated trailing edge area arising from nearly 70% of the chord. The vortices present in this area are strongly affected by the pulsation of the shock foot separated area: in more detail, when the shock foot separated area is not present, vortices of high intensity are created since high variations of velocity are taking place across a small region (high shear levels). Differently, when the separated area is increasing its dimensions, vortices of lower intensity are shed. Hence, the strength of the UTWs is supposed to be modulated in accordance to the buffet frequency by means of the pulsation of the separated area, which in this Chapter has been demonstrated to oscillate with the buffet frequency at 160 Hz (see blue line in Fig. 5.20, *right*). This hypothesis will be further investigated in the following Chapter (6).

Both the schlieren instantaneous images (Fig. 5.2) and the phase averaged PIV velocity fields (Fig. 5.6) showed that also the orientation of the SW changes with the variation of the separated area, with the SW appearing more oblique during its upstream movement and more normal during its downstream motion. It is also worth stressing that the shock abruptly changes its inclination at the beginning of the upstream movement. This event is associated with a simultaneous change in the size of the shear layer, which is well described by the second POD mode (see Fig. 5.21). This mode is also activated at the beginning of the downstream travel, but with lower relevance, emphasizing the inherent asymmetry present in the flow between the upstream and the downstream movement.

POD has, therefore, demonstrated to be a useful tool for analysing the fluid-dynamic phenomena that occur, revealing in particular the asymmetry in the buffet cycle, as well as the interrelation between the different flow features involved (shock, shear layer, separated area).

6

SPANWISE ORGANIZATION OF UPSTREAM TRAVELING WAVES

The objective of this chapter is providing new insight into the role of upstream traveling waves (UTWs) in the transonic buffet phenomenon, using the background oriented schlieren (BOS) technique and corroborating the results with particle image velocimetry (PIV). The experiments were carried out on the OAT15A airfoil at a Mach number of 0.7, an angle of attack of 3.5° , and a chord-based Reynolds number of $2.6 \cdot 10^6$. The specific scope of this chapter is the characterization of the spanwise organization of the buffet phenomenon. Therefore, the measurements consider a streamwise-spanwise oriented field of view on the suction side of the airfoil. A particular topic of interest is the propagation and orientation of upstream traveling pressure waves (UTWs) that occur in transonic buffet. The experimental set-up used allowed to confirm the two-dimensionality of the velocity field and of the shockwave, but revealed that the UTWs propagate at a non-zero orientation. Processing of the BOS images with two different procedures (normal and differential), has furthermore allowed to extract the frequency and propagation velocity of the UTWs, which have been confirmed to behave as acoustic waves, traveling at the speed of sound relative to the flow. A further analysis has given hints that the strength of the UTWs is modulated during the buffet cycle and therefore in support of the feedback-mechanism description of transonic buffet.

6.1. INTRODUCTION

As summarized in Section 2.3, a key element of the transonic buffet cycle is the occurrence of upstream and downstream traveling waves (UTWs and DTWs), which are considered responsible for sustaining the shock oscillation. In this description the shock oscillation is sustained by an interaction between the shock itself and the UTWs, which, depending on the phase in the buffet cycle, force the shock to move either upstream

Parts of this chapter have been published in [D'Aguanno et al. \(2021b\)](#)

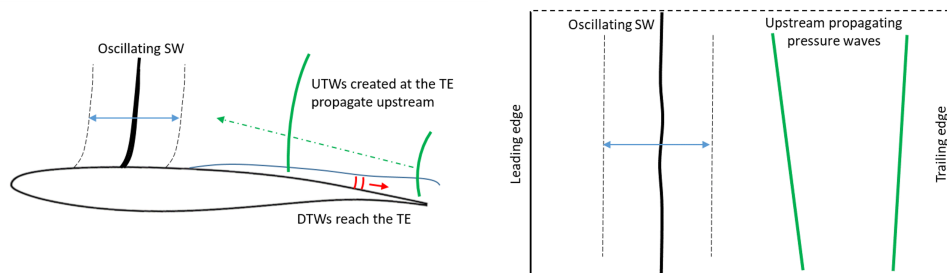


Figure 6.1: Sketch of transonic buffet in side (left) and top view (right).

or downstream. Similar conclusions have been reached by the numerical work of [Deck \(2005\)](#) which states that the origin of the upstream traveling waves is due to an interaction between the trailing edge shear layer and a sharp trailing edge. The model of [Lee \(1990\)](#) has been updated by a further study of [Deck \(2005\)](#), which considered the UTWs to be able to travel along the pressure side too, confirming the previous experimental results of [Finke \(1975\)](#).

Actually, the first author to report the occurrence of upstream propagating pressure waves was [Tijdeman \(1977\)](#), in a study of the behavior of a transonic flow around an oscillating airfoil. In this study, the presence of a phase delay between the oscillation of the airfoil and the accompanying oscillation of the shockwave was revealed. In addition, through changing the Mach number an almost linear relation between the frequency and the phase lag was found, therefore indicating a fixed time lag between the two oscillations. This time lag was consistent with the time required by changes at the trailing edge to reach the shockwave. Since these waves were considered to be produced in order to satisfy the Kutta condition at the trailing edge, they were called Kutta waves.

The main flow features appearing in the feedback loop description are shown in a sketch in [Fig. 6.1](#), where an oscillating shock wave, the downstream propagating disturbances and the corresponding upstream propagating pressure waves are visualized. These structures are displayed in both a side view of the airfoil and for a top view of the suction side of the airfoil, with the downstream propagating structures omitted in the latter case for simplicity.

A detailed experimental study on the characterization of UTWs on an airfoil was carried out by [Hartmann et al. \(2013\)](#), where high speed stereo-PIV was used in order to corroborate the findings of [Lee \(1990\)](#). The following results of [Hartmann et al. \(2013\)](#) confirmed the presence of a feedback loop between the shockwave and the disturbances produced at the trailing edge (where the UTWs are generated). It is stated that the UTWs start reaching the shock in the final phases of its downstream movement, inducing the shock to start moving upstream again. During the upstream movement of the shock, the widened area of separated flow behind it reduces the formation of DTWs and consequently of UTWs. Therefore, the shock upstream movement is not sustained by the UTWs interaction anymore and so it stops its upstream travel, which closes the feedback mechanism.

In the recent study of [Feldhusen-Hoffmann et al. \(2021\)](#), a vortex shedding mode with

the same characteristic frequency of the UTWs is obtained by using dynamic mode decomposition (DMD), supporting the feedback loop description of buffet.

Notwithstanding these observations, there is still no clear consensus in literature whether the UTWs are created only during part of the cycle, or during the whole buffet cycle but with a modulated strength. The difficulties in obtaining this kind of information is associated with the fact that is not easy to detect the UTWs, because as pressure waves, they are relatively weak flow features. An easy and sensitive way of detecting pressure waves is by using the schlieren technique, albeit that the presence of three-dimensionality effects, in particular in correspondence of the side walls of the wind tunnel, does not permit a clear identification of these waves, as shown in [Jacquin et al. \(2009\)](#). Similarly, a visualization from velocity fields, such as from laser doppler velocimetry (like in [Jacquin et al. \(2009\)](#)) or from particle image velocimetry technique (PIV) does not permit a direct detection of these waves, because of the relatively small velocity fluctuations induced by the pressure waves, as shown in [Hartmann et al. \(2013\)](#), where in order to detect these waves it was necessary to apply a high pass filter on the PIV data. Another possibility is using pressure measurements directly on the surface of the airfoil, however, despite the UTWs being produced at the trailing edge, they propagate upstream in the full velocity field and therefore cannot be easily detected by pressure measurements at the surface of the airfoil. [Jacquin et al. \(2009\)](#), as well, witnessed the difficulty in evaluating the velocity of the UTWs, commenting that more studies on this topic should be accomplished. In contrast, on the pressure side of the airfoil where no relevant flow separation occurs, it was possible to detect structures propagating upstream with a velocity close to the speed of sound relative to the velocity of the flow. In the same work, a cross-correlation of the unsteady pressure data on the suction side showed the fluctuations to propagate downstream (DTWs) with a velocity of 17 m/s which is in agreement with the one obtained by [Hartmann et al. \(2013\)](#).

An alternative technique that allows to detect the pressure waves is background oriented schlieren (BOS) as introduced by [Raffel \(2015\)](#). This techniques is based on the same principle of the schlieren technique but does not require optical access from both sides of the wind tunnel, but just from one side. It employs a speckle pattern, which can be directly attached to the model under investigation or used as a background on a wall of the wind tunnel. BOS has been applied in a variety of compressible flow studies, including transonic conditions, like in the work of [Klinge et al. \(2003\)](#) where BOS is used together with PIV in order to investigate the wing-tip vortex.

In this chapter, BOS will be used to investigate transonic buffet and in particular the UTW behavior. To the best of the authors' knowledge, no other application of BOS for detecting UTWs in transonic buffet is present in literature. By having direct optical access on the suction side of the airfoil, it has been possible to investigate the spanwise organization of buffet on a two-dimensional airfoil. Similar kind of investigations have been reported for three-dimensional wings (like in [Dandois \(2016\)](#)), but not for two-dimensional airfoils. However, despite the general flow field is expected to be two-dimensional, is still relevant to check whether also particular instantaneous features, such as the UTWs, propagate in a two-dimensional way since they are expected to be caused by structures which propagates in a region where three-dimensional effects are present. The study makes additional use of PIV to verify the findings from BOS, as well

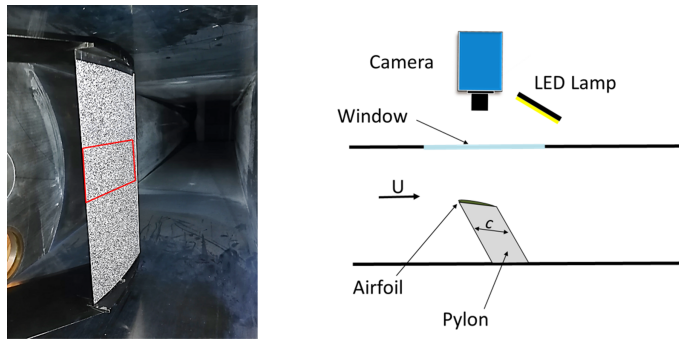


Figure 6.2: Airfoil with speckle pattern on the left and top-view of the sketch of the BOS set-up on the right.

as to complement them with the velocity field information.

The organization of this chapter is as follows. The next section (Section 6.2) describes the experimental procedures. In the following section (Section 6.3) the main characteristics of the shockwave dynamics are documented using experimental results from both BOS and PIV. Later, in Section 6.4, the propagation properties and the strength of the UTWs are obtained using BOS and they are validated using the PIV data. Finally, Section 6.5 provides a synthesis of the study, discussing the buffet cycle characteristics based on the results obtained and highlighting the main observations and conclusions.

6

6.2. EXPERIMENTAL PROCEDURES

6.2.1. MODEL

The model used is the vertical OAT15A airfoil model, with a chord (c) of 100 mm and a span (b) of 200 mm. As mentioned in Section 3.4, the configuration used in this chapter offers a convenient optical access on the suction side of the airfoil, allowing to study the spanwise organization of the UTWs. The experiments were carried out at a Mach number of 0.7, an angle of attack of 3.5° and a chord-based Reynolds number of $2.6 \cdot 10^6$.

6.2.2. MEASUREMENT TECHNIQUES

To investigate the flow field two optical techniques were used: background oriented schlieren (BOS) to investigate the (unsteady) wave pattern and particle image velocimetry (PIV) to capture the instantaneous velocity field.

For the BOS measurements, the surface of the airfoil was covered with a speckle pattern foil as shown in Fig. 6.2 (left). Here the rectangular area (indicated in red) corresponds to the field of view (FOV) of interest, which ranges from 15% to 100% of the chord (c) in the streamwise direction and from -30% to 30% of c (relative to the mid span location) in the spanwise direction. The speckle pattern consisted of black synthetic particles printed on a white background, with the particles having a size of 3 to 5 pixels, as suggested by Raffel (2015). The speckle pattern was directly printed on a sheet of paper of 0.09 mm of thickness and attached to the airfoil with glue paint. In order to observe and track the speckle pattern distortion in time, a high speed camera (Photron

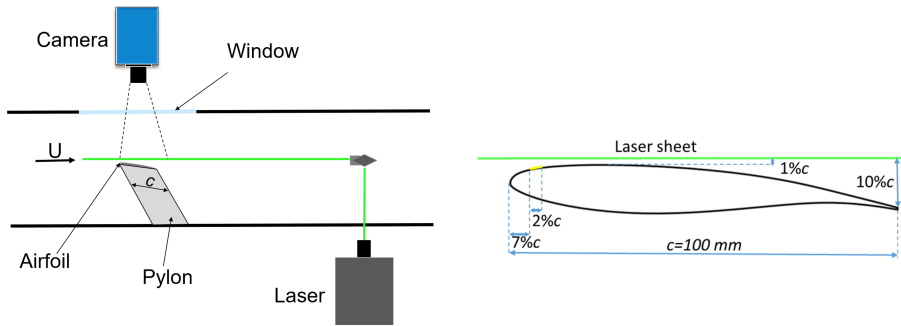


Figure 6.3: PIV set-up. On the left sketch of the top view and on the right visualization of laser sheet position with respect to the airfoil.

Fastcam SA1.1.) was used together with an LED continuous lamp, as shown in Fig. 6.2 (right) which provides a top view sketch of the set-up. The acquisition frequency of the camera is 5 kHz, which is sufficient to resolve the shock oscillation in time which occurs at a typical frequency of 160 Hz for this specific airfoil and chord size (as observed in Chapter 5). The images have been acquired through the camera software PFV (Photron Fastcam Viewer) with a resolution of 1024 x 640 pixel, and using a 105 mm lens, an f-stop of 2.8 and an exposure time of 15 μ s. Thanks to the 8 Gb internal memory of the camera, 8000 images could be stored for each test.

In Fig. 6.3 (left) the set-up of the PIV experiment is shown. A Photron Fastcam SA1.1 camera was again used, with an acquisition frequency of 4.65 kHz and a resolution of 1024 x 640 pixels, with the camera operating in planar PIV mode in order to reconstruct the streamwise and the spanwise velocity components (4365 image pairs). In this experiment the laser sheet is parallel to the vertical side walls of the wind tunnel and therefore oriented in the direction of the flow, with a thickness of 1.5 mm. As displayed in Fig. 6.3 (right), the area illuminated by the laser is at a non-constant distance from the surface of the airfoil. The laser sheet was located at a distance of 1 mm from the airfoil at its thickest point and at a distance of nearly 10 mm from the surface at the trailing edge. The projection of the FOV on the suction side of the airfoil is similar to the one of BOS, ranging from 15% of the chord to the trailing edge and depicted in Fig. 6.4 (left), where the average velocity field is shown superimposed on the model as well. In the figure also the black foil that was applied to the model to reduce the intensity of the laser light reflections can be seen.

In Fig. 6.4 (right) the average PIV velocity field is given in an enlarged form, confirming that the selected FOV represents part of the fully supersonic area upstream of the shock (between 15 and 25 %c), and the subsonic area downstream. Streamlines verify the two-dimensionality of the flow.

6.2.3. DATA PROCESSING

For both the PIV and the BOS measurements, the data have been processed using Davis 8.4.0. For the BOS measurements first reference images (with the wind tunnel off) were acquired and then the ones in presence of the flow. Two different processing approaches

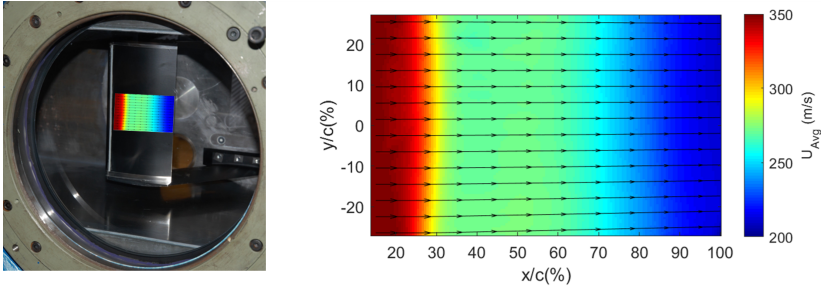


Figure 6.4: PIV FOV on the left and average horizontal velocity field on the right (also superimposed on the airfoil surface, left).

have been applied to the BOS images. The first is a standard procedure in which each BOS image is correlated with a (no-flow) reference image. The second takes a differential approach in which each image is correlated with the following one (both with the wind tunnel on). In both cases a multi-pass approach has been chosen for the correlation, using two initial passes with a window size of 64×64 pixels and two subsequent passes with a circular window of 24×24 pixels and an overlap of 75%.

For the PIV measurements, the minimum subtraction (see Section 4.1) is achieved using a Butterworth filter with a filter length of seven images. The cross correlation is computed with the same parameter settings as used for the BOS data, therefore with two passes of 64×64 pixels and two passes with a final window size of 24×24 pixels and an overlap of 75%. For both BOS and PIV measurements a resulting vector spacing of 0.55% of the chord was obtained. The main acquisition and processing parameters for PIV and BOS are also reported in Tab. 6.1.

Further processing for the BOS and PIV data was carried out in *MATLAB*.

Table 6.1: BOS and PIV settings

Setting	BOS	PIV
Acquisition frequency	5 kHz	4.65 kHz
Number of images	8000	4365 (pairs)
Final resolution	1024×640 pix	1024×640 pix
Vector spacing	0.55 mm	0.55 mm
Final window size	24×24 pix	24×24 pix
Window overlap	75%	75%

6.2.4. UNCERTAINTY ANALYSIS

The attention is here focused on the sources of error associated with the measurement techniques itself and to the corresponding processing procedures, yielding the error estimates summarized in Tab. 6.2. Since the cross-correlation procedure used for computing the BOS displacement field and for the PIV velocity field is the same, the uncertainties ϵ_{cc-PIV} and ϵ_{cc-BOS} are evaluated in the same way (Rajendran et al. (2019)). The imaged

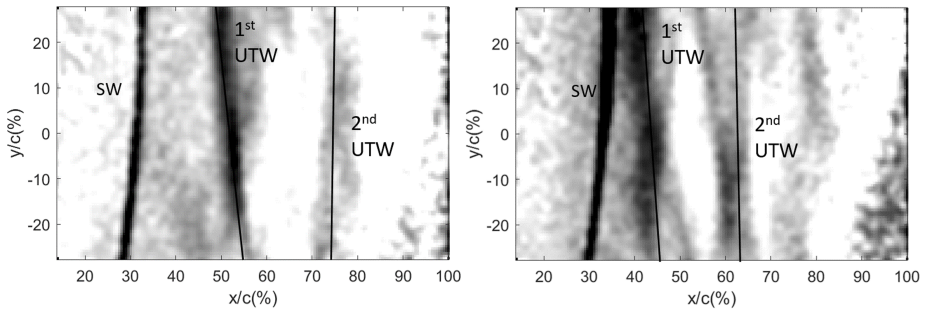


Figure 6.5: BOS instantaneous images at time t_0 (left) and $t_1 = t_0 + 0.2$ ms (right).

particle displacement due to density gradient in BOS is much smaller than the seeding particle displacement in PIV. Thus, the former is evaluated with higher accuracy even if it results in higher relative errors (in the order of 2-3%) with respect to PIV (1%), as shown by Raffel (2015). With BOS there is an uncertainty in the detection of the shock position associated with the density gradients being integrated in the full line of sight, which goes from the camera to the surface of the airfoil. This error can still be quantified as half of the thickness of the shockwave imprint on the BOS image, which is in the order of 3 mm as reported in Tab. 6.2 ($\epsilon_{sight-BOS}$). This value is not as big as the one which could be obtained for a schlieren experiments (like in Jacquin et al. (2009) or in the experiment discussed in the previous chapter), where strong interactions at the side walls cause the shock to appear even thicker.

Table 6.2: Uncertainty errors

Uncertainty source	Value
Cross-Correlation PIV (ϵ_{cc-PIV})	≤ 3.1 m/s
Particle Slip ($\epsilon_{slip-PIV}$)	≤ 60 m/s
Cross-Correlation BOS (ϵ_{cc-BOS})	≤ 0.1 pix
Line of sight effect BOS ($\epsilon_{sight-BOS}$)	≤ 1.5 mm

6.3. SHOCKWAVE DYNAMICS

6.3.1. SHOCK POSITION

From the BOS results it is possible to obtain both qualitative and quantitative information regarding the shock buffet mechanism. In Fig. 6.5 (left) a typical BOS instantaneous result is shown, visualizing the displacement map of the speckle pattern, with the flow oriented from left to right. Two of the main features of buffet are highlighted: the shock wave (SW, which appears at around 30% of the chord) and the presence of UTWs (in Fig. 6.5 (left) two UTWs are observed, at 55 and 75% of the chord, respectively) which are moving from the trailing edge towards the shock position; the remaining regions in the FOV do not present any relevant density gradient. This image has been obtained us-

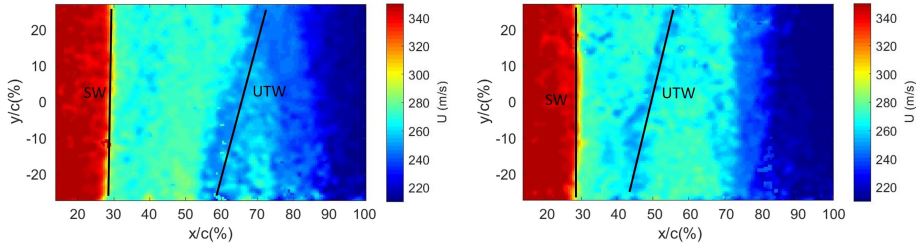


Figure 6.6: PIV instantaneous images at time t_0 (left) and $t_1 = t_0 + 0.22$ ms (right).

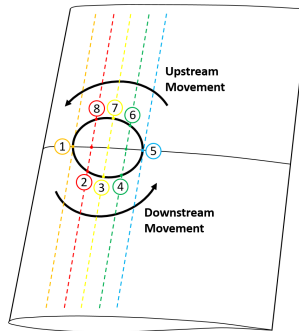


Figure 6.7: Sketch of phase definition with spanwise view of the model.

ing the standard processing procedure, by correlating the deformed image of the speckle pattern with the no-flow reference image. To better visualize the density gradient, in the images the horizontal component of the displacement of the speckle pattern has been depicted. Fig. 6.5 (right) shows the same wave pattern one time step later ($\Delta t = 0.2$ ms), revealing an upstream movement of the UTWs and a downstream movement of the shockwave.

Similar features can be obtained from the PIV data, as evident from Fig. 6.6 where two consecutive instantaneous PIV images are shown for the horizontal velocity component. The shockwave is obtained as a strong velocity gradient, whereas the UTW is represented by a small perturbation in the velocity field traveling upstream. For PIV the shock position was identified by finding the maximum of the gradient of the horizontal velocity, whereas in BOS, the maximum of the displacement map was taken. In both cases the shock position X_{SW} has been tracked at the mid span ($y/c = 0$) of the airfoil.

The BOS images have been divided in two bins: one for the upstream shock movement, i.e. when the shock is moving from the trailing edge to the leading edge and one for the downstream movement (refer to Fig. 6.7), with the upstream travel covering 3814 images and the downstream travel 4186 (respectively 47.7% and the 52.3% of the total number of images). This information implies an asymmetry in the buffet cycle, in that the downstream movement takes longer, therefore indicating that the average downstream velocity of the SW is lower. A similar behavior has been obtained for the PIV

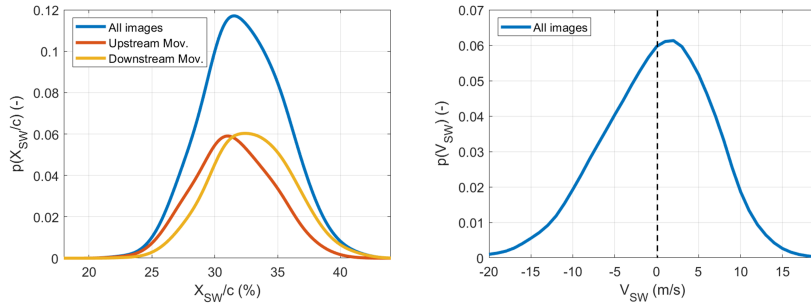


Figure 6.8: PDF of the shock position (left) and velocity (right) from BOS images.

images where 52.2% of the images are associated with the downstream movement.

To further quantify the SW behavior, the distribution of all the BOS instantaneous SW positions is plotted in Fig. 6.8 (left) in terms of the probability density function (pdf) $p(X_{SW}/c)$, using a bin size of 1% of the chord. In Fig. 6.8 (left) the pdf of all the instantaneous images ("all images" in the legend) shows that the region in which the shock is most likely to be found ranges between 25 and 40% of the chord. The figure also contains the pdf of the shock position for both the upstream and downstream movement separately, in all cases the pdf is normalized with respect to the total number of images. The fact that the pdf of the shock position during the downstream movement (yellow line in Fig. 6.8, left) appears to be shifted downstream (with respect to the upstream travel) suggests that the SW is moving faster in the first part of its downstream travel. The pdf relative to the upstream movement is instead almost symmetric with respect to the average shock position (32% c).

From the information of the shock position in time, the shock velocity has been computed and the relative pdf $p(V_{SW})$ (in this case with a bin size of 1 m/s) is shown in Fig. 6.8 (right). From the pdf it is clear that the velocity of the shock wave ranges from -20 to 18 m/s, therefore being more likely to have slightly higher velocities during the upstream movement (negative velocities) compared to the downstream movement (positive velocities). As a consequence average SW velocities of -5.5 m/s and 4.9 m/s are obtained respectively for the upstream and downstream travel. This result was expected in view of the lower number of images present in the upstream travel phase with respect to the downstream travel phase.

A similar asymmetry is also documented in Sartor et al. (2015), where the URANS time evolution of the lift coefficient is asymmetric in the two buffet phases with respect to the mean flow value.

6.3.2. SPECTRAL ANALYSIS

A spectral analysis of the shock location in time has been performed to evaluate the amount of energy associated with the shock oscillation and its main frequency contributions. For this purpose, the power spectral density (P) associated with the shock position, computed with the Welch method (with a procedure similar to the one used by

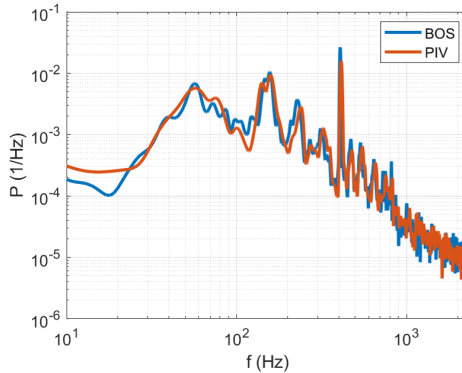


Figure 6.9: Psd of the shock position for BOS and PIV data.

Wang et al. (2020)) is plotted in Fig. 6.9, comparing both BOS (blue line) and PIV (red line).

A good agreement is observed between the PIV and the BOS results over the complete frequency range. It is evident that the main contributions to the shock oscillation are at 160 Hz and 410 Hz, confirming the results of Chapter 5 for the "horizontal model". As previously mentioned, the peak present at 410 Hz ($St = 0.172$) is associated with a characteristic frequency of the wind tunnel, which is particularly evident for this experimental configuration. A similar frequency contribution is also observed in Feldhusen-Hoffmann et al. (2017) and attributed to the presence of a cavity in the wind tunnel. A broad frequency distribution connected with vibrations of the model is also present at around 55-70 Hz. An additional peak at 240 Hz is present, with the corresponding physical meaning not being clarified yet.

6.3.3. PHASE AVERAGE DESCRIPTION

In agreement with Section 4.2, the phases are defined according to the shock position and its direction of movement. Thus, as also shown in Fig. 6.7, in Phase 1 and Phase 5 the SW is, respectively, in its most upstream and downstream position.

Table 6.3: % of images per phase and per technique

Technique \ Phase	Phase							
	1	2	3	4	5	6	7	8
BOS	20.6	9.2	10.8	9.1	21.2	10.1	9.5	9.5
PIV	16.1	9.0	11.3	11.0	16.9	13.1	12.1	10.5

In Tab. 6.3 the relative number of images belonging to each phase are reported for both BOS and PIV images. The numbers clearly show that the first and fifth phase contain most images, which is not surprising since those are the two phases in which the shockwave switches direction of motion. Good agreement is present between the two techniques, even if for the BOS data the shock tends to be located more often in the

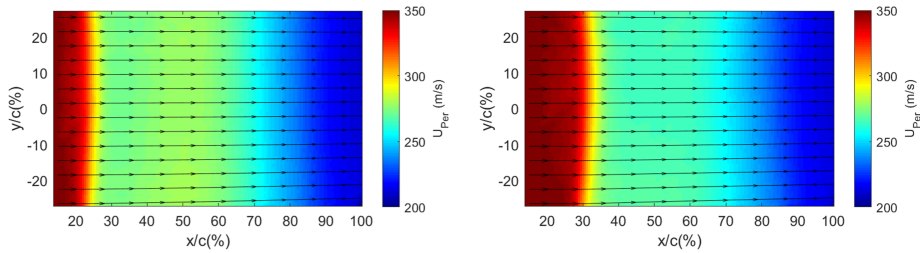


Figure 6.10: Phase averaged velocity field in the most upstream (left) and downstream (right) shock position.

most extreme positions. This difference could be justified by the fact that with BOS all the density gradients are integrated in a direction orthogonal to the surface of the airfoil. Therefore the resulting BOS images are not able to distinguish between situations in which the shockwave is just changing its inclination (in the streamwise-vertical plane), which is usually happening in correspondence of the turning points in the buffet cycle.

In Fig. 6.10 the phase averaged velocity field ($u_{phs} = u_{avg} + u_{per}$) for the horizontal component is shown for the first (Fig. 6.10, left) and for the fifth phase (Fig. 6.10, right). These velocity fields demonstrate that the distance between the shock position in the most downstream and upstream position is approximately 10% of the chord, ranging in locations between 25 and 35% c and therefore included in the wider range of oscillation previously shown in Fig. 6.8 (left) for the BOS images. However, it is useful to recall that the amplitude of the shock oscillation is not constant for each cycle, causing the phase averaged velocity field to be somewhat smoothed out. In addition, in the previous Chapter (Chapter 5) it was shown that the SW is supposed to be almost normal (with respect to the surface of the airfoil) in the most downstream position and more oblique in the most upstream position. Therefore, the projected range of oscillation of the SW in the PIV FOV of this investigation is reduced with respect to the range in correspondence of the surface of the airfoil.

Although the separated flow region cannot be observed directly due to the distance of the light sheet from the airfoil surface (no reverse flow occurs in the FOV), when taking the low-velocity region as a proxy for this, it can be tentatively concluded that no large difference is present between the two discussed phases, at least not at this distance from the model surface. The velocity fields furthermore confirm that the buffet on a two-dimensional airfoil behaves predominantly as a 2D phenomenon in terms of overall flow features, not having important variations in the spanwise direction (both for the shock wave and for the separated area). This applies at least for the imaged region, sufficiently far away from the wing tips, as further confirmed by the nearly parallel orientation of the streamlines (shown for both phases).

6.4. UTWS ANALYSIS

6.4.1. DETECTION OF UTWS

To detect and characterize the UTWs the BOS images have been processed using the differential procedure, where the distorted BOS speckle pattern at time step t_0 is cross-

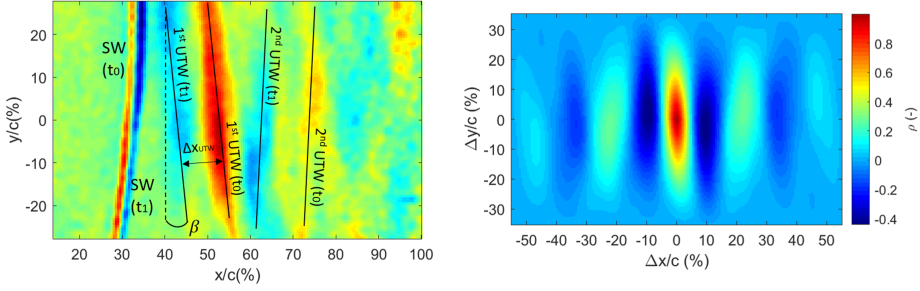


Figure 6.11: Instantaneous differential BOS image (left) and corresponding autocorrelation map (right)

correlated with the speckle pattern at the subsequent time step $t_1 = t_0 + \Delta t$ (where $\Delta t = 0.2 \text{ ms}$), in order to highlight the dynamics of the unsteady flow features. This procedure is similar to what has been referred to as "monoscopic BOS" in literature and it is described in more details by [Bauknecht et al. \(2014\)](#) and [Raffel \(2015\)](#).

The differential BOS result shown in Fig. 6.11 (left) has been obtained using the same images as those to produce the standard BOS images of Fig. 6.5 (left, t_0 and right, t_1). The differential BOS image shows the relative displacement of the speckle pattern between the two successive images. As a result, the image contains the presence of both the shock at time t_0 (in red) as well as at the following time step ($t_1 = t_0 + 0.2 \text{ ms}$) (in blue), where the two shockwave signatures appear with opposite sign in the displacement map. The distance between the two imprints represents the distance covered by the shock within the time separation Δt . Similarly, also the UTWs observed at both the time steps appear in the same image (in red the UTWs corresponding to the first and in blue corresponding to the second time step). It is relevant to consider that this differential method is meaningful only for applications in which the density gradient is moving relative to the field of view and the time between two consecutive images is large enough in order that the density gradients belonging to the two different time steps do not overlap, yet small enough such that the same flow features is present in both images; for the current investigation both these conditions are satisfied, allowing the UTW behavior to be extracted.

In Fig. 6.11 (left) the UTWs appear sharper in more upstream positions, closer to the shock. In more downstream positions instead, they are less defined due to the masking effect of the separated area.

Each differential image indicates whether the shock is moving upstream or downstream, depending on the relative location of the local maximum and local minimum displacement. The exact distance between the different density features, together with the time separation allows the computation of the velocity of the shockwave and of the UTWs. In Fig. 6.11 (left) the distance Δx_{UTW} indicates the distance covered by the (first) UTW in one time step and the propagation is considered to be approximately orthogonal to the front of the wave. For the first UTW a $\Delta x_{UTW}/c = 10\%$ is found, hence, it is propagating upstream with a velocity of nearly $0.01/0.0002=50 \text{ m/s}$ ($\Delta x_{UTW}/\Delta t$) with respect to the flow. From Fig. 6.11 (left) it is furthermore observed that the UTWs propagate with a non-zero angle (β) in the spanwise-streamwise plane, similar as can be observed in Fig. 6.6. For the situation of Fig. 6.11 (left) the first UTW is inclined at an angle $\beta_1 = 6^\circ$,

Table 6.4: UTW properties

Property	Upstream Mov.	Downstream Mov.
Mean UTW inclination (β_{avg})	0.1°	-0.3°
STD of UTW inclination (σ_β)	11.6°	9.6°
Mean UTW velocity ($(V_{UTW})_{avg}$)	83.3 m/s	77.4 m/s
STD of UTW velocity ($\sigma_{V_{UTW}}$)	27.0 m/s	24.3 m/s

while for the second UTW this is $\beta_2 = -3^\circ$.

For a systematic detection of the UTWs an autocorrelation analysis of the displacement field of the differential BOS images was performed. To investigate whether the occurrence of UTWs is associated with just one of the two directions of movement of the shockwave, the upstream and the downstream phases are treated separately. The region in which the autocorrelation is evaluated ranges from 40% to 95% of the chord in the streamwise direction corresponding to the region located downstream of the shock oscillation area, and it extends from -20% to +20% of the chord in the spanwise direction.

In Fig. 6.11 (right) the instantaneous autocorrelation map corresponding to the differential BOS image of Fig. 6.11 (left) is shown. In the center of the autocorrelation map there is the main central peak and both to the right and left of this peak, two negative peaks can be observed ($\Delta x \approx \pm 10 \text{ mm}$, $\Delta y \approx 0 \text{ mm}$). The location of the off-center peak corresponds to the distance covered by the UTWs in the time between two consecutive images ($\Delta t = 0.2 \text{ ms}$). The secondary positive peaks present in the autocorrelation map ($\Delta x \approx \pm 20 \text{ mm}$, $\Delta y \approx 0 \text{ mm}$) are instead associated with the distance between the two consecutive UTWs at the same time step.

It is possible to visualize the presence of UTWs also from PIV instantaneous images as shown in Fig. 6.6, where the horizontal component of the velocity field (in the free-stream direction) is shown for two instantaneous consecutive PIV snapshots, with a time interval of 0.22 ms. In these plots the shock wave is moving upstream, while the UTW at first emerges from the separated area and then moves towards the shock location with a non zero inclination. Notwithstanding the inclination of the UTW, it is possible to see how the background flow field is nominally 2D, without appreciable changes in velocity in the spanwise direction both in the supersonic and subsonic region, including the separated (low velocity) area. Between the two images of Fig. 6.6 the UTWs is moving upstream of nearly 18% c , thence with a velocity of 82 m/s.

6.4.2. PROPAGATION PROPERTIES OF UTWS

To obtain the quantitative propagation properties of the UTWs, the autocorrelation procedure described in the previous section was applied to all the images. Although Fig. 6.11 (left) clearly shows the presence of the UTWs, these were not detected in all the images. In order to not contaminate the statistics, all images without UTWs were removed from the ensemble. For this, recordings having a negative peak with $\rho > -0.1$ in the autocorrelation map were discarded. In total 3708 out of 8000 images were removed.

The correlation maps are analyzed to extract for each time step the inclination (β) and the velocity of the UTWs (V_{UTW}). The results are subsequently sorted, based on the shock motion direction to differentiate between its upstream and downstream move-

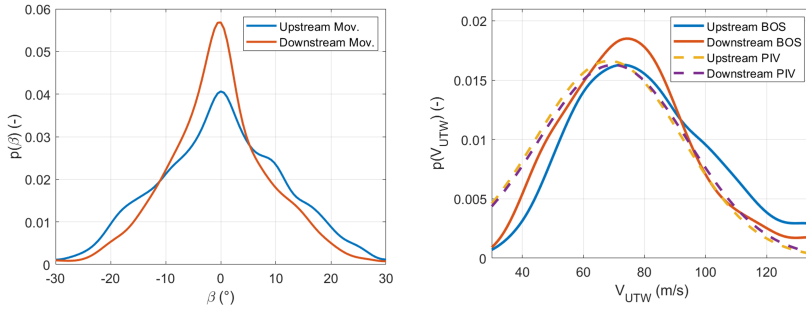


Figure 6.12: Pdf of the inclination (left) and of the velocity (right) of the UTWs.

ment. The pdf of the UTW inclination $p(\beta)$ is illustrated in Fig. 6.12 (left). The mean value of the inclination of the UTWs is (close to) zero for both the analyzed phases (see Tab. 6.4) and the pdfs are almost perfectly symmetric with respect to $\beta = 0$. Although the values of inclination range from -25° to $+25^\circ$ in both phases, the pdf is narrower for the downstream compared to the upstream shock movement. This observation results in a higher standard deviation of the inclination of the UTWs for the upstream phase (11.6°) with respect to the downstream movement (9.6°). From a spectral analysis of the value of the UTW inclination in time no clear peak is observable anywhere in the spectrum, suggesting that the variation of the inclination in time does not change with the buffet frequency and neither is it correlated with the SW position. According to the feedback loop description of buffet, the production of the UTWs is associated with the arrival of vortical structures (DTWs) at the trailing edge. Since the latter structures are highly three-dimensional, the arrival of the DTWs at the trailing edge along the span is not synchronized. This aspect is supposed to be the cause of the non-zero orientation of the UTWs.

An additional explanation of the non-zero inclination of the UTWs could be the presence of corner flow separation at the sides of the airfoil, however, preliminary investigations have excluded this hypothesis. A qualitative visualization of an UTW propagating in the spanwise-streamwise plane with a non-zero inclination is also observed in the numerical study of [Hermes et al. \(2013\)](#) and attributed again to the three-dimensionality of the vortices in proximity of the trailing edge.

Similarly to the UTW inclination, the range of velocities of the UTWs is plotted in Fig. 6.12 (right), for both the upstream and downstream shock motion phases. The average UTW velocity obtained during the upstream and downstream travel is respectively 83.3 m/s and 77.4 m/s as summarized in Tab 6.4, hence obtaining values which are close to those obtained by [Hartmann et al. \(2013\)](#) (80 m/s, under similar experimental conditions). But in addition to what is shown in that study, the pdf of the UTW velocity ($p(V_{UTW})$) shows that there is a wide range of velocities for the UTWs, that varies from 30 to 130 m/s (in terms of absolute values). Pressure waves propagating upstream from the trailing edge of a supercritical airfoil with a similar range of velocities are also observed in the experimental study of [Alshabu and Olivier \(2008\)](#), although for non-buffet conditions. This velocity range can be justified by the assumption that the UTWs, be-

having like pressure waves, travel at the speed of sound relative to the flow and therefore with an absolute velocity which differs according to the local velocity of the flow, which is changing with the buffet phase and with the chordwise location. This is also in agreement with the velocity of an UTW estimated for an instantaneous PIV image in Section 5.6. Thus, there is a difference in the velocity of the UTWs for the upstream and downstream movement of the shock, with the velocity distribution moved to higher (absolute) values during the upstream shock movement. This result can be understood, considering that during the upstream phase, the separated area is expected to be wider and the flow velocity near the airfoil surface lower (Jacquin et al. (2009)) and therefore, higher velocities for the UTWs are expected.

A detailed evaluation of the UTW velocity for the PIV images is more complicated than for BOS, since in the former case it is not always possible to correctly detect the UTWs because of the relatively low velocity fluctuations accompanying the UTWs. For this reason, in most of the PIV images it was not possible to visualize UTWs. However, starting from the PIV data it has been verified whether the range of velocity of the UTWs obtained with BOS agrees with the assumption that the UTWs propagate at the velocity of sound relative to the flow. Thus, the local velocity of the UTWs is expressed as the difference between the local velocity and the local speed of sound:

$$U_{UTW} = U_{loc} - a_{loc} \quad (6.1)$$

Assuming an ideal gas and the flow to be adiabatic (constant total temperature T_0), the local speed of sound can be expressed in terms of the velocity magnitude $U = \sqrt{u^2 + v^2}$ (with the flow being nominally 2D, the contribution of the out-of-plane velocity component w is not taken into account):

$$a = \sqrt{\gamma RT} = \sqrt{\gamma R(T_0 - \frac{U^2}{2c_p})} \quad (6.2)$$

Applying this procedure to all the instantaneous images, the theoretical velocity of the UTWs is obtained for each location in the FOV. Restricting the area of interest to a region extending from 40 to 95%c in the streamwise direction and from -20 to 20%c in the spanwise direction (which is the same area used for the autocorrelation for the BOS images), the normal distribution of the estimated UTW velocity is obtained (Fig. 6.12, right). The range of velocity derived from the PIV flow velocity data matches the BOS experimental results very well (see dashed lines in the plot) confirming the acoustic nature of the UTWs.

The average velocity for the UTWs estimated with this procedure is around 70 m/s (in absolute value), which is 10 m/s (or some 15%) lower than the BOS average value. This discrepancy could be justified in view of the distance of the PIV measurement plane from the surface of the airfoil. Hence, the flow is less influenced by the presence of the separated area, bringing to an overestimation of the effective downstream flow velocity and an underestimation of the UTW velocity. This result is confirmed in Fig. 6.12 (right), where the estimated PIV velocity range for the UTWs (dashed lines) is moved to the left (lower velocities) compared to the BOS results (solid lines). Just negligible differences between the upstream and downstream movement are observed for the PIV results, in

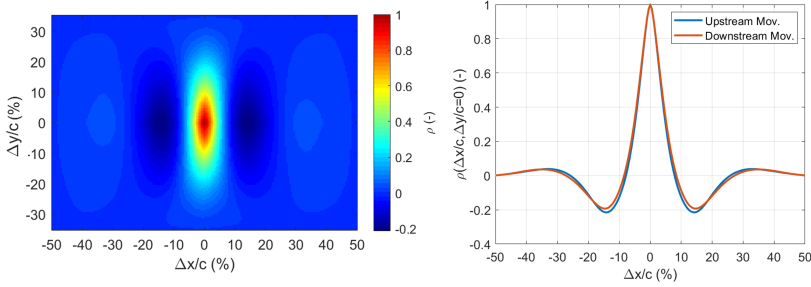


Figure 6.13: Average autocorrelation map of the differential BOS images during the downstream movement of the shock (left) and relative profile (right).

contrast to the BOS results. This is attributed to the fact that the PIV measurement plane does not capture the pulsation of the separated area, which can be considered responsible for the differences between the upstream and downstream shock motion phases.

Since the velocity of the UTWs changes according to the local velocity of the flow, the non-zero inclination of a UTW is supposed to decrease during its upstream travel (in view of the increase of the local velocity of the flow).

6

6.4.3. FREQUENCY OF UTWS

From the average distance between consecutive UTWs, the corresponding propagation frequency can be extracted. To obtain this information the instantaneous autocorrelation maps are averaged, for the upstream and the downstream shock movement phases separately. In Fig. 6.13 (left) the average autocorrelation map for the downstream movement is shown. In this map, as in the instantaneous one, adjacent to the main central peak ($\Delta x = 0 \text{ mm}$, $\Delta y = 0 \text{ mm}$), additional negative and positive peaks occur. Because of the occurrence of a certain amount of variability in the flow field, these additional peaks are smoothed out with respect to those in an instantaneous correlation map. For the same reason, further secondary peaks do not show up in the average map.

The average correlation maps for the upstream and downstream shock movement (which profiles are shown in Fig. 6.13 (right) for $\Delta y = 0$) are very similar and nearly indistinguishable. As no important difference can be discerned between both graphs in Fig. 6.13 (right), this implies that the production of the UTWs occurs very similarly for both phases. From the average autocorrelation map, the average spacing between subsequent UTWs, Δx_{UTW} is obtained as the distance between the central and the secondary positive peaks. Therefore, the average frequency with which the UTWs are produced is estimated (knowing the average velocity of the UTWs, $u_{UTW} = 77.4 \text{ m/s}$, and the average distance between subsequent UTWs, $\Delta x_{UTW} = 0.32c$) as:

$$f_{UTW} = \frac{u_{UTW}}{\Delta x_{UTW}} \quad (6.3)$$

This frequency is equal to 2400 Hz and corresponds to a Strouhal number of 1.07, which is in good agreement with the value reported by Hartmann et al. (2013), (value which has been compared to the estimated frequency of downstream propagating structures

in Section 5.6). It is important to mention that this frequency value is on the limit of the one which could be obtained by a direct spectral analysis of the BOS displacement map given the acquisition frequency of 5 kHz (in view of the Nyquist sampling criterion). However, the procedure used in the present analysis is based on spatial correlation and is therefore not limited by the frequency of acquisition. The symmetry observed in the average autocorrelation map confirms that the UTWs propagate with a zero average inclination value.

6.4.4. UTW STRENGTH

As anticipated in Section 6.4.2, the UTWs are not always clearly detectable in the BOS images. An example of an instantaneous differential BOS image, which has been rejected is given in Fig. 6.14 (left), where apart from the presence of the shockwave at both time steps t_0 and t_1 , the different UTWs are not unambiguously visualized. The fact that under comparable conditions the UTWs are not easily detectable may be tentatively associated with a variation in strength of the UTWs. Therefore, the information regarding the relative number of images which have been rejected because of unsatisfactory visualization of the UTWs is used to monitor the production of the UTWs over the buffet cycle. For this purpose, in Fig. 6.14 (right) for each phase in the cycle, as defined in Fig. 6.7, the ratio of images included in the analysis (R_{incl}) is shown.

For all the phases, the percentage of included images is ranging between 50 and 60% of the relative total number of images for that phase, revealing an increasing trend during the downstream movement, reaching a maximum just before that the shock reaches its most downstream position (phase 5), while decreasing during its upstream travel. This information suggests that UTWs of higher intensity are produced when the shock is close to its most downstream position, with the shock eventually stopping its downstream travel, because of the strong interaction with the UTWs. In contrast, UTWs of lower intensity are produced when the shock is near its most upstream position (phase 1), with the shock not being forced anymore to continue its upstream travel. However, for each phase, the ratio of images in which at least one UTW is detectable, is never lower than 50 %. This result would suggest that the UTWs are produced along the full buffet cycle, albeit with an intensity which is modulated according to the phase in the buffet cycle, as theorized by Hartmann et al. (2013). These results are in agreement with the feedback loop description of transonic buffet.

6.5. CONCLUSIONS

This chapter has investigated the characteristics of upstream traveling waves (UTWs) in transonic buffet on the OAT15A airfoil using background oriented schlieren (BOS) and PIV, as main experimental diagnostic techniques. Particular attention has been given on the spanwise organization of the transonic buffet flow features.

The selected orientation of the FOV facilitated an unambiguous analysis of spanwise features, in contrast to the traditional chordwise-vertical plane. In the latter case the density gradient present in a schlieren image is integrated along the spanwise direction and therefore it is heavily affected by edge effects in correspondence of the side

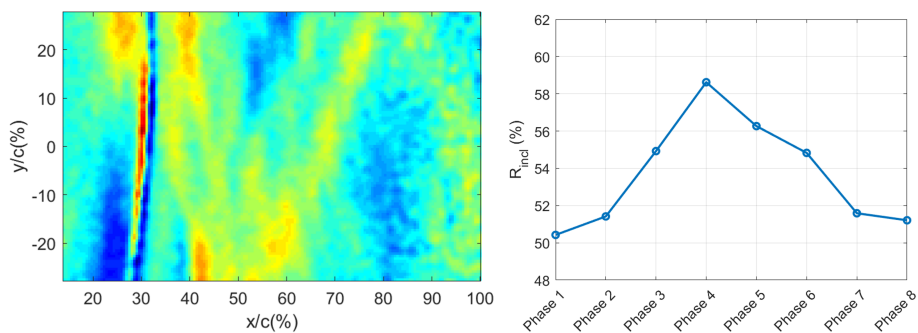


Figure 6.14: Example of differential BOS image excluded from autocorrelation analysis (left). Ratio of included images (R_{incl}) per phase (right).

walls, where the presence of the developing boundary layer influences the shape of the shockwave and of the other pressure waves present, like in the schlieren data of [Jacquin et al. \(2009\)](#). Differently, since the pressure gradients are much more coherent along the vertical direction (i.e. normal to the surface of the airfoil), for the streamwise-spanwise FOV less artifacts are introduced in the corresponding BOS image. The simultaneous use of differential BOS, has facilitated the analysis of the UTW propagation velocity and demonstrated to be more efficient than PIV in doing so. From the PIV images only an estimation of the UTW properties could be inferred (Fig. 6.12, right), because of the low variation of velocity associated with the UTWs.

The FOV allowed to investigate the two-dimensionality of buffet which was demonstrated to be strongly coherent along the span of the airfoil both in the supersonic and in the subsonic flow regions (including specific features, such as the SW and the separated area). This evidence was supported by the shape of the shockwave from the BOS images (Fig. 6.5) as well as by the PIV average results, as shown in Fig. 6.10. In the latter the streamlines obtained from the two velocity components appear almost completely oriented along the chordwise direction. The shockwave oscillation is observed to occur between the 25 and 40 % of the chord of the airfoil (Fig. 6.8, left), in both the PIV and the BOS measurements. Notwithstanding the two-dimensional instantaneous organization of the large scale flow features, it was illustrated that although the average inclination of the UTWs is near zero, they display a non zero instantaneous angle of inclination in the spanwise-chordwise plane, without important differences between the statistics for the upstream and downstream phases of the buffet cycle (Fig. 6.12, right). This inclination is assumed to be connected with highly three-dimensional structures which upon reaching the trailing edge cause the formation of the UTWs. An additional investigation of these structures from the PIV data was not possible in the current study, because of the distance of the FOV plane with respect to the trailing edge.

By using BOS, it has been further clarified that the propagation velocity of the UTWs is not constant, but ranges between 30 and 130 m/s (Fig. 6.12, right), which is consistent with the concept that the UTWs are pressure waves that travel at the speed of sound relative to the local flow. This concept was confirmed by an analysis based on the PIV velocity data. This allows to understand how, as the local flow velocity changes throughout

the buffet cycle, the velocity of the UTWs changes accordingly.

The subdivision of the buffet cycle in an upstream and downstream shock movement phase has confirmed that the UTWs are produced throughout the entire buffet cycle with a shedding frequency of 2400 Hz, which is in good agreement in terms of Strouhal number ($St = f \cdot c / U_\infty = 1.07$) with [Jacquin et al. \(2009\)](#) and [Hartmann et al. \(2013\)](#). However, an analysis of the relative number of BOS snapshots in which the UTWs were not perfectly defined suggests that a modulation in the strength of the UTWs is present during the buffet cycle. The results showed that the strongest UTWs are produced when the shock is approaching its most downstream position, forcing the SW to stop its travel and start the upstream movement (see Fig. 6.14, right). Strong UTWs are still reaching the SW in the first part of its upstream movement while they later reduce their strength in the last part of the SW upstream travel. According to literature the strength of the UTWs is considered to be connected with the strength of vortical structures which when reaching the trailing edge area and passing from a wall bounded shear layer to a free shear layer, are responsible for the production of the UTWs in order to respect the Kutta condition. In view of the current results which show that the UTWs are detected throughout the full buffet cycle, these vortical structures are believed to originate in the separated trailing edge area rather than the shock foot separated area, which is present only in part of the buffet cycle. However because of the simultaneous pulsation of the shock foot separated area, the strength of these vortices (and as a consequence of the UTWs) is modulated by the former pulsation, which is occurring at the buffet frequency of 160 Hz. These promising results obtained, may clarify how a phenomenon which has a propagation frequency of 2400 Hz can influence the buffet dynamics which has a main contribution at 160 Hz, although further study may be required on this matter. Therefore, these results provide evidences that are in agreement with the feedback loop description of transonic buffet.

7

FINITE WING AND SWEEP EFFECTS

This chapter experimentally investigates the effects of sweep angle and finite wing on transonic buffet, studying two-dimensional (2D) and three-dimensional (3D) wing configurations. Background oriented schlieren (BOS) and stereographic particle image velocimetry (PIV) have been used as measurement techniques, performing experiments on an ONERA OAT15A airfoil (clamped to both the side windows of the wind tunnel), an unswept wing and two swept wings with a sweep angle of 15° and 30° respectively. The three wings are also based on the OAT15A airfoil and are clamped at the wind tunnel only at their root (free wing-tip). All wings have been tested at a constant normal Mach number ($Ma_{\infty n} = 0.7$) with respect to the leading edge. The results show that the buffet oscillations are much stronger for the airfoil than for the three finite-span wings. A large difference in the buffet behavior can be noticed between the airfoil and the unswept wing, as also seen in oil flow visualizations. This difference is particularly evident in correspondence of the more outboard spanwise locations suggesting that for the unswept wing an important role could be played by finite-wing effects, notably the tip vortex. A spectral analysis has shown that for the swept wings the classical 2D buffet peak (occurring at $f=160$ Hz for the present conditions) is substantially attenuated, while additional contributions in the range of 450-850 Hz appear. The PIV results showed, for the 30° sweep angle wing, a periodical occurrence of a secondary supersonic area downstream of the main shockwave structure, which is absent for the other wing models. The stereographic PIV configuration allowed the reconstruction of the spanwise oriented velocity component, obtaining in the trailing edge area, spanwise outboard velocities (80-100 m/s) which are in agreement with the spanwise convection of buffet cells observed in literature in this region.

7.1. INTRODUCTION

Most of the studies on transonic buffet of the last 30 years were conducted on airfoils, corresponding to unswept, infinite-wing conditions, while more dedicated research on swept wings has been pursued only in more recent years. The growing interest brought

Parts of this chapter have been published in [D'Aguzzo et al. \(2022b\)](#).

to an extensive knowledge although a complete comprehension of the phenomenon is still far from being achieved as summarized in Section 2.3.

In experimental studies it is also relevant to assess the effect of finite wing effects on swept wings. These effects have been summarized by [Iovnovich and Raveh \(2015\)](#), who noticed the presence of tip vortices which influence the transonic buffet behavior, as already commented in Section 2.3. In contrast, finite-wing effects on transonic buffet in connection to unswept wings have received relatively little attention in literature and require further research. Nevertheless, some studies have been conducted on the confinement effects on airfoils (therefore in absence of free wing-tip), such as in the numerical study of [Thiery and Coustols \(2006\)](#), where differences in the airfoil performance are noted when modeling top, bottom and side walls of the wind tunnel. [Jacquin et al. \(2009\)](#) by analyzing oil flow visualization results, commented that possible 3D side wall effects are contained in proximity of the two extremities of the airfoil model. In the recent study of [Sugioka et al. \(2022\)](#) confinement effects are studied for fully clamped airfoil and 10° swept model, highlighting the relevance of corner separation for the shockwave oscillation in proximity of the side walls. However, there is not such a study in literature which experimentally compare the performance of an airfoil and a finite unswept wing under transonic buffet conditions.

It should also be considered that the experimental swept-wing models investigated in literature, as in the experimental database discussed by [Paladini et al. \(2019\)](#), differ from 2D buffet models not only for the presence of the sweep angle, but also for the taper ratio and the presence of a fuselage. Therefore, it is difficult to isolate the effect of the sweep angle in transonic buffet. To achieve this goal in the current study, wings with different sweep angles and with constant chord have been studied and compared to the behavior of an airfoil that fully spans the wind tunnel test section, in order to quantify both sweep and tip effects.

Most of the experimental studies present in literature make use of pressure measurements on the suction side of the wing employing either unsteady pressure transducers ([Paladini et al. \(2019\)](#), [Dandois \(2016\)](#), [Koike et al. \(2016\)](#)) or pressure sensitive paint ([Sugioka et al. \(2015\)](#), [Masini et al. \(2020\)](#), [Lawson et al. \(2016\)](#)). In this chapter, the main investigation is conducted by using stereo-particle image velocimetry, for reconstructing the three velocity components in several planes of measurement oriented along the free stream direction, at different spanwise locations. The use of PIV is not uncommon in the study of transonic buffet on airfoils (see for example [Hartmann et al. \(2013\)](#), [Feldhusen-Hoffmann et al. \(2021\)](#)), however, to the best of the authors' knowledge no previous study has considered PIV to study transonic buffet on swept wings. The application of PIV could help to visualize and analyze the main flow structures characterizing transonic buffet on swept wings, which is not always allowed with wall pressure measurements. In addition to PIV, the background oriented schlieren (BOS) technique has been used to provide a further characterization of the flow field. BOS was already successfully adopted in Chapter 6 for the study of transonic buffet on a 2D airfoil, but its application in this intrinsically three-dimensional application has not been demonstrated yet and will be tested by comparing the results with PIV.

7.2. EXPERIMENTAL INVESTIGATION

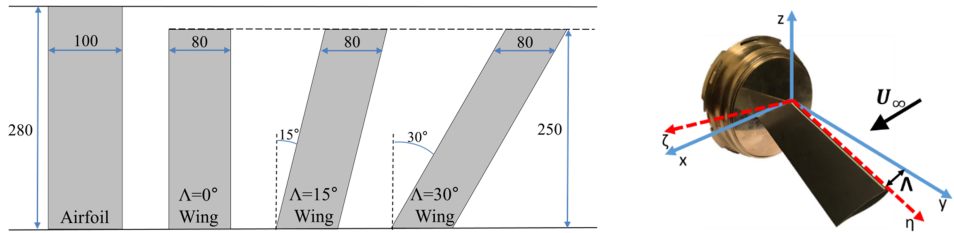


Figure 7.1: Sketch of the models based on the OAT15A airfoil (left) with dimensions in mm and angles in degrees. On the right, the 15° sweep angle model attached to the clamping piece with indication of the two coordinate systems used.

7.2.1. WING MODELS

The models used for the experiments are wings obtained from the extrusion of an OAT15A airfoil with three different sweep angles, $\Lambda = 0^\circ$, $\Lambda = 15^\circ$ and $\Lambda = 30^\circ$, a chord (c) of 8 cm and a span (b) of 25 cm. The choice of the airfoil (OAT15A) and the values of the sweep angle are motivated by similar studies present in literature (see Paladini et al. (2019), Giannelis et al. (2017)). The wings are clamped at the root to one of the side walls (see Fig. 7.1, right), with optical access provided from the opposite side of the test section, thus using the third wind tunnel configuration shown in Section 3.4. In addition to the three wings, the airfoil employed in Chapter 5 has been tested as well. This airfoil has a chord of 10 cm and a span of 28 cm and is clamped at both sides of the wind tunnel. For the finite-span wings, the distance of the wing tip to the side windows (3 cm) has been chosen to ensure that the wing tip was not immersed in the turbulent boundary layer developing on the side wall of the test section.

A sketch of the top view of the different wing models is shown in Fig. 7.1 (left), with the main geometric characteristics included. In Fig. 7.1 (right) the 15° swept wing is shown together with the clamping piece by which the models are mounted to the wind tunnel side wall.

The goal of this Chapter is not that of evaluating and comparing the most developed buffet condition for the different models, but rather to study the occurrence and the impact of finite wing and sweep effects on transonic buffet while keeping all the other parameters constant. For this reason, in this investigation the different wings are tested with the same value of the normal Mach number with respect to the leading edge ($Ma_{\infty n} = 0.7$), although the values of $Ma_{\infty n}$ and α for which the most developed buffet conditions are experienced may be different for the various models. The values of the freestream Mach number and angle of attack used for each model are summarized in Table 7.1, together with the respective geometric parameters (chord and span).

Table 7.1: Flow and geometric properties of the models

Model	$Ma_{\infty n}$ (-)	Ma_{∞} (-)	α ($^{\circ}$)	c (m)	b (m)
Airfoil	0.70	0.70	3.5	0.10	0.28
$\Lambda = 0^{\circ}$ wing	0.70	0.70	3.5	0.08	0.25
$\Lambda = 15^{\circ}$ wing	0.70	0.72	3.4	0.08	0.25
$\Lambda = 30^{\circ}$ wing	0.70	0.81	3.4	0.08	0.25

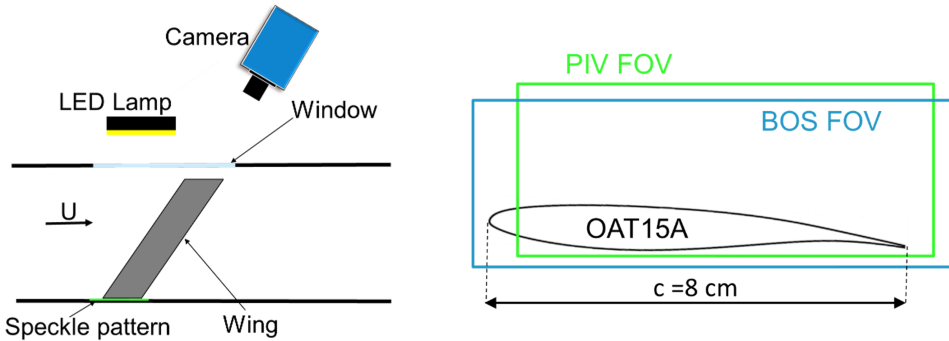


Figure 7.2: Top view of BOS set-up (left). On the right the BOS and PIV FOVs.

7.2.2. EXPERIMENTAL SET-UP

The experiments have been conducted using two different optical techniques, background oriented schlieren (BOS) and particle image velocimetry (PIV). BOS has been selected instead of schlieren because for the three finite wings the optical access was possible only from one side of the wind tunnel. The set-up used for the BOS experiments consists of a LED lamp for illumination and a high speed recording camera directly looking at a speckle pattern, the latter being attached to the clamping piece at the wing root. A sketch of the BOS set-up in top view is shown in Fig. 7.2 (left). A LaVision Imager Pro HS4 camera is used with an acquisition frequency of 4.65 kHz which allows to resolve the shock oscillation in time. To reach that acquisition frequency, the resolution of the camera has been cropped to 1008×468 pixels, acquiring 4000 images per wind tunnel test. By using a 105 mm lens a field of view (FOV) including the entire chord of the models has been obtained, as indicated in Fig. 7.2 (right).

The speckle pattern has been realized with black dots on a white background. An example of the speckle pattern used is given for the unswept wing in Fig. 7.3 (left), with clear compressibility effects revealed in the area where the speckle pattern is deformed. The region in which high compressibility effects are evident is not a line, as it should be in presence of a normal shockwave at a given spanwise position. The reason for this is associated with the integration of the variable density gradient along the span of the wing/airfoil. In order to minimize the 3D effects in the BOS images the viewing direction of the camera has been aligned along the leading edge of the different wings, as also sketched in Fig. 7.2 (left).

To quantitatively investigate the flow field, stereo-PIV tests have been performed us-

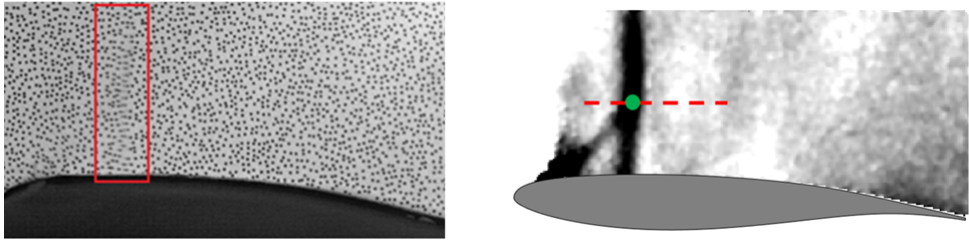


Figure 7.3: Instantaneous image of the deformed speckle pattern (left) together with the processed BOS image, which displays the horizontal displacement of the speckle pattern (right).

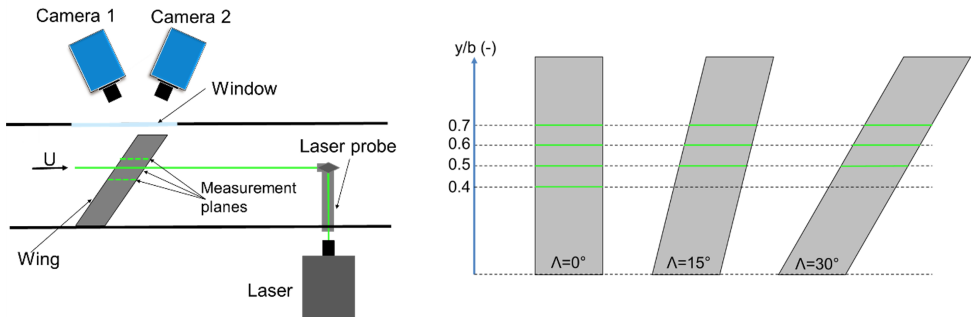


Figure 7.4: Stereo-PIV set-up (left) and location of the PIV planes of measurement (right).

ing the set-up shown in Fig. 7.4 (left). Two high speed cameras (Photron Fastcam SA1.1) in stereo configuration with an acquisition frequency of 4.65 kHz and in double pulse mode (pulse separation $\Delta t = 3\mu s$) have been used for acquiring images for a total time duration of $t=0.94$ s (4365 pairs of images per camera). In order to achieve the selected acquisition frequency the sensor of the cameras has been cropped to 1024×640 pixels. Both cameras have been equipped with lenses with a focal length of 105 mm and an f-stop, $f_{\#} = 8$; in addition, two Scheimpflug adapters have been used to align the focal plane with the image plane (laser plane). These settings resulted in a field of view in the chordwise plane which is 8 cm long and 5 cm high (12 pix/mm) as sketched in Fig. 7.2 (right). Limitations in the optical access have constrained the angle between the cameras to approximately 60° . The use of the stereo configuration allows the determination of the out-of-plane velocity component, which is of crucial importance to characterize a 3D flow.

In this investigation the DEHS seeding particles are once again illuminated by a high speed dual cavity Mesa PIV laser (Nd:YAG), forming a light sheet of 1.5 mm thickness. The laser illumination was synchronized with the cameras using a LaVision high speed controller (art. 1108075). By simultaneously sliding the laser probe and the cameras, tests at different span locations have been performed, in particular at $y/b=0.4, 0.5, 0.6$, and 0.7 for the unswept wing and at $y/b=0.5, 0.6$, and 0.7 for the remaining two wings, as indicated in Fig. 7.4 (right).

7.2.3. DATA PROCESSING AND UNCERTAINTY

Both the BOS and the PIV images were collected and partly processed in LaVision Davis 10.0.5. For the BOS images, each instantaneous snapshot of the speckle pattern in presence of density gradients was cross-correlated with a reference image (obtained with the wind tunnel off). A multi pass approach with an initial window size of 32×32 pixels and a final window size of 16×16 pixels and an overlap of 75% was applied, reaching a final vector spacing of 0.028 cm (corresponding to 0.28% c for the airfoil and 0.35% c for the wings). In Fig. 7.3 (right) an example of a BOS processed image is shown, resulting from a cross-correlation of the raw image in Fig. 7.3 (left) with the reference no-flow image. This processed image clearly quantifies the deformation of the pattern due to the (density) compressibility effects, and as such visualizes the near-normal shockwave as well as the oblique Mach wave originating from the transition trip.

For the PIV images, to reduce the laser reflections from the model, a minimum subtraction has been used by means of a Butterworth filter with a filter length of seven snapshots (see for more details [Sciacchitano and Scarano \(2014\)](#)). Subsequently a stereo cross-correlation procedure was performed, using again a multi-pass approach with an initial window size of 96×96 pixels and a final window size of 32×32 pixels and an overlap of 75%. These settings resulted in a vector spacing of 0.82% c . The vector uncertainty associated to the cross-correlation procedure can be computed similarly for BOS and PIV, as described in Chapter 6. The associated value is lower than 0.1 pix and therefore leads to an uncertainty in the PIV velocity evaluation lower than 6.7 m/s.

In Table 7.2 the main PIV and BOS settings and corresponding uncertainties are summarized (for a more detailed derivation of the PIV uncertainties, the reader is referred once again to 3.9). Further processing for both BOS and PIV data has been carried out in *MATLAB*.

Table 7.2: BOS and PIV settings and uncertainties.

Parameter	BOS	PIV
Acquisition frequency	4.65 KHz	4.65 KHz
Number of images	4000	4365
Final image resolution	1008×468 pix	1024×640 pix
Final window size	16×16 pix	32×32 pix
Window overlap	75%	75%
Vector spacing	0.28% c (airfoil) – 0.35% c (wings)	0.82% c
Cross-correlation unc.	< 0.1 pix	< 6.7 m/s
Particle slip	N.A.	< 60 m/s (in SW areas)

7.3. COMPARISON OF AIRFOIL AND UNSWEPT WING BEHAVIOR

7.3.1. FLOW FEATURES ANALYSIS BY MEANS OF OIL FLOW VISUALIZATIONS

Although there are many studies in literature which describe transonic buffet behavior on airfoils, there is no study where a comparison between the performance of an airfoil (clamped to both sides of the wind tunnel) and an equivalent unswept wing of finite span (with a free wing tip) is addressed. In this section, these two behaviors are directly com-

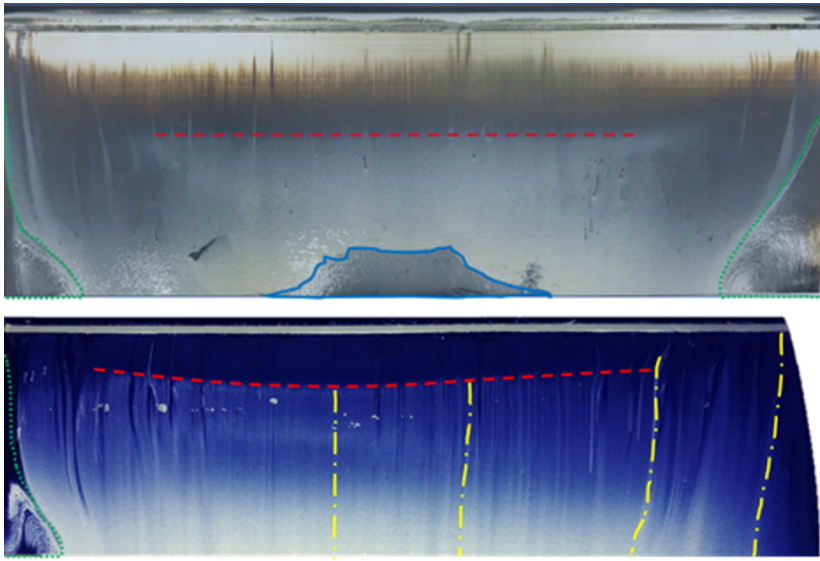


Figure 7.5: Comparison of oil flow visualizations for airfoil (top) and unswept wing (bottom). The red dashed lines indicate the average shockwave position and the blue solid line the separated area. Green dotted and yellow dashed lines indicate corner effects and streamlines orientation respectively.

pared, using oil flow visualizations on two models at the same flow conditions ($Ma = 0.7$ and $\alpha = 3.5^\circ$).

The main differences between the two oil flow visualizations (see Fig.7.5) regard the shockwave position and shape (red dashed lines), the separated area (blue solid line) and the tip effects. For the airfoil case the shockwave appears relatively uniform along the span (except near the two extremities of the model due to sidewall influences) and is located around $40\%c$. For the finite unswept wing the shockwave position varies significantly along the span, with the most downstream shockwave position experienced in proximity of the mid-span plane (slightly more inboard). It is also evident that for the unswept wing the shockwave is located more upstream, with the average position at approximately $25\%c$.

In correspondence of the clamping locations of the models (at both sides for the airfoil and at one side for the unswept wing), corner effects are highlighted with green dotted lines, with vortical structures indicating flow separation being present near the trailing edge of both the models tested. Moreover, for the unswept finite wing, a tip effect is also present, which results in an inboard flow contribution on the suction side of the model, in view of the pressure difference between the two sides of the model in agreement with literature (see for example Petrilli et al. (2013)). As a result, the streamlines on the suction side of the unswept wing are clearly diverted inboard near the tip. Streamlines oriented along the freestream direction are only recovered at around $y/b=0.5$ (see yellow dashed lines). It is worth pointing out that since the boundary layer thickness on the side walls is about 20 mm (Tambe (2022)), while the distance of the wing tip to the side wall is of 30 mm, it is reasonable to assume that no interaction between the wing tip

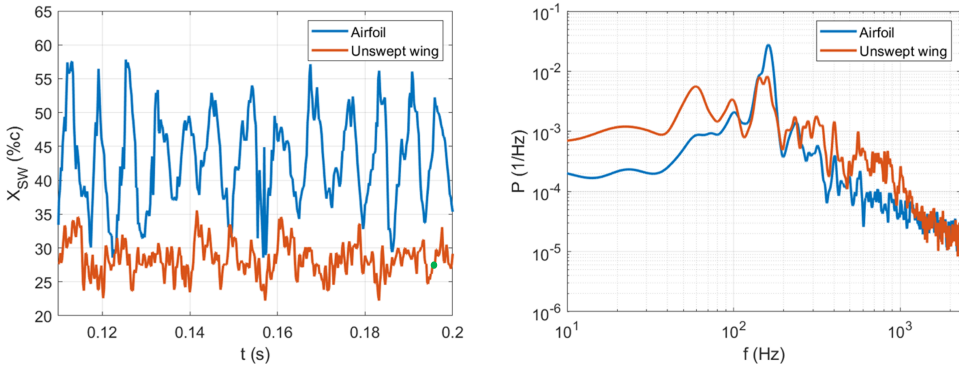


Figure 7.6: Time behavior of the shock position for airfoil and unswept wing (left) with relative power spectral density (right). The green marker on the left indicates the snapshot shown in Fig.7.3.

vortex and the side wall boundary layer takes place.

Another important difference is the absence of a separated region for the unswept wing, at least in an average sense. Differently, this flow feature is clearly present for the airfoil, as underlined by the blue line in Fig.7.5 (top).

7.3.2. SHOCK DYNAMICS COMPARISON BY MEANS OF BOS

Once a first qualitative visualization of the flow field is given by means of oil flow visualizations, the shock position has been tracked for both configuration, using the BOS images. In detail, the shock position has been tracked by evaluating the maximum of the gradient of the density field along horizontal lines, at 0.15c from the surface of the airfoil, as sketched in Fig.7.3 (right).

The variation of the shock position in time is shown in Fig 7.6 (left). As qualitatively observed from the oil flow visualizations, it is evident that the shockwave is located much more upstream for the unswept wing (the mean shock position for the unswept wing is $X_{SWAVG} = 28.3\%c$ of the chord, while for the airfoil this is $X_{SWAVG} = 42.8\%c$) and that the amplitude of oscillation is larger for the airfoil. This is confirmed by the standard deviation (STD) of the shock position which is $X_{SWSTD} = 7.1\%c$ for the airfoil and $X_{SWSTD} = 2.7\%c$ for the unswept wing (these data are also summarized in Table 7.3). The values of the average shock position and STD reported for the airfoil, are very similar to the values reported in Chapter 5 for same flow conditions, as obtained with schlieren and PIV techniques, confirming the accuracy of BOS for 2D applications. When analyzing the shock position, it is evident that for the unswept wing case, the shock behavior is less periodic, with higher frequency contributions being observable in the shockwave behavior.

To complete this discussion the spectral content associated with the shock position for both the airfoil and the unswept wing is represented by its power spectral density (PSD) and shown in Fig. 7.6 (right). The PSD is computed with the Welch method and each PSD is normalized by their respective variance. Both the configurations display a main peak at 160 Hz (similar to Chapter 5). However, for the airfoil, a distinct peak is present at exactly 160 Hz, while for the unswept wing there is a more broadband contribution with two relative peaks at 142 and 160 Hz. The general behavior of the PSD

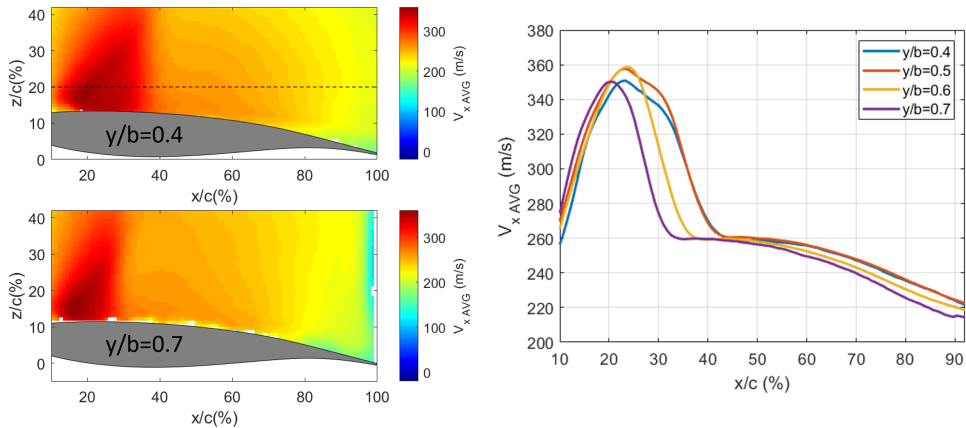


Figure 7.7: Average streamwise velocity component (V_x) for the $\Lambda = 0^\circ$ wing for $y/b=0.4$ and $y/b=0.7$ (left). On the right, comparison of average velocity profiles for $z/c=0.2$ and for $y/b=(0.4, 0.5, 0.6, 0.7)$.

greatly differs for the two models, with the airfoil configuration having only minor contributions at frequencies other than 160 Hz, in contrast to the unswept wing. For the latter, additional contributions are present at 280-320 Hz, which frequency values are the double of the main buffet contributions (142-160 Hz). The reason for a higher energetic contribution at the first harmonic of the buffet frequency for the unswept wing is not certain. Nonetheless it is supposed to be associated with a more irregular behavior of the shockwave position signal (also in view of the shockwave position variations along the span), which introduces contributions at the first harmonic of the buffet phenomenon. For the unswept wing, additional contributions associated with the structural vibration of the wing, occur at 60 Hz and 100 Hz. Although for frequencies above 1050 Hz there is a good agreement between the two PSDs, the frequency contributions between 500 and 1050 Hz are more relevant for the unswept wing. These frequencies correspond to Strouhal numbers $St = 0.18 - 0.4$, which are in the same broadband range of St that is often associated with the transonic buffet behavior of a swept wing (Giannelis et al. (2017)). This observation suggests that the buffet phenomenon is highly influenced by finite wing effects and clamping conditions.

7.3.3. FLOW FIELD ANALYSIS FOR THE UNSWEPT WING

To better address the clamping condition effects, the PIV measurements carried out for the unswept wing at different spanwise positions ($y/b=0.4; 0.5; 0.6; 0.7$) are discussed. For this purpose the average velocity field is shown in Fig. 7.7 (left) for the two most extreme measurement planes ($y/b=0.4$ and $y/b=0.7$). The comparison shows that in the most inboard section, the supersonic area encompasses a much wider region than for the plane of measurement in the neighborhood of the tip of the unswept wing. To better compare the average horizontal velocity fields, in Fig. 7.7 (right) the velocity profiles for $z/c=0.2$ and for $0.1 < x/c < 0.95$ (corresponding to the dashed line in Fig. 7.7, left) are shown for all four measurement planes. The plot confirms an upstream shift of the average terminating shock position when moving from the most inboard test location to

the most outboard. In addition, for the most outboard location, a further reduction of the velocity is observed for $0.5 < x/c < 0.95$. Very similar results are obtained for $y/b=0.4$ and $y/b=0.5$ both in terms of shockwave position and velocity development downstream of the shockwave.

These observations are in good agreement with an oil flow visualization performed on the same model and flow conditions (Fig. 7.5, bottom) where the most downstream shockwave position is observed between $0.4 < y/b < 0.5$. In addition the presence of both wing root and wing tip interaction is noted.

The shockwave has been tracked using the PIV data by monitoring the gradient of the horizontal velocity component. The computed values of average shock position and standard deviation are reported in Table 7.3. The results confirm the observations from Fig. 7.7, with more downstream shockwave positions being present for $y/b=0.4$ and $y/b=0.5$, where the widest range of oscillation of the shockwave are also achieved. By comparing the shockwave properties of the unswept wing computed with both BOS and PIV, it is evident that the BOS data are closer to the range of values observed for the most outboard PIV planes of measurement.

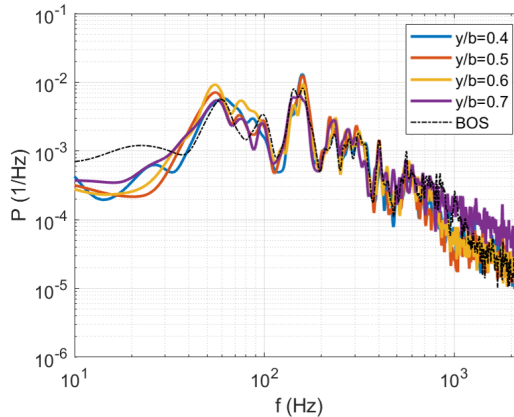
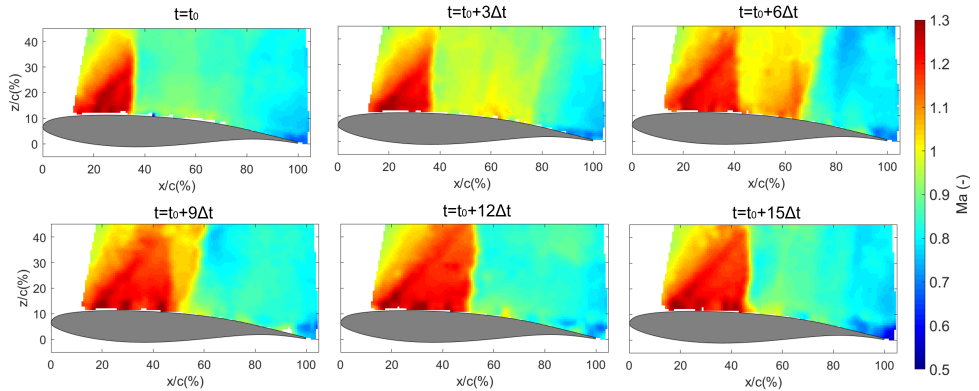


Figure 7.8: Power spectral density of SW position tracked in the four different measurement planes from PIV measurements.

The power spectral density associated with the shockwave position in the different measurement planes have been plotted in Fig. 7.8 and compared to the spectrum obtained with BOS measurements (black dashed line). The different PIV spectra are practically overlapping over the entire spectrum, except for the most outboard location ($y/b=0.7$). It is also interesting to note that only for the more outboard locations ($y/b=0.6$; 0.7) the main buffet frequency contribution appears more broadband (as observed from the BOS data), while at more inboard locations a distinct peak at 160 Hz is observed. Comparing the spectral analysis in Fig. 7.8, based on the PIV data and BOS data, a very good match between the two techniques is achieved. This confirms that BOS is able to characterize the main features of buffet on an unswept wing, although not being capable to characterize the flow features at different spanwise locations.

Table 7.3: Average and standard deviation of shockwave position for different configurations.

Configuration	SW_{AVG} (%c)	SW_{STD} (%c)
BOS, Airfoil	42.8	7.1
BOS, $\Lambda = 0^\circ$	28.3	2.7
PIV, $\Lambda = 0^\circ$ wing, $y/b=0.4$	35.3	3.5
PIV, $\Lambda = 0^\circ$ wing, $y/b=0.5$	35.2	3.3
PIV, $\Lambda = 0^\circ$ wing, $y/b=0.6$	30.5	2.8
PIV, $\Lambda = 0^\circ$ wing, $y/b=0.7$	27.7	2.4

Figure 7.9: Instantaneous visualization of the Mach number field in 6 different time steps for the $\Lambda = 30^\circ$ wing for $y/b=0.6$.

7.4. EFFECT OF SWEEP ANGLE

7.4.1. INSTANTANEOUS FLOW FIELD

To describe the behavior of transonic buffet in presence of sweep angle, the instantaneous Mach number field (computed from the velocity data with the assumption of constant total temperature) is discussed for one entire buffet cycle for the $\Lambda = 30^\circ$ wing. To analyze the cycle, 6 snapshots with a time separation of $3\Delta t$ (i.e., 0.645 ms; with $\Delta t=0.215$ ms being the time interval between subsequent acquisitions) are taken into consideration (see Fig. 7.9).

In the first time step (t_0) the shockwave is located in its most upstream position ($x/c=0.35$). In the following image ($t = t_0 + 3\Delta t$), the shockwave moves downstream and a region of accelerated flow is observed for $0.4 < x/c < 0.7$. In the following time step (image in the top right) this region has become locally supersonic and a secondary shockwave structure appears at $x/c=0.65$. In the figure in the bottom left the main shockwave structure has moved downstream, while the secondary shockwave is moving upstream. As a result of the opposite motion of the two shockwave structures, they are observed to merge in the $t = t_0 + 12\Delta t$ image, with a primary shockwave structure reaching its most downstream position ($x/c=0.5$). In the following time step the shockwave starts again its upstream movement. A similar description of secondary supersonic areas can be found

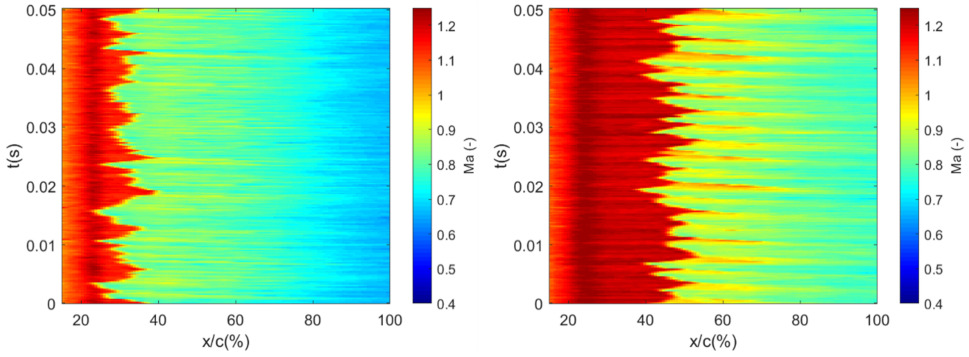


Figure 7.10: Mach number profile for $y/b=0.6$ and $z/c=0.2$, for the $\Lambda = 15^\circ$ (left) and the $\Lambda = 30^\circ$ wings (right).

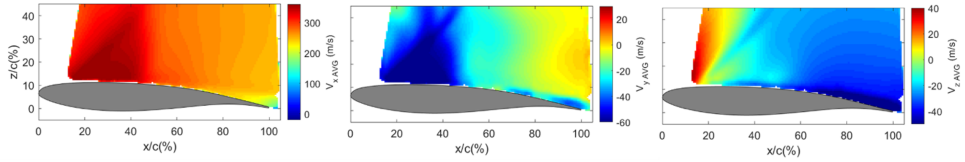


Figure 7.11: Average velocity field for V_x (left), V_y (center) and V_z (right) for the 30° swept wing for $Ma = 0.81$ and $\alpha = 3.4^\circ$ at 60% of the span.

in [Kuzmin \(2014\)](#) for a similar range of flow conditions (although for non-buffet conditions) and is attributed to the curvature of the airfoil.

To characterize the time evolution of the Mach field for a larger interval, the profile of the Mach number field for $y/b=0.6$ and $z/c=0.2$ is shown in [Fig. 7.10](#) for the $\Lambda = 15^\circ$ and the $\Lambda = 30^\circ$ wings. The Mach number profile of the latter ([Fig. 7.10](#) right) clearly reveals the oscillation of the primary shockwave structure (between 40 and 55% c) and the intermittent presence of a secondary supersonic area, which extends approximately until 80% c . As shown from the instantaneous images in [Fig. 7.9](#), the secondary supersonic area is formed during the second half of the downstream travel of the primary shockwave and disappears when this shock reaches its most downstream position. Differently, the time evolution of the profile of the $\Lambda = 15^\circ$ wing ([Fig. 7.10](#) left) shows a more upstream shockwave location (between 25 and 35% c) with only subsonic expansions of the flow downstream of the supersonic area.

7.4.2. AVERAGED VELOCITY FIELDS

In [Fig. 7.11](#) the time-averaged velocity fields for each of the three components (oriented along the x , y and z axes, as defined in [Fig. 7.1](#), right) is shown for the $\Lambda = 30^\circ$ swept wing for $y/b=0.6$ (and with $Ma = 0.81$ and $\alpha = 3.4^\circ$). The extent of the supersonic area is quite evident from both V_x (streamwise velocity component, in the direction of the wind tunnel center line) and V_y (velocity component along the y -axis, in the direction normal to the wind tunnel side wall).

For this configuration, at least in an average sense, no appreciable separated area

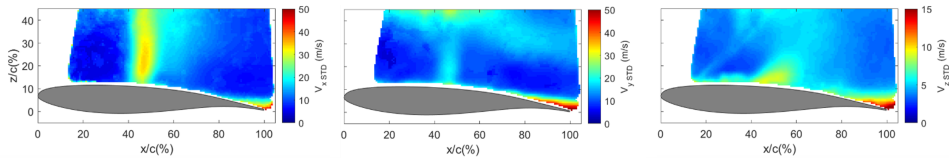


Figure 7.12: Standard deviation of velocity for V_x (left), V_y (center) and V_z (right) for the 30° swept wing for $Ma = 0.81$ and $\alpha = 3.4^\circ$ at 60% of the span.

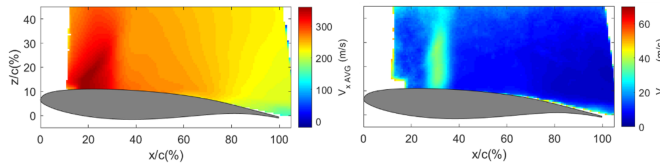


Figure 7.13: Average (left) and standard deviation (right) of velocity field for the V_x -component of the 15° swept wing for $Ma = 0.72$ and $\alpha = 3.4^\circ$ at 60% of the span.

can be observed, with a relevant reduction of the streamwise velocity component occurring only in proximity of the trailing edge of the wing. The vertical velocity component (V_z , in the direction normal to the plane of the wing) has its maximum value in the most upstream region of the FOV, due to the curvature of the airfoil. A slight increase of vertical velocity is also observed in the shockwave oscillation area, for $x/c \approx 0.45$. Regarding the out-of-plane velocity component (V_y), in addition to the supersonic area, a region of negative velocity is observed in the area close to the trailing edge. In the remaining portion of the FOV the variations of velocity of the out-of-plane component remain limited.

To quantify the unsteadiness present in the velocity field the standard deviations of the three velocity components are shown in Fig. 7.12 for the same plane of measurement ($y/b=0.6$). The plot clearly shows unsteadiness due to the shock oscillation for both the streamwise (left) and the out-of-plane velocity component (center) in the range $0.4 < x/c < 0.5$. Although upstream of the shockwave the unsteadiness is very limited, additional unsteadiness (caused by the pulsating formation of the secondary supersonic region) is observed downstream ($0.5 < x/c < 0.6$). Further fluctuations occur, for all the velocity components, in proximity of the trailing edge, suggesting the presence of an intermittent separated area. For the vertical velocity component (right), relevant oscillations are observed between 40 and 60% of the chord and are attributed to fluctuations of the shockwave position and inclination throughout the buffet cycle.

For brevity, for the 15° sweep angle wing only the horizontal velocity component and the corresponding standard deviation are presented (see Fig. 7.13). It is clear that, compared to the 30° wing, the extent of the supersonic area is much more limited, with the shockwave located more upstream ($x/c \approx 0.3$) and the relative amplitude of oscillation reduced to 10% c. No unsteadiness is present at the trailing edge of the wing, suggesting that for this configuration and flow conditions, the separated area is not even present in an intermittent fashion. No velocity fluctuations are observed downstream of the shockwave oscillation range, confirming the absence of a secondary supersonic area.

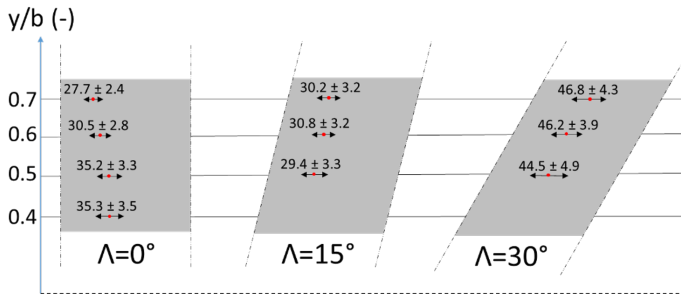


Figure 7.14: Sketch of the three wings with indication of average and standard deviation of shockwave oscillation for each plane of measurement.

7.4.3. SHOCK DYNAMICS

To quantitatively compare the behavior of the shockwave for the different configurations, its position has been tracked in all the PIV measurement planes, as commented previously for the unswept wing in Section 7.3.2. In Fig. 7.14, the region of oscillation of the shock position is indicated for all the wings and for all the span locations, providing its average value and the relative standard deviation. The wing with the largest amplitude of oscillation is the $\Lambda = 30^\circ$ wing, for which the values of STD are in the range 3.9-4.9% c. From the BOS images a slight underestimation of the fluctuations of the shock position is obtained for the $\Lambda = 30^\circ$ wing, with $SW_{STD-BOS} = 3.8\%$ c. The PIV data confirm that in presence of the largest sweep angle, the most downstream average shockwave positions are achieved ($0.44 < X_{SWAvg}/c < 0.47$). In contrast, for both $\Lambda = 0^\circ$ and $\Lambda = 15^\circ$ wings values close to 30% c are computed. However, it should be remembered that, although the normal Mach number is constant, the freestream Mach number differs for each of the wings. From the comparison of the range of the shockwave oscillations, it emerges that only for the unswept wing there is a relevant variation of the shockwave position along the span. This observation may be explained by the fact that in presence of sweep angle the tip vortex affects a smaller extent of the span.

From the time behavior of the shock position, the corresponding power spectral density has been determined for all the measurement planes. To have a comparison between the spectral content of the shockwave position for the different wings, the PSD of the shock position is shown for all the wings, for the same spanwise plane $y/b = 0.6$, in Fig 7.15 (left). The wings exhibit a similar spectral content, with main contributions at 60 Hz (oscillation of the model), 160 Hz (2D buffet frequency) and 400 Hz (wind tunnel contribution). In addition to these peaks additional energetic contributions are observed in the range 450-850 Hz, which, as previously commented, is in the same range of frequencies obtained in literature for 3D buffet. However, in view of their limited energetic content, it cannot be unambiguously stated that this range of frequency is associated with the convection phenomena characterizing buffet on swept wings. When comparing the different configurations it is also observed that, with the increasing value of the sweep angle (also associated with an increase of the freestream Mach number), there is an increase in the wind tunnel contribution at 400 Hz.

To verify variations in the spectral content of the shockwave oscillation along the

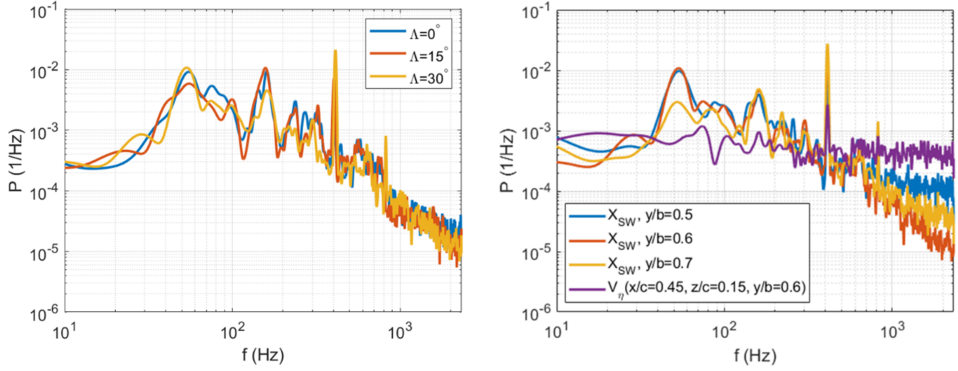


Figure 7.15: Comparison of the PSD of the SW position for different wings for $y/b=0.6$ (left). On the right comparison of the PSD of the SW position for different measurement planes ($y/b=0.5, 0.6, 0.7$) for the $\Lambda = 30^\circ$ wing. The purple line indicates the PSD of the spanwise velocity component in $x/c=0.45, z/c=0.15, y/b=0.6$.

span, the PSDs of the shockwave position are compared for the different measurement planes of the 30° sweep angle wing (see Fig. 7.15, right). Also in this case a similar distribution of the PSDs is observed, with no variation in the relevance of the 2D buffet peak (at 160 Hz) or in the range 450-850 Hz. However, an increase of the values of the PSDs for $f > 1000$ Hz is observed for both $y/b=0.7$ and $y/b=0.5$, as compared to $y/b=0.6$.

7.4.4. SPANWISE VELOCITY COMPONENT

To analyze the spanwise behavior of the velocity field, a rotated coordinate system oriented along the leading edge of the wings (η) and in the orthogonal direction (ζ) has been adopted (see the two coordinate systems in Fig. 7.1, right). The velocity component orthogonal to the leading edge (V_ζ) and the one oriented along the leading edge direction of the wing (V_η) are computed as:

$$V_\zeta = V_x \cos \Lambda - V_y \sin \Lambda \quad (7.1)$$

$$V_\eta = V_x \sin \Lambda + V_y \cos \Lambda \quad (7.2)$$

With V_η being positive going from the root to the tip of the wing. In Fig. 7.16 the average spanwise velocity is shown for the $\Lambda = 30^\circ$ wing for all the measurement planes ($y/b=0.5$ on the left, $y/b=0.6$ in the center and $y/b=0.7$ on the right). In large part of the FOV there is a nearly uniform outboard velocity of approximately 120 m/s in the shockwave oscillation region and in the range from 70 to 100 m/s in the trailing edge area.

The values of the spanwise component in the trailing edge area are very close to the convection velocity obtained by Dandois (2016) for the buffet cells. Differently, the value of spanwise velocity in the shockwave oscillation range is higher than the convection velocity obtained by Paladini et al. (2019), Dandois (2016) (where a convection velocity of approximately 60 m/s was reported).

In Fig. 7.15 (right) the spectral content of the time variation of the spanwise velocity component (V_ζ) in a point in the shockwave oscillation range is reported ($x/c=0.45$,

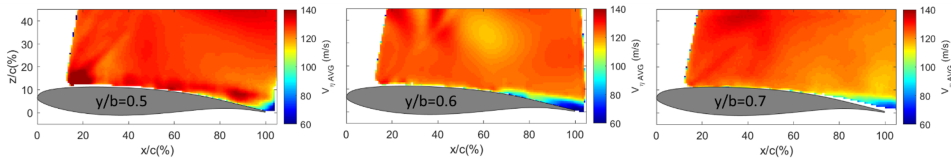


Figure 7.16: Comparison of spanwise component of velocity for the $\Lambda = 30^\circ$ wing for $y/b=0.5$ (left), $y/b=0.6$ (center) and $y/b=0.7$ (right).

$z/c=0.1$, $y/b=0.6$). No relevant contributions are observable at the 2D buffet frequency (160 Hz), while relative higher energetic contributions are present at higher frequencies.

7.5. CONCLUSION

In this chapter, transonic buffet has been studied experimentally to investigate finite wing and sweep effects. This study showed an appreciable difference in the transonic buffet behavior between a full span unswept wing (airfoil) and an unswept wing of finite span (clamped on just one side of the wind tunnel). The results clearly reveal that the buffet oscillations are more relevant and periodic in the case of the airfoil than for the unswept wing (see Fig. 7.6), with the shockwave located much more downstream in the former case. The use of PIV in different planes of measurement demonstrated that the shockwave is located more upstream and oscillating in a more restricted region at outboard locations (Fig. 7.7). These results suggest that at those locations an effect of the wing tip vortex on the buffet behavior is felt, as also supported by additional oil flow visualization. Spectral analysis showed that the presence of the free tip of the wing also gives rise to structural oscillation of the wing, which occurs at 60 Hz (Fig. 7.8).

To analyze the effect of sweep angle, the behavior of wings with different sweep angle ($\Lambda=0^\circ$, 15° , and 30°) have been compared, using for each wing the same normal Mach Number (with respect to the wing leading edge). At these flow conditions, much more downstream shockwave positions and a wider range of oscillations are achieved for the $\Lambda = 30^\circ$ wing, while similar results are observed for the other two wings (see Fig. 7.14). For the configuration with the larger sweep angle a periodic formation of a secondary supersonic area characterizes the shockwave oscillations during the buffet cycle. An analogous behavior was not observed for the $\Lambda = 15^\circ$ and the unswept wings (Fig. 7.10).

Evidence was found of an intermittent separated trailing edge area that occurs only for the larger sweep angle wing (Fig. 7.11 and Fig. 7.12). Near the trailing edge region of the $\Lambda = 30^\circ$ wing, spanwise velocity components are found which are in the same range of the convection velocities obtained by Paladini et al. (2019) and Dandois (2016) for the buffet cells. To better visualize the buffet cells, a PIV analysis in a measurement plane oriented along the span or with a volumetric set-up (tomographic PIV) is suggested for further studies.

A similar frequency content of the shockwave dynamics has been observed for the three wings. For all the models there is a reduction of the 2D buffet peak compared to the airfoil case, together with an increase for frequencies in the range of 450-850 Hz. Regarding the primary buffet frequency, a reduced relevance of the peak at 160 Hz has been

noticed for the $\Lambda = 30^\circ$ compared to the other wings. No relevant variations are instead visualized along the span of the swept wing. The increase of frequency contributions in the range between 450 and 850 Hz is in agreement with literature, in terms of Strouhal number ($St = 0.18 - 0.4$).

Although these results show some variations in the shockwave buffet oscillation in presence of an increasing sweep angle, the current findings also indicate that an aspect which could influence the comparison of the behavior of an airfoil and that of a wing is the different boundary conditions associated with the clamping of the model, which leads to different structural oscillations and to the occurrence of tip effects for the wings. These differences introduce a non-symmetric spanwise flow distribution for the unswept wing with respect to the airfoil (see Fig.7.5).

PART II

CONTROL OF TRANSONIC BUFFET

8

UPPER TRAILING EDGE FLAP FLOW CONTROL

This chapter investigates the possibility of controlling transonic buffet by means of a trailing edge flap with an upward deflection (referred to as "upper trailing edge flap", or: UTEF). Different geometries (straight and serrated) and dimensions of UTEFs (with heights ranging between 1% and 2% of the chord) have been studied with respect to their impact on the buffet behavior. The effectiveness of the UTEFs has been investigated with schlieren and particle image velocimetry (PIV) in the transonic-supersonic wind tunnel of TU Delft at $Ma = 0.7$, $\alpha = 3.5^\circ$. The schlieren results demonstrated the efficacy of the use of UTEFs for reducing the range of the buffet oscillations when the height of the UTEF was equal to at least 1.5% c . This result was corroborated by a flow characterization with PIV data and which highlighted that, in presence of a control system, not only the shock oscillation range is reduced but also the intensity of the separated area pulsation. The use of serrated UTEFs, despite having an effect on the local flow field, was found to be ineffective in alleviating buffet oscillations. The adoption of the best behaving UTEF configuration (straight 2% c UTEF) proved to only slightly alter the circulation value compared to the clean configuration, indicating that the lift was not appreciably affected, while it also proved to be effective in an off-buffet condition ($Ma = 0.74$ and $\alpha = 2.5^\circ$).

8.1. INTRODUCTION

In view of the described feedback mechanism of buffet (see Section 2.3), an alternative strategy of controlling buffet could be achieved by attempting to inhibit the communication between the separated trailing edge area and the trailing edge itself, which is responsible for the creation of UTWs. This motivates the implementation of a fixed flap with a vertical upward deflection at the trailing edge of the airfoil, also referred to as upper trailing edge flap (UTEF).

Parts of this chapter have been published in [D'Aguanno et al. \(2022a\)](#).

From a geometrical point of view, this device resembles a Gurney flap (GF), which has been first used in automotive applications (with an upward flap deflection) and subsequently on aircraft as well (but then with a downward orientation, see [Suresh and Sitaram \(2011\)](#)-[Wanga et al. \(2008\)](#)) with the goal of increasing the downforce or the wing lift, respectively. However, the working principles of a UTEF and of a GF are very different, with the former not being associated with a modification of the lift coefficient when its height is modest, since the UTEF would be completely immersed in the trailing edge separated area. An application of a UTEF for controlling transonic buffet is described in the numerical investigation by [Tian et al. \(2018\)](#), which showed the possibility of shifting the buffet onset to higher values of angle of incidence and lift coefficient. Different heights of UTEFs were studied, with the UTEF having a height of 1.5% of the chord of the airfoil giving the most promising results. [Sartor et al. \(2019\)](#) have also investigated the possibility of using a fluidic UTEF in the form of air jets operated at the trailing edge of the airfoil on the pressure side.

In the present Chapter an experimental investigation on the use of upper trailing edge flaps for controlling transonic buffet is performed using schlieren and particle image velocimetry as measurement techniques. In addition to straight UTEF configurations and a baseline configuration without flap, serrated UTEFs will be investigated as well. The latter may provide information on the effect of serrated trailing edge in compressible flows. To the best of the authors' knowledge no similar experimental study of this type has been previously reported in literature.

Although UTEFs may be considered as a particular form of passive TED, they differ in several aspects. First of all, both [Caruana et al. \(2003b\)](#) and [Despre et al. \(2001\)](#) considered only downward deflections of the TEDs ($0^\circ < \delta < 50^\circ$), while in the study by [Lee \(1992\)](#) in view of the large chord of the flap ($c_{flap} = 13\%c_{airfoil}$), only small deflections were considered. Thus, UTEFs are a particular TED geometry which has never been studied experimentally in literature for controlling transonic buffet. More importantly, the mechanism by which a UTEF is supposed to mitigate buffet is quite different from that of conventional TEDs, namely not by affecting the circulation around the airfoil, but by interacting with the feedback loop referred to above. Therefore, the study of UTEF-based control configurations will also allow to achieve further insight into the physics of transonic buffet, particularly regarding the feedback mechanism occurring between the trailing edge of the airfoil and the oscillating shockwave. This aspect will be addressed by comparing the behavior of the different UTEF configurations (straight and serrated) with respect to the clean airfoil.

In the next section (Section 8.2) the experimental procedures are described. Subsequently (Section 8.3), a characterization of the shock dynamics is shown for all the tested configurations, using the schlieren visualization data. In Section 8.4 the differences between the most significant configurations are further discussed, based on the particle image velocimetry (PIV) velocity field, also evaluating the aerodynamic effects induced by the presence of a UTEF. In Section 8.5 the sensitivity of the UTEF to the flow condition is discussed by analyzing the performance of a UTEF in a less developed buffet condition. In the conclusions (Section 8.6) the results are summarized and further discussed.

8.2. EXPERIMENTAL PROCEDURES

8.2.1. MODEL

The model used is the "horizontal" supercritical OAT15A airfoil and has been tested at $Ma = 0.7$ and $\alpha = 3.5^\circ$. In addition, to assess the behavior of the UTEFs for less developed buffet conditions, tests with $Ma = 0.74$ and $\alpha = 2.5^\circ$ have also been carried out.

8.2.2. UPPER TRAILING EDGE FLAPS

The tested UTEFs have been realized as iron add-on profiles, with different heights and shapes. The three values of the height (h) (with respect to c) are:

- $h = 1.0 \% c$;
- $h = 1.5 \% c$;
- $h = 2.0 \% c$.

These values have been chosen because of the results in Chapter 5, which hinted that the structure responsible for the production of UTWs are traveling in a thin layer in proximity of the airfoil surface. The proposed values of h are in the order of the thickness of the boundary layer δ at the trailing edge ($\delta = 1.5\text{mm}$), estimated for a turbulent boundary layer developing on an equivalent flat plate. However, it is worth mentioning that downstream of the shockwave, the boundary layer will become thicker, as shown by [Babin-sky and Harvey \(2011\)](#), and a further increase of the thickness of the boundary layer is present for a separated flow, thus, this value is only used as a proxy of the real boundary layer thickness at the trailing edge.

The height (h) is measured with respect to the suction side of the airfoil at the trailing edge (which for production reason has a thickness $t_{TE} = 0.75\%c$) and therefore, the real height of the flap (with respect to the pressure side) is given by the sum $h + t_{TE}$ (see Fig. 8.1). For each value of h , three different shapes of UTEFs were tested:

- a straight UTEF;
- a wide serrated UTEF ($\lambda/h = 4$);
- a narrow serrated UTEF ($\lambda/h = 1$).

where λ indicates the spanwise wavelength, i.e. the distance between consecutive teeth in the serration. A sketch of the different UTEFs is given in Fig. 8.1 while in Fig. 8.2 (left) the $\lambda/h = 4$, $h = 2\%c$ UTEF is visualized as mounted on the OAT15A airfoil.

8.2.3. EXPERIMENTAL TECHNIQUES

The experimental data which are used in this chapter are obtained with the same set-up described in Chapter 5, thus for more details on the parameters of this experiment refer to this section. Also in this Chapter, the schlieren data is used to visualize and quantify the shock movement for the different UTEFs studied, while the PIV data to quantify the velocity field.

To understand the behavior of the serrated UTEFs (for the wide serrated configurations) the PIV measurements have been conducted with the laser aligned either with the

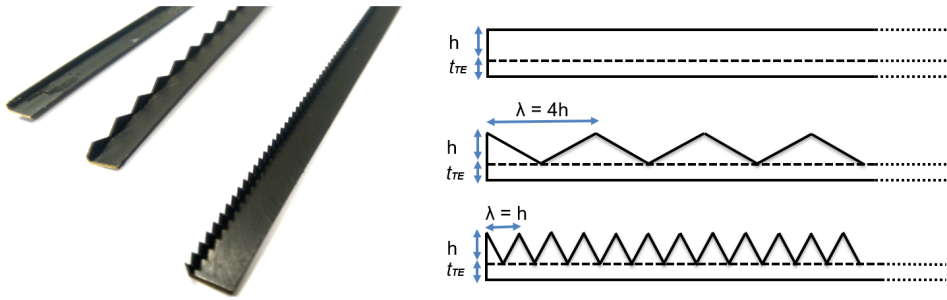


Figure 8.1: Shape of the upper trailing edge flaps, from the top to the bottom: straight, wide serration and narrow serration.

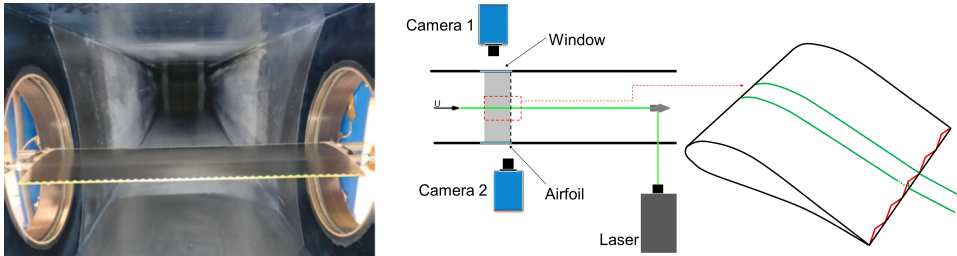


Figure 8.2: OAT15A in presence of serrated UTEF (left). Sketch of PIV set-up, with detail for the two measurement planes used for the wide serrated UTEFs (right).

peak or the valley of the serration, in both cases in proximity of the mid span of the airfoil (see the enlargement in Fig. 8.2 (right)).

8

8.2.4. DATA PROCESSING

To reduce the effect of laser light reflections on the airfoil, particularly evident at the trailing edge in presence of an UTEF a sliding time-minimum subtraction has been applied to the data sets, with the minimum evaluated for a kernel size of 11 images. For the cross-correlation parameters the reader is referred to Section 5.2.3.

8.2.5. UNCERTAINTY ANALYSIS

A quantification of the uncertainty of the collected data is of utmost importance when it comes to a comparative analysis among different configurations, like in this investigation. In Tab.8.1 the main sources of uncertainty are shown. The strongest effect is the uncertainty associated with the particle slip and it is governed by the value of the relaxation time (τ_p) of the seeding particles (see Section 3.8.3).

8.3. SHOCK DYNAMICS

In this section, the unsteady behavior of the shock wave is scrutinized for the different configurations by means of schlieren visualizations. First, the instantaneous images belonging to a typical buffet cycle are discussed for the airfoil equipped with a straight

Table 8.1: Uncertainty errors

Uncertainty source	error	Unit
Cross-correlation (ϵ_{cc})	≤ 6.7	m/s
Spatial resolution (ϵ_{sr})	≤ 1	%
Particle slip (ϵ_{slip})	≤ 60	m/s
Line of sight effect ($\epsilon_{schlieren}$)	0.003	m

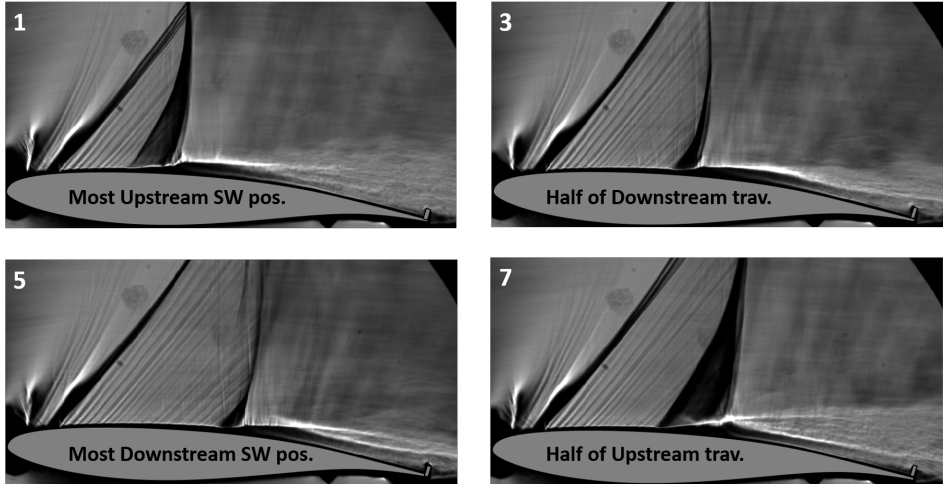


Figure 8.3: Instantaneous schlieren images in four main phases for straight 2% UTEF configuration.

UTEF with a height of $2\%c$ (see Fig. 8.3). The cycle is visualized showing representative snapshots for four relevant buffet phases: with the shock wave in its most upstream position; during the downstream travel; in the most downstream position and during the upstream travel. Considering the more extensive phase definition shown in Section 4.2, these schlieren images correspond respectively to phases 1, 3, 5, and 7.

The selected FOV offers a complete view of the suction side of the airfoil, as observed in Section 5.3. It is worth recalling that the presence of the transition trip located at $7\%c$ results in an oblique pressure wave close to the leading edge in all the images. Notwithstanding the relatively prominent appearance of this wave in the visualization, the flow can be considered isentropic up to the location of the main shock wave that terminates the supersonic region.

In the first image on the top left of Fig. 8.3, the shock wave is in its most upstream position. In this phase the shock is visualized by a wide black line (in particular close to the surface of the airfoil) and it is located at around $30\%c$. The width of the shock wave line is connected to the presence of 3D effects along the span (developing, in particular, close to the side windows of the wind tunnel) and to the presence of a λ -shaped shock wave close to the surface of the airfoil. In the following phase (sub-figure on the top right) the shock wave is moving downstream (with the shock wave located at $x \approx 40\%c$) and the separated area is reduced. As a result of this, the black line indicating the shock wave

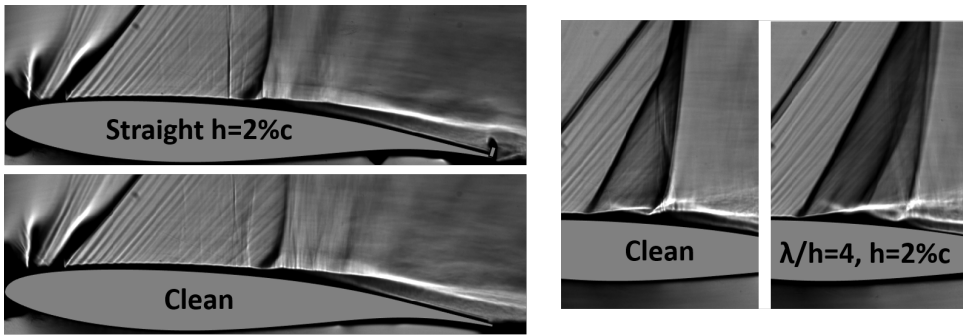


Figure 8.4: Difference in flow structures at the trailing edge, for the clean and straight UTEF configurations (left). Shock wave structures for clean and serrated UTEF ($\lambda/h = 4, h = 2\%$) configurations during upstream movement (right).

appears thinner and more normal with respect to the surface of the airfoil than in the previous image. In the visualization on the bottom left (phase 5) the shock wave reaches its most downstream location at $x \approx 55\%c$, with the separated area almost completely reattached. When the shock wave starts its upstream travel again (sub-figure on the bottom right), it acquires the highest velocity with respect to the flow, triggering a strong separation and a change in inclination of the shock wave.

For this discussion the straight 2% c configuration was used, while schlieren images relative to the clean airfoil were discussed in Section 5.3, displaying a similar general behavior of the flow field for these configurations. Nevertheless, some recurrent differences between some of the tested configurations have been observed as shown in Fig. 8.4. Starting from the sub-figures on the left, when a UTEF is used an upwash appears at the trailing edge of the airfoil, this feature is particularly evident when the separated area reattaches during the last part of the downstream travel (as shown in Fig. 8.4). Differently, during the upstream travel, additional 3D contributions to the shock wave visualization appear in presence of a serrated UTEF as visualized on the right of Fig. 8.4. This observation suggests that the subsequent peaks and valleys of the teeth of the serration cause differences in terms of shock wave position and separated area along the span. This behavior is expected due to the upstream traveling waves which have a different strength in the peak or valley of the serration. This evidence supports the idea that the presence of UTEFs has a significant effect on the whole buffet mechanism and consequently on the shock position. The effect of the serration will be discussed in more details in Section 8.4.3.

8.3.1. SHOCK POSITION

From the schlieren images the shock position has been tracked in time by looking at the gradient of luminosity in each image. In order to reduce the errors associated with the shock detection, the shock wave position has been tracked along multiple horizontal lines at a vertical distance from the airfoil surface of 1 cm and the results are averaged. In Fig. 8.5 an example of the behavior of the shock position is shown for the clean and for

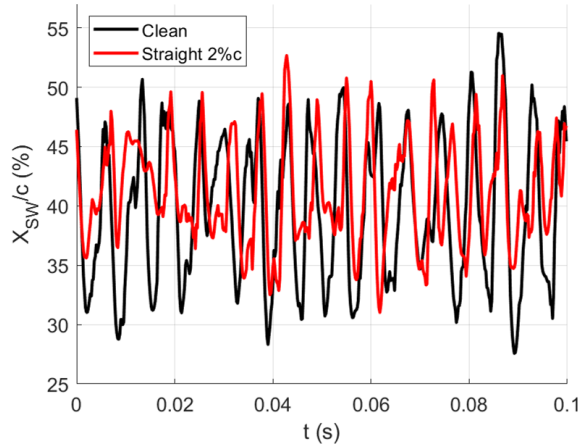


Figure 8.5: Comparison of the time behaviors of the shock position for clean and straight 2% configurations.

the straight 2% UTEF configurations. The plot shows that, in the selected time interval, the shock oscillation amplitude is reduced (of nearly 20%) for the UTEF case with the average shock position a bit further downstream (2–3% c more downstream). Furthermore, it seems that for the 2% UTEF case, the shock position behavior is less periodic.

To quantitatively compare the range of oscillation of the shock wave, its distribution has been plotted (Fig. 8.6, left) in terms of probability density function (pdf) for different configurations (clean, straight $h = 1\%c$, straight $h = 2\%c$, and serrated $\lambda/h = 4$ with $h = 2\%c$) using a bin size of 1% c . A reduced range of the shock wave position is obtained for the straight 2% UTEF compared to the clean configuration. As a consequence, there is a narrower distribution of the pdf ($p(X_{SW}/c)$), in comparison to the clean configuration where the most probable shock locations are spread over a wider range of chordwise positions. For the straight 2% configuration, as seen in Fig. 8.5, the shock wave behavior is less periodic including significant amplitude variations, suggesting that the coherence of the buffet mechanism is somehow decreased. To substantiate the latter consideration, the oscillation amplitude of each buffet cycle (Δ_{SW} , considered as the chordwise distance between consecutive locations in which the shockwave inverts its direction) has been computed and its distribution $p(\Delta_{SW}/c)$ is visualized in Fig. 8.6 (right). In the case of the clean airfoil, the most frequent amplitude of oscillation is in the order of 10% c , which is significantly higher than for the straight $h = 2\%c$ UTEF. For the latter case, cycles with an amplitude of oscillation lower than 5% c are very common.

In presence of a straight 1% UTEF the range of oscillation of the shock wave is very similar to that of the clean airfoil, suggesting that this height of the UTEF is not sufficient for yielding a relevant impact on the transonic buffet mechanism. For the $\lambda/h = 4$, $h = 2\%c$ serrated UTEF, the amplitude of the shock wave oscillations is very similar to the clean case, but with a distribution ($p(X_{SW}/c)$) that is moved to more downstream positions. Despite the different ranges, for all considered configurations the average shock position is between 40 and 45 % of the chord.

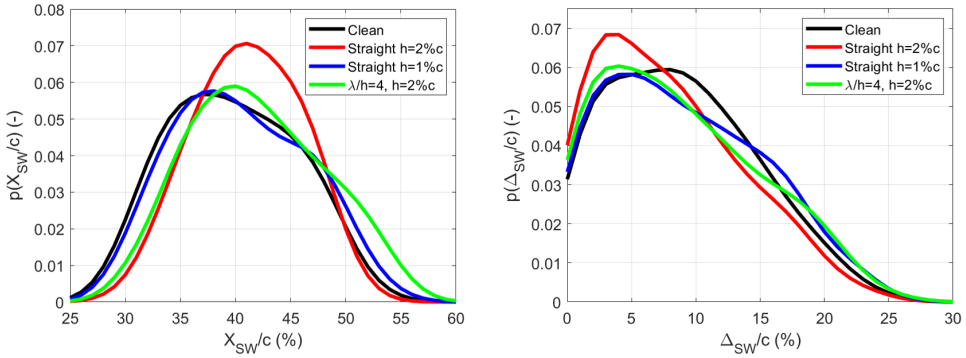


Figure 8.6: Comparison of the distribution of the shock position (left) and of the amplitude of shock wave oscillation (right) for different configurations.

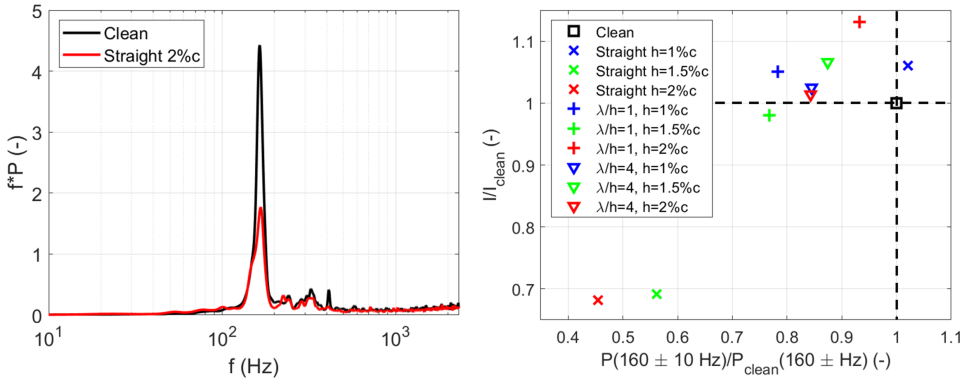


Figure 8.7: Comparison of PSD for clean and straight 2% configurations (left) and integral value of PSD for all the configurations studied (right).

8.3.2. SPECTRAL ANALYSIS

The spectral content of the shock location in time is investigated by looking at the power spectral density (PSD), using the Welch method. A maximum detectable frequency of 2500 Hz (half of the acquisition frequency) and a frequency resolution of 4.9 Hz are achieved. In Fig. 8.7 (left) the PSD of the shock position (P) is shown in its pre-multiplied form ($f \cdot P$). To ease the visualization of the data, only the results for the clean and the straight 2% configuration have been plotted, with both PSDs normalized by the variance of the shock oscillation signal for the clean case. Both configurations have a main peak at a frequency of 160 Hz ($St = U_\infty \cdot f / c = 0.07$). As already shown in Chapter 5 for the clean airfoil, secondary peaks arise at 320 Hz (second harmonic of buffet) and at 410 Hz, which is a contribution associated to the characteristic noise of the wind tunnel. Fig. 8.7 (left) shows that the application of the UTEF does not have an effect on the value of the main frequency contribution (160 Hz) but reduces the amplitude of this frequency peak by nearly 60% compared to the clean airfoil, without any apparent increase of energy for the secondary peaks. This observation confirms that, by using UTEFs, the feedback

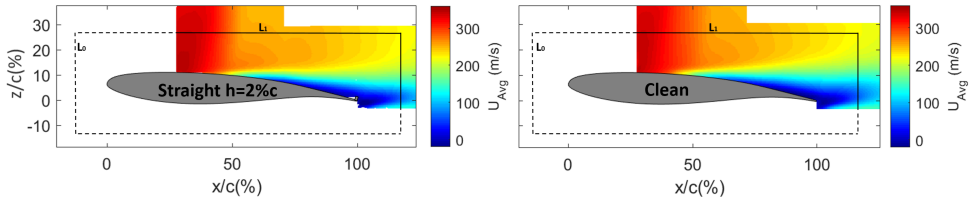


Figure 8.8: Time-average horizontal velocity component for straight 2% c and clean configuration. The solid black line indicates the line (L_1) on which the contribution to the circulation in the FOV is computed, while on the dashed line (L_0) outside the FOV, the flow conditions are assumed to be independent from the trailing edge configuration.

mechanism is not completely eliminated, but attenuated.

To quantitatively verify whether, with the use of a UTEF, the energy associated with the shock oscillation is just reduced overall or distributed to secondary frequency contributions, the PSD is integrated in the frequency range $f=0$ -1000 Hz, excluding high frequency contributions. These contributions are typically associated with erroneous shockwave detections caused by the inherent uncertainty in tracking the shockwave position due to the spanwise integration of the density gradients. The corresponding integral value (I) plotted in Fig. 8.7 (right) against the value of $f \cdot P$ at 160 ± 10 Hz (main peak). Both values are normalized by the values of I and $f \cdot P$ for the clean configuration. By definition the value for the clean configuration is 1 for both the abscissa and the ordinate.

It is evident that the UTEFs which behave best in reducing the buffet intensity are the straight configurations with heights of 1.5% and 2% of the chord, for which a reduction of integral energy of respectively 31 and 32% and of the main peak of 45% and 55% is observed (compared to the clean airfoil). Therefore, for $h \geq 1.5\%c$ a very similar performance of the UTEFs is obtained, however, to have a more precise optimization of the choice of the height of the UTEF further tests should be carried out on UTEFs with larger values of h . The results for $h \geq 1.5\%c$ differ very much from the performance of a straight UTEF with a height of only 1% c , for which a behavior similar to the clean configuration is present. This observation confirms that the height of 1% c is insufficient to affect the structures developing below the separated shear layer and boundary layer.

The use of the serrated UTEFs leads to either a negligible reduction of the relevance of buffet or even a small increase, confirming the inefficacy of serrations in compressible applications.

8.4. VELOCITY FIELD COMPARISON

8.4.1. FLOW FIELD STATISTICS

The straight UTEF with a height of 2% c was one of the two best performing configurations (together with the 1.5% c straight UTEF) and is analyzed more in detail in this section, in comparison to the clean configuration. The effect of serrated UTEFs will then be addressed in subsection 8.4.3.

Fig. 8.8 provides a comparison of the time-average horizontal component of the ve-

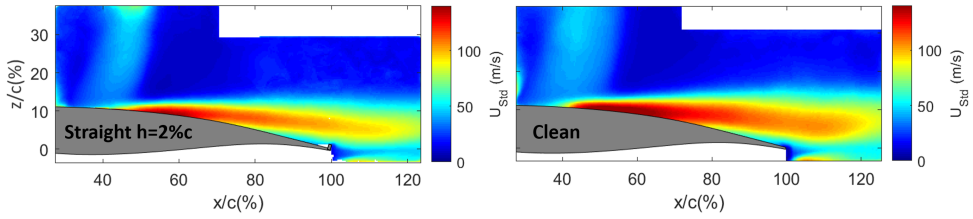


Figure 8.9: Standard deviation of the horizontal velocity component for straight 2% and clean configuration.

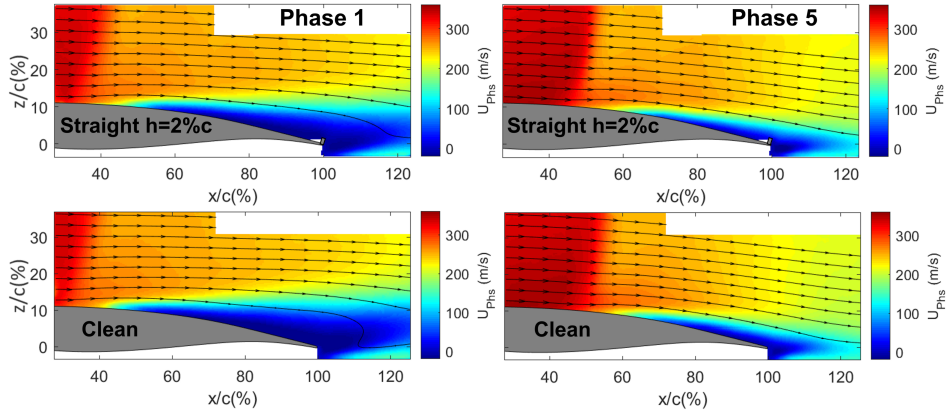


Figure 8.10: Comparison of horizontal phase-averaged velocity field in phases 1 and 5.

locity field for the two configurations of primary interest. With respect to the clean configuration, a small reduction of the separated area is observed in presence of the straight UTEF. To better appreciate the differences in flow unsteadiness between the two configurations, the standard deviation of the horizontal velocity component (u_{STD}) is shown in Fig. 8.9. Main differences are visible in both the shock wave oscillation area and in the separated region. It is evident that with the use of a UTEF there is a relevant reduction of the shock wave oscillation range (reducing from 20%c for the clean case to around 10%c for the UTEF configuration). A similar reduction is present for the fluctuations in the separated area, as shown by the vertical extent of the region in which the values of u_{STD} are larger than 80 m/s, which drops from 6.6%c to 4.2%c for the UTEF configuration. This comparison confirms that the unsteadiness in the flow field is substantially reduced with the UTEF.

In order to appreciate how these variations are reflected in the different buffet stages, a phase average of the velocity field is computed following the same procedure shown in Section 4.2, dividing the buffet cycle once again in eight phases.

In Fig. 8.10, the phase averaged horizontal velocity field (given by the sum of the mean and the periodic contributions, $u_{phs} = u_{avg} + u_{per}$) is shown for the clean and UTEF configurations in the phases in which the shock wave is either in the most upstream (phase 1) or in the most downstream position (phase 5). For a more detailed

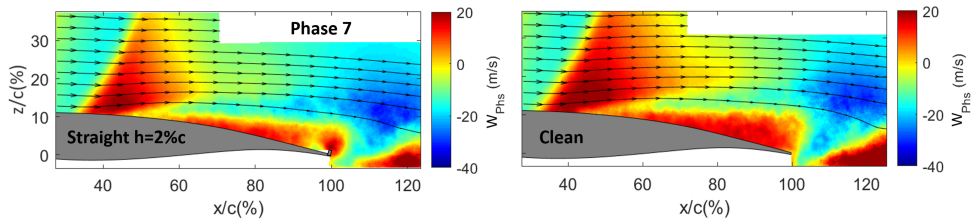


Figure 8.11: Comparison of vertical phase-averaged velocity field in the 7th phase.

analysis of the phase averaged velocity field for the clean airfoil, the reader is referred to Section 5.4.

From a first comparison of the velocity fields, the UTEF appears to reduce the oscillation range of the shock wave (in agreement with the results shown in Section 8.3.1). In more detail, in phase 1 the shock wave is located more upstream and the separated area is wider for the clean configuration, as is also observable from the direction of the streamlines close to the surface of the airfoil. In phase 5 the shock wave has reached its most downstream position and it is located more upstream for the UTEF configuration. No important difference is instead observable for the extent of the separated area size (the flow is almost completely reattached in this phase) or for the direction of the streamlines.

Another significant phase of transonic buffet is phase 7, in which the shock wave is halfway during its upstream travel. At this stage the shock wave has the highest relative velocity with respect to the flow. Therefore, this is the phase in which the extent of the separated area is at its maximum and as a consequence the shock wave is more oblique. This phase is best characterized by the behavior of the vertical component of the velocity field, as shown in Fig. 8.11. A wide area of positive vertical velocity occurs at the shock foot because of the presence of the oblique shock wave as well as a wide separated trailing edge area extending from the the trailing edge up to the shock. These features occur for both the configurations, but with important differences being observable just upstream of the UTEF. The extent of both these regions is reduced in presence of a UTEF suggesting that accordingly the strength of the shock wave is reduced as well. This behavior may be attributed to the lower velocity of the shock wave in presence of the straight 2%c UTEF, since the shock wave oscillation range is reduced but the buffet frequency remains constant. The reduction of the separated area has also been associated with the presence of a clockwise vortex at the back of the flap and upwash behind the airfoil, as shown by Tian et al. (2018) in their numerical investigation.

8.4.2. SEPARATED AREA EXTENT

Together with the shock position behavior, which has been analyzed in detail in Section 8.3.1, another key element of transonic buffet is the pulsation of the separated area size. The extent of the separated area has been computed for each instantaneous PIV image, by determining the percentage of vectors (S) with a velocity lower than 0 m/s in a rectangular region which ranges from 60%c to 100%c and for a height of 25%c over the surface of the airfoil. The average extent of the separated and its standard deviation

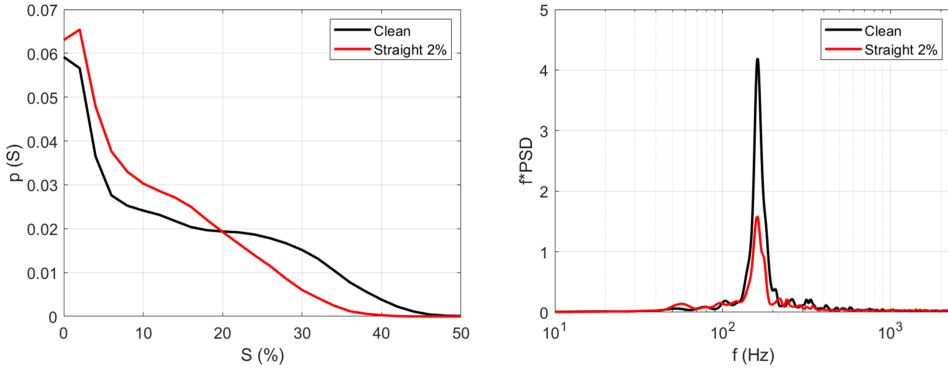


Figure 8.12: Comparison of distribution of separated area size (left). Spectral analysis of separated area extent (right).

value are reported in Tab.8.2, confirming a reduction of more than 20% of both the average extent (S_{avg}) and the pulsation (indicated by its standard deviation, S_{std}) of the separated area size in presence of the straight 2% UTEF.

The distribution of the separated area extent for the two studied configurations is plotted in Fig. 8.12 (left). For both the clean and the UTEF configuration the higher values of the distribution are obtained for $0\% < S < 4\%$, which corresponds to a very limited (but not zero) separated area. This peak confirms that, usually, when the shock foot separation is absent, there is still a small area in the FOV (for both the configurations), in which an area persists where the velocity is smaller than 0 m/s. This corresponds to the trailing edge separated area and is also visible in Fig. 8.10 (right). For the clean configuration, values of S between 10 and 30% are similarly probable, indicating that, along the buffet cycle, the separated area is expanding and shrinking in a wide range. Differently, for the straight UTEF configuration very few snapshots have values of S higher than 25% ($p(S) < 0.01$). This distribution suggests that in the majority of the buffet cycles the separated area remains relatively small compared to the clean configuration.

Knowing the extent of the separated area in each time step, the relative spectral content has been determined, as plotted in Fig. 8.12 (right) in the form of a pre-multiplied PSD. Both the configurations have a main contribution at 160 Hz, but the value is reduced by more than 50% in presence of the straight 2% UTEF; in good agreement with the spectral analysis of the shock position (again in terms of amplitude, see Fig. 8.7 left).

To further characterize the temporal behavior of the separated area, the autocorrelation of the separated area signal (S) is plotted in Fig. 8.13. For a time separation equal to one complete buffet cycle period ($\tau = 6.2$ ms), the autocorrelation value is 0.32 for the UTEF case (green line), while 0.58 for the clean configuration (blue line). This indicates that in presence of UTEF the oscillations of the separated area are not only of lower amplitude but also more irregular (i.e., less coherent), with the extent of the separated area varying significantly in different buffet cycles (as already pointed out for the shock position in Fig. 8.6 (right)). To check whether the relationship between the separated area extent and the shock wave position is influenced by the presence of the straight 2% UTEF, the cross-correlation between these two quantities is shown in Fig. 8.13 as well.

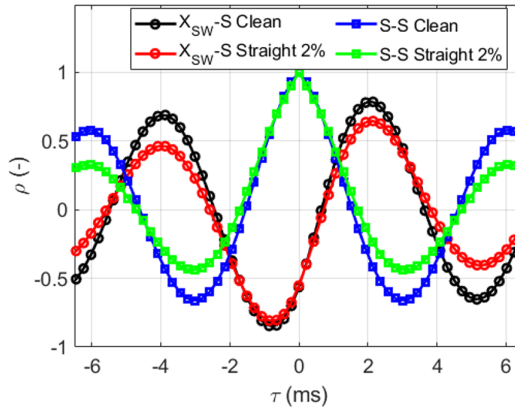


Figure 8.13: Autocorrelation in time of separated area extent and cross-correlation in time between shock wave position and separated area extent.

The correspondence between the two results (all the positive and negative peaks of the cross-correlation occur for the same values of τ) confirms that the physics of the phenomenon has not changed substantially. However, once again the correlation drops off with time separation more rapidly for the UTEF case, similar as for the shock-position autocorrelation. The main peak (in terms of absolute value) is obtained for $\tau = -0.65$ ms. This indicates that the widest separated area is obtained shortly before the most upstream shock position is reached. However, it is evident that the values of the different minimums and maximums of the cross-correlation are smaller in presence of UTEFs (red line). Hence, the dependence between shock wave and separated area is less defined in presence of UTEF than for the clean airfoil (black line).

Table 8.2: Separated area extent statistics

Configuration	S_{avg} (%)	S_{std} (%)
Clean	13	12
Straight 2% c UTEF	9	9
Serrated, wide UTEF 2% c valley	18	12
Serrated, wide UTEF 2% c peak	16	12

8.4.3. EFFECT OF SERRATED UTEF

As already observed in the schlieren images, strong 3D effects arise when mounting a serrated UTEF. To better understand these effects, the PIV results are analyzed for the $\lambda/h = 4$, $h = 2\%c$ serrated-UTEF configuration and compared to the straight 2% c and the clean configuration. For the serrated case the velocity field data is shown for two spanwise locations, the peak and the valley of the serration (see Fig. 8.2, right).

In Fig. 8.14 a comparison is shown of the average vertical velocity field (w) for the previously mentioned configurations. Since no important difference was present for the horizontal component of velocity, these results are omitted. For the vertical velocity field

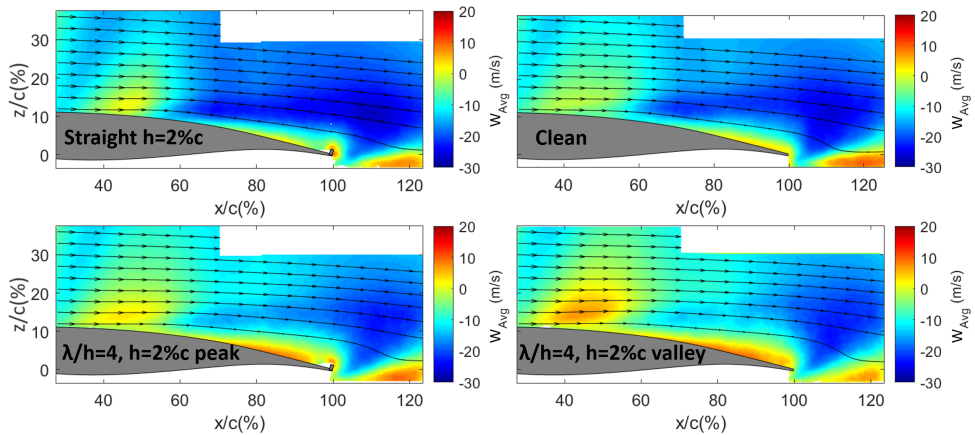


Figure 8.14: Comparison of the vertical averaged velocity field for clean, straight $h = 2\%$ and $\lambda/h = 4$, $h = 2\%$ in the peak and in the valley of serration.

corresponding to the peak of the serration (Fig. 8.14, bottom-left), a small reduction of velocity at the trailing edge is observed with respect to the data collected in the plane corresponding to the valley of the serration (Fig. 8.14, bottom-right). This difference is particularly evident in proximity of the serration ($95\% \leq x/c \leq 100\%$), where upwash is present. This evidence is in good agreement with the comparison between the straight $h = 2\%$ and the clean configuration, confirming the effect of the UTEF on the flow near the trailing edge.

As commented in the previous section (8.4.2), a reduction in the extent of the separated area is obtained for the straight UTEF compared to the clean configuration. For both the serrated configurations an increase of the separated area extent is observed with respect to both the clean and the straight 2% configurations. However for the serrated $\lambda/h = 4$, $h = 2\%$ UTEF a reduction of the separated area is obtained in the plane corresponding to the peak with respect to the plane corresponding to the valley. These qualitative observations are quantified by the data shown in Tab. 8.2 where the average values of S have been given for the different configurations. In particular, for the serrated configurations, the occurrence of shock-foot separated area appears to be less intermittent, with the separated area apparently extending from the shock foot till the trailing edge also in the mean flow field. When looking at the standard deviation of S , comparable values for the two planes of the $\lambda/h = 4$, $h = 2\%$ serrated-UTEF configuration (peak and valley of serration) are obtained, with significantly lower values achieved for the straight UTEF configuration. Thus, although there is an increase in the average extent of the separated area for the serrated configurations, the corresponding fluctuations are unchanged with respect to the clean configuration, in agreement with the unsteadiness of the shockwave position (see 8.7, right).

Comparing the velocity fields in Fig. 8.14, additional differences are present in the shock oscillation area, with a larger increase of the vertical velocity in the measurement plane corresponding to the valley of the serration (as compared to the peak location). As previously commented, in this measurement plane the separated area is on average

wider than for the measurement plane aligned with the peak, and therefore, the shock wave is more inclined (oblique), resulting in a higher increase of vertical velocity at the shock foot.

The results discussed in this subsection show that in presence of a serrated UTEF, the flow behaves differently according to the span location of the measurement plane. In particular, in the plane passing at the peak of the serration, the flow field is locally more similar to the flow field for the straight UTEF configuration, while in the valley it is more similar to the clean configuration. No strong difference is obtained in terms of the unsteadiness (shock oscillation and separated area pulsation). This suggests that the local presence of the peak or of the valley of the serration is influencing the flow distribution in the vicinity of the UTEF, but does not affect the overall buffet mechanism.

8.4.4. CIRCULATION EVALUATION

From the previous sections it is clear that the use of a straight UTEF has a positive effect by reducing the unsteadiness associated with fully developed transonic buffet. Nevertheless, it could be conceived that the application of a UTEF might induce a reduction in lift and by that could move the most developed buffet conditions to higher values of Ma and α . In order to investigate this possible effect, the PIV data have been further processed to get an estimation of the change in circulation (Γ) when introducing the UTEF. This has been done first for the average and later for the phase averaged velocity fields.

The circulation around the airfoil can be described as:

$$\Gamma = \Gamma_0 + \Gamma_1 \quad (8.1)$$

With Γ_1 being the contribution of the circulation computed in the PIV FOV (along the partial contour L_1 as indicated in Fig. 8.8) and Γ_0 the contribution on the remaining sector (L_0). In this analysis only the Γ_1 term is evaluated explicitly, while it is tentatively assumed that the value of Γ_0 is similar for the different configurations. This assumption is associated with the fact that no difference in the velocity field is expected to be present in the supersonic area upstream of the selected FOV (since disturbances cannot travel back from the subsonic trailing edge area to the supersonic area) or along the pressure side (in view of the upward vertical deflection of the trailing edge flap). In addition, in the approximation of a potential flow it can be derived that a change in the partial circulation Γ_1 is proportional to a change in the total circulation Γ ($d\Gamma_1 = c_1 \cdot d\Gamma$, where c_1 is a constant depending on the specific choice of L_1 , while $d\Gamma$ the result of a change in the angle of attack, or a local modification of the TE geometry).

Although the relation between lift and circulation (Kutta-Joukovsky) is in general valid only for potential incompressible flow, the concept of circulation as proxy for the lift also under the current compressible flow conditions is used with the particular objective to assess if the measured flow fields allow to infer whether the UTEF affects circulation, hence, the (mean) lift value. This choice is substantiated by the study of Liu et al. (2015), which shows that in the low transonic Mach numbers regime (as in this thesis) the classical lift equation derived by Joukovsky can be applied to evaluate the lift coefficient obtaining a good estimation of the lift coefficient also for a circulation contour passing in proximity of the trailing edge of the airfoil.

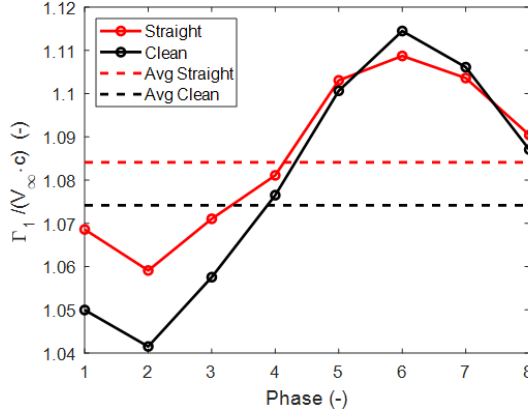


Figure 8.15: Circulation value ($\Gamma_1/(V_\infty \cdot c)$) per buffet phase.

Γ_1 has been evaluated sufficiently far from the surface of the airfoil and from the trailing edge (see Fig. 8.8), and results in a value of $\Gamma_1/(V_\infty \cdot c) = 1.08$ for the straight 2% UTEF and 1.07 for the clean configuration. This estimation shows that the use of a UTEF does not significantly reduce the value of the circulation and therefore of the lift, with the value of the latter being actually slightly increased (although this difference is of the same order of the uncertainty in the evaluation of the circulation). As similar values of Γ_1 are found along L_1 , with and without UTEF, this justifies the assumption of considering Γ_0 constant and thus, gives a reasonable argument to conclude that also the total circulation Γ is not appreciably changed by the UTEF under the current conditions. This observation brings to the conclusion that the use of a UTEF is expected to mitigate buffet, not affecting the operative flight condition (same Ma and approximately same lift coefficient).

8

Table 8.3: Circulation

Configuration	Clean	Straight 2%c
$\Gamma_1/(V_\infty \cdot c)$ ($Ma = 0.70, \alpha = 3.5^\circ$)	1.07	1.08
$\Gamma_1/(V_\infty \cdot c)$ ($Ma = 0.74, \alpha = 2.5^\circ$)	1.04	1.08

In addition, this analysis has been repeated for the phase averaged velocity fields, for both the clean and the straight UTEF configurations and the results plotted in Fig. 8.15. The plot shows that the values of circulation are distributed almost sinusoidally along the different buffet phases. In presence of UTEFs not only does the average value of $\Gamma_1/(V_\infty \cdot c)$ slightly increase (by about 1%) but also the amplitude of oscillation of $\Gamma_1/(V_\infty \cdot c)$ during the buffet cycle is reduced by nearly 50% when compared to the clean airfoil. Under the assumption that the variation of Γ_0 with phase is the same for both configurations, this result further suggests that in presence of UTEFs, the oscillation of the aerodynamic loads is diminished as well.

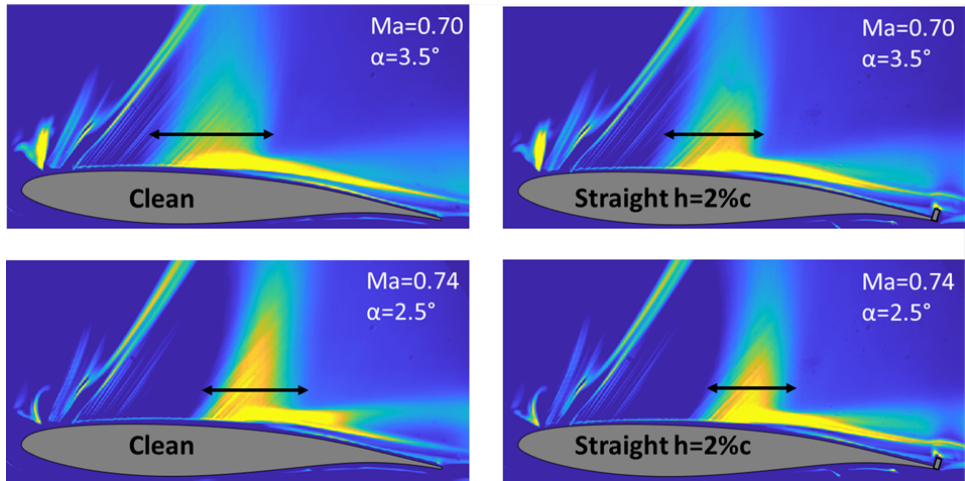


Figure 8.16: Standard deviation of schlieren images for $Ma = 0.7$, $\alpha = 3.5^\circ$ and $Ma = 0.74$, $\alpha = 2.5^\circ$. The arrows indicate the shockwave oscillation ranges.

8.5. SENSITIVITY OF UTEF OPERATION TO THE FLOW CONDITION

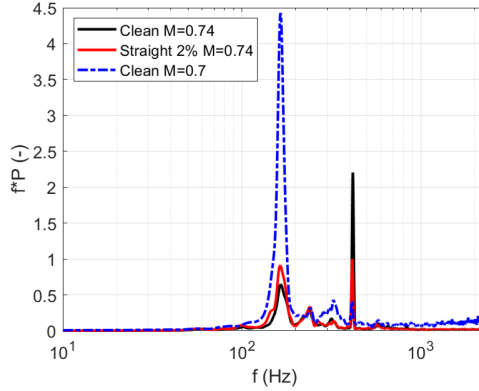
To show the sensitivity of the UTEF to the specific flow condition, the behavior of both the clean and the straight UTEF 2% configuration is investigated for an additional flow condition: $Ma = 0.74$ and $\alpha = 2.5^\circ$ (a condition where buffet is less developed). In order to provide a comparison of the relevance of the shock oscillations for both the flow conditions and configurations, the standard deviation of the intensity of luminosity of the schlieren images is shown in Fig. 8.16. The first thing that stands out in the plots is the reduced spatial range of the shock wave oscillation at $Ma = 0.74$, $\alpha = 2.5^\circ$ compared to $Ma = 0.7$, $\alpha = 3.5^\circ$, for both the UTEF and the clean cases. In addition, the average shock wave position is located more downstream for $Ma = 0.74$ and $\alpha = 2.5^\circ$, as expected. This data is summarized in Tab. 8.4, which confirms that the fluctuations of the shock wave position are reduced for $Ma = 0.74$, $\alpha = 2.5^\circ$.

When comparing the clean configuration with the 2% UTEF for $Ma = 0.74$, $\alpha = 2.5^\circ$ (Fig. 8.16, bottom), the range of oscillation appears very similar with a slight reduction of the shock wave oscillation area in presence of the UTEF. An upwash is again visible at the trailing edge when the UTEF is used, together with higher fluctuations in the shear layer. These observations suggest that the UTEF has still a beneficial effect in reducing the separated region extent. An evaluation of the Γ_1 term of the circulation from the PIV data shows that, also for this flow condition, there is a slight increase of circulation in presence of UTEF (as reported in Tab. 8.3).

The spectral content of the shock position is once again evaluated by means of a PSD (see Fig. 8.17) and the values compared to the PSD of the clean configuration at $Ma = 0.7$, $\alpha = 3.5^\circ$ (dashed line). There is a sharp reduction of the peak at the main buffet frequency of 160 Hz, when moving to the off-buffet condition, both for the UTEF

Table 8.4: Shock position statistics

Configuration	$(X_{SW})_{avg}$ (%c)	$(X_{SW})_{std}$ (%c)
Clean $Ma = 0.7$, $\alpha = 3.5^\circ$	40	7
Clean $Ma = 0.74$, $\alpha = 2.5^\circ$	48	4
Straight 2%c $Ma = 0.7$, $\alpha = 3.5^\circ$	41	5
Straight 2%c $Ma = 0.74$, $\alpha = 2.5^\circ$	50	4

Figure 8.17: PSD of shock wave position for $Ma = 0.74$, $\alpha = 2.5^\circ$ for clean and straight 2% configurations.

and the clean case. With the increase of the Mach number, an increase of the peak at 410 Hz is observable (although this peak is reduced by more than 50% in presence of the straight UTEF). As previously mentioned this peak is associated with wind tunnel noise, which becomes more important at a higher Mach number. A similar contribution of the buffet peak (at 160 Hz) is observed for the two configurations tested at $Ma = 0.74$ (slightly lower for the clean configuration), in agreement with the values of $(X_{SW})_{std}$ (see Tab. 8.4). These results show that buffet unsteadiness is not increased for this secondary flow condition, however, to experimentally exclude that the use of a UTEF simply shifts the occurrence of the most developed buffet condition, additional tests at other values of Ma and α are required.

8.6. CONCLUSION

In this chapter, the use of trailing edge flaps with an upward deflection (UTEFs), demonstrated to be effective in controlling transonic buffet, in particular when using a straight 2%c UTEF.

The results show that buffet is not completely suppressed, but significantly reduced in intensity. Both the shock wave and separated area are characterized by a reduced amplitude of oscillation in the UTEF case, although always with a main frequency contribution at 160 Hz (see Figs. 8.7 and 8.12). In addition to the reduced pulsation of the separated area in presence of a straight UTEF, the separated area is also characterized

by a reduction of its extent (see Tab. 8.2), having important consequence in alleviating shock buffet. Although an estimation of the drag coefficient was out of the scope of this work, using as a proxy the size of the separated area, it is speculated that for the straight UTEF configuration, the drag coefficient would be reduced as well.

The behavior of the shock wave position appears more irregular in presence of the straight $2\%c$ UTEF configuration compared to the smoother behavior for the clean airfoil (see Fig. 8.5) and a similar behavior is present for the separated area. These results confirm that with the use of the UTEF the coherence of the buffet oscillation can be considered to be interrupted, as also shown in Fig. 8.13, where the correlation between the shock wave position and the separated area extent weakens for the straight UTEF compared to the clean airfoil.

The analysis of the data for the serrated UTEFs has assisted the understanding of the performance of the straight UTEFs. As shown in Section. 8.4.3 the presence of a serrated UTEF has a non-negligible effect on the mean flow, with a different behavior in the planes corresponding to the peak or the valley of the serration. Nonetheless, no significant variation is observed in terms of the overall transonic buffet properties, confirming the inefficacy of a serration in compressible flows, in agreement with Nies and Oliver [Nies and Olivier \(2013\)](#).

When straight UTEFs are used, the direct communication between the suction side of the airfoil and the trailing edge is inhibited. As a consequence fewer (or weaker) UTWs are generated resulting in a reduction of the shock oscillation range. The hesitation of the shock position could be associated with the fact that the UTWs are still reaching the shock wave but in a more intermittent fashion (at least in strength). On the other hand, when a serrated UTEF is used, the communication between the vortical structures in the separated area (DTWs) and the trailing edge itself remains present, particularly in correspondence to the valley of the serration. Since the UTWs are pressure waves that travel upstream in a quasi-hemispherical way, the UTWs created in the valley area of a serration do not only communicate with the shock wave at that specific span location, but along a spanwise extended area. This suggests that the UTEFs are effective in reducing buffet properties only when the connection between the separated area and the trailing edge is inhibited along the full span, as in the case for a straight UTEF. The possible effect of the straight UTEFs on the production of the UTWs at the trailing edge, and the consequent reduction of the shock wave oscillations, supports the feedback mechanism description of transonic buffet.

The performance of UTEFs of different heights has shown that a relevant reduction of the shock oscillation properties is obtained only when the height of the UTEF is equal or higher $h = 1.5\%c$, as is clear from the results shown in Fig. 8.7 (right). This evidence suggests that the vortices which are responsible for the production of UTWs are traveling downstream very close to the surface of the airfoil in agreement with what has been proposed in Chapter 5.

The use of UTEFs clearly modifies the geometry of the airfoil, so it could be conceived that the observed buffet reduction is the result of a change of the airfoil operating condition, which shifts the most developed buffet condition to higher Mach numbers or angles of attack, because of a possible change in circulation around the airfoil. However, estimates obtained from the PIV data showed that the average circulation value is not

affected appreciably by the introduction of UTEFs while its oscillation range is reduced by nearly 50%. These results confirm findings obtained in the numerical study of [Tian et al. \(2018\)](#), where an increase of the buffet onset for both the angle of attack and the lift coefficient was achieved when using similar devices. The performance of the UTEF has also been checked for a less developed buffet condition, corresponding to a Mach number of 0.74 and $\alpha = 2.5^\circ$. The results showed that even under this condition the use of a straight 2%*c* UTEF proved beneficial, achieving a slight reduction of the shock buffet oscillation range (see Fig.8.16) with respect to the clean configuration and a slight increase of the circulation value. Thus, differently from other passive systems used for the control of transonic buffet, UTEFs demonstrated to be more versatile in reducing the unsteadiness connected with buffet and their efficacy proved not to be strongly dependent on the specific buffet condition, since their working principle is associated with the disruption of the communication between DTWs and UTWs in the feedback cycle rather than of a change (reduction) of the circulation, as opposed to the working mechanism of more conventional TEDs.

9

SHOCK CONTROL BUMPS

This chapter investigates the use of shock control bumps (SCBs) for controlling transonic buffet. Three-dimensional SCBs have been applied on the suction side of the OAT15A supercritical airfoil for fully developed buffet conditions ($Ma=0.7$, $\alpha = 3.5^\circ$ and $Re = 2.6 \cdot 10^6$). The effectiveness of the SCBs for different spanwise spacings (ranging from 20% to 30% c) was verified using schlieren visualization and particle image velocimetry (PIV). Both techniques showed the possibility of controlling buffet using such devices, resulting in a reduction of the unsteadiness present in the flow, both in terms of shock oscillation and pulsation of the separated area. A dedicated PIV investigation in a spanwise-chordwise measurement plane was then conducted in order to understand the effect of the spatial distribution of the bumps, focusing on the interaction of the shockwave structures along the span. The configuration with a spacing of $\Delta y_{SCB} = 25\%c$ demonstrated to be the most efficient in reducing the transonic buffet oscillations and was also able to reduce the reverse flow region when compared to the clean configuration. A loads determination algorithm based on PIV data, has shown a reduction of drag and an increase of lift in presence of SCBs with respect to the clean configuration.

9.1. INTRODUCTION

The usefulness of 3D SCBs for controlling transonic buffet on an airfoil is not univocal [Bogdanski et al. \(2014\)](#) and depends on the SCB size and position, as shown by the numerical study of [Geoghegan et al. \(2020\)](#). Hence, to achieve an efficient control system the location of SCBs on the airfoil should be selected carefully, with the necessity of having the quasi-normal shockwave on the crest of the bump in on-design conditions. In this way no re-expansion or second shockwave would occur, as described by [Bruce and Babinsky \(2012\)](#). The use of 3D SCBs also cause a curvature of the oblique shockwave around the bump, a phenomenon that was described by [Ogawa et al. \(2008\)](#). When a spanwise array of bumps is used, overlapping shock structures appear, with the effectiveness of this interaction highly dependent on the relative spacing between the bumps.

Parts of this chapter have been published in [D'Aguanno et al. \(2022c\)](#).

The aim of this chapter is to achieve a deeper understanding of the influence and effectiveness of 3D SCBs on transonic buffet, and to reach this goal an experimental study was carried out, employing two complementary optical diagnostic techniques. Schlieren visualizations are used to provide a qualitative description of the shock dynamics, whereas a more detailed quantification of the velocity field is achieved with particle image velocimetry (PIV). Particular attention is also given to characterize the effect of the bump spacing, for which a detailed PIV study on a plane parallel to the suction side of the airfoil is performed, for different spacing between the bumps. To the best of the authors' knowledge, no detailed study on the bump spacing has been previously reported, except for the study of [Konig et al. \(2009\)](#) for a swept wing (where the optimal spacing is mainly influenced by the value of the sweep angle). Therefore, this aspect has also been addressed in this chapter with a detailed PIV study on a plane parallel to the suction side of the airfoil for different spacing between the bumps.

The employment of SCBs clearly changes the geometry of the airfoil, therefore a determination of the aerodynamic loads is of utmost importance and has been carried out in this Chapter.

9.2. EXPERIMENTAL INVESTIGATION

9.2.1. MODELS

For this investigation, both the "horizontal" and the "vertical" airfoil models have been used, for more details see Section 3.4. To eliminate any additional tip vortex effects, two side plates (fences, see Fig.3.7) were mounted in correspondence of the two extremities of the "vertical" airfoil (see Fig.9.1, right). All the tests have been performed for $Ma = 0.7$ and $\alpha = 3.5^\circ$ and $Re_c = 2.6 \cdot 10^6$, conditions for which buffet is fully developed, as discussed in Chapter 5.

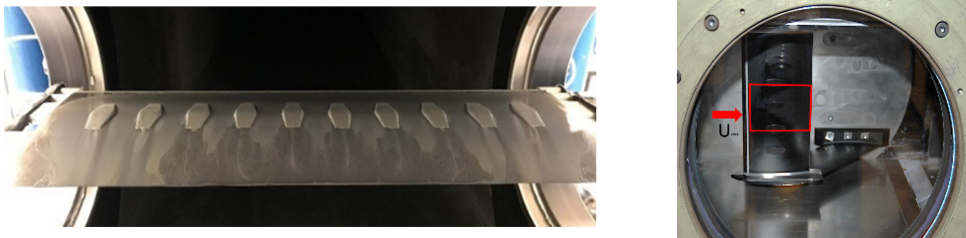


Figure 9.1: SCBs (spacing 25%) mounted on the "horizontal" OAT15A airfoil with oil flow visualization ($Ma = 0.7$, $\alpha = 3.5^\circ$) on the left and "vertical" airfoil mounted in the wind tunnel with relative FOV (right).

9.2.2. SHOCK CONTROL BUMP GEOMETRY

The SCBs used in this investigation have been produced with a 3D printer in plastic material (PLA) with an accuracy of $20 \mu\text{m}$. The use of SCBs in SWBLI in literature is widespread, but nevertheless, there is not much information regarding their geometrical design and location. Designing a new geometry of SCB is out of the scope of this

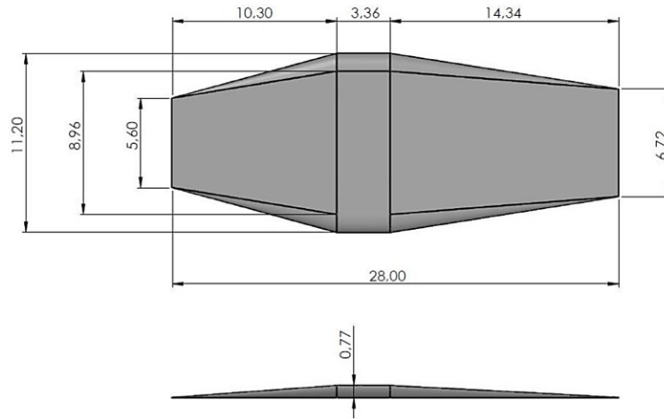


Figure 9.2: Geometry of a shock control bump with dimensions in mm.

investigation. Therefore, the SCB design was based on the SCB geometries present in other studies in literature (Colliss et al. (2016) and Mayer et al. (2018)).

The geometry and dimensions of the realized SCB are shown in Fig.9.2, with an overall length of 28 mm and a maximum height of 0.9 mm. The height of the bumps (including the double sided adhesive tape with which the bumps are attached to the airfoil) has been selected equal to the local height of the boundary layer, which was evaluated for an equivalent flat plate. The crest of the bump has been centered at the average shock location for the clean airfoil for the most developed buffet conditions ($Ma=0.7$ and $\alpha = 3.5^\circ$), which corresponds to 45% of the chord. This SCB location was suggested by Ogawa et al. (2008) to avoid the occurrence of pressure losses due to additional secondary shockwave structures. It is expected that for this buffet condition the oscillating shockwave will acquire the familiar λ structure, stabilizing the shock oscillation.

The spanwise spacing between the bumps is a crucial parameter, as it determines if the interaction among the different shockwave structures in correspondence of the bumps will be detrimental or beneficial. Since there is no evidence in literature of a systematic study of this parameter, range of spacings (Δy_{SCB}) have been tested, namely: 20, 22.5, 25, 27.5, 30% c (selected in the range of values reported in other publications, see for example Ogawa et al. (2008) and Mayer et al. (2018)). Figure 9.1 (left) shows the oil flow visualization on the OAT15A airfoil model with bumps after a run at $Ma = 0.7$ and $\alpha = 3.5^\circ$ for a spacing between the bumps of 25 mm ($\Delta y_{SCB} = 25\% c$).

9.2.3. EXPERIMENTAL SET-UP

In this Chapter, with high speed schlieren (which set-up is described in Section 3.6.2) the different spacings between the bumps were analyzed for the “horizontal” model. Subsequently, a quantitative study of the velocity field was performed with PIV and in this case three different experiments were performed.

In the first experiment high speed PIV was carried out for the “horizontal” airfoil us-

Table 9.1: Model parameters

Parameter	Symbol	Value	Unit
Chord	c	0.1	m
Span ("horizontal model")	b_1	0.28	m
Span ("vertical model")	b_2	0.20	m
Angle of attack	α	3.50 ± 0.05	$^\circ$
Reynolds number based on chord	Re_c	$(2.62 \pm 0.01) \cdot 10^6$	

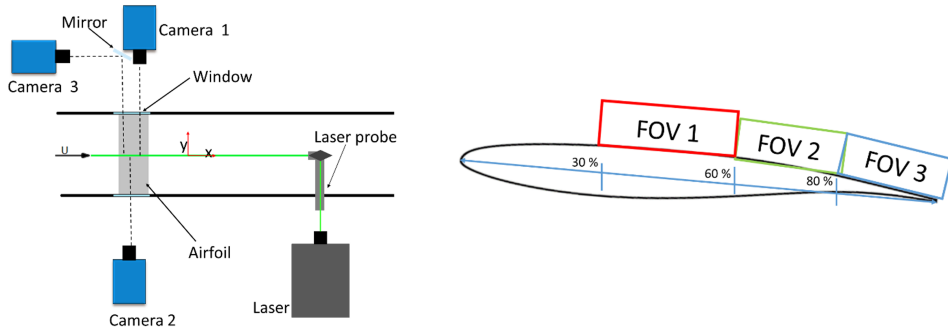


Figure 9.3: First PIV configuration: PIV set-up (left) and sketch of airfoil with FOVs used (right).

ing three high speed cameras (three Photron Fastcam SA1.1). All these measurements were performed in the chordwise-vertical plane at mid-span, in correspondence of the central bump. An acquisition frequency of 15 kHz was selected in order to temporally resolve the shock position, the vortex shedding and the propagation of upstream traveling pressure waves. To achieve this acquisition frequency, the sensor of each camera (operating in double pulse mode with a time separation $dt=3\mu s$) was cropped to a resolution of 576×320 pixels. Despite this, a good spatial resolution was still achieved by simultaneously using three cameras in planar mode. Each camera was fitted with a 180 mm lens with an f-stop of 4. To insert the three cameras and lenses in a relatively narrow area, a mirror was used, as shown in the sketch of the set-up in Fig.9.3 (left). As a result, the first FOV was extending from 28% c to 61% c (thus including the entire range of the shockwave oscillation), FOV_2 from 59% c to 81% c and FOV_3 from 79% c to 101% c (a sketch of the different FOVs is given in Fig.9.3, right). The vertical extent (along z) of the FOVs is of roughly 17% c for FOV_1 and 12% c for the other two FOVs.

In order to appreciate the spanwise distribution of the shockwave a further PIV experiment was completed in a spanwise-chordwise oriented plane using the "vertical" model configuration, which allows a direct access from the side window towards the suction side of the airfoil (Fig.9.4, left). One high speed camera (again a Photron Fastcam SA1.1) in planar configuration has been used, with a selected frequency of acquisition of 4.65 kHz (camera sensor cropped to 1024×640 pixels) and fitted with a 105mm lens with f-stop of 8. These settings resulted in a FOV extending from 15% c to the trailing edge along the streamwise direction and from -26% c to 26% c in the spanwise direction with respect to the model centerline. Similarly to the previous experiment, the camera was

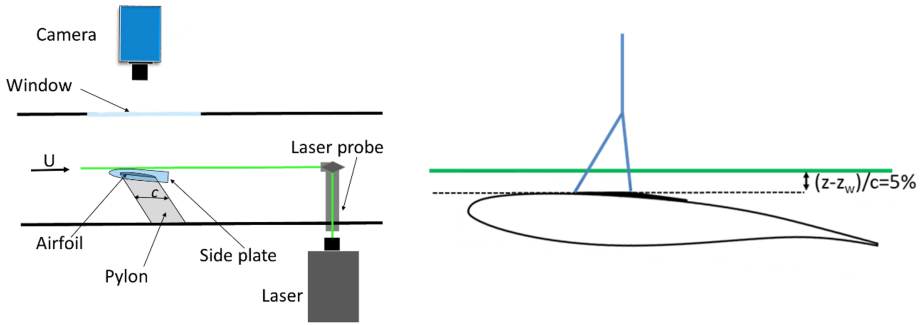


Figure 9.4: Second PIV configuration: Top view of PIV set-up (left) and sketch of the airfoil with the plane of measurement in green and indicative λ -shock structure in blue (right).

operated in double pulse mode with $dt=3\mu s$. As illustrated in Fig.9.4 (right), the plane of measurement is located at a vertical distance of $z - z_w(x_{thick})=0.5$ cm from the thickest point of the airfoil ($z_w(x_{thick})$).

For both the PIV measurements, a dual cavity high speed laser (Nd:YAG) and additional optics were used to create a laser sheet of 1.5 mm of thickness which illuminates the DEHS seeding particles ($\tau_{DEHS} = 2\mu s$). The synchronization between the cameras and the laser was achieved through a synchronization box (LaVision High Speed Controller, art. 1108075).

To evaluate the aerodynamic loads, velocity data around the full airfoil are needed and for this purpose an additional PIV experiment is needed. In this case, experiments have been carried out on the "horizontal" model using a low speed acquisition system. This system was preferred in view of the higher spatial resolution which can be achieved (with respect to the high speed cameras used in the other experiments). A LaVision sC-MOS 5MP camera (Resolution 2560×2160 pixels) was operated in planar mode and fitted with a 105 mm lens with an f-stop of 8. The resulting FOV extends around the entire airfoil (see Fig.9.5) in a streamwise-vertical oriented FOV. To obtain velocity vectors around the entire airfoil (suction and pressure sides), two consecutive runs were conducted for each test case, with the airfoil being flipped upside down in the second run. In Fig.9.5 FOV_1 refers to the first run and FOV_2 to the second. In such a way, the velocity data are retrieved around the entire airfoil (apart from a small region at the leading edge, in view of the shadow created by the airfoil itself), with the FOV extending from roughly 20% of the chord upstream of the airfoil up to 20% downstream of the trailing edge and vertically from $z/c=-60\%c$ to $z/c=60\%c$.

The flow field for the clean configuration can be considered 2D, thus the loads evaluated on a particular measurement plane are representative of the loads on the entire model, however, this is not the case for the shock control bump configuration. To account for the spanwise variation of the loads, the PIV measurements have been repeated at three different spanwise measurements planes (see 9.6):

- in correspondence of the centerline of the central bump ($y/c = 0$);
- for $y/c = \Delta y_{SCB}/4$;

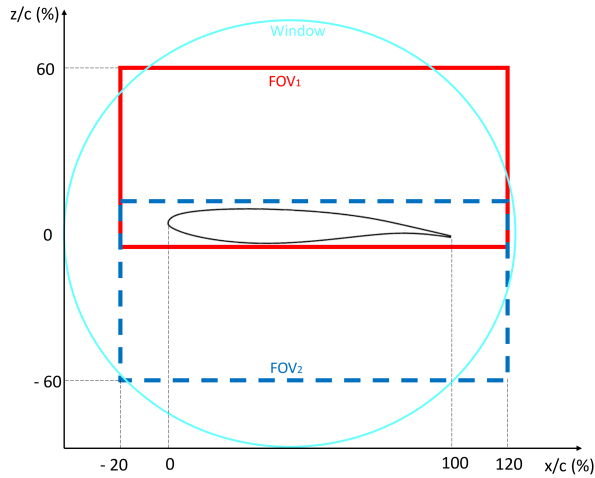


Figure 9.5: FOV on the suction (FOV_1) and on the pressure side (FOV_2) of the airfoil for third PIV configuration.

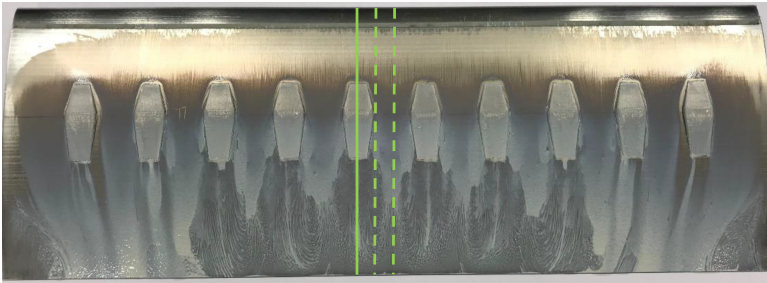


Figure 9.6: Oil flow visualization for $\Delta y_{SCB} = 25\% c$. The three measurement PIV planes are indicated with the green solid and dashed lines.

- for $y/c = \Delta y_{SCB}/2$ (at half distance between two consecutive bumps).

9

For each test case 700 images have been taken, acquired in 2 runs of 350 images each (23.6 s of acquisition) The measurements planes were illuminated by a Quantel Evergreen 200 dual cavity laser, with an acquisition frequency of 15 Hz and, once again, with a pulse separation $dt=3\mu s$.

9.2.4. PROCESSING PARAMETERS

For the PIV image processing, first a Butterworth filter was applied to reduce the laser reflections on the airfoil and on the SCBs (using a filter length of seven images [Sciacchitano and Scarano \(2014\)](#)), later the cross-correlation was computed with a multi-pass approach.

For the first PIV configuration, one pass with a window size of $64 \text{ px} \times 64 \text{ px}$ ($2.5 \text{ mm} \times 2.5 \text{ mm}$) and three passes with a final window size of $48 \text{ px} \times 48 \text{ px}$ ($1.9 \text{ mm} \times 1.9 \text{ mm}$) were adopted, in both cases with an overlap of 75% of the window size. On the other

hand, for the second PIV configuration, one pass with a window size of 48 px × 48 px (4.0 mm × 4.0 mm) and three passes with a final window size of 32 px × 32 px (2.7 mm × 2.7 mm) were selected, again with an overlap of 75%. Correspondingly, the resulting spacing between the vectors is 0.47% c (0.47 mm) for the first PIV configuration, and 0.67% c (0.67 mm) for the second. For the third PIV configuration one pass with a window size of 64 px × 64 px (2.5mm × 2.5mm) and an overlap of 50% and then two passes with a final window size of 32 px × 32 px (1.9 mm × 1.9 mm) and an overlap of 75% were chosen. The main PIV processing settings are also summarized in Table 9.2.

Table 9.2: PIV parameters and uncertainties.

Parameter	1 st PIV config.	2 nd PIV config.	3 rd PIV config.
Model orientation	horizontal	vertical	horizontal
Acquisition frequency	15 KHz	4.65 KHz	15 Hz
Pulse separation	3 μs	3 μs	3 μs
Number of images	15000	4365	700
Final image resolution	1600×320 pix	1024×640 pix	2560×2160 pix
Final window size	48×48 pix	32×32 pix	32×32 pix
Window overlap	75%	75%	75%
Vector spacing	0.47%c	0.67% c	0.44% c
Cross-correlation unc.	< 4 m/s	< 10 m/s	< 15 m/s
Particle slip	40 – 60 m/s	40 – 60 m/s	40 – 60 m/s

9.2.5. UNCERTAINTY ANALYSIS

An uncertainty analysis is carried out to verify whether the differences in performance of the SCBs observed in the measurements can be considered (statistically) significant. The most important experimental uncertainty sources are briefly discussed below, and the corresponding values are reported in Table 9.2. It is worth mentioning that for the three PIV configurations, different values of uncertainty are obtained. For example the cross-correlation uncertainty is higher for the PIV data obtained for the vertical model and in the third configuration, since in these cases a lower magnification (M) is present.

As mentioned in Section 3.9 the particle slip effect is particularly important in correspondence of shockwave structures, reaching theoretical values of uncertainty of 60 m/s for the clean configuration and 40 m/s for the SCB configurations. The reduction of this uncertainty for the SCB configuration is associated with the presence of two jumps in velocity across each of the SW structures, instead of the single more intense jump observed for the clean configuration. Notwithstanding the high values of uncertainty across the shockwaves, the particle slip effect is completely negligible in the remaining FOV.

Regarding the schlieren measurements, the major source of uncertainty is once again associated with the tracking of the shockwave position, for which half of the apparent width of the normal shockwave can be used as an indicator as commented in Section 3.9 (< 3 mm).

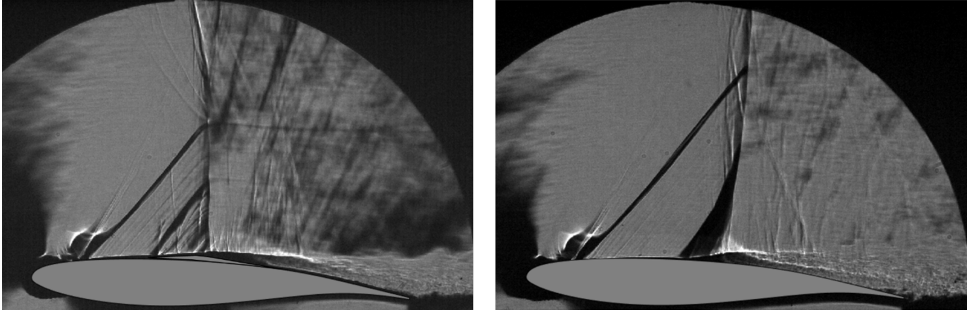


Figure 9.7: Example of a schlieren image of the OAT15A at $Ma = 0.7$, $\alpha = 3.5^\circ$ with bumps (left) and without (right).

9.3. SHOCK DYNAMICS

In Fig.9.7 instantaneous schlieren images are shown for both the clean airfoil (right) and the SCB configuration with a spanwise spacing of $25\%c$ (left). In addition to the Mach line caused by the transition trip (at 7% of the chord) a second oblique line appears at the leading edge of the bumps. This line consists in a oblique shockwave which is then followed by a quasi-normal shockwave (forming a λ -shock structure). Inside the λ shockwave additional “thinner” oblique lines, associated with 3D structures integrated along the span of the model, are observable. In correspondence of the interactions of the quasi-normal shockwave with the Mach line and the oblique SW, two slip lines are observed. For the clean airfoil (Fig.9.7, right) as already pointed out in Chapter 5 a single shockwave structure is present. Both schlieren images correspond to the phase in the buffet cycle in which the shockwave travel upstream, when a wide separated area develops, extending from the shock foot downstream (as exhaustively described in Chapter 5). As a result, for the clean configuration the shockwave appears slightly inclined.

For comparison, in Fig.9.8 instantaneous PIV images belonging to the same configurations are shown in the chordwise-vertical plane (capturing approximately the same phase as the schlieren images of Fig.9.7, so during the upstream travel of the shockwave). For the clean configuration a single moving oblique shockwave is observed at $35\%c$. Differently, for the controlled configuration (as already commented for the schlieren images) there is both a steady oblique shockwave in correspondence to the leading edge of the bumps and a secondary unsteady shockwave close to $x \approx 45\%c$. The velocity fields confirm the qualitative schlieren information of the presence of a wide separated area (approximated by the blue region in the colormap) developing from the shock foot. It is worth clarifying that these PIV data have been acquired in the symmetry plane of the airfoil, which coincides with the symmetry line of the central bump for the SCB configurations. Differently, the schlieren data integrate all the density gradients present along the line of sight.

From the schlieren recordings, the shock position has been tracked in time by evaluating the minimum luminosity intensity in each image. In Fig.9.9 (left) the probability density function $p(X_{SW}/c)$ for the shock position is shown for both the clean, as well as for the SCB configurations with different spacings. The result clearly illustrates that with

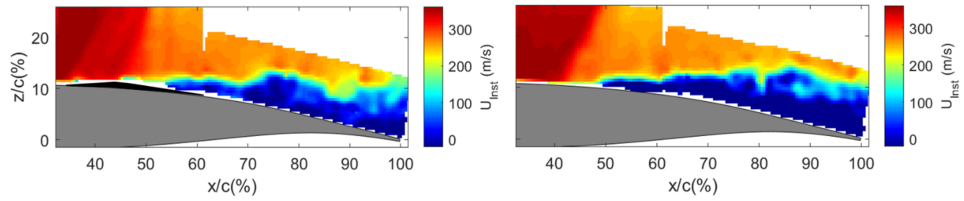


Figure 9.8: Example of a PIV image of the OAT15A at $Ma = 0.7$, $\alpha = 3.5^\circ$ with bumps (left) and without (right).

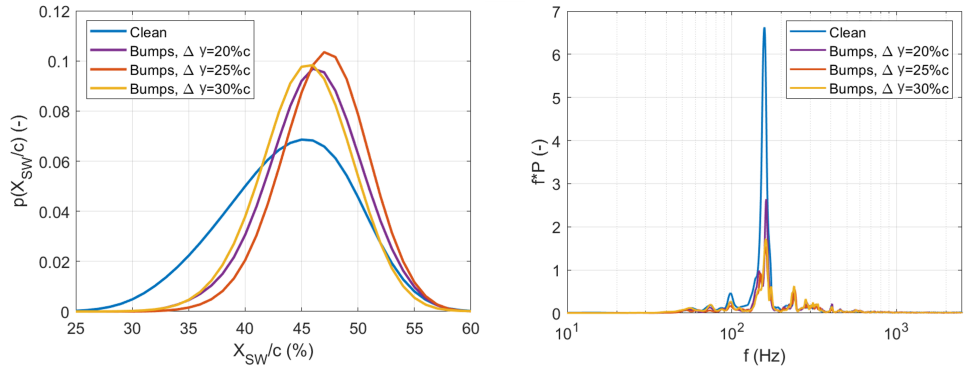


Figure 9.9: Distribution (left) and spectrum (right) associated with shock position for configurations with and without SCBs.

any SCB configuration, a reduction of the oscillation range of the SW is obtained. Furthermore, the average shock position is slightly shifted towards more downstream positions. The best performance in terms of shockwave oscillation reduction is obtained for a bump spacing of $25\%c$ while good performance is also achieved for the $\Delta y_{SCB} = 27.5\%c$ and $\Delta y_{SCB} = 30\%c$ spacings. These observations are confirmed by the average values of the shock position (X_{SW}) and the relative standard deviation ($\sigma(X_{SW})$) reported in Table 9.3. The figures clarify that for $\Delta y_{SCB} = 25\%c$, the weakest fluctuations of the shockwave, but also the most downstream average shock position occur.

The spectral content of the shock position signal is computed in the form of a power spectral density $P(f)$ by using the Welch method and plotted in Fig.9.9 (right) (as a pre-multiplied spectrum $f \cdot P$ for the clean configuration and for the airfoil in presence of bumps, with spacings of $20\%c$, $25\%c$ and $30\%c$). The image reveals that the buffet characteristic frequency is not affected by the use of SCBs, with all the configurations having a main peak at 160 Hz. All the SCB configurations achieve a relevant reduction of the main peak of $f \cdot P$, although the best performance is obtained for $\Delta y_{SCB} = 25\%c$. The values of $f \cdot P$ at 160 Hz are summarized in Table 9.3 for all the tested configurations.

By computing the maximum of the gradient of velocity for the PIV images, the shock position has been tracked for the velocity data as well. The corresponding power spectral density (Fig.9.10), confirms the result shown in Fig.9.9 (right), with a reduction of more than 50% of the main peak at 160 Hz when the SCBs are used. Similar results are obtained for both $\Delta y_{SCB} = 25\%c$ and $\Delta y_{SCB} = 30\%c$, although with a slight improvement with the

Table 9.3: Comparison of shock position properties for different SCB spacings from schlieren data.

	$\bar{X}_{SW}(\%c)$	$\sigma(X_{SW})(\%c)$	$f \cdot P(f = 160\text{Hz})(-)$
Clean configuration	43.8	5.3	6.6
$\Delta y_{SCB} = 20.0\%c$	46.1	3.7	2.7
$\Delta y_{SCB} = 22.5\%c$	45.5	3.9	3.0
$\Delta y_{SCB} = 25.0\%c$	47.0	3.3	1.5
$\Delta y_{SCB} = 27.5\%c$	45.9	3.4	2.0
$\Delta y_{SCB} = 30.0\%c$	45.4	3.6	1.7

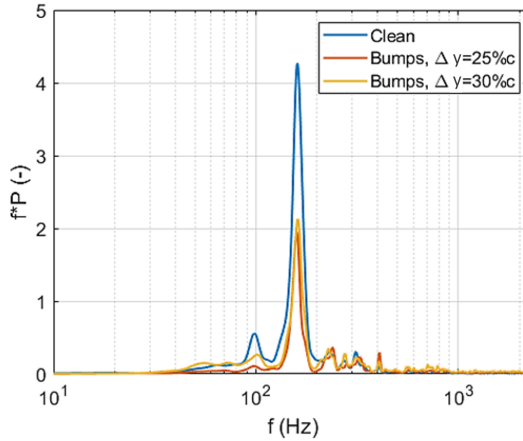


Figure 9.10: Spectral analysis of PIV shock position for different configurations.

former. Therefore, the results are considered to be in good agreement with the schlieren data.

9.4. FLOW FIELD ANALYSIS

9.4.1. BUFFET CYCLE DYNAMICS

In order to gain further insight on the effect of 3D SCBs on the buffet cycle, PIV instantaneous images are shown for the $\Delta y_{SCB} = 25\%c$ configuration in Figs.9.11 and 9.12 for two particular stages of the buffet cycle, corresponding to the most upstream and the most downstream position of the shock oscillation, respectively. Both flow fields show the presence of a separated area, whose extent is significantly smaller than the region present in Fig. 9.8 (left). Similar as for the clean airfoil (Chapter 5), also in presence of SCBs the variation of the separated area through the buffet cycle is such, that it reaches its maximum extent during the upstream travel of the SW (see Fig. 9.8) and its lowest extent during its downstream travel (not explicitly shown here).

The snapshot in Fig.9.11 (left) shows the velocity field in the most upstream position with the moving shockwave located slightly upstream (41%*c*) of the crest of the SCB. Fig.9.11 (right) visualizes the corresponding instantaneous spanwise organization of the velocity field. Note that this snapshot was not acquired simultaneously with the one in

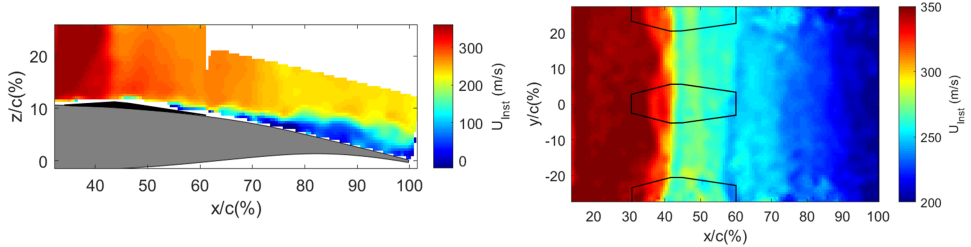


Figure 9.11: Uncorrelated instantaneous horizontal velocity fields in presence of SCBs ($\Delta y_{SCB} = 25\%c$) with the SW in its most upstream position. On the left the velocity field is shown in the chordwise-vertical plane, while on the right another snapshot is displayed in the chordwise-spanwise plane together with the outline of the bumps.

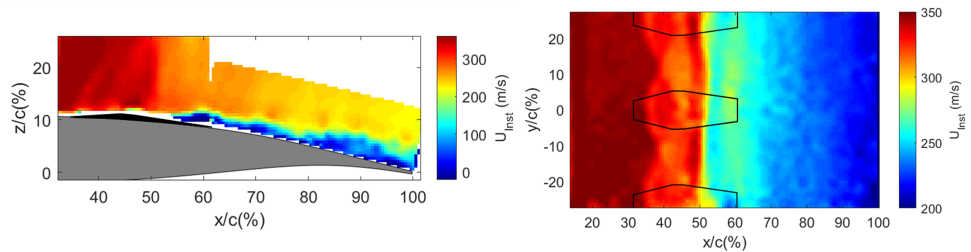


Figure 9.12: Uncorrelated instantaneous horizontal velocity fields in presence of SCBs ($\Delta y_{SCB} = 25\%c$) with the SW in its most downstream position. On the left the velocity field is shown in the chordwise-vertical plane, while on the right another snapshot is displayed in the chordwise-spanwise plane together with the outline of the bumps.

Fig.9.11 (left), using the data on the vertical airfoil, yet it has been selected to correspond to the same phase in the buffet cycle. This visualization clarifies that the oblique shockwaves which originate at the leading edge of the SCBs curve around the bumps, with the SW structures eventually interacting with each other. Downstream of this feature, the quasi-normal unsteady shockwave displays a very coherent distribution along the span of the airfoil.

Figure 9.12 (left) shows the instantaneous velocity field with the quasi-normal SW in proximity of the most downstream position (close to $50\%c$) and with the separated area extent again quite limited. By looking at the chordwise-spanwise distribution of velocity, the presence of the different curved steady shockwaves originating at the leading edge of the bumps are still evident. The supersonic area is terminated again with a 2D quasi-normal shockwave at $x/c \approx 50\%$.

Despite this observed spanwise coherence, the separated area is not expected to be 2D, as suggested by the oil flow visualization in Fig. 9.1 (left). From this image, it appears that the separated regions at the back of the individual SCBs merge with each other from only $\approx 70\%c$ onwards. This information cannot be extracted from the PIV data from the vertical airfoil, since the measurement plane was detached from the surface of the airfoil, and located just above the separated area region (see Fig.9.4, right).

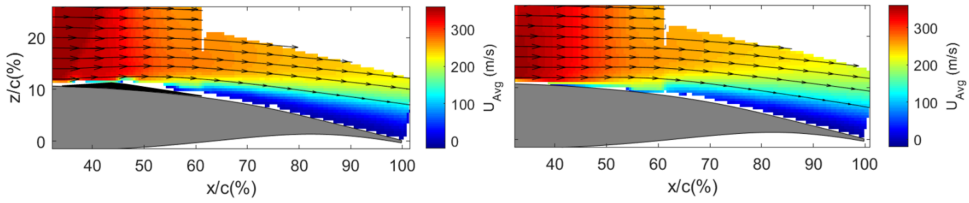


Figure 9.13: Average horizontal velocity component for the airfoil in presence of SCBs with $\Delta y_{SCB} = 25\%c$ (left) and clean configuration (right).

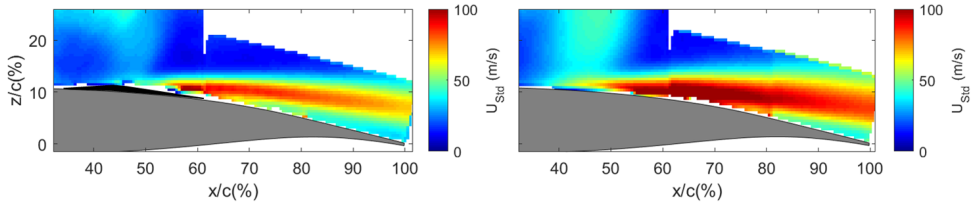


Figure 9.14: Standard deviation of the horizontal velocity component for the airfoil in presence of SCBs with $\Delta y_{SCB} = 25\%c$ (left) and clean configuration (right).

9.4.2. MAIN STATISTICS OF THE VELOCITY FIELD

A first quantitative description of the velocity field is provided by the distribution of the average horizontal velocity component for both the clean airfoil and the airfoil in presence of the best performing SCB configuration, i.e., with $\Delta y_{SCB} = 25\%c$ (Fig.9.13). The main flow structures are easily observed in both configurations. For the uncontrolled airfoil, the mean SW location is not easily identifiable because of the SW oscillation, which results in a gradual compression rather than a sharp interface. In contrast, in presence of control devices, an oblique SW at the leading edge of the SCB is clearly distinguished. From this comparison no important difference is noticed in terms of extent of the separated area, however, a wider shear layer (approximated by the green/yellow area in the velocity field) seems to be present for the clean airfoil. Streamlines are included in the velocity, with their general behavior being very similar for the two configurations. As expected, for the SCB configuration a variation of the inclination of the streamlines is noticeable in correspondence of the oblique shockwave.

To highlight the unsteadiness present in the flow field, the standard deviation of the horizontal velocity component is plotted in Fig.9.14 for the same configurations shown in Fig. 9.13. In terms of SW position, the results are in good agreement with those presented in the previous section, with a smaller range of oscillation of the SW for the controlled case. These ranges are in accordance with those shown in Fig. 9.9 (left), and furthermore confirm the stabilizing effect obtained with the λ -shape of the SW. In proximity of $z/c=25\%$ and $x/c=45\%$ there is an increase of the standard deviation values for the SCB configuration. This growth is associated with the moving shockwave also traveling (at that location) upstream of the steady oblique shockwave when reaching its most upstream position. The distribution of standard deviation downstream of the shockwave confirms a reduction of the fluctuation of both the separated area and of the shear layer

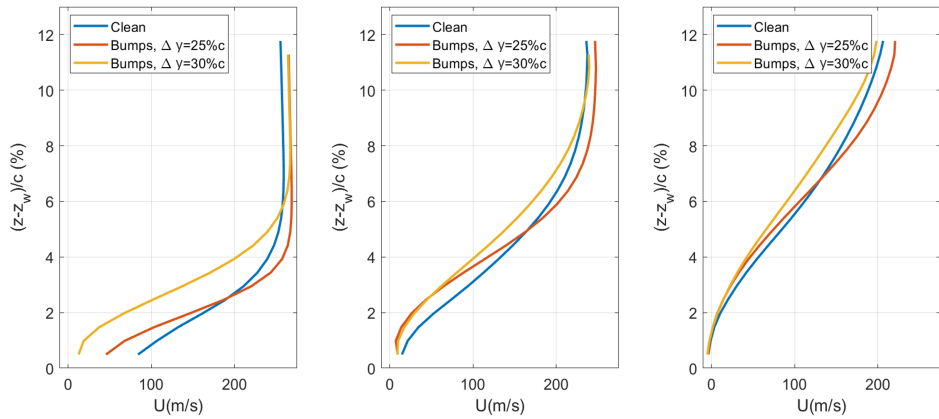


Figure 9.15: Horizontal velocity profile in the centerline ($y/c=0\%$) at $x/c=60\%$ (left), $x/c=80\%$ (center) and $x/c=100\%$ (right) for the three configurations tested.

in presence of SCBs.

9.4.3. SEPARATED AREA BEHAVIOR

A first view of the separated area and shear layer structure is provided in Fig.9.15 by the profiles of the horizontal velocity component for three different chordwise positions: $x/c=60\%$, $x/c=80\%$ and $x/c=100\%$. The data are here shown for the clean, the $\Delta y_{SCB} = 25\%c$ and the $\Delta y_{SCB} = 30\%c$ configurations. All the velocity profiles are shown with respect to the local height of the airfoil surface $z_w(x/c)$ therefore, the vertical axis always indicates the local distance from the surface of the airfoil, $(z - z_w)/c$. It is observed that the $\Delta y_{SCB} = 25\%c$ profiles are all on the left of the profiles for the clean case in proximity of the surface of the airfoil (in the separated area) and on the right above the inflection points of the former. The shape of the profile suggests a thinning of the shear layer for the SCB configuration with a spacing of $25\%c$. On the contrary, this effect is not observed for the second spacing tested ($\Delta y_{SCB} = 30\%c$), with its profile almost overlapping the profile of the clean configuration for $(z - z_w(x/c))/c > 10\%$. When comparing the behavior of the two bump configurations, lower values of horizontal velocity are observed for the $30\%c$ configuration, suggesting the presence of higher momentum losses for this case.

In Fig.9.16, the profiles of the standard deviation of the horizontal velocity component are shown for the same chordwise locations and configurations. The graphs clarify that, with a spacing of $25\%c$, the fluctuations in the separated area are always reduced when compared to the clean configuration. On the other hand, the $\Delta y_{SCB} = 30\%c$ displays a reduction of the fluctuations at $x/c=80\%$ and $x/c=100\%$ but an increase just downstream of the SW oscillating range, for $x/c=60\%$. As expected, the reduced values of standard deviation for the $25\%c$ configuration are observed in the full region analyzed (except for a restricted region for $z - z_w(x/c) > 10\%c$) and expected to be associated with the reduced shockwave oscillations. What stands out is that, for the clean configuration, the standard deviation of the velocity near the airfoil surface is much higher than for the SCBs configurations. This increase in standard deviation could be attributed to

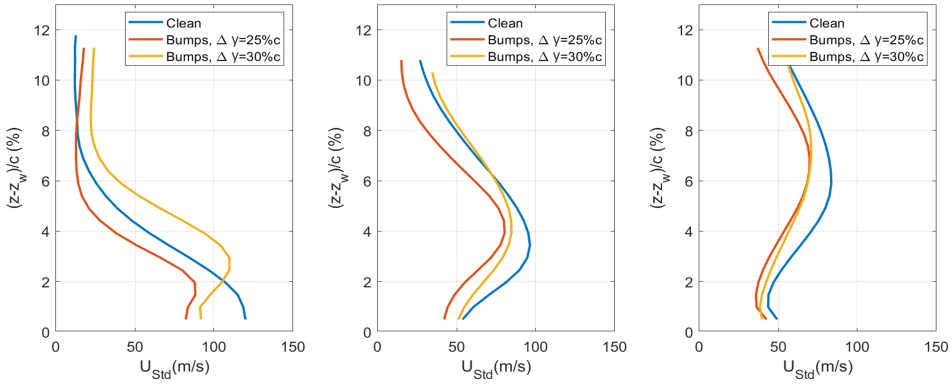


Figure 9.16: Profile of STD of horizontal velocity at $x/c=60\%$ (left), $x/c=80\%$ (center) and $x/c=100\%$ (right) for the three configurations tested.

the fact that for the clean configuration there is an established oscillation between stages in which the flow is fully attached and stages in which shock foot separation is triggered (for an understanding of the separated area behavior for the clean configuration see the phase averaged analysis in Chapter 5). For the bump configuration, on the other hand, the velocity at 60% of the chord is highly influenced by the proximity of the bump, as also suggested by the low velocity in the average profiles in Fig.9.15 (left).

To quantitatively analyze the extent of the separated area, the probability of separated flow is evaluated by showing the percentage of vectors with a negative streamwise velocity (reverse flow), with an approach similar to that of Giepmans et al. (2018). The results of this analysis are plotted in Fig.9.17 for the $\Delta y_{SCB} = 25\%c$ (top) and the clean (bottom) configurations. The plot suggests that there is quite a similar probability of having separated flow close to the surface of the airfoil. However, for the SCB configuration there is a slightly increased probability of having separated flow for $65\% < x/c < 77\%$ (immediately downstream of the SCB). Notwithstanding the previous consideration, in the remaining FOV, the region of the flow in which reverse flow is likely to be present is wider for the clean configuration, confirming a beneficial effect of using SCBs for reducing the extent of the separated area.

The probability of separated area plot was spatially integrated, to obtain quantitative information regarding the extent of the reverse flow region (A_{Sep}). These data have been summarized in Table 9.4, which reveals a reduction of the separated area for the $\Delta y_{SCB} = 25\%c$ configuration compared to the clean case. This integration procedure has also been applied to the $\Delta y_{SCB} = 30\%c$ (although the relative reverse flow probability plot has not been included for brevity) and the table clearly shows an increase of the separated area for this configuration, confirming the relevance of the spacing parameter once again.

The reduction in the reverse flow area for the $\Delta y_{SCB} = 25\%c$ case could be a result of the vortical structures developing from the tail of the bumps (accurately described in Ogawa et al. (2008) and in Colliss et al. (2016)). Furthermore, for the SCB case the simultaneous presence of an oblique and of a quasi-normal shockwave is less dissipative

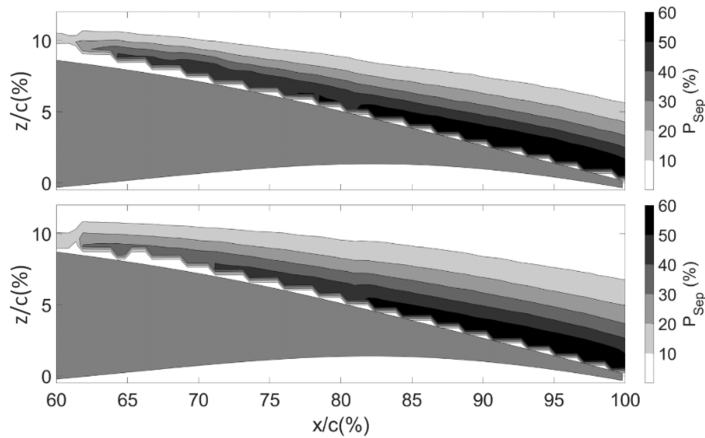


Figure 9.17: Probability of reverse flow ($U_\infty < 0$) for airfoil in presence of SCBs with $\Delta y_{SCB} = 25\%c$ (top) and clean airfoil (bottom).

compared to the single shockwave structure present for the clean configuration, hence a reduction of the adverse pressure ratio could be expected.

In addition to the calculation of the average extent of the reverse flow area, the extent of this region has also been computed in each instantaneous snapshot. From the time evolution of the extent of the separated region, the relative standard deviation is obtained (see $\sigma(A_{Sep})$ in Table 9.4). The values highlight that the extent of the reverse flow area is fluctuating in time more intensely for the clean configuration than for the $\Delta y_{SCB} = 25\%c$ case, in good agreement with Fig. 9.14, where the standard deviation of the horizontal velocity field showed a decrease of the fluctuations in the separated area. For the $\Delta y_{SCB} = 30\%c$ configuration a poorer performance is obtained, with the average separated area larger than for both the other two configurations, however, a slight decrease of the pulsation of the separated area is observed compared to the clean configuration.

Table 9.4: Separated area extent per configuration.

	Clean	$\Delta y_{SCB} = 25\%c$	$\Delta y_{SCB} = 30\%c$
$A_{Sep}(\%)$	15	13	17
$\sigma(A_{Sep})(\%)$	19	13	18

From the time behavior of the extent of the reverse flow region, the relative spectral content has been derived in the form of a pre-multiplied PSD (Fig. 9.18). This reveals that the dominant frequency is the same as the shockwave oscillation (160 Hz). The amplitude of this main peak is once again reduced in presence of SCBs and the performance optimized for $\Delta y_{SCB} = 25\%c$. This reduction is very similar to the decrease observed for the shock position in Fig. 9.10, confirming that the SW oscillation and the pulsation of the separated area are closely related (as shown in Chapter 5 and in Grossi et al. (2014)).

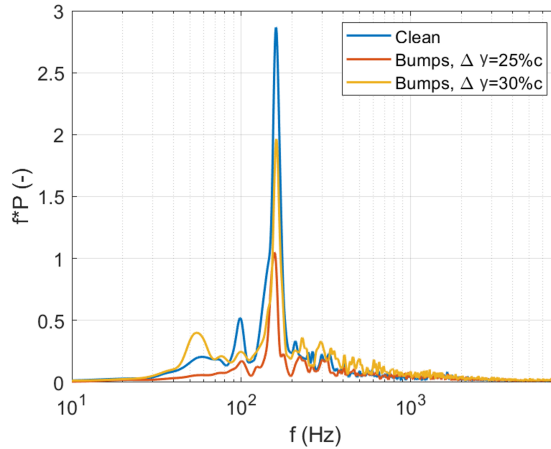


Figure 9.18: Spectral analysis of reverse flow area for the different configurations.

9.4.4. EFFECT OF SCB SPACING ON THE AVERAGE FLOW FIELD

To better understand the difference in behavior between the bump configurations with spacing $\Delta y_{SCB} = 25\%c$ and $\Delta y_{SCB} = 30\%c$, the corresponding average velocity fields in the spanwise-chordwise plane are shown in Fig.9.19 (the reader interested in the plot of the average velocity field for the clean configuration is referred to Fig.6.4). The spanwise structure of the shockwave is once again highlighted, with the presence of both a curved SW, originating from the leading edge of the bumps, and the quasi-normal SW which is located close to the crest of the bumps.

For geometric reasons the curved shockwaves developing around neighboring SCBs interact with each other at a distance $\Delta y_{SCB}/2$ from the symmetry planes of the bumps. Figure 9.19 clarifies that the curved shockwaves are still present after interacting with each other, interacting one more time in correspondence of the symmetry plane of the different bumps. It is clear that the chord position of this second interaction depends strongly on the spacing Δy_{SCB} , with it happening more downstream for the wider spacing. Therefore, in the case of the smaller spacing ($\Delta y_{SCB} = 25\%c$), curved shockwave are not present beyond $x/c=45\%$. In contrast, for $\Delta y_{SCB} = 30\%c$, the presence of the curved SW is observed until the most downstream position of the quasi-normal shockwave ($x/c=50\%$).

This difference results in a not negligible dissimilarity in the velocity field for $35\% < x/c < 50\%$. Consequently, the effect of this interaction is assumed to have an influence on the buffet oscillations and on the 2D coherence of the flow field. This observation is in agreement with the works of Bruce and Babinsky (2012) and Ogawa et al. (2008), where it is stated that (although for flow conditions different than those discussed in this Chapter) properly spaced 3D SCBs can induce a favorable quasi-2D SW along the full span.

To better substantiate the differences in the velocity field along the span of the airfoil, profiles of the horizontal velocity component are plotted in Fig. 9.20 for four different chordwise locations: 30, 40, 50, 60 %c. In addition to the two SCB configurations, the

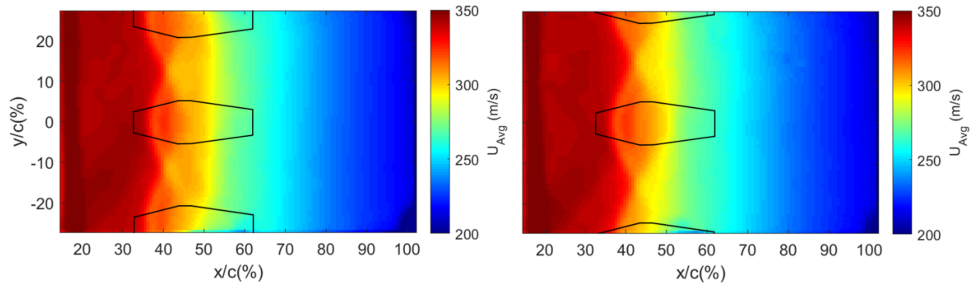


Figure 9.19: Average horizontal velocity field in the spanwise-chordwise plane in presence of SCBs with $\Delta y_{SCB} = 25\%c$ (left) and with $\Delta y_{SCB} = 30\%c$ (right). In both cases the outline of the bumps is specified.

clean configuration is also added for reference. Slightly upstream of the leading edge of the SCBs ($x/c=30\%$), the three velocity profiles are, as expected, very similar.

At 40% of the chord, the velocity is higher for the clean configuration than for the other two configurations because in most of the snapshots the flow is still supersonic (average shockwave location at about 45% c). Differently, for the SCBs configurations, the horizontal velocity is affected by the upstream oblique (curved) shockwave. Close to the centerline of the airfoil ($-0.08 < y/c < 0.08$), similar velocity profiles are visualized for the two SCB configurations while at more outboard locations, the velocity profiles are highly influenced by the different spacing. The fact that adjacent curved shockwaves interact at more outboard spanwise locations for the wider spacing, also affects the chordwise location of this interaction (taking place about 5% more downstream for $\Delta y_{SCB} = 30\%c$), as confirmed by the behavior of the profiles.

At 50% c all velocity distributions are relatively uniform, but with lower velocity values for the clean configuration than for the two SCB configurations, due to the presence of the single quasi-normal shockwave for this configuration. When comparing the two SCB configurations mutually, lower velocity values are observed for the configuration with the wider bump spacing, which could possibly be caused by a more dissipative secondary shockwave structure. Further downstream at $x=60\%c$, which is in proximity of the trailing edge of the bumps, the differences between the three velocity profiles have become even smaller, with lower velocities for the clean configuration and slightly higher velocities for the 25% c configuration, similar as at the previous station.

To emphasize the spanwise behavior of the flow field, the average of the spanwise velocity component is shown in Fig 9.21 for the two SCB configurations, highlighting non-negligible differences. The velocity fields are here plotted for $30\% < x/c < 100\%$ and for $-16\% < y/c < 16\%$, indicating the symmetry planes between adjacent bumps with dashed lines. First of all, in the region enclosed between the leading edge curved shockwave of a given bump and the curved shockwave originating from an adjacent bump, a spanwise deflection of the flow away from the bump is observed. Since for the wider spacing case the curved shockwaves interact with each other at a further spanwise location, the region of high (absolute) spanwise velocity is consequently wider as well.

Other relevant differences are observable in correspondence of the side flanks of the bumps. For the $\Delta y_{SCB} = 25\%c$ spacing, the signature of a streamwise vortex pair is ob-

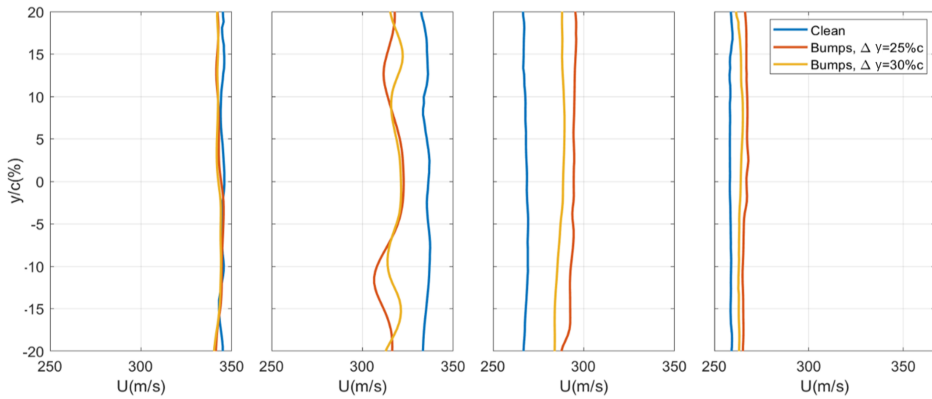


Figure 9.20: Horizontal velocity profile along the span at $x/c=0.3; 0.4; 0.5; 0.6$ (from left to right) for the three configurations tested.

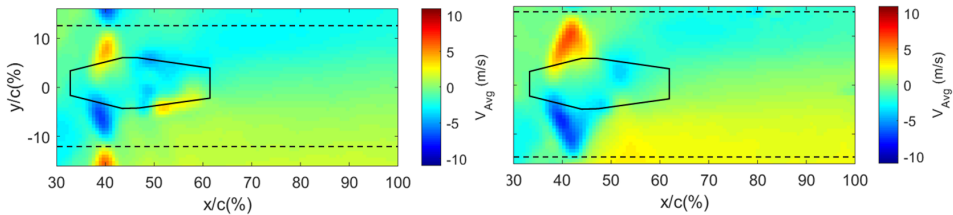


Figure 9.21: Average vertical velocity field in the spanwise-chordwise plane in presence of SCBs with $\Delta y_{SCB} = 25\%c$ (left) and with $\Delta y_{SCB} = 30\%c$ (right). In both cases the outline of the bumps is specified.

servable downstream of the crest of the bump, recognizable as the two regions of spanwise flow towards the centerline of the bump occurring at the opposite bump sides. The formation of this vortex pair in on-design conditions has been documented in detail in both [Bruce and Colliss \(2015\)](#) and [Colliss et al. \(2016\)](#). As has been reported there, the presence of this vortex pair induces a downwash region in the bump wake, which assists in energizing the flow with a beneficial effect on the suppression of the separated area. This vortex production is also qualitatively visualized in the oil flow visualization in [Fig 9.1](#) (left). Similar structures are not observable in the PIV data in [Fig 9.21](#) (right) for the $\Delta y_{SCB} = 30\%c$ configuration (at least not in this detached measurement plane), for which there is only a small region of negative spanwise velocity in correspondence of the tail of the SCB. This difference in behavior for $\Delta y_{SCB} = 30\%c$ could possibly be caused by a reduced strength of the streamwise vortex pair and by the flow being already separated downstream of the crest of the bumps. Although the oil flow visualization plot is provided for the $\Delta y_{SCB} = 25\%c$ case only, the present results provide clear evidence that the distance between the SCBs directly influences the behavior of the separated area by changing the character of the vortical structures developing from the tails of the different SCBs.

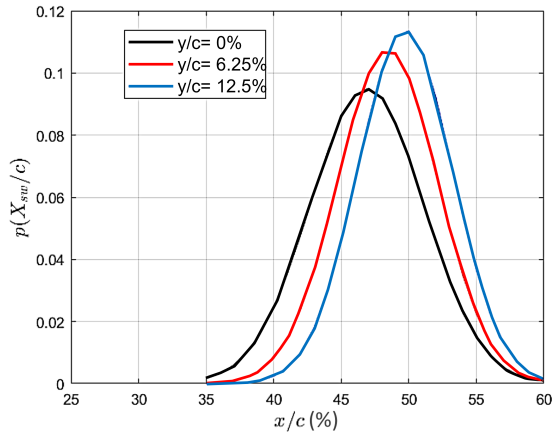


Figure 9.22: Pdf of shock position for the three measurement planes for the $\Delta y_{SCB} = 25\%c$ case.

9.5. LOADS DETERMINATION

To further evaluate the behavior of the SCBs, a load determination is carried out for both the clean and the best behaving SCB configuration ($\Delta y_{SCB} = 25\%c$), using the procedure discussed in Section 4.5.

In this section, the loads are first discussed for the measurement plane passing in correspondence of the centerline of the central bump ($y/c = 0$) and then for the other measurement planes. The loads obtained in each measurement plane are then averaged out to obtain a more representative estimation of the aerodynamic loads on the entire model.

To give an idea of how the different flow features are dependent on the spanwise position, the distribution of the shockwave position is given for the three measurement planes (see Fig.9.22). The range of oscillation of the shockwave is clearly wider for $y/c = 0$, while it is decreased at more outboard locations. In addition, the shockwave appears located much more upstream at the centerline. This behavior was expected in view of the presence of the curved front shockwave.

Before discussing the loads, the average velocity field around the full airfoil is shown for the clean configuration in Fig.9.23 for both the horizontal and the vertical velocity components. For comparison, Fig.9.24 shows the average streamwise velocity field for the SCB case, highlighting the presence of the oblique shockwave in correspondence of the leading edge of the SCB. The integration contour used for the evaluation of the lift coefficient is also reported in the same figure with the dashed line.

With the assumption of an adiabatic and inviscid flow, the pressure field is obtained using the isentropic relation (Eq.4.13), with the results plotted in Fig. 9.25. This model predicts high values of pressure in the wake and low in correspondence of the supersonic area. However, as commented in Section 4.5 this model yields to wrong values in the wake area, where the flow is clearly rotational. In this region (delimited by the dashed contour in Fig. 9.26, left) the static pressure field has been obtained using Eq.4.18 and the results plotted in Fig.9.26 (right). As discussed in Section 4.5, the drag coefficient is

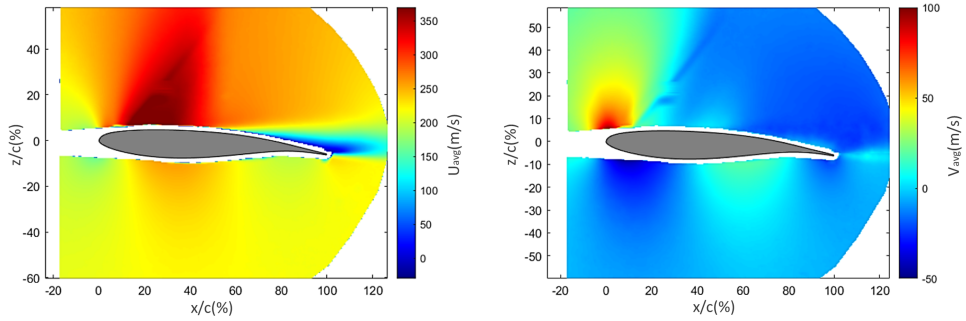


Figure 9.23: Average horizontal (left) and vertical (right) velocity field for clean configuration.

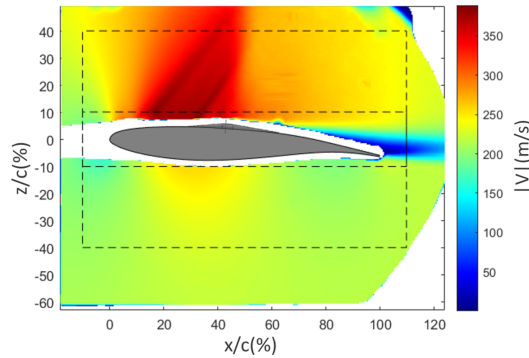


Figure 9.24: Average horizontal velocity field for SCB configuration.

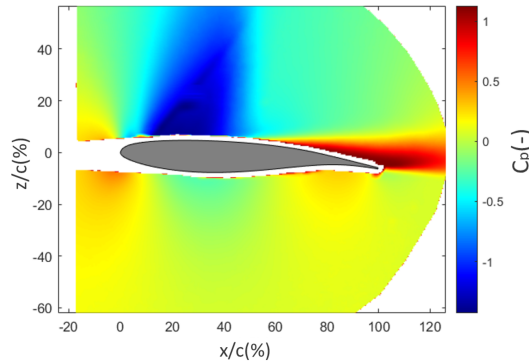


Figure 9.25: Isentropic static pressure field for clean configuration.

computed from the momentum deficit in the wake, using Eq. 4.19.

From the velocity and pressure fields the drag and lift coefficients are obtained for both the clean and the shock control bump configurations (for $y/b = 0$). The average value of the lift coefficient is evidently increased for the SCB configuration, while oppo-

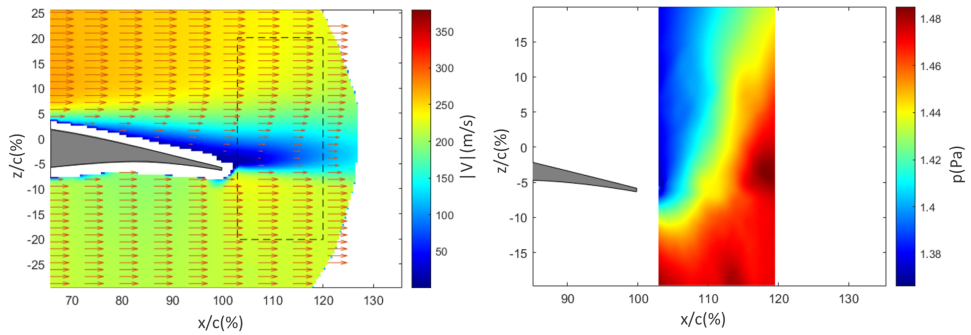


Figure 9.26: Pressure field in rotational region.

site trend is present for the drag coefficient. This behavior suggests that the use of SCBs not only brings to a decrease of the buffet oscillations, but also to beneficial effects on the loads experienced by the airfoil. This is supposedly associated with an extension of the supersonic area and a decrease of the extent of the separated area for the SCB configuration. The exact values of C_l and C_d are also reported in Fig.9.27 which shows an increase of 4% of lift and a decrease of 17% of drag coefficient.

From the instantaneous PIV images it was once again possible to obtain the phase averaged velocity fields. For this specific case, in view of the lower number of snapshots per configuration tested (700), only four PIV phases have been defined (differently from the analysis in Chapter 5): with the shock in its most upstream position (1), during the downstream movement (2), with the shockwave in the most downstream position (3) and with the shockwave moving upstream (4). Because of the selected acquisition frequency (15 Hz), the images belonging to the different phases are completely uncorrelated with each other, differently than for the phase average analysis of Chapter 5.

Since the shock position was not tracked in time, the different phases are not defined according to the shockwave velocity (information which cannot be retrieved) but according to the shock position (criterion which univocally distinguishes only Phase 1 and 3) and the extent of the separated area (with different extent during the upstream and downstream travel of the shockwave as shown in Chapter 5, allowing to distinguish between Phase 2 and 4).

From the phase averaged data, the loads coefficient were computed for each phase. The values of the coefficients confirm that not only the average value of the lift and the drag coefficients are respectively reduced but also their range of oscillation (see Fig.9.27). As anticipated, the previous values of the aerodynamic loads for the SCB case were obtained by taking into account only the behavior in the measurement plane passing for the centerline of the central SCB.

The loads for all the measurement planes are instead reported in Fig.9.28. It is clear that the differences among the values of the coefficients in the three measurement planes are significant, in particular for the drag coefficient. This behavior is supposed to be associated with the large variability of the wake condition at the three spanwise locations. For $y/c=0$ the streamwise vortices induced by the presence of the SCBs are believed to bring to a consistent reduction of the extent of the separated area, while this effect is less

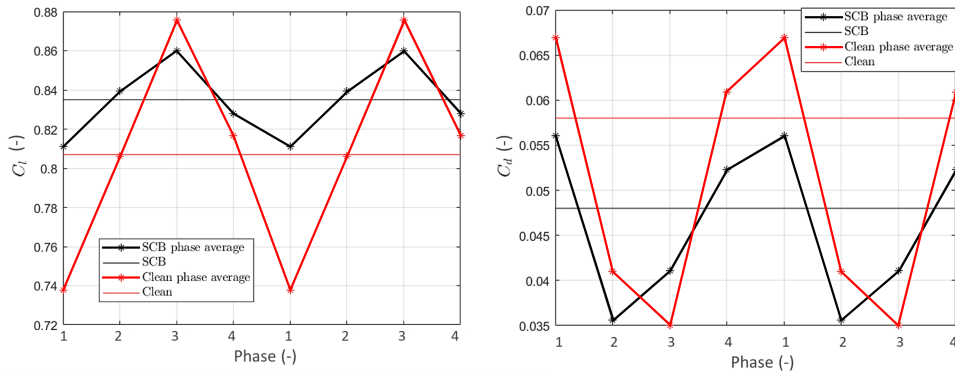


Figure 9.27: Lift (left) and drag (right) coefficients in the four buffet phases. With the horizontal lines the average values of the coefficients are indicated.

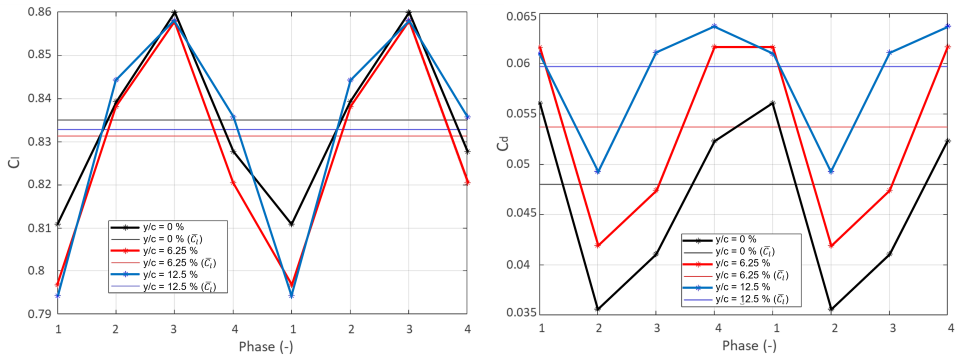


Figure 9.28: Effect of measurement plane on the aerodynamic coefficients value (on the left lift and on the right drag coefficient).

relevant at more outboard locations, bringing to higher values of C_d .

When averaging the velocity fields in the three measurement planes ($y/c=0$; $y/c = \Delta y_{SCB}/4$; $y/c = \Delta y_{SCB}/2$) the lift and the drag coefficient are computed once again. From a first overview of the results (Fig.9.29) it stands out that, also when taking account this "global" behavior, the SCB configuration appears once again beneficial with respect to the clean case. In detail, both a reduction of the drag and an increase of the lift coefficients are observed.

However, the variations of the aerodynamic loads for the SCB case is less relevant when averaging the loads on the entire model with respect to the centerline plane of measurement, in particular for the drag coefficient.

9.6. CONCLUSION

The results of this Chapter confirm that 3D SCBs are suitable devices for controlling transonic buffet. It is shown that these control devices reduce the shock oscillation while

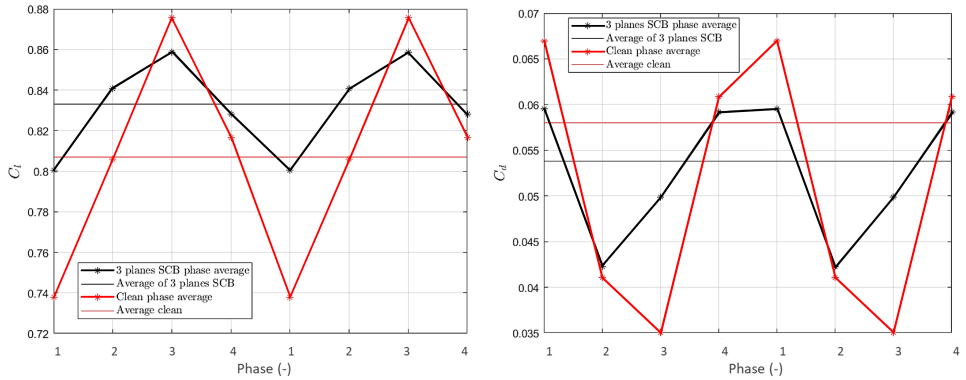


Figure 9.29: Aerodynamic coefficient values averaged among the three measurement planes (for the SCB case).

changing the structure of the shock wave into a λ -shape. From a spectral point of view, the use of these devices does not affect the buffet frequency ($f=160$ Hz) but clearly attenuates the contribution of the main peak. An optimization of performance in reducing buffet results when a spanwise array of bumps with a spacing of $25\%c$ is adopted.

In addition to the stabilization of the shock position, a diminished pulsation of the separated area is achieved with the application of SCBs. The comparison of the separated regions of the different configurations highlights a relevant influence of the spacing parameter, with the results clearly optimized for a spacing $\Delta y_{SCB} = 25\%c$, for which even a reduction of 14% of the average extent of the separated area is achieved when compared to the clean configuration.

To further investigate the difference in behavior among the various SCB configurations, PIV flow visualization in a spanwise-chordwise oriented plane was performed. This proved to be particularly meaningful for the understanding of the mutual interaction between the different bumps and the effect of changing their spacing on the relevant flow structures. This shows that the oblique shockwaves, originating at the leading edge of the three-dimensional SCBs, curve around the bumps (Figure 9.19). The velocity data has furthermore confirmed the presence of counter rotating vortex structures, developing from the tail of the bumps, which are well identified only for the $25\%c$ SCB configuration. This vortex production is also qualitatively observed in the oil flow visualization.

These PIV results also allowed to assess the two-dimensionality of the flow field. The velocity fields exhibit a spanwise coherence of the quasi-normal moving shockwave for the $\Delta y_{SCB} = 25\%c$ configuration, notwithstanding the presence of the three-dimensionality of the control system. Additional three-dimensional SW structures arise for a wider spacing of the bumps.

The similarity of results for the shockwave detection obtained with schlieren and PIV measurements confirms that schlieren visualizations can be effectively used for studying the behavior of transonic buffet on an airfoil, also in presence of three-dimensional passive control systems. However, the effect of the spacing was found to influence the separated area behavior more prominently than the shockwave behavior, whose stabi-

lization is achieved with all the SCBs configurations tested.

The quantification of the aerodynamic loads around the airfoil showed a reduction of C_d of 17% and an increase of C_l of about 4% in presence of SCBs. These variations resulted in an increase of L/D of 25%. It should be noted that this value is well above the increase reported in literature for steady impinging shockwave (see for example [Eastwood and Jarrett \(2012\)](#), where an increase of L/D of 10% is reported). This improvement is not surprising in view of the double working principle of SCBs for transonic buffet applications, which at the same time stabilize the shock position (reducing the occurrence of shock-foot separation) and promote attached flow thanks to the streamwise vortex development from the tail of the SCBs.

In conclusion this chapter demonstrates the feasibility of controlling transonic buffet using 3D SCBs, and confirms the influence of the spacing parameter. When properly spaced the SCBs also demonstrate to be effective in both their possible working principles: shockwave stabilization and reduction of the separated area extent, achieving at the same time an increase of C_l and a decrease of C_d for a fully developed buffet condition.

EPILOGUE

10

CONCLUSION AND PERSPECTIVES

In this thesis, transonic buffet has been investigated experimentally in the TST-27 wind tunnel of TU Delft with the aim of a better understanding of the physics of the phenomenon and to attempt to control it. In the following sections first some conclusions (Section 10.1) are given and followed by some perspectives and recommendations (Section 10.2).

10.1. CONCLUSION

Large scale flow features

The combined analysis of the flow field on a chordwise-vertical plane of measurement and on a spanwise-chordwise plane of measurement has allowed the investigation of the main large and small flow features which characterize transonic buffet. In particular, the time behavior of both the shockwave and of the separated area has been carefully scrutinized. The oscillations observed are of Type II-A and therefore, characterized by a quasi-periodic oscillation of the shockwave on the suction side of the airfoil. The choice of the specific OAT15A airfoil also resulted in a separated area which extends from the shockfoot to the trailing edge only in the upstream stage of the shockwave movement.

The velocity data on the airfoil model have shown a two-dimensionality of the flow, at least in terms of shockwave position and extent of the separated area, with the results being therefore comparable with two-dimensional CFD simulations.

A correlation analysis has revealed that the movement of the shockwave is highly correlated with the pulsation of the separated area even though with a phase delay. In particular, it has been observed that the shockwave reaches its most downstream position approximately one eighth of the buffet cycle before that the separation area is at its biggest extent.

To better analyze the large scale structures, the behavior of the first POD modes of the velocity field had been evaluated, confirming that the most energetic flow features are associated with shockwave, separated area and shear layer unsteadiness. The analysis of the POD modes has also shown that, although the oscillation of the shockwave is

quasi-periodic, an asymmetric behavior is observed with the shockwave moving faster during its upstream travel. This aspect should be further investigated but is supposedly associated with the different separated area condition, shockwave and UTWs strength in the different buffet phases.

A spectral analysis has instead shown that the large scale flow features are all characterized by a frequency peak at 160 Hz, with only the shear layer having an additional relevant contribution at double this frequency (320 Hz).

Small scale flow features

The most relevant small scale flow features which are known to influence transonic buffet cycle are upstream traveling waves (UTWs) and downstream traveling waves (DTWs). The UTW behavior has been scrutinized with a BOS analysis in the spanwise-chordwise plane of measurements, showing that these waves propagate in the velocity field with a certain inclination which is (supposed to be) associated with the three-dimensional distribution of DTWs. An analysis of the UTW propagation has shown that the shedding frequency of the UTWs is of about 2000 Hz, which is of one order of magnitude higher than the buffet frequency (160 Hz). This mismatch is justified by the observation that the strength of the UTWs is modulated at the buffet frequency, and therefore changes in the different stages of the transonic buffet cycle.

The POD analysis on the chordwise-vertical plane of measurement has also been used to extract the small scale flow features from the PIV images by subtracting the most energetic POD modes. This analysis has highlighted the presence of downstream propagating vortical structures, moving in the shockfoot separated area with a shedding frequency in the range of 5000-8000 Hz. It should be noted that this frequency value is clearly higher than the computed shedding frequency of the UTWs (2000 Hz) which demonstrates that the vortical structures which are developing in the shockfoot separated area cannot be considered responsible for the formation of UTWs. Another important aspect is that the UTWs are produced during the entire buffet cycle, while the shockfoot separated area is present only during the upstream phase of the shockwave travel, confirming an inherent asymmetric behavior of the buffet cycle. Thus, it is supposed that the structures responsible for the formation of UTWs are concentrated in the separated trailing edge area, which instead survives during the entire buffet cycle. To demonstrate the presence of these flow structures a new experiment with a FOV focused in proximity of the surface of the airfoil is suggested.

Discussion of transonic buffet cycle for an airfoil

To clarify the buffet mechanism a full cycle of oscillation is described according to the results obtained in this thesis and previous findings present in literature. An illustration of the main flow features of the transonic buffet cycle is also given in Fig. 10.1. When the shock starts its downstream travel, its movement is sustained by a region of decreasing pressure at the shock foot, because of the decrease of the extent the separated area (indicated with a blue arrow in Fig.10.1). Simultaneously with the reduction of the dimensions of the separated area and shear layer, vortical structures (DTWs) produced in the separated area start to be convected downstream. These vortices are relatively strong in this stage, as a large gradient in velocity is occurring over a small region (in these phases

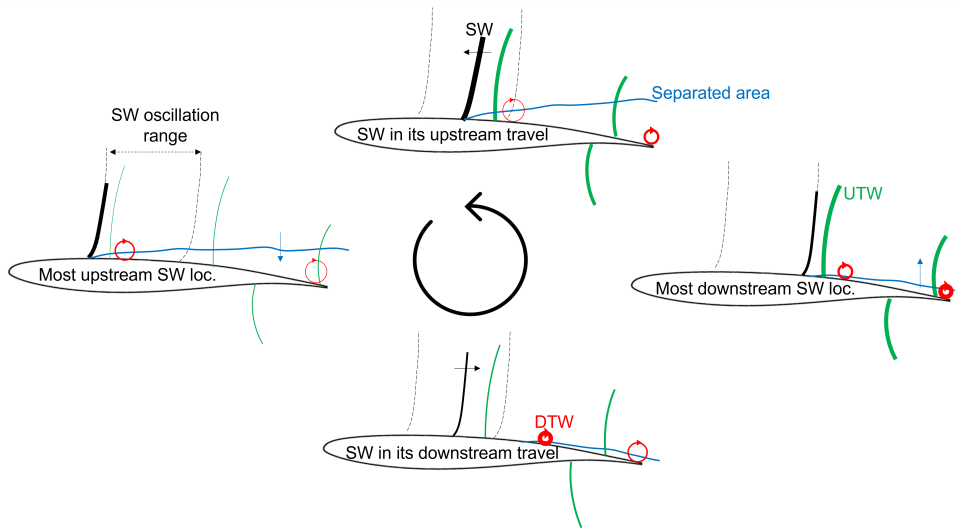


Figure 10.1: Sketch of the transonic buffet cycle in four relevant stages: with the shockwave in the most upstream (left) and downstream location (right) and during its downstream (bottom) and upstream travel (top). The width of the SW, UTW, DTW lines qualitatively indicates their strength.

the separated area is small as described in Chapter 5). When these vortices reach the trailing edge, pressure waves (UTWs) are created that propagate in the full velocity field and communicate with the shockwave along both the pressure and the suction side of the airfoil. The latter reach the shockwave before it arrives in its most downstream position and therefore earlier and with a higher intensity than the UTWs passing through the pressure side. As the pressure behind the UTWs is slightly higher, they require the shockwave to move towards a region with a lower Mach number. This results in a reduction of the velocity of the SW itself and eventually to a stop of its movement. With the further arrival of pressure waves, the shockwave starts its upstream travel, obtaining a velocity of opposite sign with respect to the flow. As a consequence in this stage, shock foot separation is triggered, which increases the velocity of the SW even further. With the increase of the extent of the separated area the vortices, which are responsible for creating the UTWs, become weaker and with them the strength of the UTWs (the strength of these waves is qualitatively indicated by the width of the respective lines in Fig. 10.1). This is happening because with the increase in size of the separated area and shear layer, the jump in velocity between the surface of the airfoil and the undisturbed flow is happening in a wider region. In addition the UTWs traveling in a wide separated area are partly mitigated by this region. The shockwave eventually is not sustained anymore by the increase in pressure due to the presence of the UTWs and stops its upstream travel, which also reduces the size of the separated area. With the beginning of the downstream travel, one full buffet cycle is completed.

Finite wing and sweep effects

As previously commented, transonic buffet can be considered 2D for an airfoil model, with the shockwave and the separated area (in terms of average quantities) being coherent along the entire span of the tested model. Differently, when other experimental models are taken into account, see for example the case of an unswept wing clamped only at its root, some relevant differences arise. For the unswept wing case, the shockwave is much less coherent along the span of the wing with respect to the airfoil case and located more upstream. The variation of the shockwave position for the latter case is thought to be associated with wing tip effects. This hypothesis has been corroborated by both oil flow visualizations and PIV data at different spanwise locations.

Although not directly shown in this thesis, finite wing effects were also found to influence the behavior of the vertical airfoil model studied, in particular, in terms of amplitude and average position of the shockwave oscillation. Shockwave properties closely matching to the fully clamped airfoil case are only achieved by means of side plates mounted at the tips of the "vertical" model.

The comparison of swept and unswept finite wings has revealed the presence of spanwise convection phenomena which have been already observed for the unswept model and become more relevant for an increasing sweep angle. Therefore, it is suggested for future research, that the buffet behavior of a finite-span swept wing is also compared with the corresponding unswept (finite-span) wing, in addition to the corresponding airfoil, to exclude that the differences observed are due to the specific clamping conditions. Similarly, the effect of the boundary conditions of an unswept wing model in transonic buffet conditions should be further studied to better visualize and investigate the effect of wing tip vortices.

Working principle and design of buffet control systems

To properly design a control system, it is of utmost importance to understand the physics of the phenomenon which is meant to be controlled and for this reason the knowledge acquired in the first Part of the thesis has been used to design an effective control system. Following the results of Chapter 5, where it is theorized that the DTWs travel in a thin layer close to the surface of the airfoil, the use of a vertical flap at the trailing edge is proposed with the goal of damaging the consequent formation of UTWs. The results obtained confirm the efficacy of this control system, which, instead of directly controlling the shock position, influences the coherence of the whole buffet mechanism and as a consequence of the shockwave position. Furthermore the results show that transonic buffet oscillations are not completely eliminated but attenuated when using a similar control device. It is also worth mentioning that no reduction of the transonic buffet properties is achieved when serrated UTEFs are used. Thus, the damage of the communication between the trailing edge and the downstream propagating DTWs is achieved only when the UTEF spans along the entire model. This observation is in agreement with the nature of UTWs, which are emitted hemispherically and therefore, the UTW which is originated at a given spanwise location influences the shock position for a wider portion of the span.

UTEFs have been compared with the behavior of another transonic control device: a SCB. This device directly controls the shock position, clearly stabilizing its oscillation

and even obtaining a better performance with respect to the UTEF device ($STD(X_{SW,UTEF} \approx 5.0\%c$, while $STD(X_{SW,SCB} \approx 3.3\%c$)). However, the SCB has the disadvantage that its effectiveness is very dependent on the particular flow condition. This thesis has also shown a strong dependency of the SCB control performance on the spacing parameter. This dependence is often overlooked in literature and when properly accounted for could bring to an optimization of the performance of the SCB by simultaneously reducing the shockwave buffet oscillation and the extent of the separated area. On the other hand, in view of its working principle, the design of an UTEF is simpler and only requires the correct height of the flap.

Effect of control systems on aerodynamic loads

The use of passive control systems can be associated with a variation in geometry of the airfoil, which could clearly affect the aerodynamic loads, thus, their variation should be accurately estimated.

In this thesis, the aerodynamic loads have been directly computed for the airfoil in presence of SCBs showing that for the most developed buffet condition, both a reduction of the drag and an increase of the lift coefficients are achieved in presence of this control device. For the UTEF, although a proper pressure estimation has not been attempted, the quantification of the circulation and of the separated area extent has hinted that neither the lift nor the drag are negatively influenced by the presence of the UTEFs. Similarly, for the UTEF case, a reduction of separated area extent is noted, suggesting a reduction of drag coefficient. It is also worth mentioning that these analyses have been carried out for the most developed buffet condition, whilst no data has been obtained for cruise-type conditions.

The fact that no reduction of the lift coefficient (or its proxy, i.e. circulation) is observed for the controlled configurations, brings to the conclusion that these control systems are not expected to influence the operative flow condition of an airplane, which will be able to respect the vertical equilibrium equation ($L=W$) flying at the same velocity (Mach number) and angle of attack and with the same required thrust (in view of the non increase of drag). Thus, by keeping the same operative conditions (Ma and lift) approximately constant, a reduction of the buffet oscillations is observed, expanding, as a consequence, the available flight envelope.

Measurement techniques

In this thesis, different optical experimental techniques have been employed to study transonic buffet, namely oil flow visualization, schlieren, BOS and PIV.

PIV resulted in being very efficient in resolving the main flow features of transonic buffet having at the same time a relatively high spatial (vector spacing of $0.3\%c$) and temporal resolution ($\Delta t = 0.0002s$). For the airfoil investigation, measurements on both a spanwise-chordwise and a chordwise-vertical oriented plane allowed the completion of the full investigation of transonic buffet using only planar PIV. This technique is also attractive for possible follow up industrial studies because of its less complex set-up (when compared to volumetric measurements). On the other hand, PIV resulted not to be capable of quantitatively characterizing the behavior of the UTWs, in view of the small perturbation in the velocity field associated with these waves. Similarly, although UTWs can

be clearly observed in the schlieren images, they could not be tracked quantitatively in view of the integration of pressure gradients along the span of the wing. Notwithstanding this aspect, schlieren demonstrated to be an efficient technique, when only quantitative information of the shockwave position and qualitative information of the flow field are required.

On the other hand, BOS demonstrated to be successful in observing and tracking the UTWs using a chordwise-spanwise oriented FOV. To the best of the author's knowledge this was the first application of this technique for a similar investigation, and is suggested for future studies aimed at obtaining further information on UTW propagation.

The application of both BOS and PIV for the study of the unswept wing, has also validated the use of the BOS technique for analyzing transonic buffet on models with 3D structures developing along the span. From the BOS images it has been possible to obtain results in agreement with the PIV data, in particular in terms of amplitude of the shockwave oscillation. Thus, the use of the BOS technique could be applied to future studies of transonic buffet on unswept wings, especially when a qualitative visualization of the flow field is needed, or for the identification of the most developed buffet conditions, for which analysis the use of PIV could be too complicated and/or time consuming. Additional discrepancies could arise from BOS measurements on swept models in view of the additional spanwise variability of the flow field. Notwithstanding this, by orienting the BOS camera in the direction of the leading edge of the wings, a good approximation (although underestimated) of the amplitude of the shockwave is obtained.

10.2. PERSPECTIVES AND RECOMMENDATIONS

The ultimate goal of this thesis is that of limiting the occurrence of transonic buffet oscillation for future generation aircrafts. The results of this research can be directly implemented in this direction by designing passive control devices similar to the ones tested in this thesis. However, although passive control systems are associated with robustness and simplicity, they are also often dependent on the specific flow condition, with possible additional losses in non-buffet conditions. To avoid detrimental effects in cruise conditions, the use of deployable devices are suggested. A similar solution has already been proposed and proved to be efficacious by [Gramola et al. \(2018\)](#) and [Jinks et al. \(2018\)](#), where adaptive SCBs have been employed, activating them under determined flow conditions only. Similarly, folding trailing edge solutions could be implemented for the industrial use of UTEFs.

It is also worth mentioning that the testing of the different control devices has proved the dependence of the control system on the specific design parameters. Thus, to properly control transonic buffet, parametric analysis are required. Unfortunately, the capability of experimentally testing a large matrix of parameters is often limited in a wind tunnel facility. Thus, to accurately carry out this parametric analysis a combined numerical and experimental study is suggested for future investigations.

As a result, an effective control of transonic buffet will lead to the expansion of the available flight envelope of a given aircraft. This, could allow airplanes to fly in a more efficient region of the flight envelope, where more sustainable flow conditions could eventually be achieved, among others in terms of fuel consumption. A possible application could also be the employment of ultra high bypass ratio engines which are supposed to

reduce the operative costs of an aircraft of 5.7% (Giesecke et al. (2018)). However, at the moment the employment of these engines is also limited by the consequent occurrence of transonic buffet on the pressure side of a wing.

However, before enlarging the flight envelope of an aircraft, there are still some aspects of the transonic buffet phenomenon which should be better clarified. One of these is related to the cause-consequence relation between the DTW propagation and the UTW production. In fact, although these flow structures have been separately observed in literature, there has not yet been a study, in which they are simultaneously detected. In this direction, this thesis has shown the experimental tools to succeed in this goal (using PIV for the DTWs detection and BOS for the UTWs visualization).

Another relevant aspect which has not been clarified yet is the mechanism by which transonic buffet occurs on swept wings. This aspect is particularly relevant considering that these are the types of wings used by real aircrafts. Following the findings of this thesis the contribution of tip-wing effects should be carefully taken into account. In the current investigation the visualization of tip vortex contributions by means of PIV visualization has been limited by lack of seeding in proximity of the wings and, therefore, should be better addressed in future studies. With this purpose tomographic PIV could be useful for also easing the visualization and investigation of the buffet cells.

BIBLIOGRAPHY

- Accorinti A, Baur T, Scharnowski S, and Kähler CJ (2022) Experimental investigation of transonic shock buffet on an OAT15A profile. *AIAA Journal* 60
- Alshabu A and Olivier H (2008) Unsteady wave phenomena on a supercritical airfoil. *AIAA Journal* 46:2066–2073
- Anderson J (2011) *Fundamentals of Aerodynamics*. McGraw Hill. 5th edition
- Aranyi P, Janiga G, Zehring K, and Thevenin D (2013) Analysis of different POD methods for PIV-measurements in complex unsteady flows. *International Journal of Heat and Fluid Flow* 43:204–211
- Astarita T (2007) Analysis of weighting windows for image deformation methods in PIV. *Experiments in fluids* 43:859–872
- Babinsky H and Delery J (2011) *Transonic Shock Wave-Boundary-Layer Interactions*. pages 87–136. Cambridge Aerospace Series. Cambridge University Press
- Babinsky H and Harvey J (2011) *Shock Wave-Boundary-Layer Interactions*. Cambridge Aerospace Series. Cambridge University Press
- Babinsky H and Ogawa H (2008) SBLI control for wings and inlets. *Shock Waves* 18:89–96
- Bannink WJ (1987) *Derde jaars praktikum compressibele aerodynamica hsl 2*
- Bannink WJ and Bakker P (1983) Transonic mach number determination in a blow-down tunnel with solid walls and a downstream throat, report lr-402
- Bauknecht A, Merz CB, Raffel M, Landolt A, and Meier A (2014) Blade-Tip Vortex Detection in Maneuvering Flight Using the Background-Oriented Schlieren Technique. *Journal of Aircraft* 51(6):2005–2014
- Baur T and Kongeter J (1999) PIV with high temporal resolution for the determination of local pressure reductions from coherent turbulent phenomena. in *3rd Int. Workshop on PIV, 16-18 September, Santa Barbara, California*. Santa Barbara
- Benedict LH and Gould RD (1996) Towards better uncertainty estimates for turbulence statistics. *Experiments in Fluids* 22:129–136
- Beresh S, Comninou M, Clemens N, and Dolling D (1998) The effects of the incoming turbulent boundary layer structure on a shock-induced separated flow. in *AIAA 1998-620, 36th AIAA Aerospace Sciences Meeting and Exhibit, 12-15 January, Reno, Nevada*

- Birkemeyer J, Rosemann H, and Stanewsky E (2000) Shock control on a swept wing. *Aerospace Science and Technology* 4:147–156
- Bogdanski S, Nubler K, Lutz T, and Kramer E (2014) Numerical investigation of the influence of shock control bumps on the buffet characteristics of a transonic airfoil. in *New Results in Numerical and Experimental Fluid Mechanics IX*. pages 23–32. Springer
- Bohning R and Zierep J (1981) Normal shock-turbulent boundary layer interaction. In *AGARD Computation of Viscous-Inviscid Interactions 8 p (SEE N81-26037 17-01*
- Briggs LJ and Dryden HL (1927) Pressure distribution over airfoils at high speeds. Technical report. NACA-TR-255
- Brion V, Dandois J, Mayer R, Reijasse P, Lutz T, and Jacquin L (2019) Laminar buffet and flow control. *Proceedings of the Institution of Mechanical Engineers, Part G: Journal of Aerospace Engineering* 234(1):124–139
- Brown JL and Naughton J (1999) The Thin Oil Film Equation. Technical report. NASA/TM-1999-208767
- Bruce PJK and Babinsky H (2008) Unsteady normal shock wave boundary layer interactions with control. in *AIAA 2008-721, 46th AIAA Aerospace Sciences Meeting and Exhibit, 07-10 January, Reno, Nevada*
- Bruce PJK and Babinsky H (2012) Experimental study into the flow physics of three-dimensional shock control bumps. *Journal of Aircraft* 49:1222–1233
- Bruce PJK and Colliss SP (2015) Review of research into shock control bumps. *Shock Waves* 25:451–471
- Brutyan M, Volkov A, and Potapchik A (2019) An experimental study of a passive method of attenuating a transonic buffet phenomenon. *Technical Physics Letters* 45:1082–1084
- Busemann A (1935) Aerodynamischer auftrieb bei überschallgeschwindigkeit. *Luftfahrtforschung* 12.6:210–220
- Caldwell F and Fales E (1920) Wind tunnel studies in aerodynamic phenomena at high speeds. Technical report. NACA Report 83
- Caruana D, Mignosi A, C R, and Corregge M (2003a) Active control of transonic buffet flow. *Flow, Turbulence and Combustion* 824:312 – 351
- Caruana D, Mignosi A, Corregge M, Pourhiet AL, and Rodde A (2005) Buffet and buffeting control in transonic flow. *Aerospace Science and Technology* 9:605 – 616
- Caruana D, Mignosi A, Robitaille C, and Corregge M (2003b) Separated flow and buffeting control. *Flow, Turbulence and Combustion* 71:221–245
- Coleman H and Steele W (2009) *Experimentation, Validation, and Uncertainty Analysis for Engineers*. John Wiley & Sons,. Third edition

- Colliss SP, Babinsky H, Nubler K, and Lutz T (2014) Joint experimental and numerical approach to three-dimensional shock control bump research. *AIAA Journal* 52:436–446
- Colliss SP, Babinsky H, Nubler K, and Lutz T (2016) Vortical structures on three-dimensional shock control bumps. *AIAA Journal* 54:2338–2350
- Crouch J, Garbaruk A, and Strelets M (2019) Global instability in the onset of transonic-wing buffet. *Journal of Fluid Mechanics* 881:3–22
- Crouch JD, Garbaruk A, and Magidov D (2007) Predicting the onset of flow unsteadiness based on global instability. *J Comput Phys* 224:924–940
- Crouch JD, Garbaruk A, Magidov D, and Jacquin L (2009) Global structure of buffeting flow on transonic airfoils. in *IUTAM Symposium on Unsteady Separated Flows and their Control*. pages 297–306
- D’Aguanno A, Schrijer FFJ, and van Oudheusden BW (2021a) Experimental investigation of the transonic buffet cycle on a supercritical airfoil. *Experiments in Fluids* 62, 214
- D’Aguanno A, Schrijer FFJ, and van Oudheusden BW (2021b) Spanwise organization of upstream traveling waves in transonic buffet. *Physics of Fluids* 33:106105
- D’Aguanno A, Schrijer FFJ, and van Oudheusden BW (2022a) Experimental Characterization of Upper Trailing Edge Flaps for Transonic Buffet Control. *Flow, Turbulence and Combustion*
- D’Aguanno A, Schrijer FFJ, and van Oudheusden BW (2022b) Finite wing and sweep effects on transonic buffet behavior. *AIAA Journal* 60:6715–6725
- D’Aguanno A, Schrijer FFJ, and van Oudheusden BW (2022c) Investigation of 3D shock control bumps for transonic buffet alleviation. *AIAA Journal* (submitted)
- Dandois J (2016) Experimental study of transonic buffet phenomenon on a 3D swept wing. *Physics of Fluids* 28:016101
- Dandois J, Mary I, and Brion V (2018) Large-eddy simulation of laminar transonic buffet. *Journal of Fluid Mechanics* 850:156–178
- de Kat R and van Oudheusden BW (2012) Instantaneous planar pressure determination from PIV in turbulent flow. *Experiments in Fluids* 52:1089–1106
- de Laval G (1894) Steam Turbine, Patent No. 522,066
- Deck S (2005) Numerical Simulation of Transonic Buffet over a Supercritical Airfoil. *AIAA Journal* 43:1556–1566
- Deng F and Qin N (2021) Vortex-generating shock control bumps for robust drag reduction at transonic speeds. *AIAA Journal* 59:3900–3909

- Despre C, Caruana D, Mignosi A, Reberga O, and Correge M (2001) Buffet active control - experimental and numerical results. in *Proceedings of RTO AVT Symposium on Active Control Technology of Enhanced Performance Operational Capabilities of Military Aircraft, Land Vehicles, and Sea Vehicles, June, Germany*
- Dolling DS (2001) Fifty years of shock-wave/boundary-layer interaction research: What next?. *AIAA Journal* 39:1517–1531
- Donker Duyvis FJ (2005) Laser sheet probe design for PIV in high-speed wind tunnels. in *PIVNET II International Workshop on the Application of PIV in Compressible Flows, 6-8 June, Delft, The Netherlands*
- Dupont P, Haddad C, and Debieve JF (2006) Space and time organization in a shock-induced separated boundary layer. *Journal of Fluid Mechanics* 559:255–277
- Eastwood JP and Jarrett JP (2012) Toward designing with three-dimensional bumps for lift/drag improvement and buffet alleviation. *AIAA Journal* 50:2882–2898
- Elsinga GE, van Oudheusden BW, and Scarano F (2005) Evaluation of aero-optical distortion effects in PIV. *Experiments in Fluids* 39:246–256
- Feldhusen-Hoffmann A, Lagemann C, Loosen S, Meysonnat P, Klaas M, and Schröder W (2021) Analysis of transonic buffet using dynamic mode decomposition. *Experiments in Fluids* 62:66
- Feldhusen-Hoffmann A, Statnikov V, Klaas M, and Schröder W (2017) Investigation of shock-acoustic-wave interaction in transonic flow. *Experiments in Fluids* 59:15
- Ferrari C (1996) Recalling the vth volta congress: High speeds in aviation. *Annual Review of Fluid Mechanics* 28:1–9
- Finke K (1975) Unsteady shock wave-boundary layer interaction on profiles in transonic flow. AGARD-CP-168 No. 28
- Gageik M, Nies J, Klioutchnikov I, and Olivier H (2018) Pressure wave damping in transonic airfoil flow by means of micro vortex generators. *Aerospace Science and Technology* 81:65–77
- Ganapathisubramani B, Clemens NT, and Dolling DS (2009) Low-frequency dynamics of shock-induced separation in a compression ramp interaction. *Journal of Fluid Mechanics* 636:397–425
- Gao C, Zhang W, and Ye K (2016) Numerical study on closed-loop control of transonic buffet suppression by trailing edge flap. *Computers & Fluids* 132:32–45
- Geoghegan JA, Giannelis NF, and Vio GA (2020) A numerical investigation of the geometric parametrisation of shock control bumps for transonic shock oscillation control. *Fluids* 5(2):46

- Giannelis NF, Levinski O, and Vio GA (2018) Influence of Mach number and angle of attack on the two-dimensional transonic buffet phenomenon. *Aerospace Science and Technology* 78:89–101
- Giannelis NF, Levinski O, and Vio GA (2020) Origins of atypical shock buffet motions on a supercritical aerofoil. *Aerospace Science and Technology* 107:106304
- Giannelis NF, Vio GA, and Levinski O (2017) A review of recent developments in the understanding of transonic shock buffet. *Progress in Aerospace Sciences* 92:39 – 84
- Gibb J (1988) *The cause and cure of periodic flows at transonic speeds*. Ph.D. thesis. Cranfield Institute of Technology
- Giepman RHM, Schrijer FFJ, and van Oudheusden BW (2018) A parametric study of laminar and transitional oblique shock wave reflections. *Journal of Fluid Mechanics* 844:187–215
- Giesecke D, Lehmler M, Friedrichs J, Blinstrub J, Bertsch L, and Heinze W (2018) Evaluation of ultra-high bypass ratio engines for an over-wing aircraft configuration. *Journal of the Global Power and Propulsion Society* 2:493–515
- Goddard GE Esther C; Pendray (1970) *The Papers of Robert H. Goddard, 3 vols.*. McGraw-Hill Book Co.
- Gramola M, Bruce PJ, and Santer M (2018) Experimental FSI study of adaptive shock control bumps. *Journal of Fluids and Structures* 81:361–377
- Grossi F, Braza M, and Hoarau Y (2014) Prediction of Transonic Buffet by Delayed Detached-Eddy Simulation. *AIAA Journal* 52:2300–2312
- Hall KC, Dowell EH, and Thomas JP (2000) Proper orthogonal decomposition technique for transonic unsteady aerodynamic flows. *AIAA Journal* 38:1853–1862
- Harris CD (1990) Nasa supercritical airfoils: a matrix of family related airfoils. Technical report. NASA, TP2926, Langley. Washington, DC. Charles D. Harris
- Hartmann A, Feldhusen A, and Schröder W (2013) On the interaction of shock waves and sound waves in transonic buffet flow. *Physics of Fluids* 25(2):026101
- Hermes V, Klioutchnikov I, and Olivier H (2013) Numerical investigation of unsteady wave phenomena for transonic airfoil flow. *Aerospace Science and Technology* 25:224–233
- Hilton WF and Fowler RG (1952) Photographs of shock wave movement. ARC R&M 2692
- Holden H and Babinsky H (2003) Shock/boundary layer interaction control using 3D devices. in *AIAA 2003-447, 1st Aerospace Sciences Meeting and Exhibit, 06-09 January, Reno, Nevada*

- Huang J, Xiao Z, Liu J, and Fu S (2012) Simulation of shock wave buffet and its suppression on an OAT15A supercritical airfoil by IDDES. *Science China Physics, Mechanics, and Astronomy* 55:260–271
- Humble RA (2009) *Unsteady Flow Organization of a Shock Wave/Boundary Layer Interaction*. Ph.D. thesis. Delft University of Technology. ISBN: 978-90-597-2295-8
- Humble RA, Elsinga GE, Scarano F, and van Oudheusden BW (2009) Three-dimensional instantaneous structure of a shock wave/turbulent boundary layer interaction. *Journal of Fluid Mechanics* 622:33–62
- Inger GR (1983) Transonic shock/turbulent boundary-layer interaction on curved surfaces. *Journal of Aircraft* 20:571–574
- Inger GR and Sobieczky H (1978) Normal shock interaction with a turbulent boundary layer on a curved wall. Technical report. Virginia polytechnic institute
- Iovnovich M and Raveh DE (2012) Reynolds-averaged navier-stokes study of the shock-buffet instability mechanism. *AIAA Journal* 50:880–890
- Iovnovich M and Raveh DE (2015) Numerical study of shock buffet on three-dimensional wings. *AIAA Journal* 53:449–463
- Jacquin L, Molton P, Deck S, Maury B, and Soulevant D (2009) Experimental study of shock oscillation over a transonic supercritical profile. *AIAA Journal* 47:1985–1994
- Jinks E, Bruce PJK, and Santer M (2018) Optimisation of adaptive shock control bumps with structural constraints. *Aerospace Science and Technology* 77:332–343
- Jones B (1936) Measurement of profile drag by the pitot-traverse. Technical report. ARC RM1688
- Jones NR, Eastwood JP, and Jarrett JP (2017) Adapting three-dimensional shock control bumps for swept flows. *AIAA Journal* 55:861–873
- Jux C (2022) *Development of robotic volumetric PIV*. Ph.D. thesis. Delft University of Technology. ISBN: 978-94-6366-519-3
- Kähler CJ, Sammler B, and Kompenhans J (2002) Generation and control of tracer particles for optical flow investigations in air. *Experiments in Fluids* 33:736–742
- Klinge F, Kirmse T, and Kompenhans J (2003) Application of quantitative background oriented schlieren (bos): Investigation of a wing tip vortex in a transonic wind tunnel. in *Proceedings of the The 4th Pacific Symposium on Flow Visualization and Image Processing (PSFVIP-4), June 3-5, Chamonix Mont-Blanc, France*
- Koike S, Ueno M, Nakakita K, and Hashimoto A (2016) Unsteady pressure measurement of transonic buffet on nasa common research model. in *AIAA 2016-4044, 34th AIAA Applied Aerodynamics Conference, 13-17 June, Washington, D.C.*

- Kokmanian K, Scharnowski S, Schäfer C, Accorinti A, Baur T, and Kähler CJ (2022) Investigating the flow field dynamics of transonic shock buffet using particle image velocimetry. *Experiments in Fluids* 63:1–14
- Konig B, Patzold M, Lutz T, Kramer E, Rosemann H, Richter K, and Uhlemann H (2009) Numerical and experimental validation of three dimensional shock control bumps. *Journal of Aircraft* 46:675–682
- Kuzmin A (2014) On the lambda-shock formation on ONERA M6 wing. *International Journal of Applied Engineering Research* 9:7029–7038
- Lawson S, Greenwell D, and Quinn MK (2016) Characterisation of buffet on a civil aircraft wing. in *AIAA 2016-1309, 54th AIAA Aerospace Sciences Meeting, 4-8 January, San Diego, California*
- Lee BHK (1990) Transonic buffet on a supercritical aerofoil. *The Aeronautical Journal* 94:143–152
- Lee BHK (1992) Effects of trailing-edge flap on buffet characteristics of a supercritical airfoil. *Journal of Aircraft* 29:93–100
- Liu LQ, Zhu JY, and Wu JZ (2015) Lift and drag in two-dimensional steady viscous and compressible flow. *Journal of Fluid Mechanics* 784:304–341
- Lynam E (1919) Preliminary report of experiments on a high trip speed airscrew at zero advance. Technical report. British ACA, R&M No.596
- Mabey D (1981) Oscillatory flows from shock induced separations on biconvex aerofoils of varying thickness in ventilated wind tunnels. Technical report. AGARD CP-296
- Mach E and Salcher P (1887) Photographische fixirung der durch projectile in der luft eingeleiteten vorgange. *Annalen der Physik* 268:277–291
- Masini L, Timme S, and Peace A (2019) Reynolds number effects on wing shock buffet unsteadiness. in *AIAA 2019-2820, AIAA Aviation 2019 Forum, 17-21 June 2019, Dallas, Texas*
- Masini L, Timme S, and Peace A (2020) Analysis of a civil aircraft wing transonic shock buffet experiment. *Journal of Fluid Mechanics* 884(A1):1–42
- Mayer R, Lutz T, and Krämer E (2018) Numerical study on the ability of shock control bumps for buffet control. *AIAA Journal* 56:1978–1987
- Mayer R, Lutz T, Krämer E, and Dandois J (2019) Control of transonic buffet by shock control bumps on wing-body configuration. *Journal of Aircraft* 56:556–568
- McDevitt JB and Okuno AF (1985) Static and dynamic pressure measurements on a NACA 0012 airfoil in the Ames high Reynolds number facility. Technical report. NASA-TP-2485
- Meier HU (2010) *German Development of the Swept Wing: 1935-1945*. AIAA

- Melling A (1997) Tracer particles and seeding for particle image velocimetry. *Experiments in Fluids* 8:1406–1416
- Moise P, Zauner M, and Sandham ND (2022) Large-eddy simulations and modal reconstruction of laminar transonic buffet. *Journal of Fluid Mechanics* 944:A16
- Molton P, Dandois J, Lepage A, Brunet V, and Bur R (2013) Control of buffet phenomenon on a transonic swept wing. *AIAA Journal* 51:761–772
- Moulden TH (1984) *Fundamentals of transonic flow*. J. Wiley and sons, New York
- Nies JM and Olivier H (2013) Dependence of upstream moving pressure waves on the Mach number and the impact of trailing edge serrations. in *62. Deutscher Luft- und Raumfahrtkongress, 10-12 September, Stuttgart*
- Nogueira J, Lecuona A, and Rodriguez P (1999) Local field correction PIV: on the increase of accuracy of digital PIV systems. *Experiments in fluids* 27:107–116
- Ogawa H, Babinsky H, Patzold M, , and Lutz T (2008) Shock-wave/boundary-layer interaction control using three-dimensional bumps for transonic wings. *AIAA Journal* 46(6):1442–1452
- Ohmichi Y, Ishida T, and Hashimoto A (2018) Modal decomposition analysis of three-dimensional transonic buffet phenomenon on a swept wing. *AIAA Journal* 56:1–13
- Paladini E, Dandois J, Sipp D, and Robinet JC (2019) Analysis and comparison of transonic buffet phenomenon over several three-dimensional wings. *AIAA Journal* 57:379–396
- Pearcey H (1955) Some effects of shock-induced separation of turbulent boundary layers in transonic flow past aerofoils. in *Proc. N.P.L. Symposium on Boundary Layer Effects in Aerodynamics*
- Petrilli J, Paul R, Gopalarathnam A, and Frinl N (2013) A CFD database for airfoils and wings at post-stall angles of attack. in *31st AIAA Applied Aerodynamics Conference, AIAA Paper 2013-2916, June 24-27, San Diego, California*
- Piccola J (2012) Flight Test Guide For Certification Of Transport Category Airplanes. Technical report. Federal Aviation Administration, Advisory Circular AC 25-7C
- Piponniau S, Dussauge JP, Debieve JF, and Dupont P (2009) A simple model for low frequency unsteadiness in shock induced separation. *Journal of Fluid Mechanics* 629:87–108
- Pirozzoli S, Bernardini M, and Grasso F (2010) Direct numerical simulation of transonic shock/boundary layer interaction under conditions of incipient separation. *Journal of Fluid Mechanics* 657:361–393
- Plante F, Dandois J, and Laurendeau E (2019) Similarities between cellular patterns occurring in transonic buffet and subsonic stall. *AIAA Journal* 58:71–84

- Plante F, Dandois J, Sartor F, and Laurendeau E (2017) Study of three-dimensional transonic buffet on swept wings. in *AIAA 2017-3903, 35th AIAA Applied Aerodynamics Conference, 5-9 June, Denver, Colorado*. volume AIAA Paper 2017-3903. Denver
- Poplinger L and Raveh DE (2022) Comparative study of the two-dimensional and three-dimensional transonic shock buffet. in *AIAA 2022-2483, AIAA Scitech 2022 Forum, 3-7 January, San Diego, California*
- Poplinger L, Raveh DE, and Dowell EH (2019) Modal analysis of transonic shock buffet on 2D airfoil. *AIAA Journal* 57:2851–2866
- Raffel M (2015) Background-oriented schlieren (BOS) techniques. *Experiments in Fluids* 56:60
- Raffel M, Willert C, Scarano F, Kahler C, Wereley S, and Kompenhans J (2018) *Particle Image Velocimetry A Practical Guide*. Springer
- Ragni D, Ashok A, Oudheusden BW, and Scarano F (2009) Surface pressure and determination of a transonic aerofoil based on particle image velocimetry. *Measurement Science & Technology* 20
- Ragni D, Schrijer FFJ, van Oudheusden BW, and Scarano F (2011) Particle tracer response across shocks measured by PIV. *Experiments in Fluids* 50:53–64
- Rajendran L, Zhang J, Bhattacharya S, Bane S, and Vlachos P (2019) Uncertainty Quantification in density estimation from Background Oriented Schlieren (BOS) measurements. *Measurement Science and Technology* 31(5):054002
- Ren K, Chen Y, Gao C, and Zhang W (2020) Adaptive control of transonic buffet flows over an airfoil. *Physics of Fluids* 32:096106
- Ren K, Gao C, Zhou F, and Zhang W (2022) Transonic buffet active control with local smart skin. *Actuators* 11
- Roos F (1985) The buffeting pressure field of a high-aspect-ratio swept wing. in *AIAA Paper 1985-1609, 18th Fluid Dynamics and Plasma Dynamics and Lasers Conference, 6-18 July, Cincinnati, Ohio*
- Samimy M and Lele SK (1991) Motion of particles with inertia in a compressible free shear layer. *Physics of Fluids* 3:1915–1923
- Sandham N, Yao Y, and Lawal A (2003) Large-eddy simulation of transonic turbulent flow over a bump. *International Journal of Heat and Fluid Flow* 24:584–595
- Sansica A, Hashimoto A, Koike S, and Kouchi T (2022) Side-wall effects on the global stability of swept and unswept supercritical wings at buffet conditions. in *AIAA 2022-1972, AIAA Scitech 2022 Forum, 3-7 January, San Diego, California*
- Sartor F (2014) *Instationnarites dans les interactions choc/couche-limite en regime transsonique : etude experimentale et analyse de stabilite*. Ph.D. thesis. Aix-Marseille Universite

- Sartor F, Mettot C, and Sipp D (2015) Stability, receptivity, and sensitivity analyses of buffet-ing transonic flow over a profile. *AIAA Journal* 53:1980–1993
- Sartor F, Minervino M, Wild J, Wallin S, Maseland H, Dandois J, Soudakov V, and Vrchota P (2019) A CFD benchmark of active flow control for buffet prevention. *CEAS Aeronautical Journal* 11:837–847
- Schrijer FFJ and Scarano F (2008) Effect of predictor-corrector filtering on the stability and spatial resolution of iterative PIV interrogation. *Experiments in Fluids* 45:927–941
- Schrijer FFJ, Solana Perez R, and van Oudheusden BW (2018) Investigation of transonic buffet using high speed PIV. in *Proceedings of the 5th International Conference on Experimental Fluid Mechanics (ICEFM 2018), July 2-4, 2018, Munich, Germany*.
- Sciacchitano A and Scarano F (2014) Elimination of PIV light reflections via a temporal high pass filter. *Measurement Science and Technology* 25(8):084009
- Sciacchitano A and Wieneke B (2016) PIV uncertainty propagation. *Measurement Science and Technology* 27:084006
- Settles GS (2001) *Schlieren and shadowgraph techniques: visualizing phenomena in transparent media*. Springer Science & Business Media
- Shapiro AH (1955) The dynamics and thermodynamics of compressible fluid flow. *ZAMM - Journal of Applied Mathematics and Mechanics / Zeitschrift fur Angewandte Mathematik und Mechanik* 35:195–196
- Shinde V, McNamara J, Gaitonde D, Barnes C, and Visbal M (2019) Transitional shock wave boundary layer interaction over a flexible panel. *Journal of Fluids and Structures* 90:263–285
- Sirovich L (1987) Turbulence and the dynamics of coherent structures. I - Coherent structures. II - Symmetries and transformations. III - Dynamics and scaling. *Quarterly of Applied Mathematics* 45:561–590
- Smits AJ and Dussauge JP (2006) *Turbulent shear layers in supersonic flow*. Springer Science & Business Media
- Stanewsky E and Basler D (1990) Experimental investigation of buffet onset and penetration on a supercritical airfoil at transonic speeds.. in *AGARD Specialists Meeting on 'Aircraft Dynamic Loads due to Flow Separation', 1-6 April 1990, Sorrento, Italy*. page 11
- Sugioka Y, Kouchi T, and Koike S (2022) Experimental comparison of shock buffet on unswept and 10-deg swept wings. *Experiments in Fluids* 63
- Sugioka Y, Numata D, Asai K, Koike S, Nakakita K, and Koga S (2015) Unsteady PSP measurement of transonic buffet on a wing. in *AIAA 2015-0025, Proceedings of the 53rd AIAA Aerospace Sciences Meeting, 5-9 January, Kissimmee, Florida*

- Sun Z (2014) *Micro Ramps in Supersonic Turbulent Boundary Layers: An experimental and numerical study*. Ph.D. thesis. Delft University of Technology. ISBN: 978-94-619-1924-3
- Suresh M and Sitaram N (2011) Gurney flap applications for aerodynamic flow control. in *Proceedings of the 9th International Conference on Mechanical Engineering, 18-20 December, Dhaka*
- Szubert D, Grossi F, Jimenez Garcia A, Hoarau Y, Hunt J, and Braza M (2015) Shock-vortex shear-layer interaction in the transonic flow around a supercritical airfoil at high Reynolds number in buffet conditions. *Journal of Fluids and Structures* 55:276–302
- Tambe S (2022) *Boundary-layer instability on rotating cones*. Ph.D. thesis. Delft University of Technology. ISBN: 978-94-6384-289-1
- Thiery M and Coustols E (2006) Numerical prediction of shock induced oscillations over a 2-d airfoil: Influence of turbulence modelling and test section walls. *International Journal of Heat and Fluid Flow* 27:661–670
- Tian Y, Gao SQ, Liu PQ, and Wang JJ (2017) Transonic buffet control research with two types of shock control bump based on rae2822 airfoil. *Chinese Journal of Aeronautics* 30:1681–1696
- Tian Y, Li Z, and Liu PQ (2018) Upper trailing-edge flap for transonic buffet control. *Journal of Aircraft* 55:382–389
- Tijdeman H (1977) *Investigations of the transonic flow around oscillating airfoils*. Ph.D. thesis. Delft University of Technology
- Timme S (2020) Global instability of wing shock-buffet onset. *Journal of Fluid Mechanics* 885 (A37):1–32
- Torenbeek E (2013) *Elements of Aerodynamic Wing Design*. chapter 10, pages 281–318. John Wiley & Sons, Ltd
- van Oudheusden BW (2008) Principles and application of velocimetry-based planar pressure imaging in compressible flows with shocks. *Experiments in Fluids* 45:657–674
- van Oudheusden BW, Jöbsis AJP, Scarano F, and Souverein LJ (2011) Investigation of the unsteadiness of a shock-reflection interaction with time-resolved particle image velocimetry. *Shock Waves* 21:397–409
- van Oudheusden BW, Scarano F, and Casimiri EWF (2006) Non-intrusive load characterization of an airfoil using piv. *Experiments in Fluids* 40:988–992
- van Oudheusden BW, Scarano F, Roosenboom EWM, Casimiri EWF, and Souverein LJ (2007) Evaluation of Integral Forces and Pressure Fields from Planar Velocimetry Data for Incompressible and Compressible Flows. *Experiments in Fluids* 43:153–162

- van Rijswijk N (2012) *TST-27 Transonic Control*. Delft University of Technology
- Vos R and Farokhi S (2015) *Introduction to transonic aerodynamics*. FMIA Vol. 110, Springer
- Wang Z, Chang J, Hou W, and Yu D (2020) Low-frequency unsteadiness of shock-wave/boundary-layer interaction in an isolator with background waves. *Physics of Fluids* 32:056105
- Wanga J, Lia Y, and Choi K (2008) Gurney flap -lift enhancement, mechanisms and applications. *Progress in Aerospace Sciences* 35:1890–1891
- Weiss J (2019) A tutorial on the proper orthogonal decomposition. in *AIAA 2019-3333, AIAA Aviation 2019 Forum, 17-21 June 2019, Dallas, Texas*
- Welch P (1967) The use of fast Fourier transform for the estimation of power spectra: A method based on time averaging over short, modified periodograms. *IEEE Transactions on Audio and Electroacoustics* 15:70–73
- Whitcomb RT and Clark LR (1965) An airfoil shape for efficient flight at supercritical Mach numbers. Technical report. NASA TMX-1109
- Wieneke B (2017) *PIV Uncertainty Quantification and Beyond*. Ph.D. thesis. Delft University of Technology. ISBN: 978-94-92516-88-6
- Zhang Y, Yang P, Li R, and Chen H (2021) Unsteady simulation of transonic buffet of a supercritical airfoil with shock control bump. *Aerospace* 8(8):203

ACKNOWLEDGEMENTS

A PhD is a long journey, which is not feasible without the technical and social support of many people, which I now have the pleasure to acknowledge.

First of all I would like to thank my two supervisors and promotors, *Ferry* and *Bas*. I remember when I wrote to you for the first time in 2017, asking you whether it was possible to join your research group for a thesis project. At that time I was excited about the possibility of doing an experimental thesis in compressible aerodynamics at TU Delft, but I could not have known how much this decision would have (positively) changed my life. I really appreciated your constant trust in giving me the freedom to build my own research path, while always being available for any discussions when required. *Ferry*, from the first moment I met you I particularly liked your insightful suggestions, your friendly approach and your ability to find solutions to problems. *Bas*, I have always admired your supervision skills, which go from the discussion of the complex physics of the phenomena investigated to the correction of a comma missing in the reference list of a paper. Dear promotors, it is needless to say that without your supervision, this thesis would have not been of the same quality. I am delighted that we will continue to work together for the next two years.

I am also very grateful to all the Committee members of my PhD defense for their insightful comments, for their time in reviewing this thesis and for taking part at my PhD defense.

I would also like to thank my HOMER colleagues; it has been a pleasure to be part of such a large project and to collaborate with some of the best experts of the field from all over Europe. Unfortunately, because of COVID we did not see each other in person as much as we would have liked, but I hope there will be plenty of possibilities in future.

During my PhD I also had the pleasure of collaborating with various Master students for their thesis (*Carlos, Pedro, Lucas, Antonello, Manfredi* and *Alessandro*). I really enjoyed working with you and I am certain that you gave me the possibility to improve as a researcher and as a supervisor.

I am definitely proud of being part of such an important university and research Section, which could not be of the same level without the positive contribution of all its staff members. I truly enjoyed the occasional chats (both scientific and not) which I had with all the Professors and I hope to have many more in future. A special thanks goes to *Colette*, for all her help in easing administrative procedures and for organizing pleasant social and scientific events. As an experimentalist I have appreciated the constant help of all the technical staff, thus I would like to thank *Henk-Jan, Dennis, Nico, Frits* and *Peter*. I am particularly grateful to *Frits* and *Peter*; without their support my experiments in TST-27 would have not been feasible, I cannot really count how many times I asked for your help during these years.

A PhD is made up of many ups and downs, but there was no single day in which I doubted my choice of doing a PhD, and this is also merit of my colleagues, who always

helped me in arriving and leaving the office with a genuine smile. First of all, I would like to thank the "older" PhD colleagues who welcomed me on the very first day of this journey (*Tiago, Zeno, Varun, Theo, Xiaodong, Mohamad, Yi, David, Haohua, Weibo, Martin, Paul* and *Wouter*). Then I would like to thank all those who shared these years with me (*Edo, Gabriel, Beto, Luis, Constantin, Alexander, Jordi, Jane, Giulio, Christoph, Sagar, Kushal, Giulia* and *Kaisheng*); I really enjoyed the many social activities we engaged in, the lunches and all the discussions we had. Finally, I would like to wish good luck to all the new PhDs of the lab (*Marina, Ata, Tyler, Adrian, Thomas, Ilda, Kherlen, Babak, Haris, Renzhi, Wencan, Sven, Ruiying, Yifu* and *Mengie*).

The hours outside the lab, would have not been the same without the support of my friends in Delft, for this I would like to thank *Mitro, Edo, Luis, Tijana, Beto, Bea, Jordi, Gabriel, Blanca, Alessandro, Luigi, Arun, Giulio, Jane* and *Varun*. I really enjoyed the time spent with all of you.

Most of my holidays were spent in my home country, Italy, and were certainly enriched by the time passed with my good friends (*Eugenio, Federica, Danilo, Carmen, Andrea, Paolo, Antonio, Alessia, Benedetta, Francisca* and all *the Bolognas*) and my relatives (my dear *Nonni (Edda, Almerindo, Carmela, Luigi)*, *Maria Angela, Francesco, Americo, Mary, Gianmarco, Gemma, Angela, Tonino, Paola, Umberto* and *Stefania*). Thanks to you all, even when distant I felt your support.

A special thanks goes to my older brother, *Damiano*, for all the time we have spent together since I was a child. As the first Doctor in Engineering of the "D'Aguanno family", you have been an example to me. I greatly admire your ambition, capabilities and mindset and I am certain that your close example has and will always positively influence me.

I cannot thank my mother and my father enough, *Rosanna* and *Franco*, for your unconditional love and for your continuous support from day 1. Most of the qualities of the person I have become today are certainly your merit and I particularly appreciated the education I received from both of you and all the values you taught me, you were my first teachers. From you I understood that everything could be reached with hard work, dedication and passion. *Mamma*, I owe you my very calm but determined nature and my love for knowledge and travel, while *Papà*, I owe you my desire for continuous improvement and my love for science.

Lastly, some words to my very first fan and supporter, my lovely girlfriend *Raffaella*. Thank you for always believing in me, encouraging me and keeping me happy even in the most difficult days. Being in a long distance relationship for so many years, could appear to be a not so easy task, but not for us, not when two people really love each other. I still remember when in 2018 I told you for the first time about the possibility of staying for four more years in the Netherlands for a PhD. I was impressed by your sincere support and happiness. I am very proud of what we did in these years together and I am looking forward to spending my future with you.

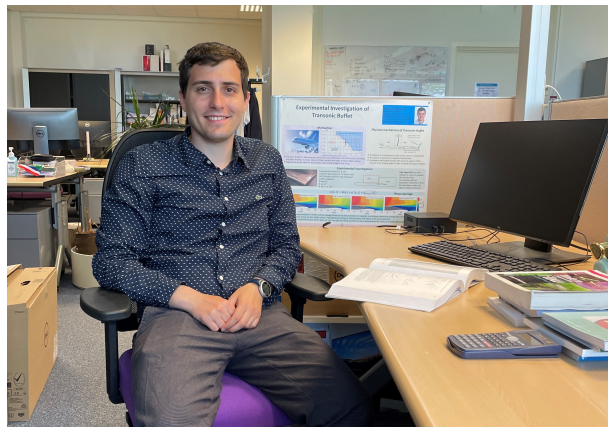
*Alessandro D'Aguanno
Delft, December 2022*

BIOGRAPHICAL NOTE

Alessandro D'Aguanno was born on 12 March 1994 in Cassino, Italy. Since he was a child, Alessandro has shown great interest in science and in particular in (Lego) engineering. Thanks to his father's passion, Alessandro developed an interest in the engineering behind motorbikes and cars, and later, with his first flights and his passion for motorsports, Alessandro became fascinated by aerodynamics. This passion motivated him to start a Bachelor's degree in Aerospace Engineering at the Sapienza University of Rome, where he was also admitted into a parallel excellence program. For his Master's, Alessandro studied Aeronautical Engineering in the same university, although he worked on his thesis as an exchange student in Delft University of Technology. He graduated cum laude in both the degree programs and was awarded a prize for being one of the best students of the Sapienza University of Rome in 2018. During his studies Alessandro also enjoyed collaborating with his colleagues in student engineering teams, such as the "Sapienza Flight Team" and the "Formula Student Team" of TU Delft.

In June 2018, Alessandro started a PhD in TU Delft under the supervision of Dr. Bas van Oudheusden and Dr. Ferry Schrijer, with the aim of experimentally studying the physics of transonic buffet, while also investigating possible control systems. This research was part of the HOMER project which was funded by the European Commission. In these years, he also investigated other phenomena in compressible aerodynamics, such as supersonic panel flutter induced by an impinging oblique shockwave.

Currently, Alessandro is working as a Postdoc in the Aerodynamics Section of TU Delft, where he is involved in the non-intrusive determination of unsteady pressure loads for launcher environment (in transonic regime). In this project Alessandro carries out both PIV experiments and LES simulations.



Summarized Curriculum Vitæ

12-03-1994 Born in Cassino, Italy.

EDUCATION

2012–2015 Bachelor in Aerospace Engineering (cum laude)
Sapienza University of Rome

2015–2018 Master in Aeronautical Engineering (cum laude)
Sapienza University of Rome

2018–2022 Ph.D. candidate in Aerodynamics
Delft University of Technology

PROFESSIONAL EXPERIENCE

2022–present Postdoc in Experimental compressible aerodynamics
Delft University of Technology

OTHER EXPERIENCE

2016–2017 Flight Student Team Engineer
Sapienza flight team, Rome, Italy

2017–2018 Formula Student Engineer
Formula student team Delft, Delft, The Netherlands

AWARDS

2014-2015 "Excellence Program" in Aerospace Engineering
Sapienza University of Rome

2018 Honor prize for the top students of Sapienza University of Rome

LIST OF PUBLICATIONS

JOURNAL ARTICLES

7. **A. D'Aguanno**, A. Corduas, F.E.J. Schrijer, B. W. van Oudheusden *Non-intrusive estimation of the buffet loads on a supercritical airfoil with SCBs* (in preparation).
6. **A. D'Aguanno**, F.E.J. Schrijer, B. W. van Oudheusden *Investigation of 3D Shock Control Bumps for Transonic Buffet Alleviation*, *AIAA Journal* (submitted).
5. **A. D'Aguanno**, P. Quesada Allerhand, F.E.J. Schrijer, B. W. van Oudheusden *Characterization of Shock Induced Panel Flutter with Simultaneous Use of DIC and PIV*, *Experiments in Fluids* **64**, 15 (2023).
4. **A. D'Aguanno**, F.E.J. Schrijer, B. W. van Oudheusden *Experimental Characterization of Upper Trailing Edge Flaps for Transonic Buffet Control*, *Flow, Turbulence and Combustion* (2022).
3. **A. D'Aguanno**, F.E.J. Schrijer, B. W. van Oudheusden *Finite wing and sweep effects on transonic buffet behavior*, *AIAA Journal* **60**, 12 (2022).
2. **A. D'Aguanno**, F.E.J. Schrijer, B. W. van Oudheusden *Spanwise organization of upstream traveling waves in transonic buffet*, *Physics of Fluids* **33**, 106105 (2021).
1. **A. D'Aguanno**, F.E.J. Schrijer, B. W. van Oudheusden *Experimental investigation of the transonic buffet cycle on a supercritical airfoil*, *Experiments in Fluids* **62**, 214 (2021).

CONFERENCE ARTICLES

6. **A. D'Aguanno**, P. Quesada Allerhand, F.E.J. Schrijer, B. W. van Oudheusden *Experimental investigation of shock induced panel flutter with simultaneous use of DIC and PIV*, 20th International Symposium on Application of Laser and Imaging Techniques to Fluid Mechanics, Lisbon, Portugal (2022).
5. **A. D'Aguanno**, C. Camps Pons, F.E.J. Schrijer, B. W. van Oudheusden *Experimental study of the effect of wing sweep on transonic buffet*, AIAA Scitech 2022 Forum, San Diego, USA (2022).
4. **A. D'Aguanno**, F.E.J. Schrijer, B. W. van Oudheusden *Investigation of 3D Shock Control Bumps for Transonic Buffet Alleviation*, AIAA Aviation 2021 Forum, online (2021).
3. **A. D'Aguanno**, L.C.J.M. Mathijssen, F.E.J. Schrijer, B. W. van Oudheusden *Experimental investigation of supersonic panel flutter*, International Conference on Flight vehicles, Aerothermodynamics and Re-entry Missions and Engineering (FAR 2019), Monopoli, Italy (2019).

2. **A. D'Aguanno**, E.F.J. Schrijer, B. W. van Oudheusden *Study of upstream travelling waves in transonic buffet*, 13th International Symposium on Particle Image Velocimetry (ISPIV 2019), Munich, Germany (2019).
1. **A. D'Aguanno**, E.F.J. Schrijer, B. W. van Oudheusden *Transonic buffet control by means of upper Gurney flaps*, 54th 3AF International Conference on Applied Aerodynamics, Paris, France (2019).

